

University of Strathclyde
Department of Chemical and Process Engineering

Monitoring Nucleation at Crystalliser Walls and Formation of Prenucleation Clusters in Solutions

Rachel Sheridan

A thesis submitted to the Department of Chemical and Process Engineering in fulfilment of the requirements for the degree of Doctor of Philosophy.

2017

Contents

DECLARATIONS	I
ACKNOWLEDGEMENTS	II
ABSTRACT.....	III
CONFERENCES AND PUBLICATIONS	V
LIST OF FIGURES	V
LIST OF TABLES	XXIV
THESIS STRUCTURE AND OUTLINE	XXVI
 1 INTRODUCTION TO THE PROJECT	 1
1.1 Project Outline	3
1.1.1 Fouling in Crystallisation	5
1.1.2 The Importance of Understanding Nucleation	6
1.2 Project Impact on Continuous Crystallisation	7
1.2.1 Batch vs. Continuous Crystallisation	7
1.2.2 Fouling in Continuous Crystallisation.....	9
 2 CRYSTALLISATION THEORY	 11
2.1 Chapter Outline	11
2.2 Solubility and Supersaturation	12
2.3 Homogeneous Nucleation	15

2.4	Heterogeneous Nucleation	20
2.5	Two-Step Nucleation Theory	24
2.6	Prenucleation Clusters	31
2.7	Model for Nucleation Rates based on Induction Time Probability Distributions	43
3	DETECTION OF PRENUCLEATION CLUSTERS WITH LIGHT SCATTERING TECHNIQUES	46
3.1	Chapter Outline	46
3.2	Dynamic Light Scattering	47
3.2.1	Autocorrelation Function	48
3.2.1.1	Decay Rate	49
3.2.1.2	Hydrodynamic Diameter	50
3.2.2	Data Analysis of Autocorrelation Functions	51
3.2.2.1	Viscosity vs. Temperature Data	53
3.2.3	Dynamic Light Scattering with the Malvern Zetasizer Nano	54
3.3	Nanoparticle Tracking Analysis with NanoSight (Brownian Microscopy)	56
4	FOULING AND SURFACE BEHAVIOUR IN THE CRYSTALLISATION PROCESS	60
4.1	Chapter Outline	60
4.2	Heat Exchanger Scaling	61

4.3	Fouling Literature Review	62
4.4	Surface Behaviour Literature Review	70
4.4.1	The Chemistry of Surfaces and their Influence on Crystallisation	70
4.4.2	Confined and/or Engineered Surfaces	78
5	MOVING FLUID OSCILLATORY BAFFLED CRYSTALLISER PLATFORM: CONSTRUCTION AND OPERATION	84
5.1	Chapter Outline	84
5.2	Compounds used in the Fouling Study	85
5.3	Oscillatory Flow and the Continuous Oscillatory Baffled Crystalliser	86
5.4	The Construction of the Moving Fluid Oscillatory Baffled Crystalliser	89
5.5	Operation of the Moving Fluid Oscillatory Baffled Crystalliser	93
5.5.1	Calibration	93
5.5.2	Imaging	95
5.5.3	Solution Preparation	95
5.5.4	Oscillation Conditions	96
6	IMAGING OF SURFACE AND BULK CRYSTALLISATION	97
6.1	Chapter Outline	97
6.2	Imaging in Crystallisation Literature Review	98

6.3 New Image Processing Methods
..... **104**

6.3.1	Method 1: Thresholding-Based Methodology	104
6.3.1.1	Issues with the Imaging Technique for Monitoring Fouling	107
6.3.1.2	Obtaining Correct Timescale	108
6.3.2	Method 2: Fouling Graphical User Interface	109
6.3.2.1	Theory and Algorithm Development	109
6.3.2.2	Cropping Methodology for Application to Experimental Work.....	111

7 EXPERIMENTAL RESULTS FROM THE MOVING FLUID OSCILLATORY BAFFLED CRYSTALLISER **113**

7.1 Chapter Outline
..... **113**

7.2 Summary of Experimental Conditions
..... **114**

7.3 L-glutamic Acid Experiments
..... **116**

7.3.1	Temperature and Supersaturation vs. Height for Moving Fluid Oscillatory Baffled Crystalliser for L-glutamic Acid Experiments	116
7.3.2	Summary of L-Glutamic Acid Conditions.....	119
7.3.2.1	Experiment Set 1:	119
7.3.2.2	Experiment Set 2:	120
7.3.3	Average Pixel Intensities of Images for L-glutamic Acid Crystallisations	120
7.3.4	Fouling Induction Times for L-Glutamic Acid	124

7.4 Glycine Experiments
..... **126**

7.4.1	Temperature and Supersaturation vs. Height for Moving Fluid Oscillatory Baffled	
-------	---	--

Crystalliser for Glycine Experiments	126
7.4.2 Summary of Glycine Conditions	127
7.4.3 Average Pixel Intensities of Images for Glycine Crystallisations	128
2.1.1 Fouling Induction Times for Glycine	129
7.5 Nucleation Kinetics for L-Glutamic Acid and Glycine	131
7.6 FoulingGUI Algorithm Data for L-Glutamic Acid and Glycine	135
7.6.1 FoulingGUI vs. Thresholding Method - Fouling vs. Bulk for Aqueous L-Glutamic Acid and	
Glycine Solutions	137
7.7 Discussion of the Moving Fluid Oscillatory Baffled Crystalliser Results	148
7.7.1 Average Pixel Intensities vs. Time.....	148
7.7.2 Estimation of Fouling Induction Times Using Graphical User Interface Algorithm	149
7.7.3 Estimation of Nucleation Kinetics	151
7.8 Conclusions from Moving Fluid Oscillatory Baffled Crystalliser Experiments.....	152
8 LIGHT SCATTERING MEASUREMENTS	154
8.1 Chapter Outline	154
8.2 Systems used in Prenucleation Study	155
8.3 Temperature Cycle Experimental Procedures	157
8.3.1 Experimental Conditions	157
8.3.2 Dynamic Light Scattering Experiments with Zetasizer	160
8.3.3 Brownian Microscopy Experiments with NanoSight.....	162

8.4	Light Scattering Measurements for Water	163
8.5	Glycine Solutions Dynamic Light Scattering Results	165
8.5.1	Glycine Solutions Autocorrelation Functions	165
8.5.1.1	Unfiltered Glycine Solutions 154.9 g/L	165
8.5.1.2	Repeat of Unfiltered Glycine Solutions 154.9 g/L	167
8.5.1.3	0.1 μm PTFE Filtered Glycine Solutions 154.9 g/L	168
8.5.1.4	Unfiltered and 0.1 μm PTFE Filtered Glycine Solutions 234.98 g/L	169
8.5.1.5	Unfiltered and 0.1 μm PTFE Filtered Glycine Solutions 299.06 g/L	172
8.5.2	Deconvolution of Autocorrelation Functions: Analysis of Three Decays vs. Temperature	174
8.5.3	Mean Cluster Diameters vs. Temperature	178
8.5.3.1	1 st Decay	179
8.5.3.2	2 nd Decay	180
8.5.3.3	3 rd Decay	181
8.5.3.4	Example of the Analysis of Curve Fitting before and after the Transition Peak in	
	Hydrodynamic Diameter Changes with Temperature	182
8.6	Glycine Solutions NanoSight Results	184
8.6.1	Particle Size Distributions	184
8.6.1.1	Unfiltered and 0.1 μm PTFE Filtered Glycine Solution 154.9 g/L	185
8.6.1.2	Unfiltered and 0.1 μm PTFE Filtered Glycine Solution 234.98 g/L	187
8.6.1.3	Unfiltered and 0.1 μm PTFE Filtered Glycine Solution 299.06 g/L	190

8.6.2	Cluster Size Distributions with 20 nm Bin Size	192
8.6.3	Changes in Average Cluster Diameter with Temperature for Glycine Solutions	196
8.7	Discussion of Light Scattering Results for Glycine Solutions	198
8.8	Conclusions for Glycine Solutions.....	201
8.9	Urea Solutions Dynamic Light Scattering Results	203
8.9.1	Urea Solutions Autocorrelation Functions	203
8.9.1.1	Unfiltered and 0.1 μm Filtered Urea Solutions 522.61 g/L	203
8.9.1.2	Unfiltered and 0.1 μm Filtered Urea Solutions 785.15 g/L	204
8.9.1.3	Unfiltered and 0.1 μm Filtered Urea Solutions 1149.74 g/L	205
8.9.2	Urea Solutions Mean Count Rates vs. Temperature	206
	Deconvolution of Autocorrelation Functions: Analysis of Three Decays vs. Temperature	208
8.9.4	Mean Cluster Diameters vs. Temperature	215
8.9.2.1	1 st Decay	215
8.9.2.2	2 nd Decay	216
8.9.2.3	3 rd Decay	217
8.10	Urea Solutions NanoSight Data	218
8.10.1	Cluster Size Distributions	218
8.10.1.1	Unfiltered Urea Solution 522.61 g/L	218
8.10.1.2	0.1 μm Filtered Urea Solution 522.61 g/L	219
8.10.1.3	Unfiltered Urea Solution 785.15 g/L	220

8.10.1.4	0.1 μm Filtered Urea Solution 785.15 g/L	221
8.10.1.5	Unfiltered Urea Solution 1149.74 g/L	222
8.10.1.6	0.1 μm PTFE Filtered Urea Solution 1149.74 g/L	223
8.10.2	Cluster Size Distributions with 20 nm Bin Size for First Run of Urea	224
8.10.3	Changes in Average Cluster Diameter with Temperature for Urea Solutions	228
8.11	Discussion of Light Scattering Results for Urea Solutions	230
8.12	Conclusions for Urea Solutions	232
9	OVERALL CONCLUSIONS	233
10	APPENDIX	235
10.1	Second Run of Glycine Solution Light Scattering Experiments	235
10.1.1	Dynamic Light Scattering Results	235 10.1.1.1
	Autocorrelation Functions and Mean Count Rates for the Three Concentrations and both Filtered and Unfiltered	235
10.1.2	NanoSight Results	239
	10.1.2.1 Cluster Size Distributions with 20 nm Bin Size	239
10.2	Urea Solution Second Run 20 nm Bin Cluster Size Distributions.....	242
10.3	Calculated Parameters from Interactive Curve Fitting Tool to Obtain Hydrodynamic	
Diameters from	Dynamic Light Scattering	245
10.3.1	First Run of Glycine Experiments	245
10.3.2	Second Run of Glycine Experiments.....	253

10.3.3	First Run of Urea Experiments	259
10.3.4	Second Run of Urea Experiments	265
11	REFERENCES	271

DECLARATIONS

This thesis is the result of the author's original research. It has been composed by the author and has not been previously submitted for examination which has led to the award of a degree.

The copyright of this thesis belongs to the author under the terms of the United Kingdom Copyright Acts as qualified by University of Strathclyde Regulation 3.50.

Due acknowledgement must always be made of the use of any material contained in, or derived from, this thesis.

Signed:

A handwritten signature in black ink, reading "Rachel Jewell". The script is cursive and fluid, with the first name "Rachel" and the last name "Jewell" clearly distinguishable.

Date: 16th January 2017

ACKNOWLEDGEMENTS

I would like to thank my supervisor Professor Jan Sefcik for all his help, support and guidance throughout my PhD.

Thanks also go to Vishal Raval and Dr Naomi Briggs for technical support in the lab and initial planning of experimental work. I express my gratitude to Dr Jerzy Dziewierz for his expertise and kind assistance with Matlab aspects of my project. Dr Christos Tachtatzis for developing the Fouling GUI algorithm used in my work. I also acknowledge the University of Strathclyde and the EPSRC for the funding to make this project possible.

I am very grateful to my parents for their continued encouragement and moral support in everything I do. To Andrew for his love and support and helping me believe in myself. I want to thank my friend Natalia for her kindness, helpful ideas and patience. She has kept me sane during the last four years by making me laugh every day!

ABSTRACT

This thesis presents the work carried out to monitor nucleation at crystalliser walls (fouling) through image analysis and the behaviour of solutions prior to nucleation using light scattering techniques.

Crystallisation is a process widely used in the pharmaceutical industry, whereby pure solid particles are obtained using supersaturation as the driving force. Fouling occurs when crystals grow on surfaces, where it is difficult to quantify. The consequences of fouling are detrimental to the process and can result in compromising product quality or process shut down. Continuous crystallisation is now increasingly considered as a way to enhance product quality and process efficiency. However, implementing continuous crystallisation in a system prone to fouling becomes problematic and greater understanding is required for either prevention or mitigation. Nucleation is

the key process through which crystallisation occurs, whether it be on surfaces or in bulk solution. It is poorly understood, but thought to occur via liquid-like clusters containing the crystallising material and the solvent or solvent mixture.

The fouling behaviour of aqueous solutions of L-glutamic acid and glycine was studied in an oscillatory flow crystalliser. Images of the glass surface were analysed to provide information regarding the fouling induction period, which has currently not been studied. Bulk and surface nucleation were decoupled by processing the images in a Fouling Graphical User Interface (GUI) algorithm. No one has attempted to do this before, as bulk nucleation is normally the focus and surface nucleation is observed but ignored. Several variables were investigated including concentration, flow conditions and temperature to test their effect on the fouling outcome. It was discovered that higher concentrations fouled more quickly and to a greater extent and that increasing the oscillatory flow decreased the fouling induction time. This novel non-invasive imaging technique provided a new method for measuring fouling and bulk induction times separately during crystallisation processes.

Dynamic light scattering and Brownian microscopy were employed to study the prenucleation behaviour of supersaturated and undersaturated aqueous solutions of glycine and urea. The solutions were exposed to temperature cycling in order to probe the nucleation mechanism and test the reversibility behaviour of the solutions during heating and cooling. It was found that the solutions underwent a reversible transformation above a certain temperature. Larger mesoscale clusters were produced at this point, most likely to aid in maintaining thermodynamic equilibrium in the solution. The larger species were not observed at lower temperatures in the cycle, this was an unexpected result for which the reason is still unclear. Currently in the literature, no studies have been carried out on the reversible effects temperature has on the structure of prenucleation clusters in both undersaturated and supersaturated solutions. Better understanding of clustering phenomena is required to improve our ability to control nucleation during crystallisation processes.

CONFERENCES AND PUBLICATIONS

Conferences:

British Association for Crystal Growth 2014, Leeds, UK

Monitoring Fouling in the Moving Fluid Oscillatory Baffled Crystalliser under Isothermal Conditions

13th – 15th July 2014

19th International Symposium on Industrial Crystallization 2014, Toulouse, France

Monitoring Fouling of L-Glutamic Acid in the Moving Fluid Oscillatory Baffled Crystalliser under Isothermal Conditions using Image Analysis

16th – 19th September 2014

Manufacturing the Future 2014, Glasgow, UK

Monitoring Fouling of L-Glutamic Acid in the Moving Fluid Oscillatory Baffled Crystalliser under Isothermal Conditions using Image Analysis

23rd – 24th September 2014

Publications:

1.Tachtatzis, C. et al., *Image-based Monitoring for Early Detection of Fouling in Crystallisation Processes*. Chemical Engineering Science, 2015. **133**: p. 82-90.

2.Sheridan, R. et al., *Studying the Effect of Oscillatory Flow Conditions on Induction Times and Fouling in the Moving Fluid Oscillatory Baffled Crystalliser Using Image Analysis*. In preparation, 2016.

LIST OF FIGURES

- FIGURE 1. SOLUBILITY DIAGRAM (CONCENTRATION VS. TEMPERATURE) DEPICTING THE UNDERSATURATED AND SUPERSATURATED ZONES WITH WAYS OF GENERATING SUPERSATURATION TO ACHIEVE CRYSTALLISATION. THE LABILE REGIONS (BOTH UNSTABLE AND METASTABLE) AND STABLE REGION ARE LABELLED. 13
- FIGURE 2. CLASSICAL NUCLEATION THEORY: HOW A NUCLEUS FORMS IN SOLUTION FROM SOLUTE MOLECULES TO FORM A NEW SURFACE. 16
- FIGURE 3. FREE ENERGY VS. NUCLEUS RADIUS GRAPH SHOWING THE POSITIONS OF THE CRITICAL FREE ENERGY AND ASSOCIATED RADIUS AT THE POINT WHERE THE SURFACE FREE ENERGY AND THE VOLUME EXCESS FREE ENERGY BALANCE TO CREATE THE CRITICAL NUCLEUS FOR FURTHER CRYSTAL GROWTH. 17
- FIGURE 4. CRITICAL FREE ENERGY AND THE EFFECT OF SUPERSATURATION ON THE CRITICAL RADIUS [27]. 19
- FIGURE 5. THE DIFFERENCES BETWEEN ALL TYPES OF NUCLEATION – HIGHLIGHTING HOW HETEROGENEOUS NUCLEATION BEHAVES DIFFERENTLY FROM THE REST [3]. 20
- FIGURE 6. FREE ENERGY PATHWAY DIFFERENCES BETWEEN HOMOGENEOUS (BLUE) AND HETEROGENEOUS (RED) NUCLEATION WITH CRITICAL RADII AND FREE ENERGIES INDICATED FOR EACH CASE. 21
- FIGURE 7. TYPICAL INTERFACIAL TENSIONS AND BOUNDARIES PRESENT BETWEEN 3 PHASES: CRYSTALLISING SUBSTANCE, THE SOLVENT PRESENT AND THE SOLID SURFACE WHERE NUCLEATION TAKES PLACE [17]. 22
- FIGURE 8. DIAGRAM SHOWING THE STEPS INVOLVED IN THE TWO-STEP NUCLEATION MODEL COMPARED TO THE CLASSICAL NUCLEATION THEORY. (A) SOLUTE MOLECULES ARE PRESENT IN A SUPERSATURATED SOLUTION (B) CLASSICAL THEORY PREDICTS THAT MOLECULES OR ATOMS AGGREGATE TOGETHER ONE AT A TIME TO FORM A CRYSTAL NUCLEUS (C) THE TWO-STEP MODEL ENVISAGES A LOOSELY STRUCTURED CLUSTER CONTAINING BOTH SOLVENT AND SOLUTE FROM WHICH A CRYSTAL NUCLEUS FORMS (D) THIS CRYSTAL NUCLEI CONTINUES TO DEplete SUPERSATURATION FROM WITHIN THE SOLUTION AND GROWS TO FORM THE FINAL CRYSTAL [28]. 25
- FIGURE 9. SEQUENCE OF STEPS SHOWING THE DIFFERENT STAGES DURING THE PROCESS OF FORMING PARTICLES TO ILLUSTRATE THE UNKNOWNs IN THIS AREA – THE SUGGESTION FOR A PRECURSOR TO CRYSTAL NUCLEATION IS MENTIONED HERE [31]. 27
- FIGURE 10. (A): HIGH-RESOLUTION CRYO-TEM IMAGE OF A 9 MM SOLUTION OF $\text{Ca}(\text{HCO}_3)_2$ AFTER THE IMAGE HAD BEEN PROCESSED WHERE NUCLEATION CLUSTERS ARE SEEN – CIRCLED IN

BLACK AND THE SCALE BAR REPRESENTS 20 NM. (B): IMAGES THAT HAVE NOT BEEN FILTERED SHOWING THE AREA HIGHLIGHTED IN RED IN (A). WHEN HIGH MAGNIFICATION IS USED HERE ALL THE PARTICLES THAT CAN BE IDENTIFIED ARE CIRCLED IN BLACK AND ANY PARTICLE BELOW THE DETECTION LIMIT OF 0.45 NM (3 TIMES THE SIZE OF THE PIXELS) ARE DEEMED TO BE NOISE. THE SCALE BAR HERE IS 5 NM. (C): THIS REPRESENTS THE PARTICLE DIAMETER DISTRIBUTION IN NANOMETRES OF THE PRENUCLEATION SPECIES DETECTED IN THE CRYO-TEM IMAGES DURING THIS STUDY [32].

29

FIGURE 11. SCHEMATIC DIAGRAM OF THE PRENUCLEATION CLUSTER STRUCTURE (THE TRUE STRUCTURE IS AT PRESENT UNKNOWN) INDICATING THAT IT IS CONSTRUCTED WITH BOTH SOLUTE AND SOLVENT MOLECULES TO CREATE A LOOSELY HELD CLUSTER WITH HIGHER DENSITY THAN THE REST OF THE SOLUTION BUT FROM WHICH NUCLEATION CAN TAKE PLACE. SOLUTE MOLECULES ARE IN GREEN, THE SOLVENT MOLECULES ARE IN GREY AND THE PRENUCLEATION CLUSTER SURFACE LIMIT IS INDICATED IN BLUE.

31

FIGURE 12. DIAGRAM REPRESENTING THE CHANGES IN STRUCTURE OF THE UREA MOLECULE AS IT UNDERGOES CRYSTALLISATION IN WATER. IN SCENARIO I, THE UREA MOLECULES SELFASSEMBLE TO CREATE THE CRYSTALLINE PHASE DIRECTLY. SCENARIO II SHOWS THAT THE UREA MOLECULES ARE ABLE TO AGGREGATE TO FORM AN AMORPHOUS STATE WHICH CAN TRANSFORM INTO THE CRYSTALLINE PHASE. PRIMARY CLUSTERS SHOWN IN SCENARIO III RESULT FROM THE AGGREGATION OF UREA MOLECULES, THEN GROWTH INCREASE OF THESE PRIMARY CLUSTERS MAKE UP THE AMORPHOUS PHASE (SCENARIO IV) OR THE UREA CRYSTAL NUCLEI (SCENARIO V) [48].

38

FIGURE 13. CRYO-TEM IMAGES OF PRENUCLEATION CLUSTERS IN UNFILTERED UNDERSATURATED SOLUTIONS, ACCOMPANIED BY THEIR ELECTRON DIFFRACTION PATTERNS FOR (A) DL-ALANINE (150 MG/ML) AND (B) GLYCINE (200 MG/ML) [50].

40

FIGURE 14. ILLUSTRATION OF THE REVERSIBILITY PROCESS OF PRENUCLEATION CLUSTERS – I.E. IF THEY REAPPEAR ON DISSOLUTION OF CRYSTALS GROWN FROM SUPERSATURATED SOLUTION I.E. THEY ARE IN EQUILIBRIUM WITH THE CRYSTALS IN SOLUTION [10].

40 FIGURE 15.

PICTURE OF GLYCINE CRYSTALS GROWN FROM A 270 MG/ML SOLUTION, CREATED BY CONTINUOUSLY INVERTING THE VIAL OF SOLUTION WITH A TUMBLING MAGNETIC STIRRER BAR FOR 3 HOURS. SMALL PORTIONS OF THE SOLUTION WERE ANALYSED ON A MICROSCOPE SLIDE AND WERE COVERED TO REDUCE EVAPORATION. THE IMAGES SHOWN HERE WERE TAKEN AT TIME (A) 0 MIN (B) 1 MIN (C) 5 MIN AND (D) 10 MIN AFTER INITIAL CRYSTALS WERE DETECTED [10].

41

FIGURE 16. DYNAMIC LIGHT SCATTERING DIAGRAM DEPICTING THE MAIN COMPONENTS OF THE SYSTEM.

47

FIGURE 17. SCREENSHOT OF THE INTERACTIVE CURVE FITTING TOOL CREATED BY DR. JERZY

DZIEWIERZ INDICATING THE INTERACTIVE CURSORS SHOWN IN RED, GREEN AND BLUE CORRESPONDING TO THE 1 ST , 2 ND AND 3 RD DECAYS PRESENT IN THE AUTOCORRELATION FUNCTION RESPECTIVELY. THE RMS ERROR VALUE AND THE COEFFICIENTS ARE GIVEN.	52
FIGURE 18. HARDWARE COMPONENTS OF THE ZETASIZER NANO SYSTEM FROM MALVERN © [58].	54
FIGURE 19. PHOTOGRAPH DEPICTING THE SETUP OF THE BROWNIAN MICROSCOPY EQUIPMENT SHOWING THE LASER BEAM PASSING THROUGH THE SAMPLE CELL.	56
FIGURE 20. NTA SCREEN CAPTURE OF RECORDING FROM NANOSIGHT EXPERIMENT DURING THE ANALYSIS OF SUPERSATURATED GLYCINE SOLUTION (S=1.1 BASED ON SOLUBILITY AT 20°C) FILTERED WITH PTFE SYRINGE FILTER.	57
FIGURE 21. DEPICTION OF FOULING ON HEAT TRANSFER SURFACES VIA CRYSTALLISATION OF CALCIUM SULFATE WHERE PRELIMINARY CALCULATIONS TO COMPARE WITH THE SIMULATION VALUES COULD BE COMPARED [69].	66
FIGURE 22. IMAGES SHOWING SYSTEMS WITH (A) AND WITHOUT (B) PULSATING FLOW WHERE WITH PULSATING FLOW THE ENCRUSTATION IS VISIBLY REDUCED DUE TO THE CHANGE IN THE FLOW PROPERTIES [71].	67
FIGURE 23. THE CYCLE OF ENCRUSTATION STARTING FROM THE INITIATION WHICH IS EITHER INDUCED BY THE WALL OR PARTICLE DEPOSITION AND FINISHING WITH GROWTH AND DETACHMENT FROM THE SURFACE [72].	68
FIGURE 24. COMPOUNDS UNDER STUDY FOR THE EFFECT DIFFERENT POLYMER SURFACES HAD ON THEIR NUCLEATION: (A) ACETAMINOPHEN (B) ACETYLSALICYLIC ACID (C) GLYCINE.	70
FIGURE 25. CRYSTALLISATION OF ASPIRIN (A) WITH AND (B) WITHOUT POLYMER FILM SHOWING THAT NUCLEATION OCCURRED QUICKER ON THE POLYMER SURFACE AND THEN DEPLETED THE MOLECULES FROM SOLUTION HENCE NO CRYSTALS WERE FOUND IN THE BULK [16].	72
FIGURE 26. NEO-PENTANOL CRYSTALLISING ON MICA SURFACE WHEN IT WAS SCRATCHED AND UNSCRATCHED SHOWING THE EFFECT SURFACE ROUGHNESS HAS ON THE NUCLEATION EVENTS TAKING PLACE. WHEN THE SURFACE IS ROUGHER, MORE NUCLEATION EVENTS TAKE PLACE [15].	73
FIGURE 27. PBMA (POLY(N-BUTYL METHACRYLATE)) AND PMMA (POLY(METHYL METHACRYLATE)) STRUCTURES [74].	74
FIGURE 28. SELECTION PROCESS FOR SUBSTRATE SELECTION FOR HETEROGENEOUS NUCLEATION IN ORDER TO CONTROL THE POLYMORPH BEING OBTAINED [75].	75
FIGURE 29. SEM IMAGE OF ADHESIVE TAPE COATED WITH SUPERHYDROPHOBIC POLYMER. INSERT: AN IMAGE OF A WATER DROPLET ON THIS SURFACE [78].	77
FIGURE 30. A GENERIC POROGEN SHOWING BASIC FEATURES OF A PORE-GENERATING MACROMOLECULE. AS THE POROGEN BREAKS DOWN WITHIN THE ORGANOSILICATE MATRIX	

(IN THIS EXAMPLE), IT FORMS SMALL MOLECULES; WHICH THEN DIFFUSE THROUGH THE MATRIX AND ESCAPE AS GASES LEAVING PORES [79].	77
FIGURE 31. PATTERNED GLYCINE CRYSTALS NUCLEATED ON 100 μM (LEFT) AND 140 μM (RIGHT) GOLD ISLANDS [80].	78
FIGURE 32. A) SCHEMATIC REPRESENTATION OF THE BIFUNCTIONAL SAMS PATTERN B) SCHEMATIC REPRESENTATION OF THE GLYCINE CRYSTALLISATION PROCEDURE; THE SUPERSATURATION LEVEL IS CONTROLLED BY THE SLOW DIFFUSION OF AN ANTISOLVENT (ETHANOL) INTO THE GLYCINE/WATER SOLUTION [81].	79
FIGURE 33. (A) OPTICAL MICROSCOPE IMAGE (X 150) OF 1600 μM^2 AND (B) AFM IMAGE OF 4 μM^2 OF THE 500 NM PATTERNED SAMS ON SILICON SUBSTRATE [81].	80
FIGURE 34. (A) SLOW COOLING AND (B) SLOW EVAPORATION METHODS TO OBTAIN GLYCINE CRYSTALS [82].	81
FIGURE 35. NUCLEATION AND GROWTH MECHANISM IN NYLON 6 NANOCOMPOSITES [84].	83
FIGURE 36. MOLECULAR STRUCTURE OF (A) L-GLUTAMIC ACID AND (B) GLYCINE.	85
FIGURE 37. A TYPICAL CONTINUOUS OSCILLATORY BAFFLED REACTOR (COBR) SETUP INDICATING THE INLET AND OUTLET AND BAFFLED STRAIGHTS CONNECTED VIA BENDS [93].	87
FIGURE 38. INNER DIMENSIONS OF THE CONTINUOUS OSCILLATORY BAFFLED CRYSTALLISER DN15 GLASS STRAIGHT [94].	88
FIGURE 39. CONTINUOUS OSCILLATORY BAFFLED CRYSTALLISER (COBC) ARRANGEMENT SHOWING ONE GLASS STRAIGHT WHICH IS OF INTEREST FOR ANALYSING FOULING BEHAVIOUR.	90
FIGURE 40. THE REMOVED GLASS STRAIGHTS FROM THE CONTINUOUS OSCILLATORY BAFFLED CRYSTALLISER (COBC) REQUIRED TO CONSTRUCT THE MOVING FLUID OSCILLATORY BAFFLED CRYSTALLISER (MFOBC) WITH THE AREA OF INTEREST FOR MONITORING FOULING BEHAVIOUR UNDER CERTAIN FLOW AND TEMPERATURE CONDITIONS CIRCLED IN RED.	90
FIGURE 41. MOVING FLUID OSCILLATORY BAFFLED CRYSTALLISER SETUP SHOWING TEMPERATURE AND CAMERA POSITIONS AS WELL AS THE MECHANISM FOR GENERATING THE OSCILLATORY FLOW – I.E. THE BELLOWS MOVED BY THE MOTOR WHICH IS CONTROLLED VIA THE CONTROL BOX WHERE THE AMPLITUDE (MM) AND FREQUENCY (HZ) OF THE OSCILLATION IS SELECTED.	92
FIGURE 42. FOULING ABOVE LIQUID LINE WHEN HEATED TO PREVENT THE SYSTEM FROM SELF-SEEDING.	94
FIGURE 43. EXPERIMENTAL SETUP FOR MICROSCOPIC STUDY OF CALCIUM CARBONATE FOULING [100].	102
FIGURE 44. MICROSCOPIC IMAGES AT MAGNIFICATION 40X TO SHOW THE PROGRESSION OF THE FOULING OF CALCIUM CARBONATE [100].	103
FIGURE 45. VISUAL REPRESENTATION OF THE CROPPING TAKING PLACE IN THE MATLAB CODE USED FOR DETERMINING THE AVERAGE PIXEL INTENSITIES OVER TIME DURING THE	

- CRYSTALLISATION AND FOR PINPOINTING THE TIME AT WHICH FOULING OCCURS. 105
 FIGURE 46. IMAGE INTENSITY MAP OBTAINED VIA METHOD 1. DARKER RED AREAS IN THE
 SCREENSHOT ARE AREAS OF DENSER FOULING ON THE GLASS WALL. LIGHTER AREAS CAN BE
 ATTRIBUTED TO CRYSTALS MOVING FREELY IN THE BULK SOLUTION AND THESE INTENSITIES
 WILL VARY SLIGHTLY AND NOT REMAIN CONSTANT DUE TO THE NATURE OF THE FLUID FLOW
 IN THE SYSTEM. 106
- FIGURE 47. RAW WEBCAM IMAGE SHOWING AREA WHERE THE TIME STAMP REGION (HIGHLIGHTED
 IN RED) WAS CUT FOR ANALYSIS BY THE MATLAB CODE FOR OBTAINING REAL TIME OF IMAGE
 CAPTURE. 108
- FIGURE 48. SIGNALS THAT ARE AVAILABLE IN ORDER TO OBTAIN TIMES FOR THE COMBINED
 INDUCTION TIME AS WELL AS THE TECHNIQUE SUGGESTED FOR SEPARATING BULK AND
 SURFACE NUCLEATION [101]. 109
- FIGURE 49. LOWER CAMERA RAW IMAGE SHOWING CROPPED REGION. 112
- FIGURE 50. UPPER CAMERA RAW IMAGE SHOWING CROPPED REGION. 112
- FIGURE 51. MOVING FLUID OSCILLATORY BAFFLED CRYSTALLISER SETUP SHOWING TEMPERATURE
 AND CAMERA POSITIONS AS WELL AS THE MECHANISM FOR GENERATING THE OSCILLATORY
 FLOW – I.E. THE BELLOWS MOVED BY THE MOTOR WHICH IS CONTROLLED VIA THE CONTROL
 BOX WHERE THE AMPLITUDE (MM) AND FREQUENCY (HZ) OF THE OSCILLATION IS SELECTED.
 114
- FIGURE 52. MEASURED TEMPERATURE AND CORRESPONDING SUPERSATURATION VS. HEIGHT OF
 THE MFOBC FOR L-GLUTAMIC ACID CONDITIONS OF 1 HZ 45 MM WHERE ○: 42.4 G/L □: 28.3
 G/L Δ: 21.2 G/L WHERE NO CRYSTALS FORMED AT THIS LOWEST CONCENTRATION OVER THE
 TIMESCALES USED AND ◇ INDICATES THE TEMPERATURE PROFILE OVER THE SYSTEM. THE
 BARS ON THE CHART REPRESENT THE POSITION OF THE COLLARS IN THE MFOBC I.E. WHERE
 ONE GLASS STRAIGHT STARTS AND FINISHES. 117
- FIGURE 53. MEASURED TEMPERATURE AND CORRESPONDING SUPERSATURATION VS. HEIGHT OF
 THE MFOBC FOR L-GLUTAMIC ACID CONDITIONS OF 2 HZ 45 MM SHOWING DATA PERTAINING
 TO THE THREE CONCENTRATIONS WHICH WERE USED: ○: 42.4 G/L; □: 28.3 G/L AND Δ: 21.2 G/L
 AND THE TEMPERATURE PROFILE: ◇. COLLAR POSITIONS ON THE MFOBC ARE INDICATED. 117
- FIGURE 54. MEASURED TEMPERATURE VS. HEIGHT OF THE MFOBC FOR ALL L-GLUTAMIC ACID
 CONDITIONS USED: 1 HZ 45 MM AND 2 HZ 45 MM FOR CRYSTALLISATION TEMPERATURES OF
 20°C AND 30°C. Δ: [20°C 1 HZ 45 MM] □: [20°C 2 HZ 45 MM] ◇: [30°C 1 HZ 45 MM] ○: [30°C 2
 HZ 45 MM]. COLLAR POSITIONS ARE INDICATED. 118
- FIGURE 55. SUPERSATURATION DETERMINED FROM MEASURED TEMPERATURE VS. HEIGHT DATA
 FOR L-GLUTAMIC ACID 42.4 G/L SOLUTION EXPERIMENTS UNDER CRYSTALLISATION

TEMPERATURE OF 30°C UNDER TWO OSCILLATION CONDITIONS: 1 HZ 45 MM [o] AND 2 HZ 45 MM [□]. COLLAR POSITIONS BETWEEN GLASS STRAIGHTS ARE INDICATED ON THE GRAPH. 118	
FIGURE 56. PLOTS OF AVERAGE PIXEL INTENSITY VS. TIME FOR ALL L-GLUTAMIC ACID 42.39 G/L EXPERIMENTS UNDER THE TWO OSCILLATION CONDITIONS OF 1 HZ 45 MM (SOLID BLUE LINE) AND 2 HZ 45 MM (DASHED GREEN LINE).	121
FIGURE 57. PLOTS OF AVERAGE PIXEL INTENSITY VS. TIME FOR ALL L-GLUTAMIC ACID 28.26 G/L EXPERIMENTS UNDER THE TWO OSCILLATION CONDITIONS OF 1 HZ 45 MM (BLUE) AND 2 HZ 45 MM (DASHED GREEN LINE).	121
FIGURE 58. PLOTS OF AVERAGE PIXEL INTENSITY OVER TIME FOR L-GLUTAMIC ACID 42.39 G/L AT 2 HZ 45 MM OSCILLATION AT CRYSTALLISATION TEMPERATURES OF 20°C: (SOLID BLUE LINE) AND 30°C: (DASHED RED LINE).	122
FIGURE 59. PLOTS OF AVERAGE PIXEL INTENSITY OVER TIME FOR L-GLUTAMIC ACID 42.39 G/L AT 1 HZ 45 MM OSCILLATION AT CRYSTALLISATION TEMPERATURES OF 20°C: (SOLID BLUE LINE) AND 30°C: (DASHED RED LINE).	123
FIGURE 60. SOLUBILITY OF L-GLUTAMIC ACID IN WATER: SOLUBILITY AT 20°C IN GREEN AND AT 30°C IN ORANGE [87].	123
FIGURE 61. CHART SHOWING ALL FOULING INDUCTION TIMES FOR L-GLUTAMIC ACID EXPERIMENTS AT CONCENTRATION 42.39 G/L UNDER THE FOLLOWING OSCILLATION CONDITIONS: o: 1 HZ 45 MM □: 2 HZ 45 MM AND 28.26 G/L AT: ◇: 2 HZ 45 MM Δ: 1 HZ 45 MM ALL AT 20°C CRYSTALLISATION TEMPERATURE.	124
FIGURE 62. SUMMARY OF FOULING INDUCTION TIMES FOR L-GLUTAMIC ACID 42.39 G/L UNDER TWO DIFFERENT CRYSTALLISATION TEMPERATURES OF 20°C AND 30°C. □: 20°C 2 HZ 45 MM o: 20°C 1 HZ 45 MM ◇: 30°C 2 HZ 45 MM Δ: 30°C 1 HZ 45 MM.	125
FIGURE 63. TEMPERATURE VS. HEIGHT DATA FOR ALL GLYCINE OSCILLATION CONDITIONS USED WITH CONCENTRATION 384.51 G/L: □: 1 HZ 23 MM; Δ: 1 HZ 45 MM; o: 2 HZ 23 MM AND ◇: 2 HZ 45 MM WITH COLLAR POSITIONS INDICATED.	126
FIGURE 64. SUPERSATURATION VS. HEIGHT FOR ALL GLYCINE CONDITIONS USED AT CONCENTRATION 384.51 G/L: ◇: 1 HZ 23 MM; X: 1 HZ 45 MM; □: 2 HZ 23 MM AND Δ: 2 HZ 45 MM. THE SUPERSATURATION PROFILE CORRESPONDING TO A CONCENTRATION OF 299.06 G/L UNDER CRYSTALLISATION TEMPERATURE 20°C AND OSCILLATION CONDITIONS OF 1 HZ 45 MM [o] WHERE AFTER 4 HOURS NO CRYSTALS WERE FORMED IN THE MFOBC. COLLAR POSITIONS ARE ALSO INDICATED.	127
FIGURE 65. PLOTS OF AVERAGE PIXEL INTENSITY VS. TIME FOR ALL GLYCINE 384.51 G/L EXPERIMENTS UNDER THE TWO OSCILLATION CONDITIONS OF 2 HZ 45 MM (RED LINE) AND 2 HZ 23 MM (BLUE LINE).	128
FIGURE 66. PLOTS OF AVERAGE PIXEL INTENSITY VS. TIME FOR ALL GLYCINE 384.51 G/L EXPERIMENTS UNDER THE TWO OSCILLATION CONDITIONS OF 2 HZ 45 MM (RED LINE) AND 1	

HZ 45 MM (BLUE LINE). INDUCTION TIMES FOR GLYCINE	129
EXPERIMENTS AT 384.51 G/L - □: 2 HZ 45 MM ○: 1 HZ 45 MM ◇: 2 HZ 23 MM AND Δ: 1 HZ 23 MM AT 20°C CRYSTALLISATION TEMPERATURE.	129
FIGURE 68. CUMULATIVE PROBABILITY DISTRIBUTIONS OF INDUCTION TIMES FOR ALL L-GLUTAMIC ACID EXPERIMENTS UNDER 1 HZ 45 MM 28.26 G/L [◇]; 2 HZ 45 MM 28.26 G/L [○]; 1HZ 45 MM 42.39 G/L [□]; 2 HZ 45 MM 42.39 G/L [X]; 1 HZ 45 MM 42.39 G/L 30°C CRYSTALLISATION TEMPERATURE [+] AND 2 HZ 45 MM 42.39 G/L 30°C CRYSTALLISATION TEMPERATURE [Δ] WITH TER HORST FITS SHOWN.	131
FIGURE 69. CHART DEPICTING THE GROWTH TIMES (○) AND NUCLEATION RATES (□) FOR LGLUTAMIC ACID EXPERIMENTS UNDER 2 DIFFERENT OSCILLATION CONDITIONS WHICH ARE 1 HZ 45 MM AND 2 HZ 45 MM AND UNDER TWO DIFFERENT CONCENTRATIONS OF 28.26 AND 42.39 G/L ALL OF WHICH ARE INDICATED.	132
FIGURE 70. CUMULATIVE PROBABILITY DISTRIBUTIONS OF INDUCTION TIMES FOR 384.51 G/L GLYCINE EXPERIMENTS UNDER 1 HZ 23 MM[◇]; 1 HZ 45 MM [□]; 2HZ 23 MM [○] AND 2 HZ 45 MM [X] OSCILLATION WITH TER HORST FITS SHOWN.	133
FIGURE 71. CHART DEPICTING THE GROWTH TIMES (○) AND NUCLEATION RATES (□) FOR 384.51 G/L GLYCINE EXPERIMENTS UNDER THE 4 DIFFERENT OSCILLATION CONDITIONS WHICH ARE 1 HZ 23 MM, 2 HZ 23 MM, 1 HZ 45 MM AND 2 HZ 45 MM INDICATED ABOVE.	133
FIGURE 72. CORRELATION PLOT BASED ON THRESHOLDING (○) AND ALGORITHM DATA (□) FOR COMPARING FOULING INDUCTION TIMES OBTAINED FOR THE SAME IMAGE SETS OF L- GLUTAMIC ACID SOLUTION AT 42.39 G/L WITH OSCILLATION CONDITIONS OF 2 HZ 45 MM.	136
FIGURE 73. CORRELATION PLOT OF ALGORITHM FOULING INDUCTION TIME [□] VS. THRESHOLDING FOULING INDUCTION TIME [○] FOR L-GLUTAMIC ACID 28.26 G/L UNDER OSCILLATION CONDITIONS OF 2 HZ 45 MM.	138
FIGURE 74. CORRELATION PLOT OF ALGORITHM FOULING INDUCTION TIME [□] VS. THRESHOLDING FOULING INDUCTION TIME [○] FOR L-GLUTAMIC ACID 28.26 G/L UNDER OSCILLATION CONDITIONS OF 1 HZ 45 MM.	139
FIGURE 75. CORRELATION PLOT OF ALGORITHM FOULING INDUCTION TIME [□] VS. THRESHOLDING FOULING INDUCTION TIME [○] FOR L-GLUTAMIC ACID 42.39 G/L UNDER OSCILLATION CONDITIONS OF 2 HZ 45 MM.	140
FIGURE 76. CORRELATION PLOT OF ALGORITHM FOULING INDUCTION TIME [□] VS. THRESHOLDING FOULING INDUCTION TIME [○] FOR L-GLUTAMIC ACID 42.39 G/L UNDER OSCILLATION CONDITIONS OF 1 HZ 45 MM.	141
FIGURE 77. CORRELATION PLOT OF ALGORITHM FOULING INDUCTION TIME [□] VS. THRESHOLDING	

FOULING INDUCTION TIME [o] FOR L-GLUTAMIC ACID 42.39 G/L UNDER OSCILLATION CONDITIONS OF 2 HZ 45 MM AND CRYSTALLISATION TEMPERATURE 30°C.	142
FIGURE 78. CORRELATION PLOT OF ALGORITHM FOULING INDUCTION TIME [□] VS. THRESHOLDING FOULING INDUCTION TIME [o] FOR L-GLUTAMIC ACID 42.39 G/L UNDER OSCILLATION CONDITIONS OF 1 HZ 45 MM AND CRYSTALLISATION TEMPERATURE 30°C.	143
FIGURE 79. CORRELATION PLOT OF ALGORITHM FOULING INDUCTION TIME [□] VS. THRESHOLDING FOULING INDUCTION TIME [o] FOR GLYCINE 384.51 G/L UNDER OSCILLATION CONDITIONS OF 1 HZ 23 MM.	144
FIGURE 80. CORRELATION PLOT OF ALGORITHM FOULING INDUCTION TIME [□] VS. THRESHOLDING FOULING INDUCTION TIME [o] FOR GLYCINE 384.51 G/L UNDER OSCILLATION CONDITIONS OF 2 HZ 45 MM.	145
FIGURE 81. CORRELATION PLOT OF ALGORITHM FOULING INDUCTION TIME [□] VS. THRESHOLDING FOULING INDUCTION TIME [o] FOR GLYCINE S=1.8 UNDER OSCILLATION CONDITIONS OF 1 HZ 45 MM.	146
FIGURE 82. CORRELATION PLOT OF ALGORITHM FOULING INDUCTION TIME [□] VS. THRESHOLDING FOULING INDUCTION TIME [o] FOR GLYCINE 384.51 G/L UNDER OSCILLATION CONDITIONS OF 2 HZ 23 MM.	147
FIGURE 83. SOLUBILITY OF GLYCINE IN WATER [104].	155
FIGURE 84. MOLECULAR STRUCTURE OF UREA.	155
FIGURE 85. SOLUBILITY OF UREA IN WATER [107].	156
FIGURE 86. INCUBATOR TEMPERATURE PROFILE DETERMINING THE POINT WHERE A STEADY STATE TEMPERATURE IS ACHIEVED WITHIN THE INCUBATOR AFTER ~45 MINUTES WITH NO PARTIAL OPENING OF THE INCUBATOR DOOR.	159
FIGURE 87. TEMPERATURE CYCLE IN THE ZETASIZER FOR DYNAMIC LIGHT SCATTERING EXPERIMENTS FOR EXPLORING THE TEMPERATURE EFFECTS ON MESOSCALE CLUSTER SIZE AND CONCENTRATION AND WHETHER OR NOT THEY ARE REVERSIBLE.	160
FIGURE 88. TEMPERATURE CYCLE IN THE NANOSIGHT FOR BROWNIAN MOTION EXPERIMENTS FOR EXPLORING THE TEMPERATURE EFFECTS ON MESOSCALE CLUSTER SIZE AND CONCENTRATION AND WHETHER OR NOT THEY ARE REVERSIBLE.	162
FIGURE 89. AUTOCORRELATION FUNCTIONS FOR UNFILTERED WATER DURING HEATING FROM 10 TO 50°C (A) AND 60°C (B).	163
FIGURE 90. MEAN COUNT RATE FOR UNFILTERED WATER DURING THE HEATING STAGE FROM 10 TO 60°C.	164
FIGURE 91. PARTICLE SIZE DISTRIBUTIONS FROM NANOSIGHT MEASUREMENTS OF UNFILTERED WATER DURING THE HEATING STAGE FROM 15 TO 50°C	164
FIGURE 92. AUTOCORRELATION FUNCTIONS FROM DYNAMIC LIGHT SCATTERING MEASUREMENTS (ANGLE 173°) OF TEMPERATURE CYCLE FROM 10-80-10°C WITH THE FIRST RUN OF	

UNFILTERED AQUEOUS GLYCINE SOLUTION OF CONCENTRATION 154.9 G/L WHICH IS UNDERSATURATED AT 10°C (AT THIS TEMPERATURE THE SOLUTION HAS SUPERSATURATION VALUE OF $S=0.95$). 165

FIGURE 93. MEAN COUNT RATE RECORDED IN KILO COUNTS PER SECOND FOR THE TEMPERATURE STAGES DURING THE DYNAMIC LIGHT SCATTERING MEASUREMENTS FOR GLYCINE CONCENTRATION 154.9 G/L FOR UNFILTERED SOLUTION WHERE DARK RED IS THE HEATING STAGE AND LIGHT RED IS THE COOLING STAGE. 166

FIGURE 94. AUTOCORRELATION FUNCTIONS FROM DYNAMIC LIGHT SCATTERING MEASUREMENTS (ANGLE 173°) OF TEMPERATURE CYCLE FROM 10-80-10°C WITH UNFILTERED AQUEOUS GLYCINE SOLUTION OF CONCENTRATION 154.9 G/L WHICH IS UNDERSATURATED STILL AT 10°C (AT THIS TEMPERATURE THE SOLUTION HAS SUPERSATURATION VALUE OF $S=0.95$). 167

FIGURE 95. AUTOCORRELATION FUNCTIONS FROM DYNAMIC LIGHT SCATTERING MEASUREMENTS (ANGLE 173°) OF TEMPERATURE CYCLE FROM 10-80-10°C WITH AQUEOUS GLYCINE SOLUTION OF CONCENTRATION 154.9 G/L WHICH IS UNDERSATURATED STILL AT 10°C (AT THIS TEMPERATURE THE SOLUTION HAS SUPERSATURATION VALUE OF $S=0.95$). THIS SOLUTION WAS FILTERED THROUGH A PTFE SYRINGE FILTER WITH PORE DIAMETER 0.1 MM. THE GRAPH SECTION IN THE TOP RIGHT CORNER SHOWS A ZOOMED IMAGE OF THE Y-AXIS ON THE SCALE FROM 0 TO 0.05 TO SHOW THE SEPARATION OF THE AUTOCORRELATION FUNCTIONS MORE CLEARLY. 168

FIGURE 96. MEAN COUNT RATE RECORDED IN KILO COUNTS PER SECOND FOR EACH TEMPERATURE STAGE DURING THE DYNAMIC LIGHT SCATTERING MEASUREMENTS FOR GLYCINE CONCENTRATION 154.9 G/L BOTH FOR UNFILTERED (RED) AND 0.1 MM PTFE FILTERED (BLUE) SOLUTION AND FOR THE FIRST (A) AND SECOND (B) REPETITION. THE HEATING STAGES ARE PRESENTED IN THE DARKER COLOUR. 169

FIGURE 97. AUTOCORRELATION FUNCTIONS FROM DYNAMIC LIGHT SCATTERING MEASUREMENTS (ANGLE 173°) OF TEMPERATURE CYCLE FROM 10-80-10°C WITH UNFILTERED (A) AND 0.1 MM PTFE SYRINGE FILTERED (B) AQUEOUS GLYCINE SOLUTION OF CONCENTRATION 234.98 G/L. 169

FIGURE 98. AUTOCORRELATION FUNCTIONS FROM DYNAMIC LIGHT SCATTERING MEASUREMENTS (ANGLE 173°) OF TEMPERATURE CYCLE FROM 10-80-10°C WITH AQUEOUS GLYCINE SOLUTION OF CONCENTRATION 234.98 G/L. THIS SOLUTION WAS FILTERED THROUGH A PTFE SYRINGE FILTER WITH PORE DIAMETER 0.1 MM. 170

FIGURE 99. MEAN COUNT RATE RECORDED IN KILO COUNTS PER SECOND FOR EACH TEMPERATURE STAGE DURING THE DYNAMIC LIGHT SCATTERING MEASUREMENTS FOR GLYCINE CONCENTRATION 234.98 G/L BOTH FOR UNFILTERED (RED) AND 0.1 MM PTFE FILTERED (BLUE)

- SOLUTION. THE HEATING STAGES ARE PRESENTED IN THE DARKER COLOUR. 171
- FIGURE 100. MEAN COUNT RATE RECORDED IN KILO COUNTS PER SECOND FOR EACH TEMPERATURE STAGE DURING THE DYNAMIC LIGHT SCATTERING MEASUREMENTS FOR GLYCINE CONCENTRATION 234.98 G/L BOTH FOR UNFILTERED (RED) AND 0.1 MM PTFE FILTERED (BLUE) SOLUTION WHEN THE SOLUTION WAS FILTERED AGAIN DUE TO UNUSUAL HIGH AUTOCORRELATION FUNCTION DIAMETERS PREVIOUSLY (A) AND (B) SHOWS THE SECOND RUN OF THE DATA. THE HEATING STAGES ARE PRESENTED IN THE DARKER COLOUR. 171
- FIGURE 101. AUTOCORRELATION FUNCTIONS FROM DYNAMIC LIGHT SCATTERING MEASUREMENTS (ANGLE 173°) OF TEMPERATURE CYCLE FROM 30-80-30°C WITH AQUEOUS GLYCINE SOLUTION OF CONCENTRATION 299.06 G/L BOTH UNFILTERED (A) AND 0.1 MM PTFE FILTERED (B). AN ENHANCED VIEW OF THE Y-AXIS ZOOMED TO SCALE 0 TO 0.08 IS GIVEN IN (B) FOR A MORE DETAILED VIEW. 172
- FIGURE 102. MEAN COUNT RATE RECORDED IN KILO COUNTS PER SECOND FOR EACH TEMPERATURE STAGE DURING THE DYNAMIC LIGHT SCATTERING MEASUREMENTS FOR GLYCINE CONCENTRATION 299.06 G/L BOTH FOR UNFILTERED (RED) AND 0.1 MM PTFE FILTERED (BLUE) SOLUTION. THE HEATING STAGES ARE PRESENTED IN THE DARKER COLOUR. (A) IS FOR THE FIRST RUN AND (B) IS FOR THE SECOND RUN OF THE SOLUTION. 173
- FIGURE 103. COEFFICIENT VALUES FROM THE DECAY FITTING WITH 3 DECAYS PRESENT IN THE AUTOCORRELATION CURVES FOR ALL 154.9 G/L AQUEOUS GLYCINE SOLUTIONS OF THE FIRST RUN OF EXPERIMENTS FOR THE 1ST DECAY [○], 2ND DECAY [□] AND 3RD DECAY [Δ]. THE HEATING STAGES ARE IN RED AND THE COOLING STAGES ARE IN BLUE. (A) 154.9 G/L UNFILTERED (B) 154.9 G/L REPEAT OF THE UNFILTERED SAMPLE AND (C) 154.9 G/L FILTERED WITH 0.1 MM PTFE SYRINGE FILTER. 175
- FIGURE 104. COEFFICIENT VALUES FROM THE DECAY FITTING WITH 3 DECAYS PRESENT IN THE AUTOCORRELATION CURVES FOR THE FIRST RUN OF THE 234.98 AND 299.06 G/L AQUEOUS GLYCINE SOLUTIONS FOR THE 1ST DECAY [○], 2ND DECAY [□] AND 3RD DECAY [Δ]. THE HEATING STAGES ARE IN RED AND THE COOLING STAGES ARE IN BLUE. (A) 234.98 G/L UNFILTERED (B) 234.98 G/L FILTERED WITH 0.1 MM PTFE SYRINGE FILTER (C) 299.06 G/L UNFILTERED AND (D) 299.06 G/L FILTERED WITH 0.1 MM PTFE SYRINGE FILTER. 176
- FIGURE 105. COEFFICIENT VALUES FROM THE DECAY FITTING WITH 3 DECAYS PRESENT IN THE AUTOCORRELATION CURVES FOR THE SECOND RUNS OF THE 234.98 AND 299.06 G/L AQUEOUS GLYCINE SOLUTIONS FOR THE 1ST DECAY [○], 2ND DECAY [□] AND 3RD DECAY [Δ]. THE HEATING STAGES ARE IN RED AND THE COOLING STAGES ARE IN RED AND THE COOLING STAGES ARE IN BLUE. (A) 154.9 G/L UNFILTERED, (B) 154.9 G/L FILTERED WITH 0.1 MM PTFE SYRINGE FILTER, (C) 234.98 G/L UNFILTERED, (D) 234.98 G/L FILTERED WITH 0.1 MM PTFE SYRINGE FILTER, (E) 299.06 G/L UNFILTERED AND (F) 299.06 G/L FILTERED WITH 0.1 MM PTFE

SYRINGE FILTER.	177
FIGURE 106. AVERAGE HYDRODYNAMIC DIAMETERS PLOTTED AGAINST TEMPERATURE FOR ALL GLYCINE EXPERIMENTS BOTH FILTERED AND UNFILTERED CORRESPONDING TO THE FIRST DECAY IN THE AUTOCORRELATION FUNCTION FOR THE FIRST (A) AND SECOND RUN (B) OF EXPERIMENTS.	179
FIGURE 107. AVERAGE HYDRODYNAMIC DIAMETERS PLOTTED AGAINST TEMPERATURE FOR ALL GLYCINE EXPERIMENTS BOTH FILTERED AND UNFILTERED CORRESPONDING TO THE SECOND DECAY IN THE AUTOCORRELATION FUNCTION FOR THE FIRST (A) AND SECOND RUN (B) OF EXPERIMENTS.	180
FIGURE 108. AVERAGE HYDRODYNAMIC DIAMETERS PLOTTED AGAINST TEMPERATURE FOR ALL GLYCINE EXPERIMENTS BOTH FILTERED AND UNFILTERED CORRESPONDING TO THE THIRD DECAY IN THE AUTOCORRELATION FUNCTION FOR THE FIRST (A) AND SECOND RUN (B) OF EXPERIMENTS.	181
FIGURE 109. SCREENSHOT OF CURVE FITTING OF 10°C HEATING STAGE FOR 234.98 G/L GLYCINE SOLUTION FROM THE FIRST RUN OF EXPERIMENTS. EXPERIMENTAL DATA IS GIVEN IN RED AND THE CURVE FITTING IS SHOWN IN YELLOW.	182
FIGURE 110. SCREENSHOT OF CURVE FITTING OF 30°C HEATING STAGE FOR 234.98 G/L GLYCINE SOLUTION FROM THE FIRST RUN OF EXPERIMENTS. EXPERIMENTAL DATA IS GIVEN IN RED AND THE CURVE FITTING IS SHOWN IN YELLOW.	182
FIGURE 111. SCREENSHOT OF CURVE FITTING OF 50°C HEATING STAGE FOR 234.98 G/L GLYCINE SOLUTION FROM THE FIRST RUN OF EXPERIMENTS. EXPERIMENTAL DATA IS GIVEN IN RED AND THE CURVE FITTING IS SHOWN IN YELLOW.	183
FIGURE 112. CLUSTER SIZE DISTRIBUTIONS FROM NANOSIGHT MEASUREMENTS OF TEMPERATURE CYCLE FROM 15-50-15°C WITH UNFILTERED AQUEOUS GLYCINE SOLUTION OF CONCENTRATION 154.9 G/L FOR THE FIRST (A) AND SECOND (B) REPETITION.	185
FIGURE 113. CLUSTER SIZE DISTRIBUTIONS FROM NANOSIGHT MEASUREMENTS OF TEMPERATURE CYCLE FROM 15-50-15°C WITH 0.1 MM PTFE FILTERED AQUEOUS GLYCINE SOLUTION OF CONCENTRATION 154.9 G/L FOR THE FIRST (A) AND SECOND (B) REPETITION.	186
FIGURE 114. CLUSTER SIZE DISTRIBUTIONS FROM NANOSIGHT MEASUREMENTS OF TEMPERATURE CYCLE FROM 15-50-15°C WITH UNFILTERED AQUEOUS GLYCINE SOLUTION OF CONCENTRATION 234.98 G/L FOR THE FIRST (A) AND SECOND (B) REPETITION.	187
FIGURE 115. CLUSTER SIZE DISTRIBUTIONS FROM NANOSIGHT MEASUREMENTS OF TEMPERATURE CYCLE FROM 15-50-15°C WITH 0.1 MM PTFE FILTERED AQUEOUS GLYCINE SOLUTION OF CONCENTRATION 234.98 G/L FOR THE FIRST (A) AND SECOND (B) REPETITION.	188

FIGURE 116. CLUSTER SIZE DISTRIBUTIONS FROM NANOSIGHT MEASUREMENTS OF TEMPERATURE CYCLE FROM 15-50-15°C WITH THE REPETITION OF THE FIRST RUN 0.1 MM PTFE FILTERED AQUEOUS GLYCINE SOLUTION OF CONCENTRATION 234.98 G/L.	189
FIGURE 117. CLUSTER SIZE DISTRIBUTIONS FROM NANOSIGHT MEASUREMENTS OF TEMPERATURE CYCLE FROM 30-50-30°C WITH UNFILTERED AQUEOUS GLYCINE SOLUTION OF CONCENTRATION 299.06 G/L FOR THE FIRST (A) AND SECOND (B) REPETITION.	190
FIGURE 118. CLUSTER SIZE DISTRIBUTIONS FROM NANOSIGHT MEASUREMENTS OF TEMPERATURE CYCLE FROM 30-50-30°C WITH 0.1 MM PTFE FILTERED AQUEOUS GLYCINE SOLUTION OF CONCENTRATION 299.06 G/L FOR THE FIRST (A) AND SECOND (B) REPETITION.	191
FIGURE 119. CLUSTER SIZE DISTRIBUTIONS FROM NANOSIGHT MEASUREMENTS OF TEMPERATURE CYCLE FROM 15-50-15°C WITH THE FIRST RUN OF UNFILTERED AQUEOUS GLYCINE SOLUTION OF CONCENTRATION 154.9 G/L WITH 20 NM BIN SIZES FOR THE X-AXIS.	192
FIGURE 120. CLUSTER SIZE DISTRIBUTIONS FROM NANOSIGHT MEASUREMENTS OF TEMPERATURE CYCLE FROM 15-50-15°C WITH THE FIRST RUN OF 0.1 MM PTFE FILTERED AQUEOUS GLYCINE SOLUTION OF CONCENTRATION 154.9 G/L WITH 20 NM BIN SIZES FOR THE X-AXIS.	193
FIGURE 121. CLUSTER SIZE DISTRIBUTIONS FROM NANOSIGHT MEASUREMENTS OF TEMPERATURE CYCLE FROM 15-50-15°C WITH THE FIRST RUN OF UNFILTERED AQUEOUS GLYCINE SOLUTION OF CONCENTRATION 234.98 G/L WITH 20 NM BIN SIZES FOR THE X-AXIS.	193
FIGURE 122. CLUSTER SIZE DISTRIBUTIONS FROM NANOSIGHT MEASUREMENTS OF TEMPERATURE CYCLE FROM 15-50-15°C WITH THE FIRST RUN OF 0.1 MM PTFE FILTERED AQUEOUS GLYCINE SOLUTION OF CONCENTRATION 234.98 G/L WITH 20 NM BIN SIZES FOR THE X-AXIS.	194
FIGURE 123. CLUSTER SIZE DISTRIBUTIONS FROM NANOSIGHT MEASUREMENTS OF TEMPERATURE CYCLE FROM 15-50-15°C WITH THE REPEAT OF THE FIRST RUN OF 0.1 MM PTFE FILTERED AQUEOUS GLYCINE SOLUTION OF CONCENTRATION 234.98 G/L WITH 20 NM BIN SIZES FOR THE X-AXIS.	194
FIGURE 124. CLUSTER SIZE DISTRIBUTIONS FROM NANOSIGHT MEASUREMENTS OF TEMPERATURE CYCLE FROM 30-50-30°C WITH THE FIRST RUN OF UNFILTERED AQUEOUS GLYCINE SOLUTION OF CONCENTRATION 299.06 G/L WITH 20 NM BIN SIZES FOR THE X-AXIS.	195
FIGURE 125. CLUSTER SIZE DISTRIBUTIONS FROM NANOSIGHT MEASUREMENTS OF TEMPERATURE CYCLE FROM 30-50-30°C WITH THE FIRST RUN OF 0.1 MM PTFE FILTERED AQUEOUS GLYCINE SOLUTION OF CONCENTRATION 299.06 G/L WITH 20 NM BIN SIZES FOR THE X-AXIS.	195
FIGURE 126. NANOSIGHT MEASUREMENTS OF THE AVERAGE CLUSTER DIAMETERS WITH TEMPERATURE FOR 154.9 G/L AQUEOUS GLYCINE SOLUTION FOR FILTERED [○] AND UNFILTERED [□] SAMPLES WITH THE HEATING STAGES GIVEN IN RED AND THE COOLING	

STAGES PRESENTED IN BLUE. THE FIRST (A) AND SECOND RUN (B) ARE SHOWN.	196
FIGURE 127. NANOSIGHT MEASUREMENTS OF THE AVERAGE CLUSTER DIAMETERS WITH TEMPERATURE FOR 234.98 G/L AQUEOUS GLYCINE SOLUTION FOR FILTERED [○] AND UNFILTERED [□] SAMPLES WITH THE HEATING STAGES GIVEN IN RED AND THE COOLING STAGES PRESENTED IN BLUE. THE FIRST (A) AND SECOND RUN (B) ARE SHOWN.	197
FIGURE 128. NANOSIGHT MEASUREMENTS OF THE AVERAGE CLUSTER DIAMETERS WITH TEMPERATURE FOR 299.06 G/L AQUEOUS GLYCINE SOLUTION FOR FILTERED [○] AND UNFILTERED [□] SAMPLES WITH THE HEATING STAGES GIVEN IN RED AND THE COOLING STAGES PRESENTED IN BLUE. THE FIRST (A) AND SECOND RUN (B) ARE SHOWN.	197
FIGURE 129. AUTOCORRELATION FUNCTIONS FROM DYNAMIC LIGHT SCATTERING MEASUREMENTS (ANGLE 173°) OF TEMPERATURE CYCLE FROM 10-80-10°C WITH UNFILTERED AQUEOUS UREA SOLUTION OF CONCENTRATION 522.61 G/L FROM THE FIRST EXPERIMENTAL RUN (A) AND SECOND EXPERIMENTAL RUN (B).	203
FIGURE 130. AUTOCORRELATION FUNCTIONS FROM DYNAMIC LIGHT SCATTERING MEASUREMENTS (ANGLE 173°) OF TEMPERATURE CYCLE FROM 10-80-10°C WITH 0.1 MM PTFE FILTERED AQUEOUS UREA SOLUTION OF CONCENTRATION 522.61 G/L FROM THE FIRST EXPERIMENTAL RUN (A) AND SECOND EXPERIMENTAL RUN (B).	204
FIGURE 131. AUTOCORRELATION FUNCTIONS FROM DYNAMIC LIGHT SCATTERING MEASUREMENTS (ANGLE 173°) OF TEMPERATURE CYCLE FROM 10-80-10°C WITH UNFILTERED AQUEOUS UREA SOLUTION OF CONCENTRATION 785.15 G/L FROM THE FIRST EXPERIMENTAL RUN (A) AND SECOND EXPERIMENTAL RUN (B).	204
FIGURE 132. AUTOCORRELATION FUNCTIONS FROM DYNAMIC LIGHT SCATTERING MEASUREMENTS (ANGLE 173°) OF TEMPERATURE CYCLE FROM 10-80-10°C WITH 0.1 MM PTFE FILTERED AQUEOUS UREA SOLUTION OF CONCENTRATION 785.15 G/L FROM THE FIRST EXPERIMENTAL RUN (A) AND SECOND EXPERIMENTAL RUN (B).	205
FIGURE 133. AUTOCORRELATION FUNCTIONS FROM DYNAMIC LIGHT SCATTERING MEASUREMENTS (ANGLE 173°) OF TEMPERATURE CYCLE FROM 10-80-10°C WITH UNFILTERED FILTERED AQUEOUS UREA SOLUTION OF CONCENTRATION 1149.74 G/L FROM THE FIRST EXPERIMENTAL RUN (A) AND SECOND EXPERIMENTAL RUN (B).	205
FIGURE 134. AUTOCORRELATION FUNCTIONS FROM DYNAMIC LIGHT SCATTERING MEASUREMENTS (ANGLE 173°) OF TEMPERATURE CYCLE FROM 50-80-30°C WITH 0.1 MM PTFE FILTERED AQUEOUS UREA SOLUTION OF CONCENTRATION 1149.74 G/L FROM THE FIRST EXPERIMENTAL RUN (A) AND SECOND EXPERIMENTAL RUN (B).	206
FIGURE 135. MEAN COUNT RATE RECORDED IN KILO COUNTS PER SECOND FOR EACH TEMPERATURE STAGE DURING THE DYNAMIC LIGHT SCATTERING MEASUREMENTS FOR UREA	

CONCENTRATION 522.61 G/L BOTH FOR UNFILTERED (RED) AND 0.1 MM PTFE FILTERED (BLUE) SOLUTION. THE HEATING STAGES ARE PRESENTED IN THE DARKER COLOUR. BOTH THE FIRST EXPERIMENTAL RUN (A) AND SECOND EXPERIMENTAL RUN (B) ARE SHOWN.	206
FIGURE 136. MEAN COUNT RATE RECORDED IN KILO COUNTS PER SECOND FOR EACH TEMPERATURE STAGE DURING THE DYNAMIC LIGHT SCATTERING MEASUREMENTS FOR UREA CONCENTRATION 785.15 G/L BOTH FOR UNFILTERED (RED) AND 0.1 MM PTFE FILTERED (BLUE) SOLUTION. THE HEATING STAGES ARE PRESENTED IN THE DARKER COLOUR. BOTH THE FIRST EXPERIMENTAL RUN (A) AND SECOND EXPERIMENTAL RUN (B) ARE SHOWN.	207
FIGURE 137. MEAN COUNT RATE RECORDED IN KILO COUNTS PER SECOND FOR EACH TEMPERATURE STAGE DURING THE DYNAMIC LIGHT SCATTERING MEASUREMENTS FOR UREA CONCENTRATION 1149.74 G/L BOTH FOR UNFILTERED (RED) AND 0.1 MM PTFE FILTERED (BLUE) SOLUTION. THE HEATING STAGES ARE PRESENTED IN THE DARKER COLOUR. BOTH THE FIRST EXPERIMENTAL RUN (A) AND SECOND EXPERIMENTAL RUN (B) ARE SHOWN.	207
FIGURE 138. COEFFICIENT VALUES FROM THE DECAY FITTING WITH 3 DECAYS PRESENT IN THE AUTOCORRELATION CURVE FOR THE FIRST RUN OF UNFILTERED 522.61 G/L AQUEOUS UREA SOLUTIONS FOR THE 1 ST DECAY [○], 2 ND DECAY [□] AND 3 RD DECAY [Δ]. THE HEATING STAGES ARE IN RED AND THE COOLING STAGES ARE IN BLUE.	208
FIGURE 139. COEFFICIENT VALUES FROM THE DECAY FITTING WITH 3 DECAYS PRESENT IN THE AUTOCORRELATION CURVE FOR THE SECOND RUN OF UNFILTERED 522.61 G/L AQUEOUS UREA SOLUTIONS FOR THE 1 ST DECAY [○], 2 ND DECAY [□] AND 3 RD DECAY [Δ]. THE HEATING STAGES ARE IN RED AND THE COOLING STAGES ARE IN BLUE.	209
FIGURE 140. COEFFICIENT VALUES FROM THE DECAY FITTING WITH 3 DECAYS PRESENT IN THE AUTOCORRELATION CURVE FOR THE FIRST RUN OF 0.1 MM PTFE FILTERED 522.61 G/L AQUEOUS UREA SOLUTIONS FOR THE 1 ST DECAY [○], 2 ND DECAY [□] AND 3 RD DECAY [Δ]. THE HEATING STAGES ARE IN RED AND THE COOLING STAGES ARE IN BLUE.	209
FIGURE 141. COEFFICIENT VALUES FROM THE DECAY FITTING WITH 3 DECAYS PRESENT IN THE AUTOCORRELATION CURVE FOR THE SECOND RUN OF 0.1 MM PTFE FILTERED 522.61 G/L AQUEOUS UREA SOLUTIONS FOR THE 1 ST DECAY [○], 2 ND DECAY [□] AND 3 RD DECAY [Δ]. THE HEATING STAGES ARE IN RED AND THE COOLING STAGES ARE IN BLUE.	210
FIGURE 142. COEFFICIENT VALUES FROM THE DECAY FITTING WITH 3 DECAYS PRESENT IN THE AUTOCORRELATION CURVE FOR THE FIRST RUN OF UNFILTERED 785.15 G/L AQUEOUS UREA SOLUTIONS FOR THE 1 ST DECAY [○], 2 ND DECAY [□] AND 3 RD DECAY [Δ]. THE HEATING STAGES ARE IN RED AND THE COOLING STAGES ARE IN BLUE.	210
FIGURE 143. COEFFICIENT VALUES FROM THE DECAY FITTING WITH 3 DECAYS PRESENT IN THE AUTOCORRELATION CURVE FOR THE SECOND RUN OF UNFILTERED 785.15 G/L AQUEOUS UREA SOLUTIONS FOR THE 1 ST DECAY [○], 2 ND DECAY [□] AND 3 RD DECAY [Δ]. THE HEATING	

STAGES ARE IN RED AND THE COOLING STAGES ARE IN BLUE.	211
FIGURE 144. COEFFICIENT VALUES FROM THE DECAY FITTING WITH 3 DECAYS PRESENT IN THE AUTOCORRELATION CURVE FOR THE FIRST RUN OF 0.1 MM PTFE FILTERED 785.15 G/L AQUEOUS UREA SOLUTIONS FOR THE 1 ST DECAY [o], 2 ND DECAY [□] AND 3 RD DECAY [Δ]. THE HEATING STAGES ARE IN RED AND THE COOLING STAGES ARE IN BLUE.	211
FIGURE 145. COEFFICIENT VALUES FROM THE DECAY FITTING WITH 3 DECAYS PRESENT IN THE AUTOCORRELATION CURVE FOR THE SECOND RUN OF 0.1 MM PTFE FILTERED 785.15 G/L AQUEOUS UREA SOLUTIONS FOR THE 1 ST DECAY [o], 2 ND DECAY [□] AND 3 RD DECAY [Δ]. THE HEATING STAGES ARE IN RED AND THE COOLING STAGES ARE IN BLUE.	212
FIGURE 146. COEFFICIENT VALUES FROM THE DECAY FITTING WITH 3 DECAYS PRESENT IN THE AUTOCORRELATION CURVE FOR THE FIRST RUN OF UNFILTERED 1149.75 G/L AQUEOUS UREA SOLUTIONS FOR THE 1 ST DECAY [o], 2 ND DECAY [□] AND 3 RD DECAY [Δ]. THE HEATING STAGES ARE IN RED AND THE COOLING STAGES ARE IN BLUE.	212
FIGURE 147. COEFFICIENT VALUES FROM THE DECAY FITTING WITH 3 DECAYS PRESENT IN THE AUTOCORRELATION CURVE FOR THE SECOND RUN OF UNFILTERED 1149.75 G/L AQUEOUS UREA SOLUTIONS FOR THE 1 ST DECAY [o], 2 ND DECAY [□] AND 3 RD DECAY [Δ]. THE HEATING STAGES ARE IN RED AND THE COOLING STAGES ARE IN BLUE.	213
FIGURE 148. COEFFICIENT VALUES FROM THE DECAY FITTING WITH 3 DECAYS PRESENT IN THE AUTOCORRELATION CURVE FOR THE FIRST RUN OF 0.1 MM PTFE FILTERED 1149.74 G/L AQUEOUS UREA SOLUTIONS FOR THE 1 ST DECAY [o], 2 ND DECAY [□] AND 3 RD DECAY [Δ]. THE HEATING STAGES ARE IN RED AND THE COOLING STAGES ARE IN BLUE.	213
FIGURE 149. COEFFICIENT VALUES FROM THE DECAY FITTING WITH 3 DECAYS PRESENT IN THE AUTOCORRELATION CURVE FOR THE SECOND RUN OF 0.1 MM PTFE FILTERED 1149.74 G/L AQUEOUS UREA SOLUTIONS FOR THE 1 ST DECAY [o], 2 ND DECAY [□] AND 3 RD DECAY [Δ]. THE HEATING STAGES ARE IN RED AND THE COOLING STAGES ARE IN BLUE.	214
FIGURE 150. AVERAGE HYDRODYNAMIC DIAMETERS PLOTTED AGAINST TEMPERATURE FOR ALL UREA EXPERIMENTS BOTH FILTERED AND UNFILTERED CORRESPONDING TO THE FIRST DECAY IN THE AUTOCORRELATION FUNCTION FOR THE FIRST (A) AND SECOND RUN (B) OF EXPERIMENTS.	215
FIGURE 151. AVERAGE HYDRODYNAMIC DIAMETERS PLOTTED AGAINST TEMPERATURE FOR ALL UREA EXPERIMENTS BOTH FILTERED AND UNFILTERED CORRESPONDING TO THE SECOND DECAY IN THE AUTOCORRELATION FUNCTION FOR THE FIRST (A) AND SECOND RUN (B) OF EXPERIMENTS.	216
FIGURE 152. AVERAGE HYDRODYNAMIC DIAMETERS PLOTTED AGAINST TEMPERATURE FOR ALL	

UREA EXPERIMENTS BOTH FILTERED AND UNFILTERED CORRESPONDING TO THE THIRD DECAY IN THE AUTOCORRELATION FUNCTION FOR THE FIRST (A) AND SECOND RUN (B) OF EXPERIMENTS.	217
FIGURE 153. CLUSTER SIZE DISTRIBUTIONS FROM NANOSIGHT MEASUREMENTS OF TEMPERATURE CYCLE FROM 15-50-15°C WITH THE FIRST RUN OF UNFILTERED AQUEOUS UREA SOLUTION OF CONCENTRATION 522.61 G/L.	218
FIGURE 154. CLUSTER SIZE DISTRIBUTIONS FROM NANOSIGHT MEASUREMENTS OF TEMPERATURE CYCLE FROM 15-50-15°C WITH THE SECOND RUN OF UNFILTERED AQUEOUS UREA SOLUTION OF CONCENTRATION 522.61 G/L.	218
FIGURE 155. CLUSTER SIZE DISTRIBUTIONS FROM NANOSIGHT MEASUREMENTS OF TEMPERATURE CYCLE FROM 15-50-15°C WITH THE FIRST RUN OF 0.1 MM PTFE FILTERED AQUEOUS UREA SOLUTION OF CONCENTRATION 522.61 G/L.	219
FIGURE 156. CLUSTER SIZE DISTRIBUTIONS FROM NANOSIGHT MEASUREMENTS OF TEMPERATURE CYCLE FROM 15-50-15°C WITH THE SECOND RUN OF 0.1 MM PTFE FILTERED AQUEOUS UREA SOLUTION OF CONCENTRATION 522.61 G/L.	219
FIGURE 157. CLUSTER SIZE DISTRIBUTIONS FROM NANOSIGHT MEASUREMENTS OF TEMPERATURE CYCLE FROM 15-50-15°C WITH THE FIRST RUN OF UNFILTERED AQUEOUS UREA SOLUTION OF CONCENTRATION 785.15 G/L.	220
FIGURE 158. CLUSTER SIZE DISTRIBUTIONS FROM NANOSIGHT MEASUREMENTS OF TEMPERATURE CYCLE FROM 15-50-15°C WITH THE SECOND RUN OF UNFILTERED AQUEOUS UREA SOLUTION OF CONCENTRATION 785.15 G/L.	220
FIGURE 159. CLUSTER SIZE DISTRIBUTIONS FROM NANOSIGHT MEASUREMENTS OF TEMPERATURE CYCLE FROM 15-50-15°C WITH THE FIRST RUN OF 0.1 MM PTFE FILTERED AQUEOUS UREA SOLUTION OF CONCENTRATION 785.15 G/L.	221
FIGURE 160. CLUSTER SIZE DISTRIBUTIONS FROM NANOSIGHT MEASUREMENTS OF TEMPERATURE CYCLE FROM 15-50-15°C WITH THE SECOND RUN OF 0.1 MM PTFE FILTERED AQUEOUS UREA SOLUTION OF CONCENTRATION 785.15 G/L.	221
FIGURE 161. CLUSTER SIZE DISTRIBUTIONS FROM NANOSIGHT MEASUREMENTS OF TEMPERATURE CYCLE FROM 15-50-15°C WITH THE FIRST RUN OF UNFILTERED AQUEOUS UREA SOLUTION OF CONCENTRATION 1149.74 G/L.	222
FIGURE 162. CLUSTER SIZE DISTRIBUTIONS FROM NANOSIGHT MEASUREMENTS OF TEMPERATURE CYCLE FROM 15-50-15°C WITH THE SECOND RUN OF UNFILTERED AQUEOUS UREA SOLUTION OF CONCENTRATION 1149.74 G/L.	222
FIGURE 163. CLUSTER SIZE DISTRIBUTIONS FROM NANOSIGHT MEASUREMENTS OF TEMPERATURE CYCLE FROM 15-50-15°C WITH THE FIRST RUN OF 0.1MM PTFE FILTERED AQUEOUS UREA SOLUTION OF CONCENTRATION 1149.74 G/L.	223

FIGURE 164. CLUSTER SIZE DISTRIBUTIONS FROM NANOSIGHT MEASUREMENTS OF TEMPERATURE CYCLE FROM 15-50-15°C WITH THE SECOND RUN OF 0.1MM PTFE FILTERED AQUEOUS UREA SOLUTION OF CONCENTRATION 1149.74 G/L.	223
FIGURE 165. CLUSTER SIZE DISTRIBUTIONS FROM NANOSIGHT MEASUREMENTS OF TEMPERATURE CYCLE FROM 15-50-15°C WITH THE FIRST RUN OF UNFILTERED FILTERED AQUEOUS UREA SOLUTION OF CONCENTRATION 522.61 G/L WITH 20 NM BIN SIZES FOR THE X-AXIS.	224
FIGURE 166. CLUSTER SIZE DISTRIBUTIONS FROM NANOSIGHT MEASUREMENTS OF TEMPERATURE CYCLE FROM 15-50-15°C WITH THE FIRST RUN OF 0.1 MM PTFE FILTERED AQUEOUS UREA SOLUTION OF CONCENTRATION 522.61 G/L WITH 20 NM BIN SIZES FOR THE X-AXIS.	225
FIGURE 167. CLUSTER SIZE DISTRIBUTIONS FROM NANOSIGHT MEASUREMENTS OF TEMPERATURE CYCLE FROM 15-50-15°C WITH THE FIRST RUN OF UNFILTERED FILTERED AQUEOUS UREA SOLUTION OF CONCENTRATION 785.15 G/L WITH 20 NM BIN SIZES FOR THE X-AXIS.	225
FIGURE 168. CLUSTER SIZE DISTRIBUTIONS FROM NANOSIGHT MEASUREMENTS OF TEMPERATURE CYCLE FROM 15-50-15°C WITH THE FIRST RUN OF 0.1 MM PTFE FILTERED AQUEOUS UREA SOLUTION OF CONCENTRATION 785.15 G/L WITH 20 NM BIN SIZES FOR THE X-AXIS.	226
FIGURE 169. CLUSTER SIZE DISTRIBUTIONS FROM NANOSIGHT MEASUREMENTS OF TEMPERATURE CYCLE FROM 15-50-15°C WITH THE FIRST RUN OF UNFILTERED AQUEOUS UREA SOLUTION OF CONCENTRATION 1149.74 G/L WITH 20 NM BIN SIZES FOR THE X-AXIS.	226
FIGURE 170. CLUSTER SIZE DISTRIBUTIONS FROM NANOSIGHT MEASUREMENTS OF TEMPERATURE CYCLE FROM 15-50-15°C WITH THE FIRST RUN OF 0.1MM PTFE FILTERED AQUEOUS UREA SOLUTION OF CONCENTRATION 1149.74 G/L WITH 20 NM BIN SIZES FOR THE X-AXIS.	227
FIGURE 171. NANOSIGHT MEASUREMENTS OF THE AVERAGE CLUSTER DIAMETERS WITH TEMPERATURE FOR 522.61 G/L AQUEOUS UREA SOLUTION FOR FILTERED [○] AND UNFILTERED [□] SAMPLES WITH THE HEATING STAGES GIVEN IN RED AND THE COOLING STAGES PRESENTED IN BLUE. (A) REFERS TO THE FIRST AND (B) TO THE SECOND EXPERIMENTAL RUN.	228
FIGURE 172. NANOSIGHT MEASUREMENTS OF THE AVERAGE CLUSTER DIAMETERS WITH TEMPERATURE FOR 785.15 G/L AQUEOUS UREA SOLUTION FOR FILTERED [○] AND UNFILTERED [□] SAMPLES WITH THE HEATING STAGES GIVEN IN RED AND THE COOLING STAGES PRESENTED IN BLUE. (A) REFERS TO THE FIRST AND (B) TO THE SECOND EXPERIMENTAL RUN.	228
FIGURE 173. NANOSIGHT MEASUREMENTS OF THE AVERAGE CLUSTER DIAMETERS WITH TEMPERATURE FOR 1149.74 G/L AQUEOUS UREA SOLUTION FOR FILTERED [○] AND UNFILTERED [□] SAMPLES WITH THE HEATING STAGES GIVEN IN RED AND THE COOLING	

STAGES PRESENTED IN BLUE. (A) REFERS TO THE FIRST AND (B) TO THE SECOND EXPERIMENTAL RUN.	229
FIGURE 174. SECOND RUN OF AUTOCORRELATION FUNCTIONS FROM DYNAMIC LIGHT SCATTERING MEASUREMENTS (ANGLE 173°) OF TEMPERATURE CYCLE FROM 10-80-10°C WITH UNFILTERED AQUEOUS GLYCINE SOLUTION OF CONCENTRATION 154.9 G/L WHICH IS UNDERSATURATED STILL AT 10°C (AT THIS TEMPERATURE THE SOLUTION HAS SUPERSATURATION VALUE OF S=0.95).	235
FIGURE 175. SECOND RUN OF AUTOCORRELATION FUNCTIONS FROM DYNAMIC LIGHT SCATTERING MEASUREMENTS (ANGLE 173°) OF TEMPERATURE CYCLE FROM 10-80-10°C WITH AQUEOUS GLYCINE SOLUTION OF CONCENTRATION 154.9 G/L WHICH IS UNDERSATURATED STILL AT 10°C (AT THIS TEMPERATURE THE SOLUTION HAS SUPERSATURATION VALUE OF S=0.95). THIS SOLUTION WAS FILTERED THROUGH A PTFE SYRINGE FILTER WITH PORE DIAMETER 0.1 MM.	
236 FIGURE 176. SECOND RUN OF AUTOCORRELATION FUNCTIONS FROM DYNAMIC LIGHT SCATTERING MEASUREMENTS (ANGLE 173°) OF TEMPERATURE CYCLE FROM 10-80-10°C WITH UNFILTERED AQUEOUS GLYCINE SOLUTION OF CONCENTRATION 234.98 G/L.	236
FIGURE 177. SECOND RUN OF AUTOCORRELATION FUNCTIONS FROM DYNAMIC LIGHT SCATTERING MEASUREMENTS (ANGLE 173°) OF TEMPERATURE CYCLE FROM 10-80-10°C WITH AQUEOUS GLYCINE SOLUTION OF CONCENTRATION 234.98 G/L. THIS SOLUTION WAS FILTERED THROUGH A PTFE SYRINGE FILTER WITH PORE DIAMETER 0.1 MM.	237
FIGURE 178. SECOND RUN OF AUTOCORRELATION FUNCTIONS FROM DYNAMIC LIGHT SCATTERING MEASUREMENTS (ANGLE 173°) OF TEMPERATURE CYCLE FROM 10-80-10°C WITH UNFILTERED AQUEOUS GLYCINE SOLUTION OF CONCENTRATION 299.06 G/L.	237
FIGURE 179. SECOND RUN OF AUTOCORRELATION FUNCTIONS FROM DYNAMIC LIGHT SCATTERING MEASUREMENTS (ANGLE 173°) OF TEMPERATURE CYCLE FROM 10-80-10°C WITH AQUEOUS GLYCINE SOLUTION OF CONCENTRATION 299.06 G/L. THIS SOLUTION WAS FILTERED THROUGH A PTFE SYRINGE FILTER WITH PORE DIAMETER 0.1 MM.	238
FIGURE 180. SECOND RUN OF CLUSTER SIZE DISTRIBUTIONS FROM NANOSIGHT MEASUREMENTS OF TEMPERATURE CYCLE FROM 15-50-15°C WITH UNFILTERED AQUEOUS GLYCINE SOLUTION OF CONCENTRATION 154.9 G/L WITH 20 NM BIN SIZES FOR THE X-AXIS.	239
FIGURE 181. SECOND RUN OF CLUSTER SIZE DISTRIBUTIONS FROM NANOSIGHT MEASUREMENTS OF TEMPERATURE CYCLE FROM 15-50-15°C WITH 0.1 MM PTFE FILTERED AQUEOUS GLYCINE SOLUTION OF CONCENTRATION 154.9 G/L WITH 20 NM BIN SIZES FOR THE X-AXIS.	239
FIGURE 182. SECOND RUN OF CLUSTER SIZE DISTRIBUTIONS FROM NANOSIGHT MEASUREMENTS OF TEMPERATURE CYCLE FROM 15-50-15°C WITH UNFILTERED AQUEOUS GLYCINE SOLUTION OF CONCENTRATION 234.98 G/L WITH 20 NM BIN SIZES FOR THE X-AXIS.	240
FIGURE 183. SECOND RUN OF CLUSTER SIZE DISTRIBUTIONS FROM NANOSIGHT MEASUREMENTS OF	

TEMPERATURE CYCLE FROM 15-50-15°C WITH 0.1 MM PTFE FILTERED AQUEOUS GLYCINE SOLUTION OF CONCENTRATION 234.98 G/L WITH 20 NM BIN SIZES FOR THE X-AXIS.	240
FIGURE 184. SECOND RUN OF CLUSTER SIZE DISTRIBUTIONS FROM NANOSIGHT MEASUREMENTS OF TEMPERATURE CYCLE FROM 30-50-30°C WITH UNFILTERED AQUEOUS GLYCINE SOLUTION OF CONCENTRATION 299.06 G/L WITH 20 NM BIN SIZES FOR THE X-AXIS.	241
FIGURE 185. SECOND RUN OF CLUSTER SIZE DISTRIBUTIONS FROM NANOSIGHT MEASUREMENTS OF TEMPERATURE CYCLE FROM 30-50-30°C WITH 0.1 MM PTFE FILTERED AQUEOUS GLYCINE SOLUTION OF CONCENTRATION 299.06 G/L WITH 20 NM BIN SIZES FOR THE X-AXIS.	241
FIGURE 186. CLUSTER SIZE DISTRIBUTIONS FROM NANOSIGHT MEASUREMENTS OF TEMPERATURE CYCLE FROM 15-50-15°C WITH THE SECOND RUN OF UNFILTERED AQUEOUS UREA SOLUTION OF CONCENTRATION 522.61 G/L WITH 20 NM BIN SIZES FOR THE X-AXIS.	242
FIGURE 187. CLUSTER SIZE DISTRIBUTIONS FROM NANOSIGHT MEASUREMENTS OF TEMPERATURE CYCLE FROM 15-50-15°C WITH THE SECOND RUN OF 0.1 MM PTFE FILTERED AQUEOUS UREA SOLUTION OF CONCENTRATION 522.61 G/L WITH 20 NM BIN SIZES FOR THE X-AXIS.	242
FIGURE 188. CLUSTER SIZE DISTRIBUTIONS FROM NANOSIGHT MEASUREMENTS OF TEMPERATURE CYCLE FROM 15-50-15°C WITH THE SECOND RUN OF UNFILTERED AQUEOUS UREA SOLUTION OF CONCENTRATION 785.15 G/L WITH 20 NM BIN SIZES FOR THE X-AXIS.	243
FIGURE 189. CLUSTER SIZE DISTRIBUTIONS FROM NANOSIGHT MEASUREMENTS OF TEMPERATURE CYCLE FROM 15-50-15°C WITH THE SECOND RUN OF 0.1 MM PTFE FILTERED AQUEOUS UREA SOLUTION OF CONCENTRATION 785.15 G/L WITH 20 NM BIN SIZES FOR THE X-AXIS.	243
FIGURE 190. CLUSTER SIZE DISTRIBUTIONS FROM NANOSIGHT MEASUREMENTS OF TEMPERATURE CYCLE FROM 15-50-15°C WITH THE SECOND RUN OF UNFILTERED AQUEOUS UREA SOLUTION OF CONCENTRATION 1149.74 G/L WITH 20 NM BIN SIZES FOR THE X-AXIS.	244
FIGURE 191. CLUSTER SIZE DISTRIBUTIONS FROM NANOSIGHT MEASUREMENTS OF TEMPERATURE CYCLE FROM 15-50-15°C WITH THE SECOND RUN OF 0.1 MM PTFE FILTERED AQUEOUS UREA SOLUTION OF CONCENTRATION 1149.74 G/L WITH 20 NM BIN SIZES FOR THE X-AXIS.	244

LIST OF TABLES

TABLE 1. DATA FOR VISCOSITY WITH TEMPERATURE FOR WATER, GLYCINE AND UREA SOLUTIONS .	
53	
TABLE 2. FACTORS AFFECTING THE FOULING DURING CRYSTALLISATION	64
TABLE 3. MOVING FLUID OSCILLATORY BAFFLED CRYSTALLISER EXPERIMENT SUMMARIES	115
TABLE 4. AVERAGE FOULING INDUCTION TIMES FOR GLYCINE EXPERIMENTS	130
TABLE 5. INDUCTION TIMES FOR L-GLUTAMIC ACID 28.26 G/L [2 HZ 45 MM]	138
TABLE 6. INDUCTION TIMES FOR L-GLUTAMIC ACID 28.26 G/L [1 HZ 45 MM]	139
TABLE 7. INDUCTION TIMES FOR L-GLUTAMIC ACID 42.39 G/L [2 HZ 45 MM]	140
TABLE 8. INDUCTION TIMES FOR L-GLUTAMIC ACID 42.39 G/L [1 HZ 45 MM]	141
TABLE 9. INDUCTION TIMES FOR L-GLUTAMIC ACID 42.39 G/L [2 HZ 45 MM] WITH CRYSTALLISATION TEMPERATURE 30°C	142
TABLE 10. INDUCTION TIMES FOR L-GLUTAMIC ACID 42.39 G/L [1 HZ 45 MM] WITH CRYSTALLISATION TEMPERATURE 30°C	143
TABLE 11. INDUCTION TIMES FOR GLYCINE 384.51 G/L [1 HZ 23 MM]	144
TABLE 12. INDUCTION TIMES FOR GLYCINE 384.51 G/L [2 HZ 45 MM]	145
TABLE 13. INDUCTION TIMES FOR GLYCINE 384.51 G/L [1 HZ 45 MM]	146
TABLE 14. INDUCTION TIMES FOR GLYCINE 384.51 G/L [2 HZ 23 MM]	147
TABLE 15. SUMMARY OF ALL LIGHT SCATTERING EXPERIMENTAL CONDITIONS	154
TABLE 16. SUMMARY OF CONCENTRATIONS USED FOR AQUEOUS GLYCINE AND UREA	158
TABLE 17. PARAMETERS FROM THE 2 ND DECAY CURVE FITTING OF 10, 30 AND 50°C OF UNFILTERED 234.98 G/L GLYCINE	183
TABLE 18. 1 ST RUN OF UNFILTERED GLYCINE 154.9 G/L	245
TABLE 19. REPEAT OF 1 ST RUN OF UNFILTERED GLYCINE 154.9 G/L	246
TABLE 20. 1 ST RUN OF PTFE FILTERED GLYCINE 154.9 G/L	247
TABLE 21. 1 ST RUN OF UNFILTERED GLYCINE 234.98 G/L	248
TABLE 22. 1 ST RUN OF PTFE FILTERED GLYCINE 234.98 G/L	249
TABLE 23. REPEAT OF 1 ST RUN OF PTFE FILTERED GLYCINE 234.98 G/L, PTFE	250
TABLE 24. 1 ST RUN OF UNFILTERED GLYCINE 299.06 G/L	251
TABLE 25. 1 ST RUN OF PTFE FILTERED GLYCINE 299.06 G/L	252
TABLE 26. 2 ND RUN OF UNFILTERED GLYCINE 154.9 G/L	253
TABLE 27. 2 ND RUN OF PTFE FILTERED GLYCINE 154.9 G/L	254
TABLE 28. 2 ND RUN OF UNFILTERED GLYCINE 234.98 G/L	255
TABLE 29. 2 ND RUN OF PTFE FILTERED GLYCINE 234.98 G/L	256
TABLE 30. 2 ND RUN OF UNFILTERED GLYCINE 299.06 G/L	257

TABLE 31. 2 ND RUN OF PTFE FILTERED GLYCINE 299.06 G/L	258
TABLE 32. 1 ST RUN OF UNFILTERED UREA 522.61 G/L	259
TABLE 33. 1 ST RUN OF PTFE FILTERED UREA 522.61 G/L	260
TABLE 34. 1 ST RUN OF UNFILTERED UREA 785.15 G/L	261
TABLE 35. 1 ST RUN OF PTFE FILTERED UREA 785.15 G/L	262
TABLE 36. 1 ST RUN OF UNFILTERED UREA 1149.75 G/L	263
TABLE 37. 1 ST RUN OF PTFE FILTERED UREA 1149.75 G/L	264
TABLE 38. 2 ND RUN OF UNFILTERED UREA 522.06 G/L	265
TABLE 39. 2 ND RUN OF PTFE FILTERED UREA 522.06 G/L	266
TABLE 40. 2 ND RUN OF UNFILTERED UREA 785.15 G/L	267
TABLE 41. 2 ND RUN OF PTFE FILTERED UREA 785.15 G/L	268
TABLE 42. 2 ND RUN OF UNFILTERED UREA 1149.74 G/L	269
TABLE 43. 2 ND RUN OF PTFE FILTERED UREA 1149.74 G/L	270

THESIS STRUCTURE AND OUTLINE

This thesis is organised such that the first section covers previously known and established knowledge in chapters 1-4; chapters 5-6 cover the implementation of new tools and techniques and chapters 7-9 present new experimental results, discussions and conclusions. The structure and outline is shown below:

Known and established theory and tools that influenced this work	Chapter 1	Introduces the project background and aims.
	Chapter 2	Covers relevant crystallisation background, including classical and two-step nucleation theories.
	Chapter 3	Deals with the theory of the light scattering techniques that were used and the data analysis required for them.
	Chapter 4	Covers effects that surfaces and the molecular interactions with surfaces have on crystallisation processes.
New tools and techniques developed during this project	Chapter 5	The construction, calibration and operation of the crystallisation platform being used is explained here as well as an introduction to oscillatory flow.
	Chapter 6	Describes literature available concerning imaging of surface and bulk crystallisation. Explanations of the new image processing techniques are given.
Experimental results and conclusions from this work	Chapter 7	Results and discussion from the imaging work with regards to surface crystallisation.
	Chapter 8	Results and discussion from light scattering measurements.
	Chapter 9	Overall conclusions and impact of the work.

1 INTRODUCTION TO THE PROJECT

Crystallisation is a separation technique commonly employed in the chemical and pharmaceutical industry as it is an effective method for deriving pure substances from impure environments. The process of crystallisation is influenced by solution composition, solvent, temperature, fluid flow, heat and mass transfer and the presence of interfaces and impurities [1]. Crystallisation is highly system dependent, so crystallising one material can require a completely different set of conditions from another. In other words, the properties of the molecule being crystallised, the properties of the solvent or solvent mixture being used, the method of crystallisation being employed and the interactions of all of these variables have a significant effect on how the crystallisation will perform.

In order for a successful crystallisation unit operation design, several key aspects are essential:

- 1) Solubility and phase relationships: where, under certain conditions, the solubility of the material being crystallised needs to be determined, as well as what solid form of the material will be produced from certain solvent conditions.
- 2) Metastability limits: this allows the crystallisation to be kept under control and not to run too far into the labile region, as this means that nucleation happens spontaneously and hence without control.
- 3) Nucleation characteristics: information such as induction time behaviour will give insight as to the timescales of nucleation and how the crystallising material nucleates under certain conditions.
- 4) Crystal growth characteristics: this is a key element when understanding how the crystals will behave in terms of their particle size distribution within a crystalliser if a specific size distribution is necessary i.e. to aid downstream processing such as filtration [1].

Crystallisation from solution is important from industry's perspective as a wide range of products are manufactured using this unit operation. This separation technique has two useful aspects: a nearly pure crystal is formed from an impure solution and the method yields a solid product that is in a useful state for storage, packaging and transportation [2].

The rate at which material is produced via crystallisation varies from grams to hundreds of tonnes per day, demonstrating its importance and flexibility. One such example is the salt and sucrose industries where production exceeds 10^8 tonnes per year on a global scale. Crystallisation is used for producing fertilizer components such as ammonium nitrate at a rate of 10^6 tonnes annually. In the pharmaceutical industry, crystallisation occurs on a smaller production scale, however it is vital for preparing highly valuable end products [3].

In order to optimise crystallisation it is imperative that nucleation in both bulk solution (homogeneous) and at solid-liquid interfaces (heterogeneous) is understood since this is key to achieving better control over the entire crystallisation process.

The idea of 'unwanted' and 'wanted' nucleation is present in this thesis. Unwanted nucleation takes place in areas which are not related to the bulk solution or the pure crystalline substance i.e. heterogeneous nucleation on vessel walls, process analytical probe surfaces or on any impurities in the solution – fouling is included in this. Wanted nucleation includes homogeneous nucleation in the bulk solution or secondary nucleation that would take place during a seeded crystallisation.

To comprehend nucleation, the behaviour and structure of supersaturated solutions must first be understood, as well as its interaction with interfaces, such as impurities in solutions or crystalliser vessel walls.

Classical nucleation theory treats a supersaturated solution as a homogeneous mixture of the solvent(s) and solute. However, in recent years the so-called 'two-step nucleation theory' has been developed to describe crystal nucleation as an alternative to the classical theory, which often does not seem to agree with

experimental data [4] [5] [6] [7] [8] [9]. In the two-step mechanism, nucleation occurs from within large disordered molecular clusters containing both the solute and the solvent(s) molecules. These species have diameters of several hundred nanometres and when these clusters reach a critical size a crystal nucleus is formed from the solute contained within the cluster [10].

Investigation of crystal nucleation both in solution and at vessel walls is imperative for better understanding of how to design crystallisation processes to increase process efficiency and to obtain products with desired characteristics.

1.1 PROJECT OUTLINE

This project deals with the subject of ‘unwanted’ nucleation, which was studied in terms of induction times for fouling on the glass wall of a crystalliser and formation of prenucleation clusters in supersaturated solutions. Fouling is the process of crystals growing on the surfaces of equipment and/or probes in a crystallisation process. This is a major problem as fouling can block pipes, alter the properties of the crystalline product and obscure the data from probes and so compromising process control. This problem becomes more significant for continuous crystallisation as pipe blockage will mean shut down of the entire unit operation as well as poor product quality.

Fouling is a difficult process to monitor and measure due to its nature. Normally it can be detected through measuring a pressure drop over the system or noticing a reduction in heat transfer, but quantitative analysis is not simple and a significant amount of fouling is necessary to make such measurements. This project aims to give insight into the early stages of fouling with induction time studies through using noninvasive image analysis and processing.

The platform being used to conduct the study was chosen as it is related to the continuous crystallisation platform (discussed in Chapter 5) and therefore the effect

of fouling in a continuous environment was also explored. Experimental work covered the fouling of L-glutamic acid and glycine in the moving fluid oscillatory baffled crystalliser (MFOBC) platform. The glass surface was imaged and then analysis was carried out on those raw images to provide information pertaining to the kinetics of the fouling process. Bulk nucleation was decoupled from surface nucleation leading to fouling and both were analysed separately via an algorithm developed in Matlab, which is described in more detail in Chapter 6. Several process variables were investigated including concentration, flow conditions (amplitude and frequency of oscillation) and temperature. The effects of these parameters on the induction time in the bulk and on the glass surface were determined.

Work carried out by Forsyth et al. [11] dealt with the effects of shear on nucleation rate, and the effect on prenucleation clusters determined from light scattering experiments. Experimental evidence supporting the existence of prenucleation clusters in solution is well documented in literature and is summarised in section 2.6. These clusters have been suggested by Jawor-Baczynska et al. to have an affinity for vessel walls and that this may aid in their coalescence and further development into crystal nuclei [10]. This motivated our investigation of solution concentration and temperature cycling on prenucleation clusters in solutions using light scattering techniques.

Undersaturated and supersaturated aqueous solutions of glycine and urea were analysed. Dynamic light scattering and Brownian microscopy were used in tandem to probe how solution concentration and temperature affect these prenucleation clusters. It is important to understand how temperature changes may affect the solution structure before nucleation occurs. This may help to explain the influence of thermal history on nucleation kinetics observed in many systems.

Through using temperature cycles, the reversibility of the prenucleation cluster properties was investigated. This temperature cycling effect has not been explored previously, but the clustering ability of both glycine and urea in water is well

documented. Three different concentrations and two filtration methods were also tested for each compound.

1.1.1 Fouling in Crystallisation

In crystallisation processes, fouling (also referred to as encrustation or scaling) occurs when crystals grow on any surface which the crystallising material comes into contact with. This can be a major problem, as the consequences are detrimental to the unit operation and can result in compromising product quality or process shut down [12]. Although crystallisation has been typically a batch unit operation, continuous crystallisation is now increasingly considered as a way to enhance product quality and process efficiency. Control of fouling is one of the key challenges in successful implementation of continuous crystallisation in pharmaceutical manufacturing.

The reasons for this are enumerated in section 1.2. Implementing continuous crystallisation in a system prone to fouling becomes problematic. Reduction in heat transfer means deviation from the optimal crystallisation cooling profile, crystal product quality can be reduced, polymorph outcome can be altered and system blockage is inevitable if the fouling becomes severe [13]. Greater understanding is required to deal with this problem whether it be in the form of prevention or mitigation.

Whilst running a continuous crystallisation, fouling will always be a possibility in the process. However, it is the time taken for this to reach a critical state which is of interest since preventative methods could be implemented, allowing a continuous crystallisation to still operate efficiently with anti-fouling measures put in place.

In the literature, the theory surrounding fouling is mainly focused on heat exchanger fouling, where it is called scaling [14]. Details on fouling measurements with respect to a crystallisation environment are limited at present. Due to the stochastic behaviour of crystal nucleation it is difficult to predict the time taken for fouling to happen, since fouling succeeds nucleation whether it takes place in bulk solution or on a surface first. The properties of the surface play a significant role for example

increasing the surface roughness provides more nucleation points and encourages fouling [15]. The interactions taking place between the solute molecules and the surface material govern how nucleation takes place. The surface energy also plays a crucial role as it determines the forces at play between the surface and the solute. More favourable interactions lessen the surface energy and so nucleation will be enhanced [3]. The molecular interactions are at the heart of this and will ultimately determine the effectiveness of the interfacial tension, whether it encourages or inhibits surface nucleation [16].

Due to the lack of understanding of crystal nucleation it is therefore not surprising that crystal nucleation on surfaces is not well understood. This project aims to shed further light on this aspect of crystallisation and the variables which may affect fouling and the rate at which it forms.

1.1.2 The Importance of Understanding Nucleation

Process conditions pertaining to crystal nucleation are key to designing a unit for crystallisation [17]. If this stage could be controlled, then crystalline products could be tailored to a specific outcome. Detailed information on this stage is arguably the most difficult to obtain due to the nature of nucleation. Nucleation occurs over small timescales, which means there is difficulty in pinpointing the complexities of the nucleation process. The nuclei will typically be at nanometre scale which is difficult to access by experiment; hence computer simulations are used as a complementary means to investigate nucleation [18]. To further our knowledge of nucleation, we must first understand the behaviour of supersaturated solutions.

In many supersaturated solutions it has been observed that a clustering phenomenon between the solvent and the solute creates loosely structured prenucleation clusters following a two-step nucleation mechanism [18]. It therefore follows that clustering in supersaturated solutions needs to be studied for better understanding and control of nucleation.

1.2 PROJECT IMPACT ON CONTINUOUS CRYSTALLISATION

1.2.1 Batch vs. Continuous Crystallisation

The pharmaceutical industry has been traditionally known for the batch approach when crystallising active pharmaceutical ingredients [19]. Switching to continuous operation would allow better control over the quality of the final product through operating at steady state conditions while fine tuning the process parameters [13].

Batch crystallisation typically involves large vessels where all materials are added in one step and are left inside the vessel for a certain time to crystallise - the residence time. The vessel is then emptied and the product is collected and identified by a batch number. Once the vessel is drained, it is prepared again for the next batch to be processed. Batch operation is a flexible method in that the equipment can be used for a variety of different products e.g. several different drugs can be created using the same reactor [20]. The unit operations concerning batch processes are well understood as they have been adopted for years.

Despite batch crystallisation being a tried and tested method, there are some issues with this type of operation. For example, heat transfer into a large vessel is difficult to control, resulting in a non-uniform temperature distribution throughout the system. Different supersaturations arise from this and hence crystals are produced with different properties. Mixing may not be efficient in a large vessel, meaning there will be a large residence time distribution causing difficulty in producing a tight particle size distribution [21]. This may cause problems further down the line when the substance has to be filtered and dried. In other words each element of solution does not undergo the same experience in a batch reactor.

Some further disadvantages of the batch method are given here [20]:

- It is a disconnected process with long throughput times and long waiting times between batches.

- The plant size can be rather large due to the large vessels required, and everything is made in large quantities resulting in the inventory of the plant being high.
- Another issue, which would be eliminated with continuous operation, is that if there is a defect in the batch then the whole batch must be discarded. In a continuous system, process analytical technology could be in place to detect such problems and correct them through the process control system and this would minimise waste and in turn save time and money for the company.

Continuous crystallisation can offer better control of the process variables that affect the crystal quality and the efficiency of the entire process. Continuous processing involves a steady in and out flow of materials whereby a product is always produced and the feed is always supplied. In theory it can carry out the same production as a batch crystalliser with equipment a fraction of the size.

The benefits associated with continuous processing are as follows:

- Continuous processing will result in a decrease in operating and capital expenditure.
- Less labour will be required for transporting the material between batch units.
- Decreased inventory and smaller facilities will save on capital costs.
- Higher yields and purities of products are achievable.
- Greater sustainability due to the minimization of waste, energy usage and raw material requirements.
- Solvent recycling can be attained more effectively with the continuous system compared to the batch, saving money and creating positive environmental implications. [13] [22]

By using a continuous set up, pharmaceutical companies are able to make use of single plants where all the manufacturing is carried out in one location. This means

that there would be a general simplification of all process steps and they could be linked together efficiently [13] [23] [24].

1.2.2 Fouling in Continuous Crystallisation

Fouling is an undesirable side process of crystallisation which can lead to shut down of the entire operation [17]. Understanding this process is key to either prevention or mitigation, especially in a continuous environment when fouling can quickly become a major obstacle.

Heterogeneous nucleation is the mechanism through which fouling starts, where the nucleating species come into contact with a surface such as the crystallisation vessel wall or a probe surface. Fouling can lead to blockages, heat transfer reduction [25], unwanted crystal properties and false information from process analytical technologies which is vital for process control. Fouling could also, in theory, result from bulk nucleation followed by attachment to the surface. However, this is extremely unlikely due to the fact that bulk nucleation in general takes longer than surface nucleation. It is possible that bulk crystals could attach to an already stable crystal that formed on a surface but in general this would be rare in the case of a bulk crystal attaching to clean surface to start the onset of fouling.

All continuous crystallisation systems must be shut down periodically because of fouling within the equipment. The time the process can be run for hinges on the severity of the fouling taking place. Fouling is a major disadvantage of the continuous set up and is a barrier to adopting such a method. Extensive cleaning is required resulting in losses in time and money during the shutdown period. Continuous crystallisation is more prone to contamination compared to the batch process; therefore developing ways of dealing with fouling will allow fairer competition between continuous and batch. Due to the lack of literature published on fouling in continuous crystallisation and batch for that matter, all knowledge is from experience within the EPSRC Centre for Innovative Manufacturing and Crystallisation.

This project was aimed at gaining further understanding of the fouling phenomenon in an oscillatory flow crystalliser in order to make continuous crystallisation a more efficient manufacturing process. A novel non-invasive imaging method was adopted, since inserting probes into the crystalliser would 1) create an extra surface where fouling could occur 2) this in turn would obscure results and 3) any probe insertion would interrupt the natural flow patterns within the crystalliser and hence would not be a true representation of the system when running continuously. The effects of concentration and oscillatory flow were analysed via the imaging technique and the collaboration with Dr Christos Tachtatzis to generate a Fouling Algorithm was used to identify fouling induction times automatically (see section 6.3.2). This provided a method for implementing a real-time warning system for fouling detection so that mitigation steps could be initiated to reduce the effects from fouling and therefore allow the continuous crystallisation to continue without issue. The aim was to ultimately decouple information regarding fouling nucleation from bulk nucleation in order to do this.

The study carried out to investigate prenucleation clusters created a baseline for further work into the effect of thermal history on the nucleation process (both in the bulk and on surfaces). The aim of this work was to test the reversibility behaviour of solutions whilst undergoing a temperature cycle to understand what happens during a cooling crystallisation process. If the nucleation mechanism for crystallisation on vessel walls could be fully understood this would lead to better methods for either avoiding or reducing the impact fouling has on continuous crystallisation and subsequently the product quality.

2 CRYSTALLISATION THEORY

2.1 CHAPTER OUTLINE

This chapter covers relevant theory concerning the crystallisation process. Crystallisation is the formation of crystalline substances from a supersaturated environment where a higher purity material is obtained. When the temperature of a mixture of solvent and solute is lowered below its saturation temperature, the driving force for crystallisation is generated so that crystallisation can proceed, subject to kinetic limitations.

There are several phenomena surrounding crystallisation, which need to be better understood in order to design better controlled and more efficient processes. One of the main questions that has not been answered satisfactorily is 'what transpires in the supersaturated solution prior to crystal formation?'. In other words, what occurs on a molecular level between the solute and solvent to initiate crystal formation? Classical nucleation theory and more recently a two-step mechanism have been developed in order to describe this crystallisation step in more detail. This can be applied to both nucleation in bulk solution or nucleation on surfaces that the bulk solution is in contact with.

The definition of crystallisation is the collective organisation of numerous molecules to create an ordered three-dimensional solid structure [26]. The molecules must overcome energy barriers to create this new solid crystalline phase out of the liquid phase. Supersaturation is the driving force for this process.

2.2 SOLUBILITY AND SUPERSATURATION

Thermodynamic considerations imply that at a specific temperature there is only a certain amount of solute that can dissolve in a particular solvent under certain conditions (for example temperature and pressure). This is the solute's solubility or saturated concentration at the stated conditions and can be expressed in terms of mass of solute and volume of solvent (for example: grams per Litre which will be used in this project: g/L).

Equilibrium between the solute in the solid state and the solute in the solution phase signifies that the chemical potentials (μ) of the solid in the crystalline and solution states are equal according to Equation 1:

Equation 1

$$\Delta\mu = \mu_{\text{solution}} - \mu_{\text{solid}} = 0$$

This is the formal definition of a solution that is saturated and hence no more solute can be dissolved in the system. If the difference in chemical potential is positive, the system is supersaturated and a negative difference in chemical potential in Equation 1 relates to an undersaturated solution [27]. These conditions are depicted in a general concentration vs. temperature plot in Figure 1. A supersaturated solution has more solute dissolved than thermodynamic solid-liquid equilibrium would allow and this is subject to phase separation towards solid phase formation.

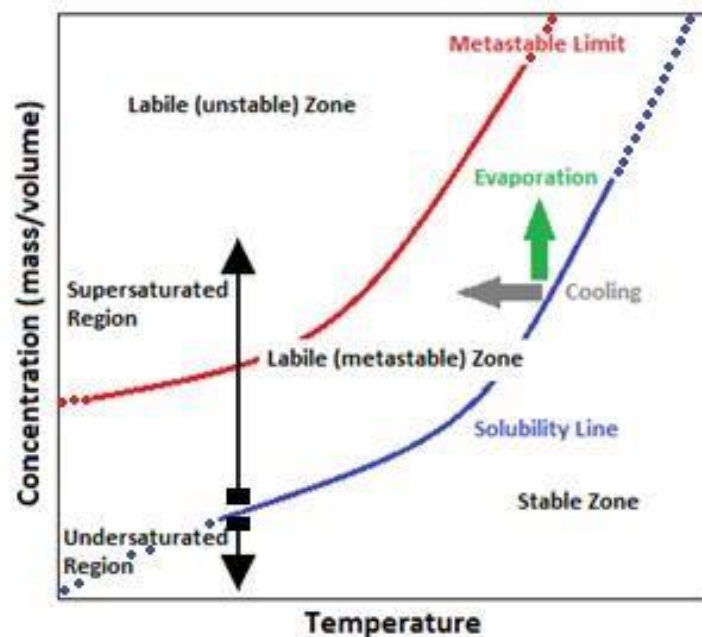


Figure 1. Solubility diagram (concentration vs. temperature) depicting the undersaturated and supersaturated zones with ways of generating supersaturation to achieve crystallisation. The labile regions (both unstable and metastable) and stable region are labelled.

Figure 1 shows that a supersaturated solution can be achieved for example via evaporation or cooling of the saturated solution [1]. The solubility diagram contains three separate sections. The thermodynamically stable area relates to undersaturated conditions and a system in this state is unable to crystallise as it lacks the required supersaturation driving force. The labile region is where solutions are thermodynamically unstable and will instantaneously crystallise as there is no energy barrier to nucleation. There is a middle region bridging these extremes named the metastable zone discovered by Ostwald in the 19th century [26]. Under these conditions the solution is supersaturated, however nucleation is subject to an energy barrier and therefore can be very slow [27]. Both the unstable labile zone and metastable zone comprise the supersaturated region where crystals can grow in the presence of the driving force of supersaturation.

Equation 2 expresses the chemical potential in terms of activity, allowing the fundamental supersaturation (S) to be calculated. Activity is a measure of concentration in non-ideal circumstances.

Equation 2

$$\mu = \mu_0 + RT \ln(a)$$

If 'a' is the standard activity of the solution phase and a* is identified as the standard activity of the crystalline phase then Equation 3 can be derived:

Equation 3

$$\frac{\Delta\mu}{RT} = \ln\left(\frac{a}{a^*}\right) = \ln(S)$$

where R is the universal gas constant and T is the absolute temperature. Due to difficulties in determining standard activities, the solutions are assumed to be ideal and subsequently the activities will not vary with changing concentration. This allows

an expression for fundamental supersaturation based on concentration to be derived given in Equation 4:

Equation 4

$$\ln(S) = \ln\left(\frac{c}{c^*}\right) \text{ hence } S = \frac{c}{c^*}$$

Where c refers to the actual concentration of solute in the solution, and c^* is the concentration of the solute at equilibrium conditions otherwise known as the saturated concentration at a stated temperature [27]. Supersaturation, S , must be stated with respect to a chosen temperature. [1]

2.3 HOMOGENEOUS NUCLEATION

The first stage to occur in the supersaturated solution during crystallisation is nucleation. Homogeneous nucleation occurs when the solid phase is obtained from a homogeneous solution phase. Nucleation has an activation energy barrier associated with it similar to that of a chemical reaction [27]. The properties of the crystals produced lie within nuclei formation and therefore a deeper understanding of the nucleation mechanism is imperative for controlling the process to a desired outcome. The crystal nucleus is defined as the minimum amount of new solid phase that can exist in isolation in the solution with great enough stability to survive without complete dissolution occurring.

Classical Nucleation Theory (CNT) is the simplest model used to describe the process of crystal nucleation. The theory was developed based on the analogy between crystallisation and vapour condensation. Therefore, the principles from condensation theory were applied. Several assumptions were made, which simplify the model but restrict its flexibility [28] as experimental evidence can attest to. There are several main assumptions connected with CNT:

- The nuclei are modelled as particles with uniform geometry and their structures and densities are taken to be equal to that of the final crystal.
- Surface tension of the nuclei is said to be independent of the size, and equal to that of the final crystal.
- Distribution of cluster concentrations is covered by their equilibrium and the nucleation rate is time independent, in other words steady state kinetics is applied.

A thermodynamic description of crystallisation was absent until Gibbs developed one in the 19th century [28]. He stated that a saturated solution contains solute molecules continually aggregating and dissolving. However, a supersaturated solution possesses the required driving force to favour aggregation, facilitating three-dimensional nucleation. The new three-dimensional structure has an energy cost associated with it, as new surface is created in solution and this is demonstrated in Figure 2.

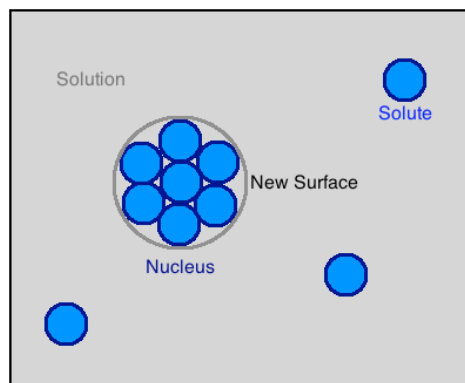


Figure 2. Classical nucleation theory: how a nucleus forms in solution from solute molecules to form a new surface.

Whether this new three-dimensional structure can form from solution or not depends on the energy required for it to do so and continue to grow into a crystal. The net free energy difference between the solute in solid and in solution is given by

the addition of the surface excess free energy G_s and the volume excess free energy G_v and is represented in Equation 5.

Equation 5

$$\Delta G = G_v + G_s$$

The volume excess free energy and the surface excess free energy are G_v and G_s respectively and are shown in Equation 6 and Equation 7:

Equation 6

$$G_v = \frac{-4\pi r^3 \Delta\mu}{3v}$$

Equation 7

$$G_s = 4\pi r^2 \gamma$$

where r is the radius of the nuclei, $\Delta\mu$ is the difference in chemical potential, v is the molecular volume and γ is the interfacial surface tension. Figure 3 represents the competing forces of G_s and G_v :

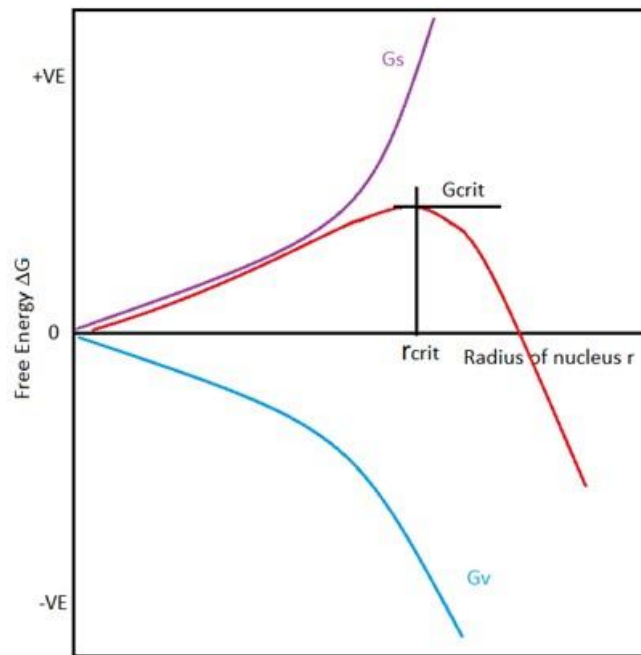


Figure 3. Free energy vs. nucleus radius graph showing the positions of the critical free energy and associated radius at the point where the surface free energy and the volume excess free energy balance to create the critical nucleus for further crystal growth.

From Figure 3 the surface excess free energy increases with the radius whilst the volume excess free energy decreases with increasing radius. The total free energy is given by the summation of the two graphs shown in red in Figure 3. The critical point occurs at the maximum of the free energy curve and it defines the point at which nuclei become stable [27]. In other words, at this point and beyond the radius of the nucleus is large enough that crystallisation can occur where the energy conditions are at their most favourable.

For a three-dimensional nucleus the critical free energy can be calculated by obtaining an equation for the critical radius r_{crit} . This is achieved by setting the first derivative of the free energy function equal to zero, because the critical point is the maximum turning point of the curve. The first derivative of the function at this point will therefore be zero. Equation 8 shows what is obtained by differentiating with respect to r .

Equation 8

$$\Delta G = \frac{-4\pi r_{crit}^3 \Delta\mu}{3v} + 4\pi r_{crit}^2 \gamma$$

$$\frac{d\Delta G}{dr} = \frac{-4\pi r_{crit}^2 \Delta\mu}{v} + 8\pi r_{crit} \gamma = 0$$

$$\text{After solving for } r \text{ gives: } r_{crit} = \frac{2v\gamma}{\Delta\mu}$$

The free energy of the critical radius is solved by inserting the value for r_{crit} into Equation 8 which results in the expression given in Equation 9.

Equation 9

$$\Delta G_{crit} = \frac{16\pi\gamma^3 v^2}{3\Delta\mu^2}$$

Using Equation 3 to substitute for $\Delta\mu$, the critical free energy of the nuclei can be expressed in terms of supersaturation as in Equation 10:

Equation 10

$$\Delta G_{crit} = \frac{16\pi\gamma^3 v^2}{3(kT \ln S)^2}$$

where S is the fundamental supersaturation and k is the Boltzmann constant with value of $1.38 \times 10^{-23} \text{ J/K}$. It is appropriate now to use the Boltzmann constant and not the universal gas constant (R) since particles are being studied and not molecules [27].

As seen from Equation 10, supersaturation plays a decisive part determining the critical free energy of the nuclei as shown in Figure 4. The larger the supersaturation, the smaller the critical radius and hence the energy barrier for their formation decreases. Eventually the supersaturation will be great enough that nucleation will be a spontaneous event [26].

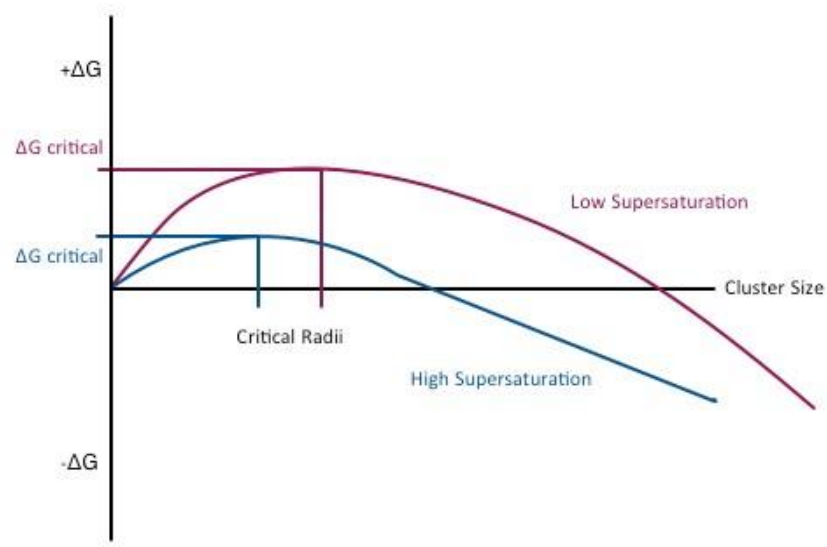


Figure 4. Critical free energy and the effect of supersaturation on the critical radius [27].

Classical nucleation theory allows the determination of the rate of nucleation, based on the Arrhenius equation in Equation 11:

Equation 11

$$J = Ke^{\left(\frac{-\Delta G}{kT}\right)}$$

where J is the nucleation rate, K is the nucleation rate constant and ΔG is the free energy, equal to $G_v + G_s$ [27].

2.4 HETEROGENEOUS NUCLEATION

More often than not it is heterogeneous nucleation that occurs in preference to homogeneous nucleation. Heterogeneous nucleation can be treated as a surface catalysed or assisted process. It is a form of primary nucleation as can be seen from the diagram in Figure 5 and differs from secondary nucleation, which has to be initiated by crystals. It is almost impossible to create a solution with no foreign species

present, but filtration can reduce these species. However, surfaces of equipment will inevitably be present and their surface properties are more difficult to predict and control [17].

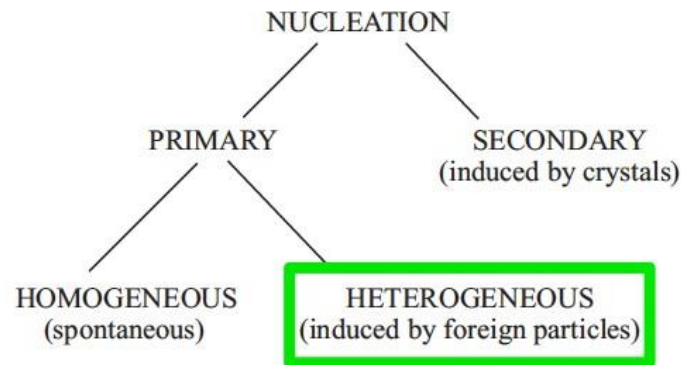


Figure 5. The differences between all types of nucleation – highlighting how heterogeneous nucleation behaves differently from the rest [3].

Any foreign substance that comes into contact with the crystallising species provides a lower free energy pathway to crystallisation. The energy pathways associated with heterogeneous and homogeneous nucleation are depicted in Figure 6.

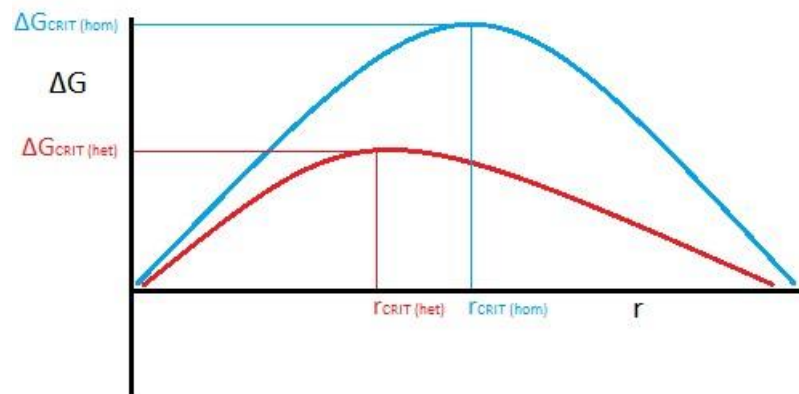


Figure 6. Free energy pathway differences between homogeneous (blue) and heterogeneous (red) nucleation with critical radii and free energies indicated for each case.

Heterogeneous nucleation allows nucleation to occur at a lower degree of supersaturation than is required for spontaneous nucleation. This means that the

overall free energy for the formation of the critical nucleus when heterogeneous nucleation is taking place must be less than the free energy corresponding to the homogeneous situation.

Equation 12 gives the relationship between the two free energies.

Equation 12

$$\Delta G_{het}^{crit} = \phi \Delta G_{hom}^{crit}$$

Where the factor ϕ is given in Equation 13 and is derived from the interfacial energy interactions present in the crystallising solution in contact with a surface.

Equation 13

$$\phi = \frac{(2 + \cos \theta)(1 - \cos \theta)^2}{4}$$

The interfacial tension (γ) is a crucial element in the heterogeneous nucleation process. The diagram in Figure 7 depicts the interfacial energy diagram for the three phases which are in contact.

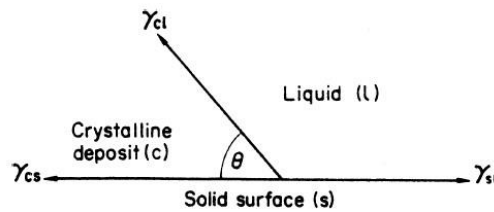


Figure 7. Typical interfacial tensions and boundaries present between 3 phases: crystallising substance, the solvent present and the solid surface where nucleation takes place [17].

The three phases are two solids and one liquid, where the interfacial tensions are denoted by γ_{cl} for the crystalline and liquid tension, γ_{sl} for the foreign surface and the

liquid tension and γ_{cs} representing the tension between the crystalline phase and the foreign surface. When these forces are resolved in a horizontal direction, Equation 14 is obtained:

Equation 14

$$\gamma_{sl} = \gamma_{cs} + \gamma_{cl} \cos \theta \quad \text{or} \quad \cos \theta = \frac{\gamma_{sl} - \gamma_{cs}}{\gamma_{cl}}$$

The angle θ is the angle of contact between the crystalline deposit and the surface providing heterogeneous nucleation. This corresponds to the wetting angle in liquid-solid systems [3]. The factor ϕ can be derived from the expressions in Equation 14 [1].

In Equation 14, when $\theta = 180^\circ$, $\cos \theta = -1$ and so $\phi = 1$. This means the energy for heterogeneous nucleation equals that of homogeneous nucleation because complete non-wetting is taking place.

When partial wetting of the surface with the liquid occurs, the contact angle θ will lie between 0 and 180° leading to ϕ having a value less than 1. This represents the liquid having an affinity for the foreign surface and so nucleation is easier to achieve and the free energy will be less than the energy for homogeneous nucleation.

When the contact angle has a value of 0, then $\phi = 0$ as well. This means that the free energy for heterogeneous nucleation is zero and demonstrates complete affinity for the surface. Seeding with crystals of the same material would be the conditions to explain this as no nuclei are required to form and hence the energy required is zero [3].

It has been seen from above that a surface can facilitate nucleation depending on the contact angle, which in turn depends on the chemistry involved within the material. The smaller the angle the stronger the wetting of the surface and depending on the

molecular interactions between the substrate and the crystallising molecule this will encourage nucleation [16]. Note that if the surface is rough, then nucleation will be hindered in this case as the solution will interact with air pockets in the rough surface rather than the surface material and typically these air pockets will hinder surface nucleation [16].

If heterogeneous nucleation could be understood better it could hold the key to either preventing fouling on surfaces during crystallisation or it could be exploited to obtain tailored materials; as well as giving further insight into the way molecules behave during crystallisation.

2.5 TWO-STEP NUCLEATION THEORY

CNT provides the conventional mathematical model for crystal nucleation, and is often used to describe the nucleation process. Experimental evidence from various systems contradicts certain assumptions made by this theory. More often than not, the classical approach fails to deliver accurate predictions regarding the dependence of the crystal nucleation rate on temperature or supersaturation. It has been found that the theory predicts values that are too low at lower temperatures and too high at higher temperatures even for nucleation of droplet from vapour. For example, when we consider the nucleation of water vapour, classical theory is correct in predicting the dependence of the nucleation rate on supersaturation. However, the temperature dependence is only correct at a temperature of 259 K, where it agrees with the experimental results. At temperatures below 259 K the agreement between theory and experiment fails. This is also seen with pentan-1-ol where the classical theory predicts nucleation rates that are 4 orders of magnitude lower than the rates given by experiment [7].

CNT gives a nucleation rate based on the assumption that the size distribution of clusters does not change over time. This results in a constant nucleation rate where there is a linear increase in the number of nuclei with time; in other words steady state conditions are assumed [28]. An experiment was carried out with the protein

lysozyme, where the nucleation time was investigated. The solutions were analysed during crystallisation by recording the NMR spectra as a function of time. Results showed a significant time delay before any nuclei appeared and the delay depended on the supersaturation of the solution. For lysozyme, this process was deemed not to be steady state because of the presence of this induction time for nuclei to appear, which contradicts the classical theory [8].

These are just a few of the miscalculations and misassumptions associated with classical nucleation theory. It cannot be ignored that if CNT fails to predict the nucleation of simple homogeneous substances like water, then its reliability for more complex systems must be brought into question [9].

Two-step nucleation theory is an alternative for explaining crystal nucleation in solutions. It is proposed that a second liquid phase forms through clustering of solute molecules and crystallisation results from these intermediates. The development of understanding two-step nucleation begins with computer simulations by ten Wolde and Frenkel. Prior to simulation, the theory existed with no supporting evidence [29]. Their study focused on the homogeneous nucleation of protein solutions. It involved a simulation based on the Monte Carlo method whereby the free energy barrier to form a critical nucleus could be calculated as a function of critical nucleus size. The results revealed that reaching the critical point occurred via the creation of a liquidlike droplet. Density fluctuations, which caused the droplet formation, were said to affect the crystallisation pathway. The route involving these droplets was deemed favourable as it lowered the free energy barrier and hence increased the rate of nucleation by a factor of 10^{13} [29] [30]. Figure 8 depicts the basic outline of the model along with the classical model for comparison.

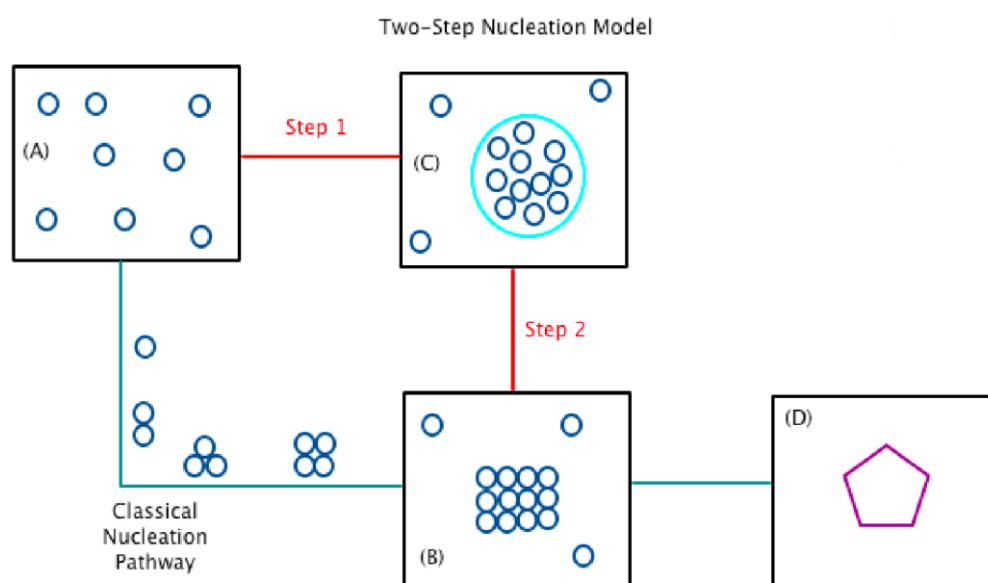


Figure 8. Diagram showing the steps involved in the Two-Step nucleation model compared to the Classical Nucleation Theory. (A) Solute molecules are present in a supersaturated solution (B) Classical theory predicts that molecules or atoms aggregate together one at a time to form a crystal nucleus (C) The two-step model envisages a loosely structured cluster containing both solvent and solute from which a crystal nucleus forms (D) This crystal nuclei continues to deplete supersaturation from within the solution and grows to form the final crystal [28].

This two-step route hypothesises that the molecules in solution (A) come together to form a dense liquid-like droplet, or a secondary liquid phase (C). This defies the classical assumptions where molecules add sequentially to form a nucleus (B).

The droplet is thought to have a loose structure containing both solvent and solute and has larger density than the rest of the solution. With this proposed model, the liquid-like clusters form in solution and the solute molecules contained within a single droplet rearrange to give the crystal nucleus (B). Growth continues to give the final crystalline product (D) [28]. In this study these structures will be referred to as prenucleation clusters even although they will be discussed in undersaturated and supersaturated solutions – clusters have been detected in undersaturated conditions despite nucleation being impossible.

A paper by Gebauer et al. [31] reviewed the recent literature on the two-step crystallisation mechanism which involves the formation of prenucleation clusters. The classical approach states that crystallisation takes place in a number of stages whereby monomers attach to one another in sequence. The non-classical approach

has a different view in that nanospecies are monomers and they combine with one another to form loosely structured crystals named here as mesocrystals. CNT cannot provide reasoning for some of the behaviours of crystal nucleation. It makes several assumptions such as the bulk energy of a young nucleus is the driver for nucleation and its structure is the same of the final crystalline product. When the solid begins to form and there is an interface formed, interfacial tension is present which in turn discourages the crystal growth. The interfacial tension that is assumed here is that belonging to a macroscopic substance. Through generating a phase interface at the critical nucleus size, the bulk energy starts to even out the energy costs of the creating the new surface of the nucleus due to the fact that the bulk scales to the cube of the radius and the surface scales with the square of the radius. Small nuclei are unstable thermodynamically and will dissolve back into solution. The free energy change for the formation of nuclei before they hit the critical radius is positive and hence thermodynamically unstable. It therefore requires stochastic variations in order for them to form as they are rare species according to CNT.

It must be noted that no concrete structural evidence for prenucleation clusters has been obtained. Figure 9 summarises all the steps involved in creating particles and where the gaps in the knowledge can be found.

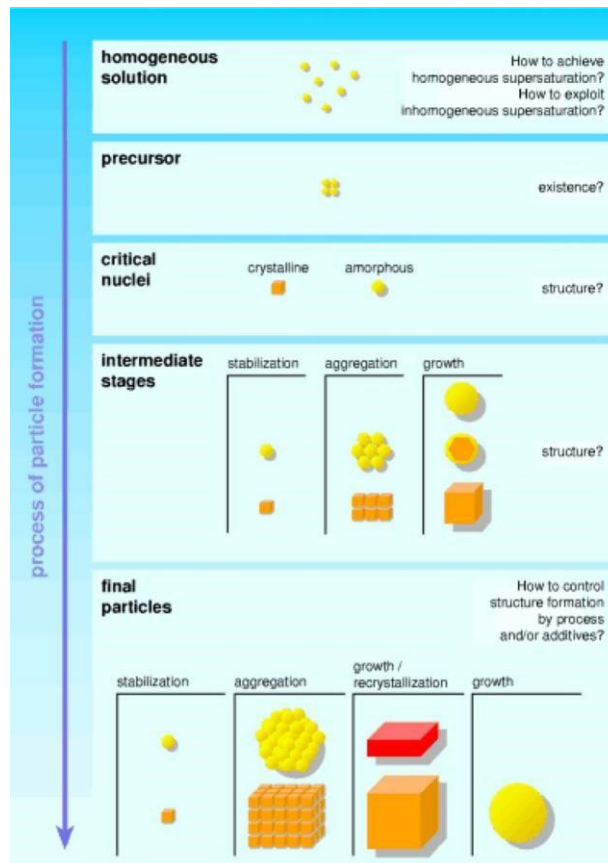


Figure 9. Sequence of steps showing the different stages during the process of forming particles to illustrate the unknowns in this area – the suggestion for a precursor to crystal nucleation is mentioned here [31].

Calcium carbonate and phosphate crystallisation has been studied and found to occur via a clustering mechanism which CNT cannot describe. Random collisions of the ions result in the formation of stable prenucleation aggregates, which are likely not to relate in any way to the structure of the final crystal. Cryogenic transmission electron microscopy has been used to show prenucleation clusters of calcium carbonate [31]. CNT is known to treat crystal formation of calcium carbonate as originating from a critical nucleus that is created from the ions that are in the solution. These ions will randomly come together to form small clusters where growth and dissolution take place until a critical size is reached. This can only be achieved when the increase in surface area can be supported by the reduction of bulk energy associated with the crystal formation [32]. Cryo-transmission electron microscopy (cryo-TEM) can image a fluid sample directly which is thermally fixed into a solid state. High-resolution

images are collected capturing the smaller units which make up the whole sample. Length scales of a few nanometres can be imaged up to several microns. In fluid systems with microstructure within, high percentages of the sample being analysed will contain water or other volatile materials. When cryo-TEM is being used for analysis, the vapour pressure has to be lowered in order to allow them to be analysed within the high vacuum in the microscope column. This also ensures that any supramolecular motion is reduced in order to reduce any blurring of the images. The samples must be approximately 250 nm in thickness to prevent inelastic electron scattering which will decrease image quality. Cryo-TEM is a technique based on the fact that when the sample is cooled fast enough to vitrify it, the microstructure can be retained and visualised. The cooling rates required here for water is approximately 100,000 K/s and this extreme rate is achieved by increasing the surface area to volume ratio as much as possible [33]. Cryo-TEM was used in a study by Pouget et al. [32] to analyse calcium carbonate crystallisation (directed by a template of macromolecules) which was found to occur via the formation of prenucleation clusters. The aggregation that takes place results in amorphous nanoparticles which form at the template until they reach a certain size at which point the loose structures become stabilised by the template and go on to form the crystal nucleus. The cryoTEM was used on fresh solutions of 9 mM calcium bicarbonate ($\text{Ca}(\text{HCO}_3)_2$) and revealed prenucleation clusters with diameters of 0.6-1.1 nm (Figure 10) with the existence of a few larger clusters with diameters < 4 nm. After the solutions were left for 2-6 mins the nanoparticle diameters detected were closer to 30 nm.

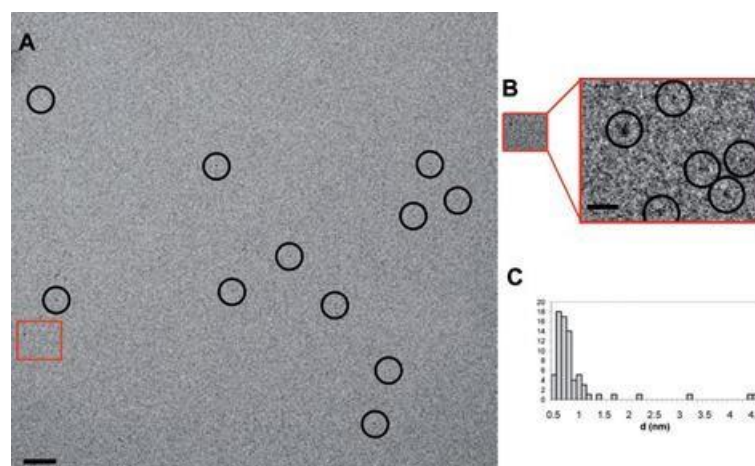


Figure 10. (A): High-resolution cryo-TEM image of a 9 mM solution of $\text{Ca}(\text{HCO}_3)_2$ after the image had been processed where nucleation clusters are seen – circled in black and the scale bar represents 20 nm. **(B):** Images that have not been filtered showing the area highlighted in red in (A). When high magnification is used here all the particles that can be identified are circled in black and any particle below the detection limit of 0.45 nm (3 times the size of the pixels) are deemed to be noise. The scale bar here is 5 nm. **(C):** This represents the particle diameter distribution in nanometres of the prenucleation species detected in the cryo-TEM images during this study [32].

Once these initial clusters form they aggregate with one another at the surface of the template until crystallisation takes place within the larger clusters. These are stabilised by the presence of the template as crystal growth continues [32].

Experimental evidence by Chattopadhyay et al. supported a two-step nucleation process. They analysed the nucleation of glycine using small angle x-ray scattering to obtain data on solution structure during the crystallisation process. It was discovered that mass fractal objects transformed into surface fractals during crystallisation. A fractal structure exhibits aggregate behaviour; therefore this change during crystallisation indicates that a two-step process was likely [34].

Analysis into mesostructured solutions in DL-valine-water-2-propanol mixtures was carried out as well as the crystallisation of valine from the solutions by JaworBaczynska et al. [35]. Dynamic light scattering and Brownian microscopy were used to detect mesostructured liquid phases in DL-valine; the same as were detected previously in other work with glycine and DL-alanine. Supersaturated and undersaturated solutions both showed mesostructured solution, the structure of which was deemed to be mesoscale clusters being formed within the optically clear

solution. Slow cooling of the solutions was carried out and on analysis the clusters were found to have a narrow size distribution with a mean hydrodynamic diameter of approximately 200 nm. Other solutions of the same composition, however were prepared differently via rapid isothermal mixing of aqueous valine with 2-propanol, were found to have clusters that were significantly larger in diameter than the ones detected in the slow cooled solutions. In these cases with the larger clusters, nucleation was found to occur much quicker than in the solutions containing smaller clusters. The mixing properties in the system were therefore having some kind of effect on the mesoscale cluster sizes. It was then proposed from this investigation that these mesoscale clusters in the solution can be the location of successful nucleation events when such clusters reach a particular critical size. Two kinds of clusters within valine solutions emerged from dynamic light scattering experiments: namely molecular clusters of diameters of 1-2 nm and solute-rich mesoscale clusters with diameters of hundreds of nanometres. The solutions that were prepared through rapid isothermal mixing crystallised 2 orders of magnitude faster than the slow cooled solutions. The fact that this couples with larger nanodroplets forming in the solution hints that larger clusters means faster nucleation and hence they are likely to play a role in the nucleation process [35].

2.6 PRENUCLEATION CLUSTERS

At the core of the two-step nucleation theory is the formation of the liquid-like droplets arising from the association of solute molecules within the solution, so-called prenucleation clusters. These were shown in stage (C) in Figure 8. Crystal nuclei are thought to emerge from the solute molecules contained in these concentrated droplets. Figure 11 gives a general representation, however their true nature and shape is unknown.

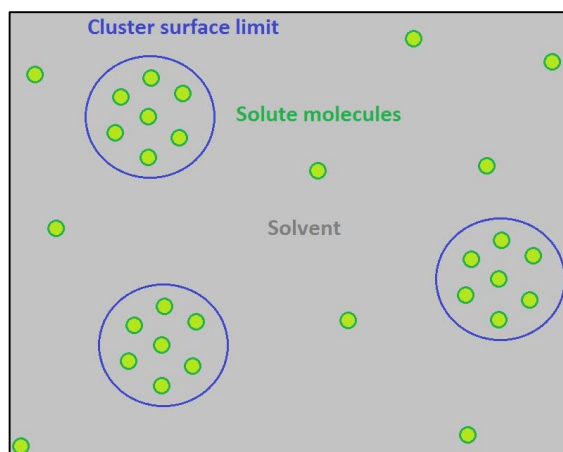


Figure 11. Schematic diagram of the prenucleation cluster structure (the true structure is at present unknown) indicating that it is constructed with both solute and solvent molecules to create a loosely held cluster with higher density than the rest of the solution but from which nucleation can take place. Solute molecules are in green, the solvent molecules are in grey and the prenucleation cluster surface limit is indicated in blue.

The solute molecules are thought to come within close proximity to create clusters of higher concentration compared with the bulk solution. It is speculated that the solute within the loose structure reorganises to give the crystal nuclei when the cluster reaches a large enough size [28].

Understanding the behaviour of supersaturated solutions and the prenucleation cluster phenomenon would be a step in the right direction to better understanding the mechanism for nucleation. This could lead to better control over crystallisation. Ambitions such as predetermining the polymorph formed and tailoring the crystal size and structure to a desired outcome may be realised. This would allow us to design and operate nucleation processes more efficiently. In addition, it would revolutionise the way science treats solution behaviour. No longer would they be considered as random and homogeneous, but having a level of internal structure. The presence of nanodroplets would mean that in some way the interaction between solvent and solute gives rise to this clustering ability, yet their existence remains a mystery at present.

This clustering phenomenon is reported to occur in molecules and particles in solution, particularly with polyelectrolytes, proteins and colloids [36] [37] [38] [39] [31] [40]. The random generation of clusters reach a state of equilibrium within these solutions and clusters only reach a certain size. This behaviour is not fully understood. To explain this phenomenon, one model (based on the study of colloidal particles in non-polar solvents) was proposed based on short-range attraction and long-range repulsion interactions. It was suggested that when molecules add to a cluster, the long-range repulsion of other clusters combined with the short-range attraction of the cluster itself is what enables it to be stable. The type of aggregation that was investigated was that of equilibrium clusters where one infinitely large aggregate or a separate macroscopic phase, does not form. This means that some method of stabilisation must be present to prevent this from happening. The existence of small portions of charge on the aggregates was the stabilisation method put forward [41]. This contradicts the general model for molecular behaviour where we consider the opposite to be true. Molecules in close contact are more likely to repel in order to minimise electrostatic forces. However, evidence supports this theory for *charged* environments where screened-coulomb interaction repels at long range and polarisation attracts at short distances [39].

The clustering phenomenon was also detected in a study of solutions of the protein lumazine synthase; where dynamic and static light scattering techniques and atomic force microscopy were employed. Dense liquid species with diameters on the nanoscale were detected. By increasing the protein concentration, the frequency of cluster detection also increased, despite their size remaining constant. The conclusion drawn from this was that an optimum size of these species seemed to exist, where the average diameter was approximately 350 nm [42].

Another area of research studying hydrophobic and hydrophilic interactions between peptides by McLain et al. revealed that clustering could occur in solution. The simulations used molecular dynamics and a model obtained through experimental data from neutron-diffraction measurements. Dipeptides were analysed in their

zwitterionic form. The radial distribution functions showed the main interaction was between the $[\text{NH}_3^+]$ and $[\text{CO}_2^-]$ groups; however the question was whether dimer interactions could be responsible for large-scale clustering? The model based on experimental data stated there was a 90% chance of clusters containing up to 50 peptide molecules. In contrast, the simulation with no limitations from the neutron diffraction data gave this a 40% probability (this shows the importance of including experimental evidence in simulations) [40].

Dynamic light scattering was used in a study by Georgalis et al. to identify clusters in aqueous electrolyte solutions. Several compounds were investigated, including sodium chloride and ammonium sulphate, in undersaturated and supersaturated conditions. Clustering was observed in both cases. Reported diameters ranged from 50-500 nm, showing that inorganic species also possess this clustering ability [43].

A series of three papers by Sedlak from 2006 investigated the phenomenon of clustering in solutions with solutes of low molecular mass. The first paper focuses on describing solution structure due to clustering effects in liquid mixtures, electrolytes and non-electrolytes using static and dynamic light scattering. It is stated that the interaction between the solvent and solute gives rise to large supramolecular organisation. Uneven distribution of the solute arises with areas of high and low concentration existing in all species analysed. The size distribution of the clusters varied, however on average the diameters reached several hundred nanometres. The so-called 'domains', or clusters, were shown to have higher solute concentration than the bulk solution with the domain diameters decreasing with increased sample dilution [36].

The second paper by Sedlak tried to unravel the kinetics of the cluster formation and their stability over longer periods of time. Constant analysis of liquid mixtures revealed that the time required for cluster formation ranged from minutes to a few weeks. Scattering intensity increased over time, hence the clusters were growing. Solutions containing solid solutes portrayed the same traits with an increase in

diameter and size distribution over time. On average, the domain structures remained stable within a fifteen-month timescale [37].

The final paper in the Sedlak series studied the interactions between solute and solvent and how they could be responsible for solute association. The main hypothesis was stated in the paper as: *'domains arise due to attractive forces between the solute molecules occurring through hydrogen bond bridges that are created from one or more solvent molecules, which are also hydrogen bonded'*. It was found that clustering was more evident in solutions where the solvent was able to form networks. Methanol and water were compared, with domains occurring in water but not methanol. Water has the higher boiling point due to its stronger hydrogen bonding capabilities. Extensive networks are facilitated via hydrogen bonding because of the electronegativity difference between oxygen and hydrogen. Some solute molecules revealed that possessing a dipole might explain clustering ability. Several non-polar and polar molecules were investigated and it was found that non-polar compounds did not exhibit this clustering phenomenon, but those with polar properties did. However, this was later quoted in the paper as a *'necessary condition, but not a sufficient condition'*. This was due to further study, which showed that some highly polarised substances did not cluster. It must be noted that these papers try and explain the clustering phenomenon based on trends and the fundamental interactions between molecules that have already been established [38].

A study by Ward et al. [44] investigated clustering in aqueous urea solutions using second-harmonic scattering. Second-harmonic scattering (SHS) is a non-linear optical method whereby the frequency of the light is doubled as the laser light is passing through a nonlinear object – i.e. a crystal structure. It was proposed that if the prenucleation clusters of urea have any type of crystalline structure or order then they will exhibit SHS. In this study supersaturated aqueous urea solutions were used to investigate the possibility of prenucleation clusters via measuring SHS using scanning microscopy. The SHS signal was measured as a function of the concentration

over several supersaturations from 0.15 to 1.86. The results from the experiments reveal a nonlinear increase in the signal from SHS with increasing concentration where a local maximum appears at $S=0.95$ and at $S=1.75$. This indicates that there are noticeable changes in the structure of the solutions at these supersaturations. When Rayleigh scattering experiments were carried out, it suggested that there were free particles present within the urea solutions. SHS experiments which were time-dependent gave peaks in the signal similar to those obtained when scanning through solutions of barium titanate (BaTiO_3) nanoparticles with diameters of less than 200 nm which exhibit bulk second harmonic generation. Due to the fact that the intensities were 20 times larger for the BaTiO_3 particles than the $S=0.98$ urea solutions, it was proposed that the urea solutions were exhibiting clustering of some order which change with supersaturation [44].

Urea is commonly used to denature proteins and in a study by Stumpe et al. [45] molecular dynamics simulations were carried out for a large variety of urea concentrations at different temperatures to probe the structure and energetics of aqueous urea. Little is known about the mechanism via which this happens, however this study looks into the clustering ability of urea molecules in water. The outcome of the investigation revealed that the hydrogen bonds between the urea and water molecules were much weaker than the ones between the water molecules on their own. In turn this results in a hydrophobic effect that encourages the urea molecules to self-aggregate. At concentrations similar to that used in protein denaturants, the urea molecules were found to aggregate at a degree of approximately 20% when the water exposed urea surface area was reduced. The urea aggregation was quantified in terms of the reduction of the total amount of water surface made available by the urea compared to the non-aggregated urea. Three different urea pair configurations were determined and their populations were studied via translational and orientational pair distribution functions. Water structure was found to be strengthened by the presence of urea when studying the hydrogen bond energies and the solvation shell population. The outcomes here were in agreement with the urea/protein interaction being the main driving force for denaturation. Another

indirect effect is that a weakening of the hydrophobic effect due to the presence of urea means that the water structure is reinforced. It was also found that there was a concentration independent number of hydrogen bonds per water molecule which means at even high concentrations the urea molecules seem to substitute for the water ones exceptionally well in terms of their geometry and steric behaviour in the hydrogen bonding system. Despite all this information not giving a complete view of the protein denaturation mechanism, the hydrogen bond energy analysis revealed that the water-water hydrogen bonds are stronger than the water-urea or urea-urea interactions. Urea can join the water network, however the differences in the hydrogen bond energies mean that the urea self-aggregates [45].

A paper by Abu-Hamdiyyah [46] gave some insight into why urea forms clusters in water. It is known that non-polar substances dissolve interstitially in water and in aqueous urea solutions. These aqueous urea solutions have physicochemical properties which suggest that the urea does not affect the water structure in the way ions would, but forms clusters. When urea is added to water the hydrophobic bonding is weakened because of the cluster formation. The urea molecules take part in creating clusters of urea and water and these clusters are the reason behind forming the small spaces in solution that can host the nonpolar parts of the solute. Urea's behaviour cannot be likened to that of ionic species. Larger spaces are more easily formed in aqueous urea than in pure water and the opposite is valid for small spaces that hold methane or ethane molecules at low temperatures [46].

Well-tempered metadynamics simulations have been used in a study by Salvalaglio et al. [47] to investigate whether the nucleation mechanism for urea in water happens via a single or two-step process based on the molecular details obtained from the simulations. As mentioned previously, the two-step process would indicate that a liquid-like cluster would form prior to nucleation. In order to study this, the free energy of the largest cluster is considered in the simulation box. Through analysing the molecular mechanisms at work throughout the simulations, density changes were observed and were essential for the nucleation of urea crystals to take place. It was

found that in the simulations nucleation occurred after disordered, short-lived urea clusters formed from the homogeneous solution. This reinforces the idea of the two-step mechanism and refutes the classical nucleation theory as growth of the nucleus does not appear to happen step by step but rather in the form of solute clusters [47].

A study by Sun et al. [48] utilises *in situ* infrared (IR) spectroscopy along with theoretical calculations to show that the liquid to solid crystallisation of urea proceeds via clusters. Experimentally this is a challenging task. IR absorption spectroscopy can help identify the symmetry of a cluster or particle based on the selection rules which determine the number of allowed transitions. In this work *in situ* attenuated total reflectance-infrared (ATR-IR) spectroscopy was used to analyse the liquid-solid change of urea in water. By means of combining this experimental data with theoretical calculations, it was shown that urea crystallisation follows CNT in that it crystallises via aggregation of smaller primary clusters. When IR band intensities were seen to increase this reflects an increase in the concentration of urea molecules in the solution. It was also noted that when the NH₂ band wavenumbers shifted, there was a change in the geometry of the urea clusters. The symmetry of urea stays constant when the crystals are produced and hence it is assumed that CNT takes place in that urea molecules form clusters which grow to a critical size which then nucleate.

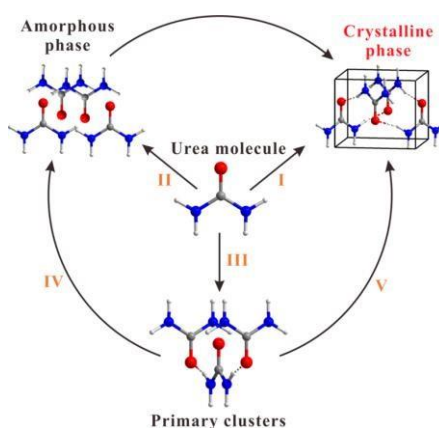


Figure 12. Diagram representing the changes in structure of the urea molecule as it undergoes crystallisation in water. In scenario I, the urea molecules self-assemble to create the crystalline phase directly. Scenario II shows that the urea molecules are able to aggregate to form an amorphous state which can transform into the crystalline phase. Primary clusters shown in scenario III result from the aggregation of urea molecules, then

growth increase of these primary clusters make up the amorphous phase (scenario IV) or the urea crystal nuclei (scenario V) [48].

Theoretical calculations were used to give further evidence for the IR data pertaining to the urea phase transformation from liquid to solid during crystallisation. Urea's crystal morphology is dependent on the processes taking place at the interface of the solid and liquid. This was calculated using the proper chemical bonding energy density at the relevant interfaces of the crystal. The results were a geometric diagram of urea whereby the common geometries and growth conditions can be seen. Therefore, through using *in situ* vibration spectroscopy and chemical bonding calculations, a deeper insight into the behaviour of urea crystallisation via the formation of primary clusters has been achieved [48].

Molecular dynamics simulations are useful when trying to understand clustering behaviour of molecules since experimental observation makes analysing this phenomenon very challenging due to their nature. A study by Hamad et al. [49] analysed glycine clusters under four different concentrations and for each concentration four different temperatures were used. The N-H \cdots O-C hydrogen bond is found to be the most common type of interaction between glycine molecules. Dimers of glycine, although they are found to form, were not observed often and when they were they dissociated quickly. Despite this they have a high tendency to reform. Different factors were looked at such as the cluster size distribution, the radii of gyration and the lifetime of the hydrogen bonds. Diffusion coefficients for the glycine clusters and water molecules were also determined and the results agreed with experimental findings. The simulations revealed the presence of small shortlived hydrogen-bonded clusters comprising glycine molecules, and no evidence of extreme dimerization of glycine. Low concentrations of these clusters were found to exist, despite this it was stated that their formation cannot be excluded as an important stage for glycine crystallisation of the α -polymorph which is the form most commonly produced experimentally [49].

Solutions of highly soluble species, such as small amino acids, are deemed to be homogeneous mixtures with no significant internal structure beyond molecular clusters and hydration shells. Some recent work has proposed evidence for the existence of larger supramolecular species in solutions of small organic and inorganic substances including proteins. DL-alanine and glycine were analysed by JaworBaczynska et al. [50] in the supersaturated and undersaturated aqueous state using dynamic light scattering and Brownian microscopy/Nanoparticle Tracking Analysis and Cryogenic Transmission Electron Microscopy. Prenucleation clusters have been found in supersaturated solutions of DL-alanine and glycine but also in undersaturated solutions where the concentration was well below the solubility line. The diameters of these nanoclusters range from 100-300 nm with the size distributions broadening when the concentration of the amino acid increases. The prenucleation clusters do not form a separate phase, they are more accurately described as ‘thermodynamically stable mesostructured liquids containing soluterich domains dispersed within bulk solute solution’. The Cryo-TEM analysis showed colloidal scale objects which could not be identified in blank water samples. The dimensions of these species were from 300-400 nm and they are likely to be the same species that are detected with DLS and NTA. The high resolution Cryo-TEM facilitated the visualisation of prenucleation clusters in undersaturated solutions of the amino acids. Electron diffraction patterns showed that the species were amorphous in nature and from the images it can be seen that they have irregular shape.

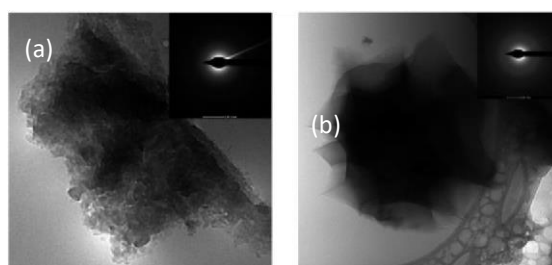


Figure 13. Cryo-TEM images of prenucleation clusters in unfiltered undersaturated solutions, accompanied by their electron diffraction patterns for (a) DL-alanine (150 mg/ml) and (b) glycine (200 mg/ml) [50].

It was found that the glycine prenucleation clusters had more liquid-like properties since they were able to pass through the PTFE 100 nm syringe filters; whereas DLalanine prenucleation clusters were found to bind to both types of filter suggesting they have a more dense structure. It should be noted that when the prenucleation clusters were 'removed' by the syringe filter, after agitating the solution for some time the prenucleation clusters reappeared. Work previously carried out with aqueous glycine indicated that a critical prenucleation cluster size may be required for successful nucleation to take place within them and hence subsequent crystal growth [50].

In a paper by Jawor-Baczynska et al. [10] it was proposed to investigate whether prenucleation clusters, that potentially provide a pathway to nucleation, also form when crystals dissolve. This is therefore the reverse process of these prenucleation clusters forming in order to allow nucleation to occur.

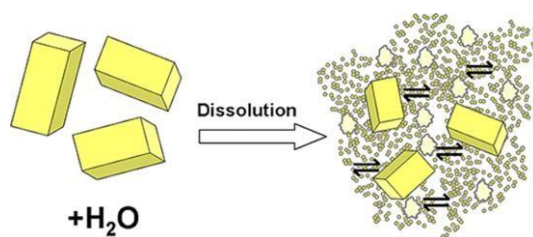


Figure 14. Illustration of the reversibility process of prenucleation clusters – i.e. if they reappear on dissolution of crystals grown from supersaturated solution i.e. they are in equilibrium with the crystals in solution [10].

The system investigated here was aqueous glycine and the techniques used to analyse this system were small-angle X-ray scattering, dynamic light scattering and nanoparticle tracking analysis. Prenucleation clusters were detected when glycine crystals were dissolved in water, with diameters of approximately 250 nm when the concentration was close to saturated. The glycine-rich clusters remained in the solution when excess glycine crystals were still present with a number concentration of 10^9 per ml at equilibrium. When quiescent aqueous glycine solutions of supersaturation 1.1 were both nanofiltered (low numbers of prenucleation clusters) and unfiltered (higher numbers of prenucleation clusters) it took approximately 30

hours for only a single glycine crystal to form. The time to crystallisation was greatly reduced when a small stirrer bar was placed into the vial and was allowed to gently tumble inside. After 3-5 hours a large number of microcrystals were produced.

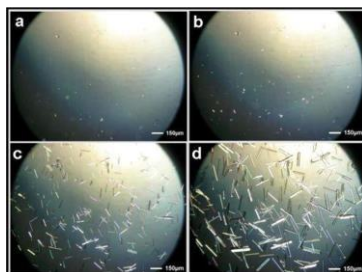


Figure 15. Picture of glycine crystals grown from a 270 mg/ml solution, created by continuously inverting the vial of solution with a tumbling magnetic stirrer bar for 3 hours. Small portions of the solution were analysed on a microscope slide and were covered to reduce evaporation. The images shown here were taken at time (a) 0 min (b) 1 min (c) 5 min and (d) 10 min after initial crystals were detected [10].

The other explanations for this behaviour such as secondary nucleation, bubble formation, glass splinters from the vial or scratches were all eliminated through control experiments. Analysis of the glycine solution just prior to the appearance of the microcrystals revealed prenucleation clusters with diameters greater than 750 nm which were not detected in the original quiescent solution. The hypothesis was therefore that prior to nucleation there is pathway which occurs via these larger prenucleation clusters since it seems logical that a critical mass of glycine within the prenucleation cluster is needed for nucleation to succeed [10].

The literature review describing work carried out to study prenucleation clusters in solution spans a variety of compounds (from salts to proteins), conditions and is covered by experiment and molecular simulation. These species were found to exist in solution to different extents depending on the system and two systems widely studied in this regard were glycine and urea, both in aqueous solution. It was reported that in general, shearing solutions increased the diameter of the clusters and that they could be detected in undersaturated and supersaturated solutions. These two systems were chosen as a basis for the light scattering work carried out in this project

because of the existing data on their behaviour. The literature has no mention of temperature cycling of these solutions and hence there is no data available on the reversibility of solutions and how they behave under continuous temperature change – as they would experience during a crystallisation experiment.

This aspect was investigated in this thesis.

2.7 MODEL FOR NUCLEATION RATES BASED ON INDUCTION TIME PROBABILITY DISTRIBUTIONS

Part of the experimental work in this project dealt with obtaining fouling induction times during crystallisation of aqueous solutions. A study by Jiang et al. [51] was used to analyse the results through making use of the probability distributions of induction times that were measured.

This study determined nucleation rates from cumulative probability distributions of induction times. The procedure utilises the stochastic behaviour of nucleation. Experimental probability distributions of the induction times obtained are fitted with Equation 20 (the derivation of which is outlined here) for describing the distribution with respect to induction time. Experiments had to be repeated many times with the same conditions and thermal history in order to obtain meaningful statistics.

When there is constant supersaturation, the creation of a crystal nuclei is deemed a random process and can be described by the Poisson distribution given in Equation 15.

Equation 15

$$P_m = \frac{N^m}{m!} \exp(-N)$$

Where N is the average number of nuclei present which will have formed in the time interval. It follows that the probability that no nuclei are formed is given by Equation 16:

Equation 16

$$P_0 = \exp(-N)$$

Subsequently, the probability that there will be at least one crystal nucleus present can be represented by Equation 17:

Equation 17

$$P_{\geq 1} = 1 - P_0 = 1 - \exp^{[10]}(-N)$$

The average number of nuclei formed in a certain time interval t_j within a specified volume V can be related to the stationary nucleation rate J via Equation 18:

Equation 18

$$N = J V t_j$$

The probability $P^*(t_j)$ that at least one nucleus has been created during that time interval t_j is therefore obtained:

Equation 19

$$P^*(t_j) = 1 - \exp^{[10]}(-J V t_j)$$

During the course of an experiment, there will be a time delay accounting for the fact that it will take appreciable amount of time for nuclei to grow to detectable sizes. This delay t_g is the growth time between the appearance of one crystal nucleus t_j until the time that crystals can be first detected, t : in other words $t_j = t - t_g$. The following equation is then used to fit to the experimental probability distribution given in Equation 20:

Equation 20

$$P(t) = 1 - \exp[-JV(t - t_g)]$$

By performing the fit the two parameters of nucleation rate (J) and growth time (t_g) are obtained. The experimental probability distribution is determined using Equation 21:

Equation 21

$$P(t) = \frac{M^+(t)}{M}$$

Where $M^+(t)$ is the number of experiments where crystals are detected at time t and M is the total number of experiments.

3 DETECTION OF PRENUCLEATION CLUSTERS WITH LIGHT SCATTERING TECHNIQUES

3.1 CHAPTER OUTLINE

Chapter 2 discussed the two step nucleation theory where prenucleation clusters within solution were proposed. In order to probe the existence of these species, light scattering methods can be implemented.

This chapter gives an overview of the two relevant light scattering techniques: dynamic light scattering (DLS) and Brownian microscopy or nanoparticle tracking analysis (NTA). These can be carried out using the Malvern© Zetasizer Nano and NanoSight instruments respectively.

The underlying theory is discussed in detail below but ultimately the two methods produce hydrodynamic diameters derived from the determination of diffusion coefficients via the Stokes-Einstein equation. Number concentrations can also be obtained from Brownian microscopy. The two light scattering techniques complement each other well.

3.2 DYNAMIC LIGHT SCATTERING

When light comes into contact with particles/molecules it can either absorb or scatter the electromagnetic radiation. If the wavelength of incident light corresponds to an energy transition within the molecule or atoms then this energy will be absorbed. If it does not correspond to an absorption band the light will scatter in all directions [52]. In a homogeneous and isotropic substance, the light scattered by the individual particles interferes destructively. This means that no scattered radiation is observed. The consequence of this is that scattered light is only seen when the sample is heterogeneous in nature.

If solutions were being studied, the scattered light would be the result of a difference in optical properties of species/particles in the solution i.e. the refractive index difference between the species/particles detected and the bulk solution [52].

The set-up for dynamic light scattering (DLS) experiments is depicted in Figure 16.

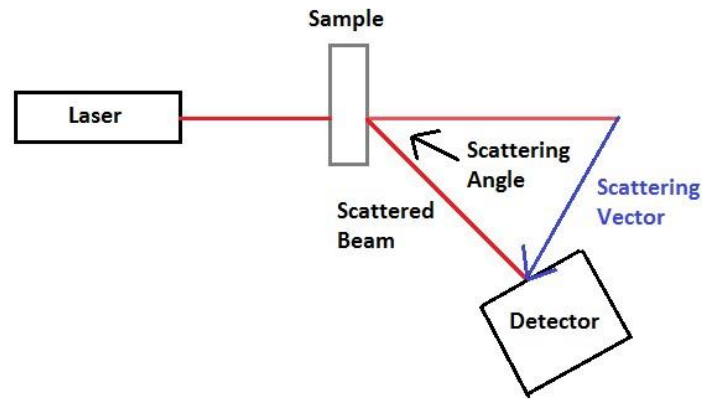


Figure 16. Dynamic light scattering diagram depicting the main components of the system.

Figure 16 shows the position of the scattering vector $q(\theta)$ in inverse metres, and the scattering angle (θ) in degrees. The vector associated with the incident beam is assumed to have the same magnitude as the vector of the scattered beam. This allows q to be calculated, and it is equal to the difference between the incident and the scattered wave vectors as is given in Equation 22:

Equation 22

$$q = \frac{4\pi n}{\lambda} \sin \frac{\theta}{2}$$

where n is the refractive index of the solution and λ is the wavelength of the laser beam [52].

Light scattering experiments give results based on intensity (I), which depends on the angle (θ) and the observation time (t): ($I(\theta, t)$). There are two types of light scattering

experiment that can be carried out: dynamic and static light scattering [52]. Dynamic light scattering is that technique that will be discussed here as this is the technique which is relevant for this work.

DLS is a time resolved experiment where one or more scattering angles are investigated and the changes in intensity over time are recorded. The resulting information deals with time dependent properties of the sample, such as the Brownian motion. The diffusion coefficient of the moving particles can then be determined. An autocorrelation function is the name given to data obtained from a DLS experiment, arising from intensity fluctuations in the light scattered by the sample as species move in and out of the laser beam. Knowing the diffusion coefficient is the key to estimating a particle size [52].

3.2.1 Autocorrelation Function

The autocorrelation function ($G_2(\tau)$) is the average value of the intensity recorded at time t ($I(t)$) multiplied by the intensity recorded after a time delay, τ . It is represented by:

Equation 23

$$G_2(\tau) = \langle I(t) \cdot I(t + \tau) \rangle \text{ [52]}$$

The result is an average value because the calculation is carried out for many values of t . When studying Brownian motion in a solution the autocorrelation function is a decaying function of time delay, τ [52]. Large decay times represent larger particles because they take longer to diffuse in solution; whereas smaller particles have larger diffusion coefficients and hence their decays will be shorter.

The autocorrelation function has a decay rate: Γ (s^{-1}). This can be related to the diffusion coefficient of the particles in solution via Equation 24:

Equation 24

$$\Gamma = Dq^2$$

where D is the diffusion coefficient (m^2s^{-1}) and q is the scattering vector.

3.2.1.1 Decay Rate

As mentioned, the decay rate, Γ , is obtained from the autocorrelation function. The function is plotted as intensity vs. delay time (on a logarithmic scale). The decay rate can be determined by fitting a third order polynomial to the plot of the natural log of $G_2(\tau)$ vs. the lag time using the cumulant analysis. For a monodisperse system this should yield a linear plot of $\ln(G_2(\tau))$ vs. lag time. However, the more polydisperse the sample, the more this plot will deviate from linearity, and hence several decay rates may be present in one autocorrelation function.

Once the third order polynomial has been fitted, the decay rate is equal to the coefficient of the first order term in the equation, i.e. the magnitude of coefficient c in Equation 25:

Equation 25

$$\ln(G_2(\tau)) = a\tau^3 + b\tau^2 + c\tau + d$$

coefficient c, or the decay rate Γ (s^{-1}), can now be used in the calculation of the hydrodynamic diameter of the particles in the sample.

3.2.1.2 Hydrodynamic Diameter

The hydrodynamic diameter is the theoretical diameter of a hard sphere, which diffuses in the same manner as the particles in the sample under examination. The

hydrodynamic diameter (d_H) is calculated from the diffusion coefficient using the Stokes-Einstein equation given in Equation 26:

Equation 26

$$d_H = \frac{k_B T}{3\pi\eta D}$$

where k_B is the Boltzmann constant with value: 1.38×10^{-23} J/K; T is the temperature in Kelvin; η is the sample viscosity in Pa.s and d_H is in metres.

Advantages of DLS include being able to obtain approximations for properties such as the polydispersity of the sample and the mean hydrodynamic diameter. DLS is able to detect a wide range of particle sizes (1-1000nm) and the sample preparation is straightforward [53].

There are some disadvantages, especially when dealing with polydisperse systems. The information obtained in these cases can be more complex. In DLS the intensity of scattered light is directly proportional to the diameter of the species in the sample raised to the 6th power ($I \propto d^6$). This results in larger particles in the sample masking the presence of smaller ones and so the data is biased towards larger species [54]. Dust and other contaminants influence the scattering process and may give false information about the sample. This is true of any light scattering technique, not just DLS.

It must be emphasised that the hydrodynamic diameter is an approximation. This is due to the assumption that the particles are hard spheres. There can also be multiple scattering that influences the data. It is caused by light from one particle striking another particle from which further scattering takes place. The likelihood of multiple scattering increases with increasing concentration, since more scattering species increases the probability of this occurring.

3.2.2 Data Analysis of Autocorrelation Functions

Due to the extreme polydispersity of the samples being studied, rarely would the autocorrelation functions correspond to one hydrodynamic diameter. The autocorrelation functions would consist of several exponential decays within one function.

It was therefore necessary in some cases to fit 2 or 3 exponential decays to one function. This was carried out using Matlab where the formula given in Equation 27 represents the actual correlation function as a sum of three exponentials that the experimental data was fitted to. This equation does not have any 3rd order terms as there would be too many fit parameters.

Equation 27

$$G_2(\tau) = Ae^{-\frac{1}{\alpha}\tau} + Be^{-\frac{1}{\beta}\tau} + Ce^{-\frac{1}{\gamma}\tau}$$

where A, B and C are coefficients which indicate the contributions of each decay as part of the whole function; $-1/\alpha$, $-1/\beta$ and $-1/\gamma$ are the decay rates pertaining to each individual decay. Equation 24 with the new notation from the fit now becomes Equation 28:

Equation 28

$$-\frac{1}{\alpha} \text{ or } -\frac{1}{\beta} \text{ or } -\frac{1}{\gamma} = Dq^2$$

where α , β and γ are taken from the curve fitting for the 1st, 2nd and 3rd decay respectively.

An interactive curve fitting tool designed by Dr Jerzy Dziewierz from the Centre of Ultrasonic Engineering at The University of Strathclyde is shown in Figure 17 was able to automatically calculate all of these parameters after uploading the time and

intensity data which makes up the autocorrelation function. This tool used initial guess values to fit the experimental data to Equation 27 and then interactive cursors represented in red, green and blue in Figure 17 could be moved on the graph to change the guess values. This resulted in the lowest error and hence best possible fit. Whenever two decays had to be fitted the model in the Matlab script was modified accordingly. The decay rate can therefore go on to be used in the Stokes-Einstein equation (Equation 26).

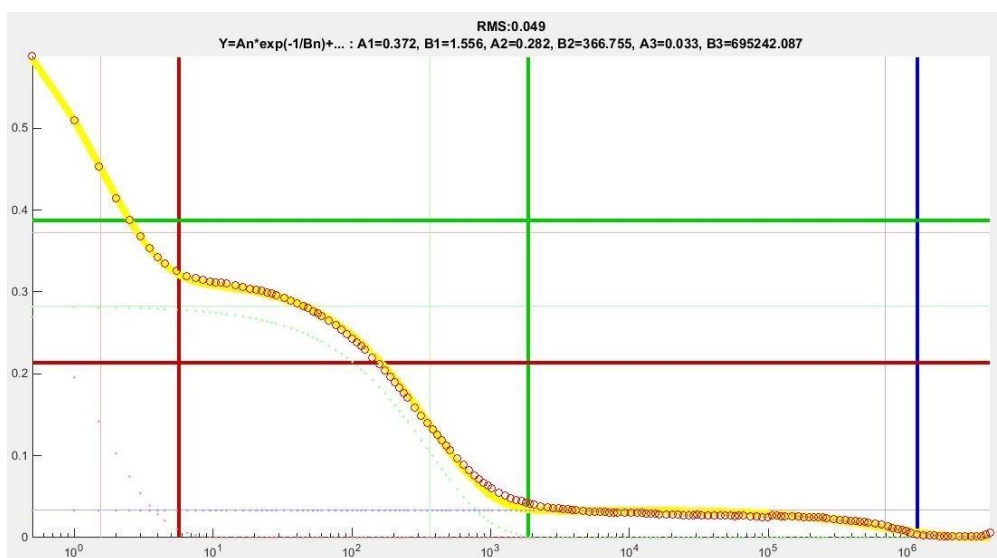


Figure 17. Screenshot of the interactive curve fitting tool created by Dr. Jerzy Dziewierz indicating the interactive cursors shown in red, green and blue corresponding to the 1st, 2nd and 3rd decays present in the autocorrelation function respectively. The RMS error value and the coefficients are given.

3.2.2.1 Viscosity vs. Temperature Data

From literature, there was limited data available for the actual viscosity of glycine and urea aqueous solutions and how this changes with temperature. Table 1 gives all the data that was found from literature for water, aqueous glycine solutions at the different concentrations used in this project at 25°C and some viscosity changes from 35-55°C at the lowest concentration of urea used.

Table 1. Data for Viscosity with Temperature for Water, Glycine and Urea Solutions

Water Temperature (°C)	Water Viscosity (Pa.s) [55]	Glycine Concentration (g/L)	Aqueous Glycine Viscosity at 25°C (Pa.s) [56]	Temperature for Urea Solutions (°C)	Urea (522.06 g/L) Viscosity (Pa.s) [57]
10	0.001307	154.9	0.00118	35	0.0010773
20	0.001002	234.98	0.0013	40	0.0009819
30	0.000798	299.06	0.0016	45	0.0009047
40	0.000653			50	0.0008273
50	0.000547			55	0.0007679
60	0.000467				
70	0.000404				
80	0.000355				

It can be seen that because all of the data for the full temperature cycle of 10-80°C could not be found, the data for pure water was used in all calculations to do with calculating the hydrodynamic diameter from the Stokes-Einstein equation. This was deemed a reasonable approximation for the calculations.

3.2.3 Dynamic Light Scattering with the Malvern Zetasizer Nano

All dynamic light scattering (DLS) experiments were carried out with the Malvern® Zetsizer Nano which has the capability of measuring three different properties of particles:

- 1) particle size
- 2) zeta potential
- 3) molecular weight
- 4) intensity of scattered light (counts per second) – related to concentration

For this project only particle size measurements were of interest and the DLS measurements were carried out at a scattering angle of 173° . Hardware components in the system are summarised in the diagram in Figure 18.

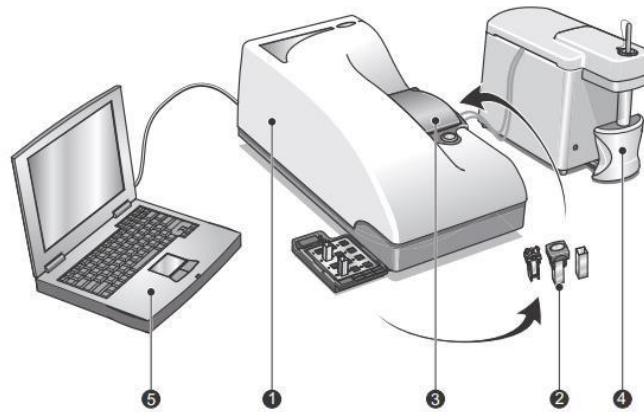


Figure 18. Hardware components of the Zetasizer Nano system from Malvern © [58].

A description of the main components numbered in Figure 18 are given here:

- 1) Zetasizer Nano optical unit which measures the sample using green and red laser wavelengths.
- 2) A selection of cells are available to carry out sample measurements where the laser light will pass through.
- 3) Cell area is where the cells are inserted so that measurements can be taken.
- 4) MPT-2 Titrator can be incorporated in the setup but was not used in this project.
- 5) A computer is required to run the Zetasizer software so that the unit can be controlled and the data that is collected can be analysed [58].

3.3 NANOPARTICLE TRACKING ANALYSIS WITH NANOSIGHT (BROWNIAN MICROSCOPY)

Nanoparticle tracking analysis (NTA) is the second method used in this study of aqueous solutions. Unlike DLS, NTA is a more recent technique. It has only been widely available for use since 2006. NTA incorporates laser light scattering microscopy, computer software and a camera. Using this technique the diffusion of individual particles in solution can be visualised when they scatter the laser light. Figure 19 gives a photograph of the equipment in use, where the sample cell is shown with the injection ports and microscope lens.

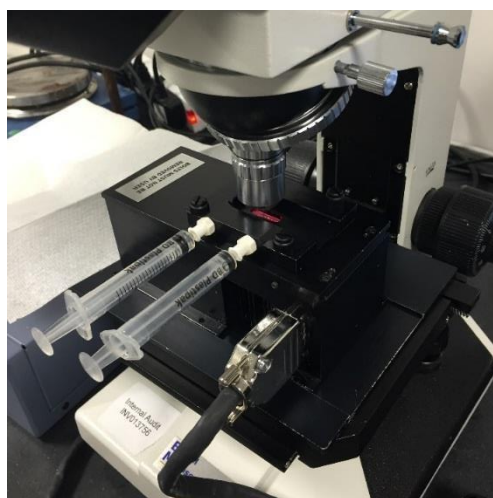


Figure 19. Photograph depicting the setup of the Brownian microscopy equipment showing the laser beam passing through the sample cell.

Particle diameters ranging from 30-1000 nm can be detected with this technique [53]. An example of the image picked up by NTA from a sample of supersaturated glycine is shown in Figure 20.

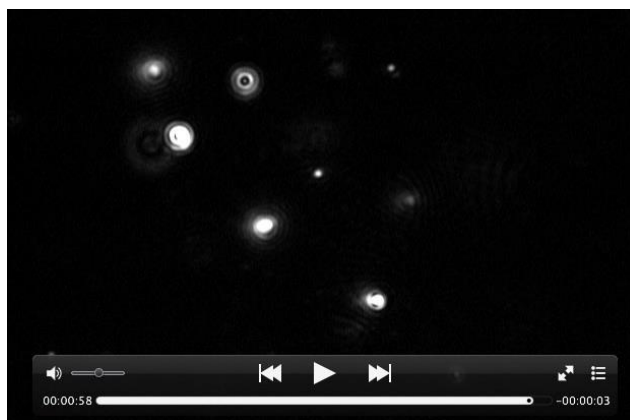


Figure 20. NTA screen capture of recording from NanoSight experiment during the analysis of supersaturated glycine solution ($S=1.1$ based on solubility at 20°C) filtered with PTFE syringe filter.

The computer software (NanoSight) monitors the Brownian motion of particles in the sample and records the individual particle pathways. These pathways are used to calculate the mean squared distance of each particle; and this can be related to a diffusion coefficient [59]. The camera's ability to follow single particles gives the mean squared displacement and the diffusion coefficient D is obtained according to Equation 29.

Equation 29

$$\bar{x}^2 + \bar{y}^2 = 4Dt$$

Note that only the x and y coordinates are applicable here as the camera only records a two-dimensional projection. The \bar{x}^2 and \bar{y}^2 terms refer to the particle displacement in the x and y direction that occur in a time interval t [60].

Einstein's theories on Brownian motion stated that molecules/particles in a stationary liquid would have significant movement that microscopes may be able to detect [61]. This paved the way for the physicist Perrin to continue his work and validate it through experiment [62]. Einstein related particle displacement to a diffusion coefficient [63] given in Equation 30.

Equation 30

$$\bar{x}^2 = 2Dt$$

However, in his paper, Einstein gives Equation 30 in the form shown in Equation 31.

Equation 31

$$\sqrt{\bar{x}^2} = \sqrt{2Dt}$$

He describes the displacement in the x-direction as the *“the square root of the arithmetic mean of the squares of displacements in the direction of the x-axis”* [61].

The random walk principle determines the probability of finding a particle at a position x at time t , where Brownian motion results in diffusion, according to Equation 32.

Equation 32

$$p(x, t) = \left(\frac{\tau}{2\pi L^2 t} \right)^{\frac{1}{2}} \exp \left(-\frac{\tau x^2}{2L^2 t} \right)$$

This equation follows a Gaussian distribution where τ is the time interval, L is the step size taken and t is the time. On average the particles are found at their original starting position [64]. The result of the random walk principle gives the diffusion coefficient:

Equation 33

$$D = \frac{L^2}{2\tau}$$

Equation 33 is of the same form as Equation 30, with units of length squared per unit time. This is how Einstein arrived at his equation for the mean square displacement given in Equation 31.

Assuming that the particles are hard spheres allows the use of the Stokes-Einstein equation (Equation 34) to obtain hydrodynamic diameters.

Equation 34

$$d_H = \frac{k_B T}{3\pi\eta D}$$

NanoSight is the computer software that enables the tracking of the particles diffusing in solution. Other useful properties such as particle concentration (particles/ml) and the number based particle size distributions can be determined through this software. These properties cannot be accessed with DLS [59].

In general it has been found, through experiments with polymer bead standards, that NTA provides diameters closer to the true value but with large errors from the method, whereas DLS offers diameters that aren't as close to the true value but the errors are much smaller. However, it is beneficial to combine the two techniques so that their findings can be compared and contrasted [53].

4 FOULING AND SURFACE BEHAVIOUR IN THE CRYSTALLISATION PROCESS

4.1 CHAPTER OUTLINE

This chapter focuses on the nucleation and crystallisation that can take place on surfaces and the wide range of effects that surfaces together with molecular

interactions can have on the crystallisation outcome. This emphasises the impact that the surface and molecular interactions have on development of industrial crystallisation processes.

Fouling occurs when the crystals in the system grow on a surface and on crystallisation equipment such as vessels and pipes. Fouling is therefore due to heterogeneous nucleation where surface properties, materials of construction and molecular interactions between solute molecules and surfaces are crucial.

4.2 HEAT EXCHANGER SCALING

Most theory surrounding the fouling phenomenon regards heat exchanger surfaces, however this can be directly applied to fouling in crystallisation. In order to ascertain the rate of accumulation of fouling on a surface, it can be defined in terms of the rate of addition and removal given in Equation 35 as outlined by Bott [12]:

Equation 35

$$\frac{dm}{dt} = \phi_D - \phi_R$$

where m is the mass of fouling substance per m^2 for example, ϕ_D and ϕ_R are the deposit and removal mass flow rates per unit area of the surface. Normally after fouling has taken place the surface roughness of the heat exchanger area will increase, meaning an increase in the turbulence of the flow near the surface. Subsequently the heat transfer will rise. This alteration in the heat transfer can be described by referring to the change in the heat transfer coefficient. Any changes in this parameter are related to the changes in thermal resistance of the fouling layer, the changes due to the roughness of the fouling layer and the change that happens when the Reynolds number is altered because of the presence of the fouling layer. In crystallisation fouling, the reduction in the heat transfer that occurs is represented by:

Equation 36

$$R_f = \frac{1}{k_f} - \frac{1}{k_0}$$

where R_f is the fouling resistance (m^2KW^{-1}); k is the heat transfer coefficient ($Wm^{-2}K^{-1}$). The subscripts f and 0 refer to the fouled surface and the clean surface respectively.

The parameters described by Bott's mathematical descriptions are difficult to obtain experimentally and so it is not always possible to quantitatively describe fouling.

4.3 FOULING LITERATURE REVIEW

As mentioned previously, analogous to the fouling that occurs in crystallisation processes is that which occurs within heat exchanger equipment, sometimes referred to as scaling. Many papers report issues with salt deposits within the system which has a negative impact on the running of heat exchangers. The efficiency of the heat exchange is reduced through fouling and time and money is spent to rectify the issue. These issues are similar to those facing crystallisation processes.

A work by Mwaba [14] analysed the heat exchanger fouling in the sugar cane industry. This can be a major problem when it occurs in the heaters and evaporators in the plant. In this industry the main substances that take part in the deposition within the equipment are silicates, sulfates and phosphates. In order for the scaling to take place, the fluid must be locally supersaturated with respect to the species responsible for the fouling. In the juice and syrup heaters, supersaturation arises due to the temperature gradient between the fluid in the bulk and the surface responsible for heat transfer. A study was carried out on samples taken from the system to determine what substance was responsible for the majority of the fouling, and it was found to be calcium sulfate (CaSO_4). A range of different system variables were altered to study the effect they had on the fouling outcome. There was specific focus on the flow velocity and the concentration of the fouling species in the solution. At low Reynolds numbers there was no influence from these factors, however at higher Reynolds number when the flow was more turbulent, the rate of scaling decreased. Due to the fact that CaSO_4 crystallisation is reaction controlled, then it seems logical that at less turbulent flow there will be less fouling. With lower turbulence there will be less mixing and the reaction rate will decrease. When the flow rate was increased the removal effects of the fast flowing fluid was eradicating the scaling from the surfaces.

The fouling was found to depend on the condition of the surface. The scaling process was delayed when the surface was smoother. Smoother surfaces have less available surface area for favourable interactions. There are a number of variables that play a role in the formation of crystalline materials on the surface of equipment [14].

A study by Paakkonen et al. [65] dealt with the fouling of calcium carbonate (CaCO_3) and examined the effects of the bulk precipitation. Experiments were carried out on a lab-scale plate heat exchanger. Generally when the flow rate was increased, the fouling decreased; and when the temperature difference between the solution and the heat exchange wall was decreased then the fouling decreased. When the solution was filtered, the result was a reduction in the fouling occurring on the walls.

Surface defects and the aging of coated surfaces can have an effect on the fouling behaviour of a system in the context of heat exchanger equipment. There are two methods through which a surface can be modified: either through chemical modification (changing the surface energy) or mechanically. It is therefore crucial that surface coatings be thermally and mechanically stable with respect to the fouling and cleaning procedures they might have to undergo. As mentioned before, the contact angles are a method through which the surface can be quantified as it describes the affinity a material has for that surface. In work by Geddert et al. [66] this was achieved by taking the contact angle readings from a range of fluids to estimate their surface energy and by measuring the surface roughness. The mechanical methods involve using smoother surfaces where there will be less nucleation sites. In turn this reduces the possibility of crystallisation taking place on such surfaces. Surface chemical modification methods would involve using surface coatings, which would either have unfavourable interactions with the crystallising material or be more easily cleaned than the original surface. The mechanisms by which these modifications work as well as the role that the surface itself plays is not well understood.

Coatings can be achieved via techniques such as chemical reactions, adsorption or adhesion. Common methods include sol gel coatings, ion implantation, sputtering or vapour deposition. The surface roughness, the layer thickness and the energetic

properties are all vital pieces of information. For example, if the coating is approximately 3 μm thick then it can be assumed that its heat transfer resistance is negligible and so will not interrupt the efficiency of the heat transfer [66]. Surface coatings have also been discussed in other areas of heat exchanger fouling. Manufactured surfaces were achieved through coating stainless steel in different types of coating. The main focus was on the crystallisation of CaSO_4 and the effect of the flow velocity (i.e. the Reynolds number) on the induction time for this substance.

In another paper by Geddert et al [67], a summary of all the factors that can have an effect on crystallisation fouling were stated and are summarized in Table 2.

Table 2. Factors Affecting the Fouling during Crystallisation

Process Conditions:	Interface Conditions:
Salt system	Temperature
Supersaturation	Surface energy
pH	Surface roughness and topography
Flow velocity and regime	Number of nucleation sites
Additives or impurities	Aging of the fouling layer and the surface

The influences reported above are able to manipulate the induction time and the crystal growth in the fouling layer. Via vapour deposition, it is not uncommon to change the energy of surfaces through coating them so as to inhibit nucleation and hence reduce fouling. Diamond-like carbon (DLC) coatings reduce crystal growth and so increase the induction times for crystallisation. DLC has a reduction in friction and is hard wearing and therefore is a suitable candidate for coating surfaces of heat exchanger equipment.

A study by Wang et al. [68] concentrated on impeding CaCO_3 fouling on the surface of heat exchanger equipment in order to encourage the precipitate to crystallise in the bulk solution. PPS (polyphenylene sulfide)/poly-tetrafluoroethylene (PTFE) coatings have been used in the past to try and correct the fouling issues faced. These materials are known as low surface energy composites. This study reported on an

'anti-fouling composite' created by taking zinc-graphite alloy powders and blending them with epoxy-silicone resin. When compared to stainless steel and epoxy-silicone resin coatings, the zinc-graphite version was able to inhibit the CaCO_3 fouling to a greater extent. It was the corrosion of the zinc-graphite powder that released $[\text{Zn}^{2+}]$ ions on the surface which could account for the reduction in nucleation and growth of CaCO_3 . It was also discovered that the morphology of the CaCO_3 that crystallised was different from that which crystallised without the composite coating present. The presence of this coating resulted in the CaCO_3 preferring to precipitate in the bulk solution and not on the walls of the equipment [68].

A study by Brahim et al. [69] simulates the process of fouling, where computer models were used to recreate the reduction in heat transfer that is accompanied by fouling. Computational fluid dynamics was utilised in this study so that the results could aid in the design and operation of heat exchangers. The simulations involved the fouling of calcium sulfate on a flat heat transfer surface. The induction period was not considered in this work. Previous work which was carried out by Hirsch [70] gave a model for calculating the density of the fouling layer as a function of position within the layer and of the time-dependent total thickness of the layer. Another model was devised to produce a heat flux distribution along the heat transfer surface. These two models aid in painting a clearer picture of the fouling process. The numerical simulations being carried out here predict the fouling resistance as a function of time as well as determining the temperature distribution within the fouling layer. The agreement between simulation and experiment is adequate, given the complex nature of encrustation and that not all variables could be considered in the simulation. Preliminary calculations involved parallel flow across flat plates; by using this simplified case, many experiments with different parameters could be investigated. Figure 21 depicts the experimental setup being used. Measurements were taken with aqueous calcium sulfate solutions and this was used to verify the simulation results.

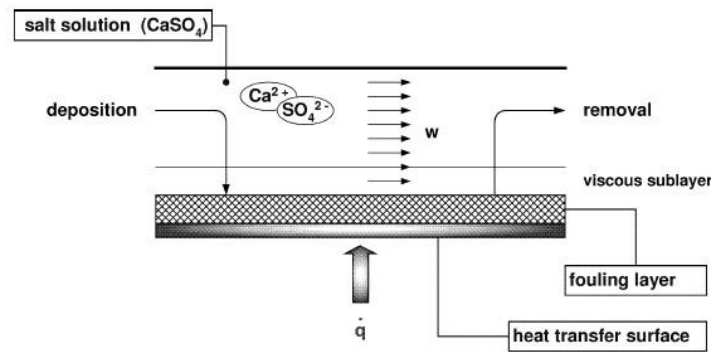


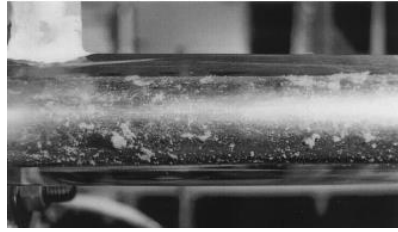
Figure 21. Depiction of fouling on heat transfer surfaces via crystallisation of calcium sulfate where preliminary calculations to compare with the simulation values could be compared [69].

For fouling resistance simulations, the results are generally less than the experimental values. Better results would be obtained if the crystal growth data was included in the simulation then the crystal geometry and the effect this would have on the flow can be included in the simulation [69].

Forster et al. [71] investigated the effect that the adhesion force between the crystal and the heat exchanger surface had on the fouling. Drop shape analysis (DSA) was used in order to measure the interaction at the crystal/surface interface. The wetting characteristics were then related to the adhesion i.e. the affinity the solution has for the surface. This methodology gives insight into surfaces which would be less likely to foul with a specific solvent/solute pairing. A fouling mitigation method discussed in this paper is one based on the flow conditions and involves introducing a pulsation technique. Individual pulses of higher velocity flow are created alongside the stationary flow. It is these pulses which change the forces within the flow to create a process whereby the fouling substance is removed from surfaces. Experimental work has shown that this is a useful technique to prevent fouling layers from becoming too severe. Other methods for dealing with fouling revolve around increasing the induction period, i.e. delaying the time for fouling as much as possible.

This study concentrated on two approaches: 1) Changing the energy and topography of the surface to increase the induction time and 2) Changing the flow conditions. A promising solution will consist of a combination of the two approaches.

(a)



(b)

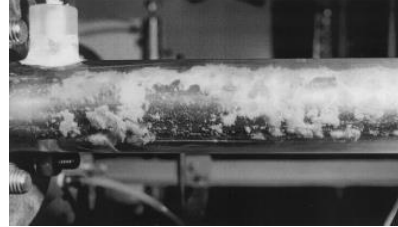


Figure 22. Images showing systems pulsating flow where with pulsating visibly reduced due to the change in

with (a) and without (b) flow the encrustation is the flow properties [71].

Diamond like carbon is a material similar to diamond but is in fact amorphous carbon and has shown to be a surface material which can increase the time taken for fouling to occur, after 475 hours the system is still in the induction period. It was found that despite having the lowest surface energy, PTFE coated steel increased fouling. The rough surface was stabilising nuclei and promoting growth on the surface. Through increasing the fluid velocity, the removal rate of crystals present on the surface is increased due to the higher shear stress between the fluid and the fouling substance. When pulsation is not in use, increasing the velocity decreases the fouling resistance and heat transfer is reduced more quickly. Using pulsating flow gives a negative value for fouling resistance and the experiment remains in the induction range after 375 hours. Random crystallisation points within the system increase the surface roughness of the heat transfer area and subsequently produces greater turbulence and hence increases the removal of fouling. This sudden increase in the shear stress prevents further crystal growth on the surface and continuously removes them. The adhesive properties are lower in strength than the forces from the hydrodynamic flow that comes into contact with the crystals. Increasing the delay time for pulsation increases the steepness of the fouling resistance curve due to the fouling layer growing more quickly. When the delay time reaches 20 minutes and above, there is no influence observed on the fouling [71].

The following paper by Vendel et al. [72] probed the mechanisms of initiating encrustation. Experimental procedures were developed where a crystalline phase

was nucleated on a solid surface at controlled local supersaturation and without influence from particle deposition. Different crystallising substances and different surfaces were studied and the results show that the solid surface may catalyze primary nucleation and therefore encourage encrustation. However this was found at very high supersaturation. Crystal collision with the surface in a supersaturated environment may also start encrustation at quite low supersaturations. The cycle of encrustation outlined in this study is summarised in Figure 23.

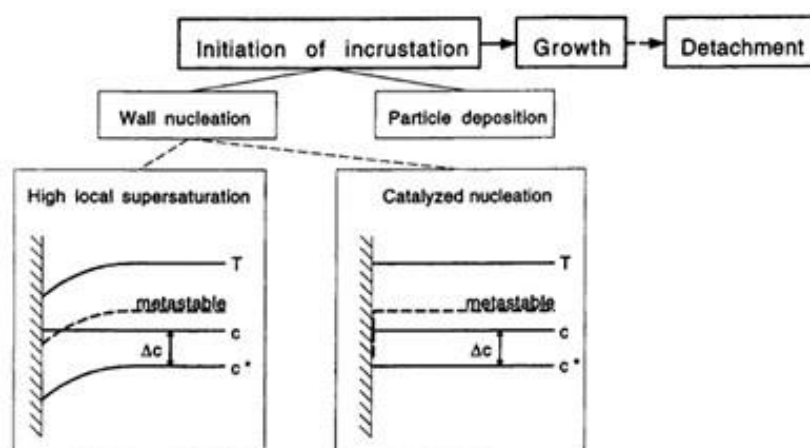


Figure 23. The cycle of encrustation starting from the initiation which is either induced by the wall or particle deposition and finishing with growth and detachment from the surface [72].

This study shows that nucleation of adipic acid, succinic acid and glycine on PTFE surfaces occur at a lower degree of supersaturation than nucleation in bulk solution. However, the supersaturation required for this is still rather high, therefore this result may not have great significance in an industrial setting as the conditions are not comparable. If the solute has a greater affinity for the surface then this will increase the catalyzed primary nucleation, the collision initiation method and the adhesion of the encrustation [72].

From investigating the existing literature concerning fouling in industry, it was found to only pertain to that of salts crystallising on the surfaces of heat exchangers and the implications this has for industry only in terms of heat exchanger equipment. In this

situation fouling is called scaling, and several studies have been carried out to test the effect that mixing effects, flowrates, surface coating, surface topography and pulsating flow have. Increasing the flow, more vigorous mixing, surface coatings which repel the heat exchanger fluid, smooth surfaces and using periodic increased pulses of flow all reduce the problem. There was no mention of any of these techniques being used during a crystallisation process. Neither was there mention of the tubular oscillatory reactor arrangement that was used in this project. Fouling induction times were not studied in great depth in any of the literature and so this was carried out in this work to give better understanding and some statistical meaning to fouling and its induction period.

4.4 SURFACE BEHAVIOUR LITERATURE REVIEW

4.4.1 The Chemistry of Surfaces and their Influence on Crystallisation

An important area of research on surface induced crystallisation involves studying the molecular interactions occurring between the crystallising substance and the surface it is in contact with. The role of the material chemistry and the structure of a variety of polymeric films were tested by Di Profio et al. [73] for their ability to heteronucleate (a) acetaminophen (Paracetamol) (b) acetylsalicylic acid (Aspirin) and (c) glycine.

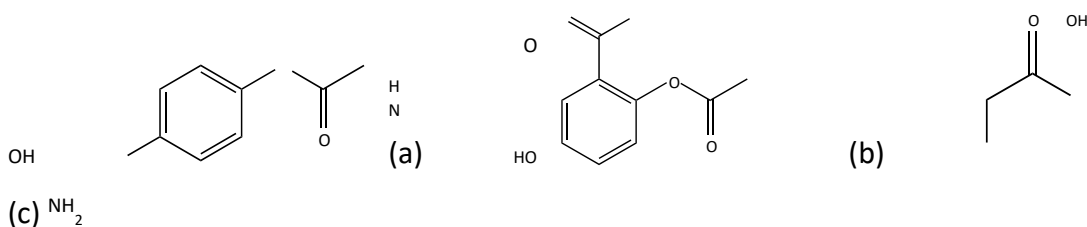


Figure 24. Compounds under study for the effect different polymer surfaces had on their nucleation: (a) acetaminophen (b) acetylsalicylic acid (c) glycine.

The different materials were all tested with each of the substances given in Figure 24 - (a) (b) and (c) - and the resulting effect on the nucleation rate was recorded by measuring the nucleation density and induction times with a microscope. Results revealed that specific designs and structures of the films would exercise some control over the nucleation through exploitation of 'molecular recognition events' taking place at the solute-polymer film interface. Surface chemistry was found to play an important role on the nucleation. Hydrophilic surfaces with surface roughness smaller than the droplet interacting with the surface became more hydrophilic with increasing roughness. This is assuming no air pockets, in other words complete wetting was achieved. For hydrophobic surfaces, air pockets would be present when a non-wetting liquid is being used. The experimental work showed that heterogeneous nucleation is extremely sensitive to the surface chemistry of the

polymer used. This property is directly related to the binding of the molecules to certain chemical functionalities within the polymer that are accessible at the surface.

When the surface roughness is altered, it is the wetting behaviour of that surface that will dictate the effect on the nucleation density when the roughness is either increased or decreased. By increasing the surface roughness of hydrophobic polymers the wetting tendency was decreased and hence the nucleation rate was also reduced. This is due to the fact that increasing the roughness increases a repulsive interaction between solution and surface. By increasing the roughness of hydrophilic polymers, the active interface is increased and so the nucleation rate increases. Physical entrapment of molecules in the irregular surface is also a benefit of the increased surface roughness in hydrophilic films as this increases the local supersaturation and subsequently the nucleation density. The investigation uncovered that the surface roughness was not the only factor influencing nucleation. The chemical nature of the surface is the parameter that will decide how efficient the polymer will be as a heteronucleant. This depends on the extent of the interaction between the molecules crystallising in the solution and the surface. It is therefore the chemical and physical properties that work together to create a successful heteronucleant [73].

Another study by Diao et al. [16] dealt with the role that surface chemistry plays while testing the ability of different polymers to nucleate aspirin from solution. It was stated that nanoscopic pores in the surface, providing there was the suitable surface chemistry, would promote nucleation. The heterogeneous nucleation rate is the number of nuclei exceeding the nucleation barrier per unit area per unit time; this is also known as the nucleation activity of the surface. This property is not easily measured and so the number of detectable crystals was used instead. By comparing the nucleation area densities on the films after a certain time period of crystallisation, all of the polymer films could be initially screened. The polymer monomers were grouped corresponding to their main chemical functionalities. The range of monomers was selected based on their ability to interact with the aspirin molecule via specific intermolecular interactions. After screening, it was found that some

groups of polymer monomers were more effective as heteronucleants than others. Despite this, there were some differences in the behaviour of monomers within the same group, but a general trend did exist. Monomers with greater polarity will result in stronger interactions between the polymer film and the aspirin and hence the greater the nucleation activity. The induction time is the time taken for the first crystal to appear in solution and is a good method of detecting the activity on the surface of the polymer. The induction time will decrease as the surface activity increases. It was stated that if pores were present in the polymer then this would increase the heteronucleant's ability significantly. Molecular interactions, particularly hydrogen bonding, are important in driving the crystal orientation in a specific way. Three polymers were chosen for an induction time study. Figure 25 shows the general results obtained with the polymer was present (a) and without (b) where only the holder was present with no polymer coating. A few large crystals grew on the polymer and many smaller crystals appeared in the bulk solution when there was no polymer. This revealed that nucleation occurred faster on the polymer and the rapid growth decreased concentration of aspirin molecules from in solution [16].

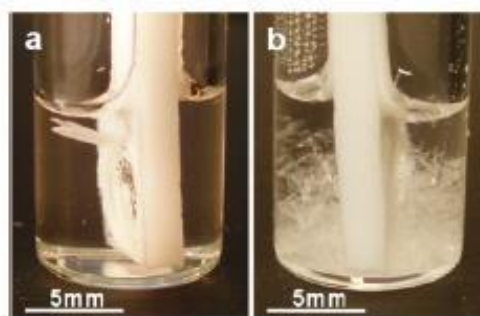


Figure 25. Crystallisation of aspirin (a) with and (b) without polymer film showing that nucleation occurred quicker on the polymer surface and then depleted the molecules from solution hence no crystals were found in the bulk [16].

A paper by Holbrough et al. [15] focused on the surface roughness of polymer films by studying the nucleating ability of surfaces with the same chemistry and wettability but differing surface topography. It involved a simple study of nucleation on surfaces

scratched with diamond particles with varying particle diameters to achieve different roughness. Despite being a crude method, it was evident that increased surface roughness increased the nucleation density.

The following image in Figure 26 shows the results from crystallising neo-pentanol on mica surfaces. A decrease in the induction time was also observed with increasing surface roughness [15].

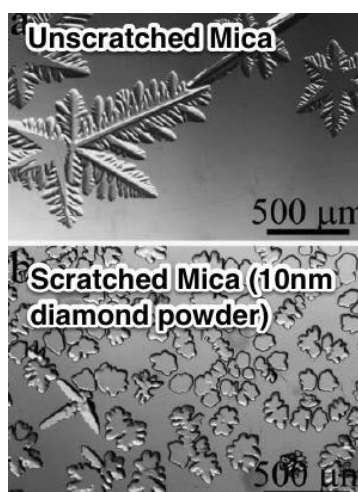


Figure 26. neo-Pentanol crystallising on mica surface when it was scratched and unscratched showing the effect surface roughness has on the nucleation events taking place. When the surface is rougher, more nucleation events take place [15].

A study by Lopez-Mejías et al. [74] employs experimental and computational methods to analyse the phase-selective crystallisation of paracetamol where insoluble polymers were used as heteronucleants. The thermodynamic product from crystallising paracetamol has a monoclinic structure and the kinetic product has an orthorhombic one. When crystallisation was carried out via supersaturated solution the thermodynamically stable polymorph was obtained on poly(n-butyl methacrylate). Using poly(methyl methacrylate) as the heteronucleant yielded the less stable orthorhombic polymorph. Through changing the method of crystallisation to vapour deposition it was only the monoclinic polymorph that was acquired on each polymer. The molecular structure of both polymers is shown below in Figure 27.

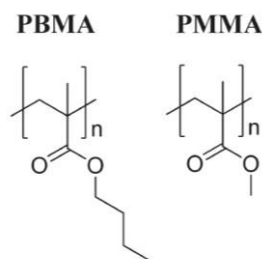


Figure 27. PBMA (Poly(n-butyl methacrylate)) and PMMA (poly(methyl methacrylate)) structures [74].

In the paper it was stated that there were two mechanisms that could be responsible for explaining the phase selection observed when using these different polymers as heteronucleants. The first suggestion is the non-specific adsorption of the solute molecules to create the crystal nuclei, and the second describes the physical position of the solute molecules on the surface. Mechanisms were rationalised to explain this difference in polymorphism. Since the solute is in contact with a solution it can only have an effect on one of the crystal faces. In turn, the interactions at this crystal/surface interface could inhibit certain polymorphs in favour of one with favourable interactions at this interface. There was an increase in the rate of crystal formation when the polymers were in place, but it was stated that the rate was dependent on the ease of access to the functional groups present in the polymer structure to maximise favourable interactions with the crystallising substance. Computer simulations were applied in order to calculate the polymer-crystal binding energies as this gave more data concerning the interactions taking place at a molecular level. Finding this information helped determine which crystal face would dominate in the experiments. By doing this it was shown that the orthorhombic orientation of the molecules in the crystal was higher in energy than the monoclinic structure and so was not favoured in the vapour deposition experiment. This study also revealed that the solvent played an important part in determining the polymorph, as there was an absence of solvent in the vapour deposition experiment [74].

The following work by Chadwick et al. [75] continues the idea of controlling the polymorphic outcome by carefully selecting a substrate. The investigation quotes a difficulty in crystallising paracetamol form II from solution and so it was attempted to selectively crystallise form II when it is form I that is the thermodynamic product. The work in this paper demonstrates a new method for choosing a three dimensional crystalline substrate that will allow form II of paracetamol to be selectively crystallised from conditions that would otherwise give form I. By achieving epitaxial matching on the chosen substrate surface, form II was encouraged to generate. It is already known that surfaces lower the free energy barrier to nucleation via complementary interactions between the surface and the pre-nucleation aggregate. A suitable substrate was chosen, namely 4-aminophenylacetic acid (4-APPA), because it had similar unit cell properties to paracetamol form II. Seeding the experiment with crystals of 4-APPA produced paracetamol form II. By choosing this substrate based on its properties and functional groups, form II was successfully crystallised out from solution and hence polymorphic control was achieved.

The substrate selection process was summarised using the following flowchart in Figure 28:

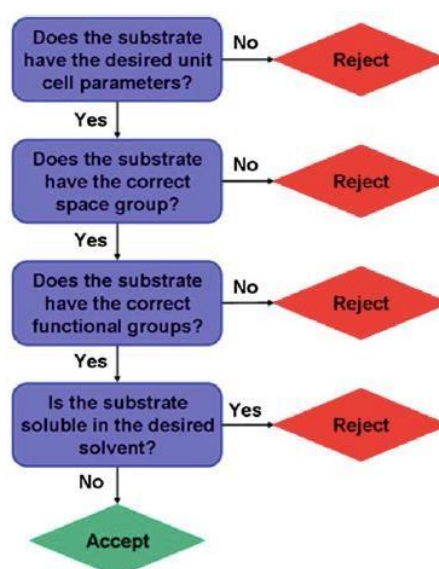


Figure 28. Selection process for substrate selection for heterogeneous nucleation in order to control the polymorph being obtained [75].

Figure 28 highlights all the factors that have to be considered when choosing a substrate with the potential to control the outcome of the crystallisation. Note that the unit cell parameters as well as the functional groups play a role so that maximum favourable interaction can be reached [75].

Bonafede et al. [76] showed that certain crystal faces of single organic crystals can be used as heteronucleants to govern the polymorph created. One experiment used organosilane monolayers on glass substrates to influence the polymorphic outcome. The mechanism proposed for this result was 'ledge-directed epitaxy' (LDE) whereby the pre-nucleation aggregate free energy belonging to a specific polymorph is lowered by a shape-fitting contact with two planes of a 'crystallographically welldefined ledge-site' [77]. The ledge refers to the section where a terrace plane and a step plane on a crystal surface meet. The principle behind LDE is based on *'geometric matching based on interplanar dihedral angles between two close-packed planes of the ledge site and two close-packed planes of a pre-nucleation aggregate corresponding to the growing phase'*. In other words the heteronucleant acts as a template surface for the crystallising species to easily nucleate on and form a structure similar to that of the heteronucleant [76].

Superhydrophobicity is an intriguing property that was discussed in a paper by Levkin et al. [78]. They investigated producing superhydrophobic coatings for various surfaces. A superhydrophobic surface is defined as having a wetting angle of greater than 150°. These surfaces are desirable because of their repulsion to water and the fact that they have self-cleaning properties. The 'Cassie-Baxter model' explains this behaviour. This states that air becomes confined in the small grooves of the rough surface and the water droplets in contact with the surface are actually resting on an environment comprising of air and the apexes of the microscopic protrusions of the rough surface.

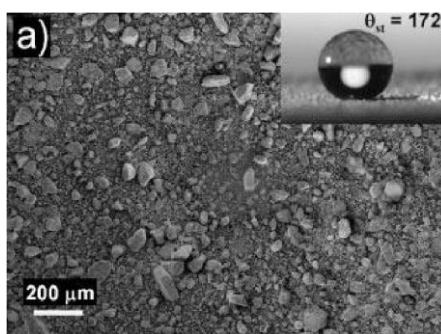


Figure 29. SEM Image of adhesive tape coated with superhydrophobic polymer. Insert: an image of a water droplet on this surface [78].

The new approach reported here involved creating microporous layers via a polymerisation in the presence of porogens (see Figure 30). This is how the superhydrophobic polymer coatings were obtained. The final product could be milled into a powder which could be applied to any surface to yield the superhydrophobic property [78].

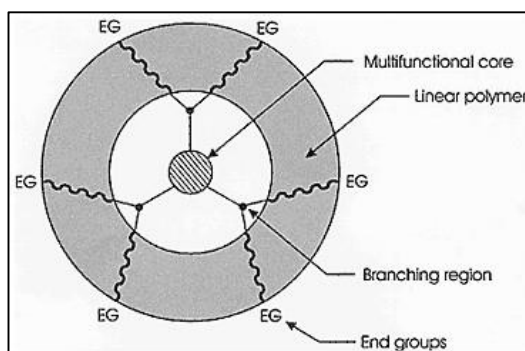


Figure 30. A generic porogen showing basic features of a pore-generating macromolecule. As the porogen breaks down within the organosilicate matrix (in this example), it forms small molecules; which then diffuse through the matrix and escape as gases leaving pores [79].

4.4.2 Confined and/or Engineered Surfaces

Another important area of research investigates crystallisation on surfaces within confined environments.

A study by Lee et al. [80] concentrated on crystallisation of glycine in confined engineered surfaces to attempt to control the size and polymorph of the crystals formed. The technique employed could create micron-sized crystals of organic substances using high and low supersaturations through controlling the domain size that is accessible by the crystallising solution. Square metallic gold islands with self-assembled monolayers (SAMs) were used as the patterned surfaces on which crystallisation took place, as shown in Figure 31. The dimensions of the monolayers ranged from 25 to 725 μm and acted as nucleation sites to control the crystal dimensions. By functionalising the metallic islands, different polymorphs could be created under different conditions.

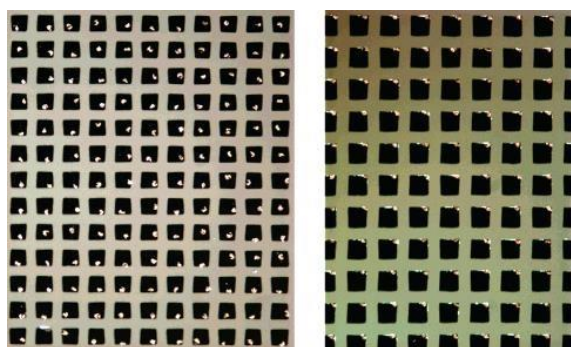


Figure 31. Patterned glycine crystals nucleated on 100 μm (left) and 140 μm (right) gold islands [80].

The monolayers play the role of the heteronucleant in this study. By surrounding the hydrophilic gold islands by hydrophobic regions, droplets of the crystallising solution were created in that confined environment. When the droplets evaporate, crystallisation transpires whereby the size of the crystal is controlled by the droplet size. An increase in the supersaturation resulted in larger crystals being formed on the islands due to the increase in the amount of glycine present in the liquid droplet. It was also discovered that different polymorphs of glycine were obtained on the same islands exposed to the same conditions the only difference being the island size. It was therefore determined that the constrained environment must influence the

arrangement of the molecules as they crystallise. Engineered surfaces were utilised in the generation of nano-organic crystals of glycine with a lateral dimension measuring less than 200 nm. This was carried out in a confined volume while controlling the supersaturation. As stated previously, hydrophobic sections can surround hydrophilic islands in order to create these smaller crystals [80].

A paper by Kim et al. [81] made use of hydrophobic and hydrophilic patterned surfaces with circular islands all with a 500 nm diameter. This was achieved by using photolithography and SAMs that can be visualised in part (a) of Figure 32. The islands were functionalised as hydrophilic leaving the rest of the surface to be modified with hydrophobic properties. The droplets reaching the islands were smaller than the island diameter and hence the crystals produced had diameters less than 500 nm. Part (b) in Figure 32 clarifies the method for manipulating the supersaturation during the experiment.

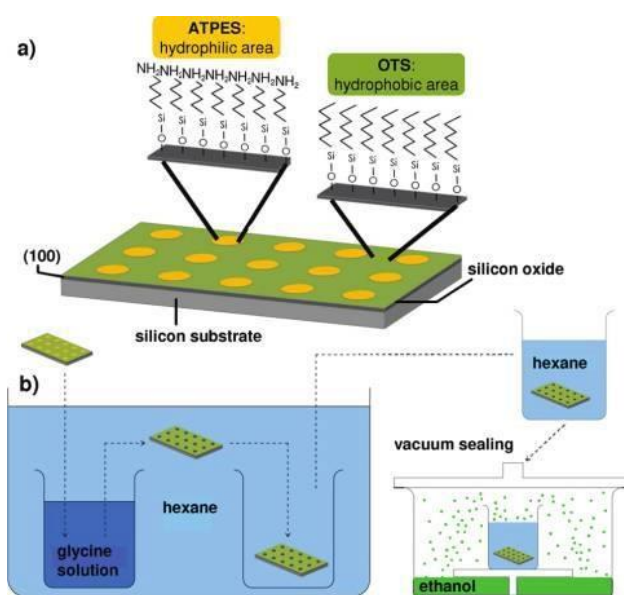


Figure 32. a) Schematic representation of the bifunctional SAMs pattern b) Schematic representation of the glycine crystallisation procedure; the supersaturation level is controlled by the slow diffusion of an antisolvent (ethanol) into the glycine/water solution [81].

Figure 33 shows images taken with a microscope and AFM of the crystals formed in the confined environment.

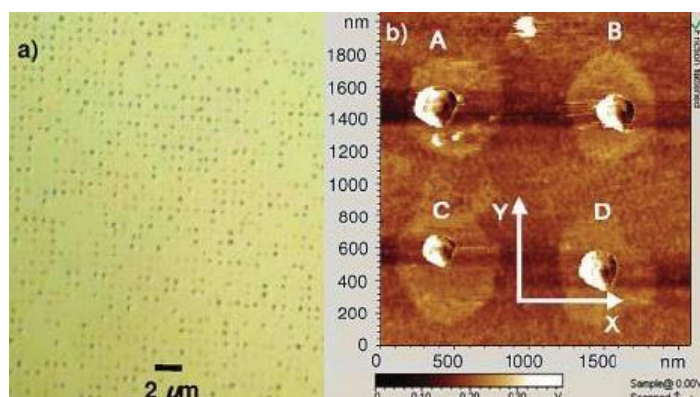


Figure 33. (a) Optical microscope image (x 150) of 1600 μm^2 and (b) AFM image of 4 μm^2 of the 500 nm patterned SAMs on silicon substrate [81].

The image on the right hand side of Figure 33 shows four glycine crystals whereas the image on the left shows the total 1600 crystals on the surface. The metastable β form of glycine was formed in each case, and this was consistent with the previous findings from studies of glycine polymorphism while using alcohol-water mixtures to obtain the crystals. This investigation revealed that, again, by restricting the environment the crystallising solution has by altering the surface properties the crystal size could be controlled successfully [81].

The previous investigation was further developed by Kim et al. [82] to control the polymorph of glycine that is formed during crystallisation on an engineered surface. The surfaces were prepared as before and the supersaturation was controlled via slow cooling or slow evaporation. The slow cooling was achieved in a similar fashion to the previous study and is depicted in part (a) of Figure 34. Slow evaporation of the solvent was accomplished by sealing the surface with the solution and then the atmosphere was saturated with the evaporating solvent. Holes with a diameter of approximately 1 mm were punctured in the seal to allow slow solvent evaporation to occur and the greater the number of holes the greater this would occur. The process is given pictorially in part (b) of Figure 34.

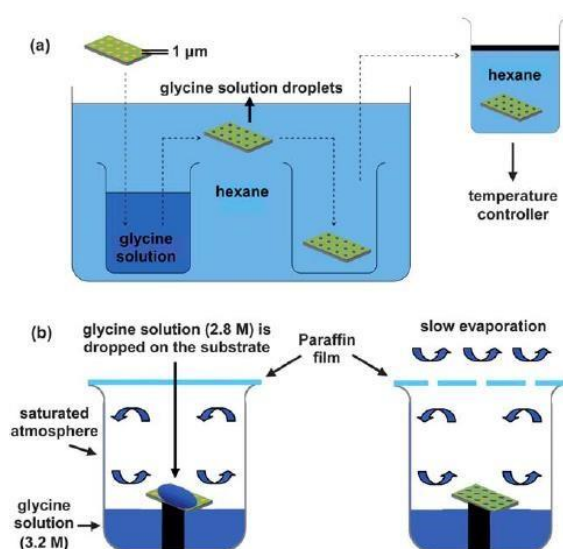


Figure 34. (a) Slow cooling and (b) slow evaporation methods to obtain glycine crystals [82].

Results from these experiments showed that different polymorphs of glycine were engineered. Slow cooling rates gave crystals with dimensions of 600 x 580 x 180 nm. The slower the cooling and evaporation procedures, the more stable the polymorph attained. For glycine there are three solid-state polymorphs: α , β and γ , where γ is the thermodynamically stable form and β is the least stable form. It has therefore been shown that not only does each polymorph compete in each droplet, but also the supersaturation generation rate is a vital factor in determining the polymorph that will result [82].

Polymer microgels, which have a modifiable microstructure and chemistry, have been used in a study by Diao et al. [83] to further understand the role of intermolecular interactions in nucleation under confined conditions and for controlling crystallisation from solution. The polymer microgels have a structure mimicking a mesh with sizes ranging from a few angstroms to several nanometres. A fine structure such as this provides the confined environment for nucleation to occur in. Their results illustrated that by optimising the polymer-solute interactions the nucleation kinetics of the solution could be increased by 4 orders of magnitude. Adding the polymer microgels into the supersaturated solutions of aspirin and paracetamol

resulted in heterogeneous nucleation where the crystals being observed through an optical microscope were found to be growing on the surface. It was inferred that nucleation occurs inside the microgel structure as there is a higher solute concentration there; yet it is only the nuclei that form close to the gel surface that can continue to grow into a crystal that can be observed. The reasoning behind this is that the diffusion of the solute in the confined environment is much lower than that in the bulk solution. Results from the scanning electron microscope indicated that there was a strong interaction between the crystal and the microgel; reinforcing the idea that nucleation occurred within the confined mesh of the gel [83].

Some other examples of heterogeneous nucleation include studies from a wider range of topics. For example, Maiti et al. [84] used light scattering experiments to reveal that pure nylon 6 crystallises faster when clay is present in particulate form. Nylon 6 has two notable polymorphs: the monoclinic α -form and the pseudo hexagonal γ -form. The γ polymorph has fewer inter-chain interactions and it was already known that the γ -form generates when clay is present, despite these observations being inexplicable. The crystallisation was controlled by the silicate surfaces that were present in the nylon 6-clay nanocomposites. A nanocomposite is defined as a material that is a multiphase solid material where one phase has 1, 2 or 3 dimensions measuring less than 100 nm. Experiments carried out at lower temperatures yield both α and γ -forms of nylon 6 crystals. When the temperature was gradually raised the γ -form was seen to diminish, yet it is only the γ -form that emerges with the nanocomposite. The reasons for this difference in polymorphism was deemed to be the difference in hydrogen bonding between having the nanocomposite present and not. In other words the epitaxial effects are influencing the outcome. Figure 35 below shows the favourable interactions for nucleation on the clay [84].

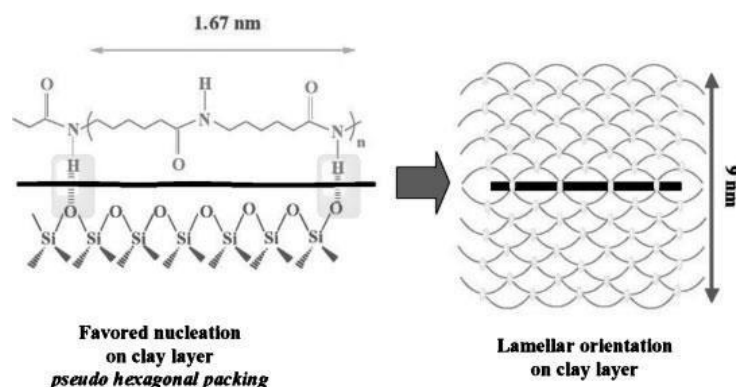


Figure 35. Nucleation and growth mechanism in nylon 6 nanocomposites [84].

Wong et al. [85] have used inorganic polymers to crystallise calcite, the most stable polymorph of calcium carbonate. The crystallisation was controlled by changing the concentration of the cross-linking catalyst that was used during the fabrication of the polymeric films. By involving different organo-functional groups into the membrane structure this either encouraged or prevented the nucleation activity of the film. It was stated that the areas of the polymer film surface with polar functional groups, either silanol or organo-functional, delivered the required nucleation sites. The main bulk of the polymer was found to have no effect on the crystallisation process [85].

The literature search on surface behaviour and its influence on crystallisation explored the effects that the molecular interactions between the surface and crystal had on the outcome. Decreased nucleation time was found with favourable interactions, which lowered the energy barrier to crystallisation. Ledge-directed epitaxy was found to increase the chances of crystallising a material if the surface had the same molecular structure as that of the final crystal. The surface 'mapped out' the molecules in the correct arrangement, making crystallisation easier. Again, no focus was on the issue of fouling – crystallisation was deliberately carried out on surfaces to explore the interactions. Therefore in this PhD thesis, fouling was studied as the unwanted nucleation event that it is, and tackled the issues that surround its formation in an industrial setting. The chosen reactor type in this project, oscillatory

baffled crystalliser, has also not been used in the literature to study the fouling phenomenon.

5 MOVING FLUID OSCILLATORY BAFFLED CRYSTALLISER PLATFORM: CONSTRUCTION AND OPERATION

5.1 CHAPTER OUTLINE

Studying crystallisation on surfaces out with the context of heat exchanger equipment is not a common procedure and so no commercial equipment is available to study this phenomenon. A platform had to be created whereby fouling could be quantified in a non-invasive way to obtain kinetic data, such as induction time, on a surface under conditions which would be applicable to real life crystallisation processes. This chapter describes the bespoke equipment that was used for the fouling study – the moving fluid oscillatory baffled crystalliser (MFOBC) and the theory behind its operation and construction.

After describing construction of the MFOBC, the operation and conditions that would be used with this platform are explained. The methods involved in setting up the MFOBC, how the equipment was calibrated, how solutions were prepared, and how the imaging process was set up is covered. All oscillation conditions and compounds that were used are given.

Areas where there were difficulties with the temperature profiles within the equipment, image capture with regards to lighting conditions and the issues raised by the boundaries of the fluid in the MFOBC are highlighted.

5.2 COMPOUNDS USED IN THE FOULING STUDY

The two compounds that were used in the MFOBC were L-glutamic acid and glycine and this was due to the extensive data available on their solubility in water and their

crystallisation behaviour. Both compounds had been known to foul to great extent during cooling crystallisations and this made them ideal for this fouling study. Their induction periods at the concentrations being used were also within a reasonable time.

L-glutamic acid was used as the starting compound because of the extensive work that has already been carried out with it in our labs. It was always recrystallised from aqueous solution.

The supersaturations of the solutions were determined using the solubility of L-glutamic acid in water at 20°C as the reference, which has a value of 7.07 g/L of water [86] [87]. Supersaturations 3, 4 and 6 have been used which correspond to concentrations 21.95, 28.26 and 42.39 g/L respectively.

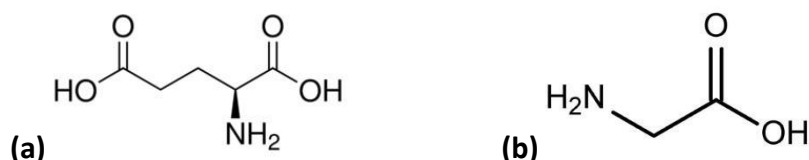


Figure 36. Molecular structure of (a) L-glutamic acid and (b) glycine.

Glycine has also been used extensively in our lab. Supersaturation was based on the solubility of glycine in water at 20°C which was taken as 213.62 g/L [88]. Supersaturation 1.4, 1.5 and 1.8 were used which correspond to concentrations of 299.06, 320.42 and 384.51 g/L respectively.

5.3 OSCILLATORY FLOW AND THE CONTINUOUS OSCILLATORY BAFFLED CRYSTALLISER

The DN15 tubular glass components of the experimental setup used in this project were taken from the continuous oscillatory baffled reactor (COBR) technology. The oscillatory flow reactor was developed in the early 1990s and can provide efficient mixing and narrow residence time distributions. Even when constructed on the mesoscale, the flow patterns that are created can be easily replicated for scale-up purposes [89]. The environment generated by such flow enhances heat and mass transfer, particle suspension and reaction rates [90].

This reactor type can achieve close to plug flow conditions and be technically under laminar flow. Plug flow can also be reached through using many continuous stirred tank reactors (CSTRs) or mixed suspension mixed product removal (MSMPR) crystallisers in a cascade; or by using a tubular reactor working under high flow to achieve high Reynolds numbers. Plug flow conditions mean that every fluid or element of the substance within the reactor will experience the same residence time. The characteristics of working under this flow regime are [91]:

- 1) Fluid elements never overtake other fluid elements in the direction of flow.
- 2) There is perfect mixing in the radial direction within the reactor.
- 3) All elements of the fluid spend the same amount of time in the reactor.

The fluid is oscillated within this type of reactor using a motor to drive either a bellow or piston mechanism which forces the fluid to move through the system. Efficient mixing and heat transfer rates are achieved due to the interaction of the baffles with the oscillating fluid. This interaction does not affect the near plug flow performance of the COBR [92]. The device itself has orifice baffles spaced equally throughout the glass pipe and are overlaid with the direction of fluid oscillation. The mixing in the COBR equipment is created through the start/stop formation of eddies. Every individual cell in the setup can be thought of as one CSTR and so this is therefore achieving a high number of tanks in a series through placing these cells in tubular glass components. A general schematic of the COBR can be seen in Figure 37:

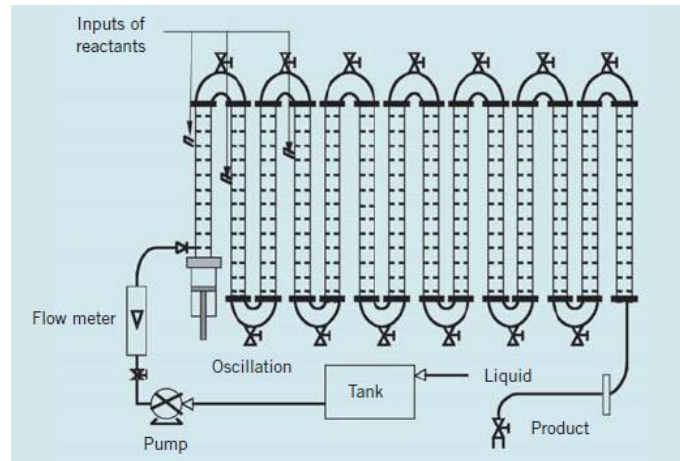


Figure 37. A typical continuous oscillatory baffled reactor (COBR) setup indicating the inlet and outlet and baffled straights connected via bends [93].

Laminar flows can be used in the COBR because the mixing is independent of the net flow and so longer residence times are available which would not be able to be achieved in systems operating with turbulent flow [93].

The fluid mechanical conditions used within oscillatory flow reactors are governed by two main dimensionless numbers: the oscillatory Reynolds number (Re_o) and the Strouhal number (St) given in Equation 37 and Equation 38 respectively.

Equation 37

$$Re_o = \frac{2\pi f x_0 \rho d_e}{\mu}$$

Equation 38

$$St = \frac{d_e}{4\pi x_0}$$

Where: ' $2\pi f x_0$ ' is the maximum oscillatory velocity in m/s, d_e is the effective tube diameter (m), f is the oscillation frequency (Hz), x_0 is the oscillation amplitude (m), ρ is the fluid density (kg/m^3) and μ is the fluid viscosity (kg/ms).

flow condition experienced in the continuous regime. This would allow controlled isothermal analysis of the system. With regards to this project, the focus was on the fouling behaviour exhibited under different flow, temperature and concentration.

This would be beneficial because when designing a continuous run, it would not be economical both financially and environmentally to run the entire setup to test flow conditions and temperature profiles on the crystallisation outcome if this could be done in a similar fashion in a smaller batch unit which can act as the larger scale continuous setup.

The Moving Fluid Oscillatory Baffled Crystalliser (MFOBC) consists of DN15 glass components which are used to construct the larger continuous oscillatory baffled crystalliser (COBC) shown in Figure 39. It is made up of tubular jacketed straights with orifice baffles spaced equally throughout. Each full glass straight is made up of 22 individual cells of volume 5 ml, and when coupled with the oscillatory flow they act as individual miniature stirred tank reactors.

A reactor with this technology can achieve high intensity mixing within each cell while overall displaying laminar behaviour because of the way the oscillation interacts with the net flow [93]. Oscillation is achieved through manipulating the frequency and amplitude of the flow via a motor (NiTech®) which drives bellows. Efficient heat transfer and mixing is achieved with this type of reactor and close to plug flow conditions can be reached [92].

In COBC the glass sections will all be under different temperatures if a cooling profile for cooling crystallisation is being followed. It would be useful to be able to monitor the behaviour of one of these sections independent from the rest of the setup to understand how different parameters affect the fouling properties without running the much larger COBC which uses more material and energy.

The COBC arrangement is shown in Figure 39 and the circled glass straight is the area of interest for monitoring fouling.

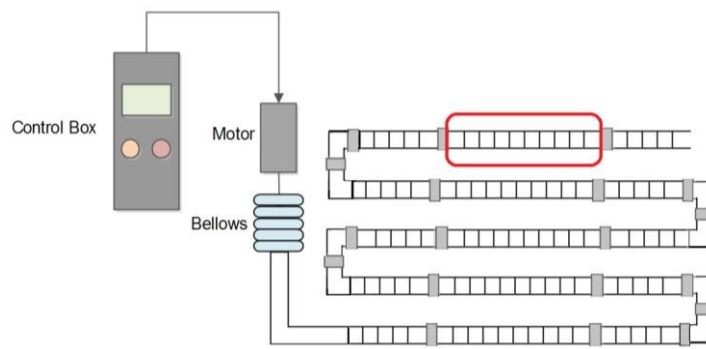


Figure 39. Continuous oscillatory baffled crystalliser (COBC) arrangement showing one glass straight which is of interest for analysing fouling behaviour.

In this work, the circled glass straight was investigated by removing this straight from the continuous setup and mounting it vertically into a batch system, hence there would no longer be net flow over this circled area. It was assumed that as long as the boundary conditions could be overcome (i.e. the fluid at the bellows and the fluid at the liquid-air level) then this would be a satisfactory method of monitoring a glass straight as it would be in the COBC under one temperature and flow condition. The boundary regions are shown as areas A and C in Figure 40 which depicts the moving fluid batch setup where area B is the area of interest.

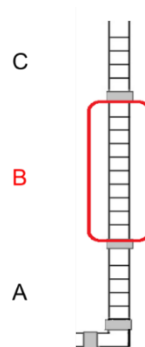


Figure 40. The removed glass straights from the continuous oscillatory baffled crystalliser (COBC) required to construct the moving fluid oscillatory baffled crystalliser (MFOBC) with the area of interest for monitoring fouling behaviour under certain flow and temperature conditions circled in red.

It was then investigated how to design this in a simpler way instead of constructing such a large piece of equipment to measure just one set of conditions. Assumptions were made in that if one full straight of the COBC could be transferred into a batch

moving fluid setup under the same flow and temperature conditions then the two situations would be analogous. Issues concerning the boundary conditions would have to be addressed as the continuous system has a constant output and input and will not have this issue. The two boundaries are the fluid in contact with the bellows and the fluid in contact with air at the liquid level at the top of the system. The moving fluid setup was achieved through mounting the full straight vertically and is shown in Figure 40 labelled with the three regions A, B and C where section B is the area of interest to be monitored via imaging techniques.

Monitoring section B will not be representative of a straight in the COBC if crystals are allowed to form in sections A and C either via nucleation in the bellows or seeded nucleation via the splashing and moving of the liquid at the liquid level. Preventing or reducing the effects of these two issues allows section B to be monitored as a full COBC straight would behave. Heating section A to achieve undersaturation prevents nucleation in the bellows. Heating section C prevents seeding from crystals forming within the amplitude region at the liquid level as evaporation occurs where crystals form above the liquid level and do not fall back in to the bulk solution.

The MFOBC is a batch version of the continuous setup with no net flow. The final experimental setup used in this project is shown in Figure 41. The positions of the two Microsoft LifeCam VX-3000 cameras and the temperature points where calibration of the temperature profiles within the setup were measured are indicated.

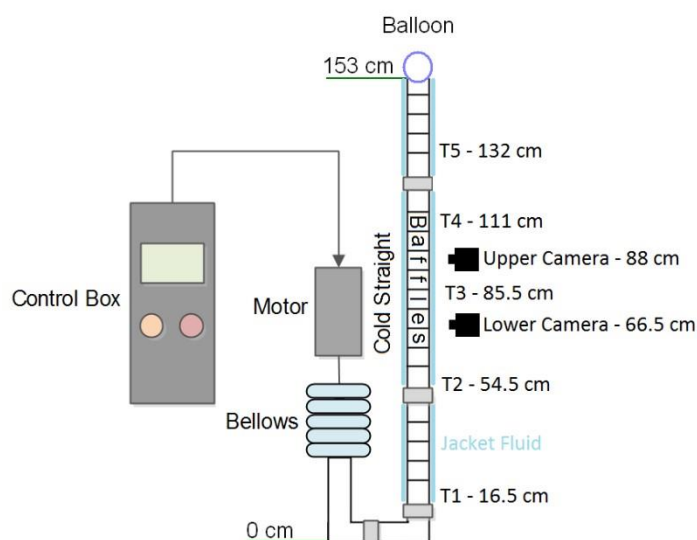


Figure 41. Moving fluid oscillatory baffled crystalliser setup showing temperature and camera positions as well as the mechanism for generating the oscillatory flow – i.e. the bellows moved by the motor which is controlled via the control box where the amplitude (mm) and frequency (Hz) of the oscillation is selected.

The principle behind this MFOBC configuration was that all three regions are well mixed, however the temperatures were calibrated so that the two cameras were always measuring regions of a predefined temperature. The two half straights above and below were kept hot to prevent seeding and nucleation at the top and in the bellows respectively. Temperatures T1 and T2 were monitored during experiments using two Teflon type K thermocouples built in to the equipment in line with the oscillatory flow. Temperatures T3, T4 and T5 were recorded for calibration purposes before each experiment, via a long stainless steel type K thermocouple that was inserted from the top of the system. Multiple thermocouples constantly within the system would affect the fouling process as they would provide further potential nucleation surfaces. Teflon thermocouples had shown to foul less than stainless steel ones, therefore this type was chosen to be the permanent thermocouples.

5.5 OPERATION OF THE MOVING FLUID OSCILLATORY BAFFLED CRYSTALLISER

Figure 41 is a diagrammatic representation of the moving fluid oscillatory baffled crystalliser (MFOBC) setup used in this project. The original design of this platform

was based on the one used by Dr Naomi Briggs during her PhD [94] and further modifications were made to the original setup to help with the fouling study.

5.5.1 Calibration

The temperature profile for the setup was required to be consistent for every experiment considering the equipment being used and the temperamental nature of the control box (NiTech®) which governs the amplitude and frequency.

Three water recirculation units were used to flow water in and out of the jackets of the glass straights in order to maintain the temperature in the bulk flow. On a daily basis the three heater/chiller unit (Julabo® F25-MB Chiller) temperatures would have to be recalibrated to match the desired temperature profile for example due to fluctuations in the lab temperature. Then checks would have to be made for the amplitude as the control box was not consistent at producing the same amplitude each day. This part was carried out with water only as only thermocouples T1 and T2 were built in to the setup. Other temperatures were checked with another thermocouple which had to be removed when the actual experiment was being run. It was assumed that once the correct conditions were achieved with water then the experiment with the supersaturated solution would be immersed in the setup under the same conditions that were calibrated.

The experimental setup shown in Figure 41 consists of 3 COBC DN15 straights: two half straights and one full straight. The volume of one full straight is approximately 110 ml as each cell has a volume of 5 ml. The full straight temperature was set to 20°C and hence this was where the crystallisation and imaging took place. The oscillation was achieved through using the motor and bellows to pulse the liquid at a set frequency and amplitude.

Experiments were carried out at several oscillation conditions: 1 Hz and 45 mm amplitude (2 cells in the straight), 2 Hz with 45 mm amplitude, 1 Hz 23 mm amplitude and 2 Hz 23 mm amplitude. The first set of experiments had the same temperature

profile each time. T1 was kept at approximately 82°C in order to prevent nucleation occurring in the bellows as all solution concentrations that were used are undersaturated at this temperature. The cold straight temperature taken at T3 and the upper camera position were kept at 20°C which was chosen as the crystallisation temperature. The heater/chiller units were working with a range of temperature values to create 20°C in the cold straight – ranging from 7°C to 18°C depending on the oscillation conditions being used and the temperature conditions in the lab. Due to the nature of the MFOBC and its arrangement, there was a slight temperature drift within the equipment which usually meant that the temperature at the lower camera position was warmer than the upper camera position by about 1-2°C depending on the oscillation used. The upper part of the setup consisted of one half straight which was set to a higher temperature of approximately 50°C. In a previous setup when this higher temperature region was not present at the liquid level, fouling and crystal growth would occur within the oscillation amplitude as shown in Figure 42.

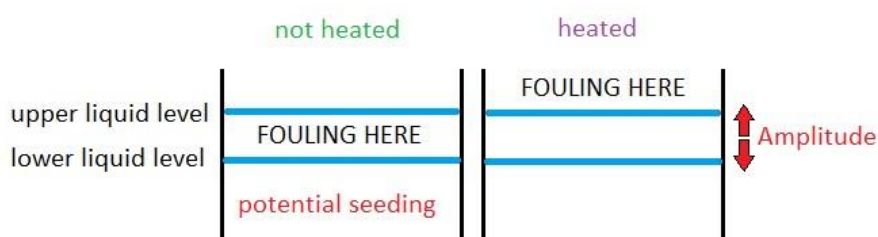


Figure 42. Fouling above liquid line when heated to prevent the system from self-seeding.

However, when the liquid was heated slightly (note: not enough to be undersaturated at this level due to competition between all three regions and having to prevent condensation taking place on the cold straight) evaporation occurred above the liquid level and hence seeding was thought to be prevented.

5.5.2 Imaging

Two Microsoft LifeCam VX-3000 webcams were used to capture the images, each one with a manual focus which was concentrated on the glass surface. YAWCAM

software, © Copyright by malun and developed by Magnus Lundvall, was used to control the cameras and to save images at certain time intervals over the course of the experiment. Initially the cameras were covered to reduce the effects of inconsistent lighting and unwanted reflections. This proved difficult and so after some time the cameras were boxed on to the setup with an LED torch placed inside. The position of the torch was chosen so as to give maximum illumination for the camera but also have minimum reflections.

5.5.3 Solution Preparation

All solutions were prepared in the same manner each time, regardless of concentration. Concentrations were defined in terms of their supersaturation value, which was determined with respect to the saturated concentration at 20°C using Equation 39:

Equation 39

$$S = \frac{C^*}{C_{sat.20^{\circ}C}}$$

where C^* is the concentration the solution has when supersaturated.

5.5.4 Oscillation Conditions

For L-glutamic acid experiments two oscillation conditions were chosen which differed only in their frequency values. The amplitude chosen for these experiments was 45 mm which equated to the height of two cells in the MFOBC. Larger amplitudes were unable to be achieved because of the competing temperature issue between the three straights in the system. Increasing the amplitude would mean a reduction in the temperature in the lower straight which would mean crystals may survive in

this area and grow further in the bellows. Increasing the amplitude further also meant that the chiller unit regulating the temperature in the cold crystallisation straight would have to run at an even lower temperature and this resulted in condensation on the outer glass wall and hence imaging the cells became impossible. Lower amplitudes were not chosen as well because of the difficulties with maintaining the same temperature profile within the system so that comparisons could be made between experiments. The two oscillation conditions were therefore [1 Hz 45 mm] and [2 Hz 45 mm]. 1 Hz and 2 Hz were chosen as previous experiments in other projects had used these conditions successfully for crystallisation. Another issue was that higher frequencies than 2 Hz resulted in the MFOBC shaking, which meant images could not be taken.

Four different oscillation conditions were used during the aqueous glycine experiments. Due to the difference in solubility with glycine and the lower concentrations that were used here the amplitude was able to be altered this time.

The four different conditions explored were [1 Hz 45 mm], [1 Hz 23 mm], [2 Hz 45 mm] and [2 Hz 23 mm]. Lower amplitude was possible with glycine as the temperature profile was different meaning the desired temperatures could be maintained with the heater/chiller units. This was not possible with L-glutamic acid as the high temperature of 80°C needed to be maintained compared to 65°C with glycine.

6 IMAGING OF SURFACE AND BULK CRYSTALLISATION

6.1 CHAPTER OUTLINE

In order to measure and quantify the onset of fouling taking place on the platform outlined in Chapters 5, imaging of the glass wall of the crystalliser was carried out.

Previously no non-invasive imaging techniques have been reported in the literature for investigating fouling behaviour in crystallisation processes.

Chapter 6 covers previous literature available on the use of imaging in crystallisation processes. It describes the image processing techniques which were used in this project to extract as much information from the raw images as possible in order to give an insight into the fouling behaviour under all the experimental conditions that were explored. The theory and decision making behind the analysis is outlined in detail. The methods behind separating the bulk crystallisation from surface crystallisation are also covered.

6.2 IMAGING IN CRYSTALLISATION LITERATURE REVIEW

External bulk video imaging has shown to be a useful technique to determine the metastable zone in cooling crystallisation processes. In a study by Simon et al. [95] the method of endoscopy-based in situ bulk video imaging is presented. Video data was processed using the mean grey intensity. Digital image processing was also deployed to identify the first crystals that appear at the nucleation point. The crystallisation process was monitored by measuring the change in the grey level in the bulk solution. The crystal recognition method using digital image processing involved viewing a larger area within the bulk to increase the probability of seeing a crystal. The area of detectable objects in the video was calculated. If the area meets the set criteria then this is deemed a crystal. This method was found to detect the induction time more quickly than the other methods used in this study [95]. Experimental work was done in a small scale calorimeter where infrared spectra and calorimeter data was recorded. It was found that the mean grey intensity information corresponded to the data from these two sources. Determining the nucleation point as accurately as possible in a crystallisation process is a useful tool and plays a major part in metastable zone width studies and process control. The sooner the induction time is detected, better control of the crystallisation process can be achieved, and the size distribution of the crystals can be optimised. Recent studies involving external bulk video imaging have proven its performance to be close to that of focused beam reflectance measurement (FBRM) and ultraviolet-visible spectroscopy. A study by Qu et al. [96] concerning the effects of two potassium salt additives on a batch cooling crystallisation was carried out using in-line image analysis. A video microscope was used for obtaining data for growth rates of particular crystal faces. The two additives were ethylene diamine tetra acetic acid (EDTA) and potassium pyrophosphate (KPY); and these were used during the crystallisation of potassium dihydrogen phosphate (KDP). The kinetics of the crystallisation were monitored by studying the metastable zone width and the induction time. EDTA usage decreased the induction time and growth rate of the KDP and KPY had the opposite effect, inhibiting the crystallisation process. It was found that the in-line video analysis was a useful method for

inspecting the crystal size and shape throughout. The high speed of the video capture makes this a desirable technique for continuous observation of the system, however there is difficulty in obtaining quantitative data from the video stream. In this study quantitative data was attained through the image processing revealing more information on the size and shape of the crystals. The software available with the imaging probe was not able to provide accurate information due to the fact that it only uses a threshold technique based on pixel intensity to distinguish objects. This was not compatible with the in-line images that were being taken because the background intensity varied due to fluid and particle movement. Other issues were that the probe could only detect within a certain volume and would not always obtain a true view of the entire sample and also any aggregation or particle overlap would result in false data regarding particle size and shape. The Canny method was used in this work to eliminate the difficulties with the inconsistency of the background through edge detection. The Canny edge detector is an algorithm with multiple stages which aims to identify a range of edges within images. Agglomerated particles were excluded by setting particular properties of real crystals in the code so as to eliminate any objects which did not meet these specifications. The method developed in MATLAB included the following steps:

- 1) All the particles were subject to the edge detection process.
- 2) Particles in the raw image were removed if they came in to contact with the image border so that all detected particles were whole.
- 3) Size and shape data analysis was carried out, such as length, width, equivalent spherical diameter, aspect ratio and solidity.
- 4) Specifications for the particles were generated using one of the parameters listed in step 3. Objects in the images which exceed the specification are therefore excluded from the image.
- 5) Using the parameters as before, aggregates and particles which overlap were eliminated.
- 6) The particle size and shape were determined with the new modified images.

It was therefore shown that the in-line video monitoring of the batch cooling process was a useful technique for monitoring the effects that additives have on the size and shape of the crystals produced [96].

In order to obtain real-time data from *in situ* imaging of a crystallisation process, a study by Sarkar et al. [97] combined traditional image analysis methods with multivariate analysis. The batch cooling crystallisation of monosodium glutamate was used to show that the technique can reveal data from the images pertaining to the crystal size and shape. The success of the method was tested by comparing results with those taken from manual analysis of the images. It was found that reasonable particle length estimations were calculated and the data was obtained quickly so as to be used for online monitoring and perhaps could be included in the process control of a crystallisation process. One of the drawbacks of this method of obtaining data is that the images can be noisy, and therefore determining and separating particles from the background of the image can prove difficult. This has normally been dealt with using edge detection methods which was mentioned previously. These methods are reliant on clear thresholds which is difficult with this type of imaging due to the noise. This paper presents a new approach to segment the images through traditional image processing and multivariate methods. Characterizing the background is the goal of this study instead of focusing on the particles themselves. Statistics and principal component analysis were performed on the images to create new images containing only the most prominent objects. Noise was therefore eliminated from the images. Smaller principal components were ignored in the analysis to achieve this noise reduction. After this, the images can be segmented using a global threshold, where the analysis threshold is approximated from the background image without any particles present. Subsequent enhancement of the particle boundaries was achieved through a discrete Fourier transform and signature curve analysis. The signature curve analysis is another method for object detection. It involves using the curvature of the object and its first derivative with respect to the arc length after being subjected to certain translations and rotations. Signature curves can be used to

ascertain the symmetry of an object and therefore its boundary [98]. After this, details of the particle size and shape can be obtained. Through comparing the results with manual image processing, the particle lengths were reasonably similar with around 5% error in the value of the median [97].

A paper by Brown et al. [99] determined growth kinetics of paracetamol in an oscillatory baffled crystalliser (OBC) during an antisolvent crystallisation using video imaging. The crystal size distribution and mean crystal size were determined and compared with results from particle size measurements using Mastersizer (laser diffraction). Parameters such as the supersaturation, antisolvent addition rate and mixing were investigated and it was found that supersaturation has the greatest effect on the kinetics, with the addition rate of antisolvent having the weakest effect. Images were taken using a CCD camera at a rate of 7.5 frames per second. After addition of the antisolvent, images were continually taken until the value of the image intensity reached a constant value. Image processing was carried out in MATLAB, via conversion to 8 bit greyscale. It was found that the smallest crystal that was able to be detected by the camera was 43 μm and so the growth rate kinetics were based on this. MATLAB code was generated to process the images, using an average of the images from the first 5 minutes of recording as a background. This background was subtracted from all images, and then they were converted to binary images where the white regions refer to possible crystals. Every white area in the final image was counted and the area and perimeters were calculated. This information allowed the equivalent mean diameter of every white region to be evaluated. Therefore, this study shows that *in situ* imaging of the crystallisation process can be used to measure particle size via a non-invasive method [99].

Microscope imaging was used in this next study by Kim et al. [100] to follow the fouling of calcium carbonate. A heat exchanger setup with small channels was set up to make use of the microscopic imaging method to monitor the fouling process. Through examining the images, fouling resistances were determined for the complete scaling process. It was evident from the images that three stages were present in the

formation of the scale; namely the induction period, a period where nuclei were generated and then the time where the scale grew in a uniform fashion.

Figure 43 shows the experimental setup being used in this study.

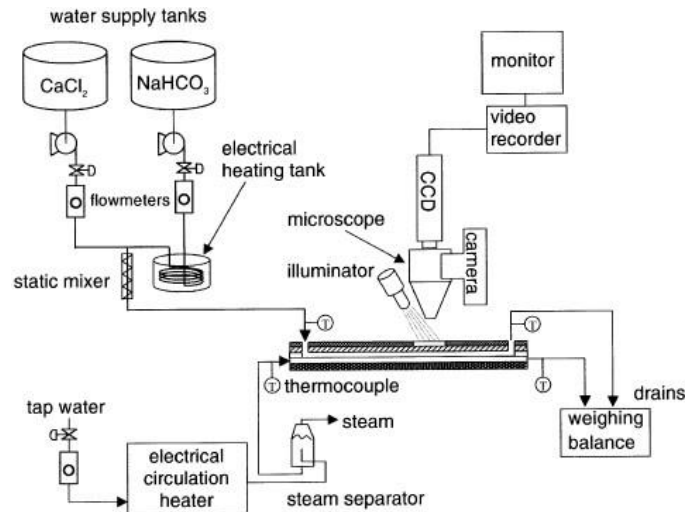


Figure 43. Experimental setup for microscopic study of calcium carbonate fouling [100].

The setup for the imaging portion of the work consisted of a microscope, an external light source for illumination, a CCD camera to observe through the microscope lens, a Nikon camera to visualise the process without the microscope, a video recorder to document what the CCD was picking up and a monitor for visualisation.

Figure 44 presents examples of microscopic images taken when the inlet temperature was 55°C and the water velocity was 1.2 m/s. It was found that increasing the velocity of the cold water prolonged the induction period for scaling. Despite different conditions resulting in different configurations of scale growth, when the heat transfer surface was covered in calcium carbonate the fouling resistances were very similar [100].

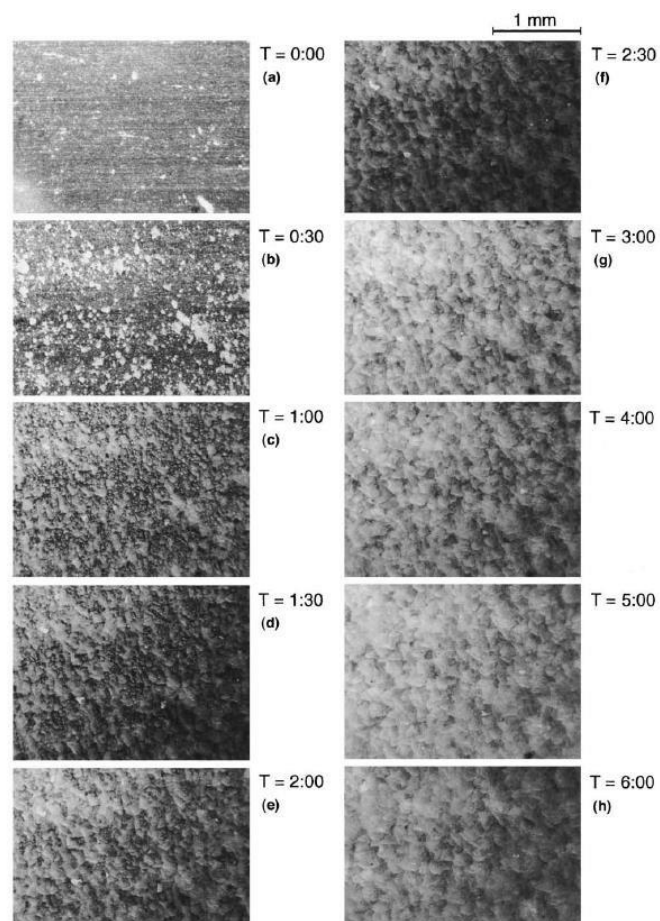


Figure 44. Microscopic images at magnification 40x to show the progression of the fouling of calcium carbonate [100].

The literature study on imaging used during crystallisation revealed that imaging has been used to study bulk nucleation to obtain information regarding induction time, size distribution and crystal shape. Other parameters such as the supersaturation and mixing conditions were also investigated using the imaging technique. However, there was no information concerning the fouling induction times using this imaging technique. In this thesis, fouling induction time was studied independently from bulk nucleation.

6.3 NEW IMAGE PROCESSING METHODS

The aim of this section of work was to take the raw webcam images obtained from the experiments with the MFOBC and deduce information regarding the fouling induction time. Using the same images, separating the bulk induction time and fouling

induction time was attempted. This was the first of the two methods that were used named a thresholding method carried out in Matlab. A FoulingGUI was the second method and it was used to separate bulk nucleation and fouling nucleation. This was carried out in collaboration with Dr Christos Tachtatzis from the Electronic and Electrical Engineering Department at the University of Strathclyde. The idea behind this second method was to extract as much data as possible from the images that were being captured during crystallisation experiments. An algorithm was developed through which the fouling induction time on the glass wall could be identified separately from the induction time in the bulk fluid. The paper by Tachtatzis et al. [101] further explains the theory behind this work but the main points will be summarised in this section.

6.3.1 Method 1: Thresholding-Based Methodology

At first, the program 'ImageJ' was used to determine the average pixel intensities of the image, however with the volume of images being produced and the need for a more robust and repeatable method, Matlab was used to carry this out. The image analysis tools available in Matlab were used to analyse the images taken during the experiments. Dr Jerzy Dziewierz from the Centre for Ultrasonic Engineering at The University of Strathclyde developed code that was used here for image analysis. The webcam generates JPEG images with a size of 320 x 240 pixels. The code carries out the following set of operations on the set of images:

- 1) The background is defined as the first image converted to the greyscale intensity image.
- 2) All of the images in the experiment are then converted to greyscale where all pixels have a value from 0 to 255 based on their intensity.
- 3) The background is subtracted from all of the images.
- 4) A pixel range is defined as the region where the analysis will be carried out- this is the same for all image sets. This is represented visually in an

experimental example shown in Figure 45 where the values of the pixel coordinates are labelled within the figure.

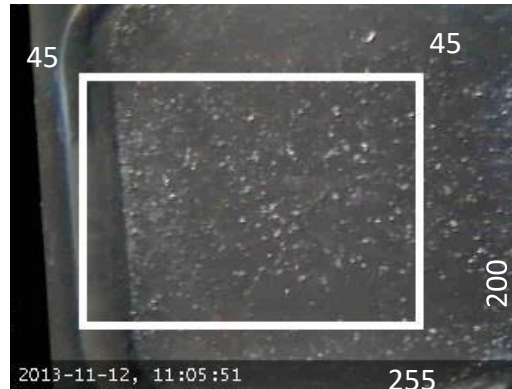


Figure 45. Visual representation of the cropping taking place in the Matlab code used for determining the average pixel intensities over time during the crystallisation and for pinpointing the time at which fouling occurs.

- 5) The threshold value is set. If a pixel within the region of interest has a value of less than the threshold value then this pixel value is set to zero when the average pixel intensity is calculated. The value in each case was set to 5 as this was low enough to detect all important pixel intensities but high enough to reduce minor noise.
- 6) The average pixel intensity of the whole area in the image is determined for all the images in the experiment and is plotted against time.

In this way there is a plot of intensity versus time. The image intensity maps obtained is useful for detecting fouling on the glass wall. Since the crystals growing on the glass surface will have a higher intensity in the grayscale image as they are closer to the camera and also visually more intense then it is logical to say that they will only be picked up as colours representing higher threshold values. The induction times reported were determined through examining the image intensity maps until they showed an area of pixels which were constant. This was the onset of fouling in that

image. The image intensity maps, like the one shown in Figure 46, were used to determine the fouling induction period for method 1.

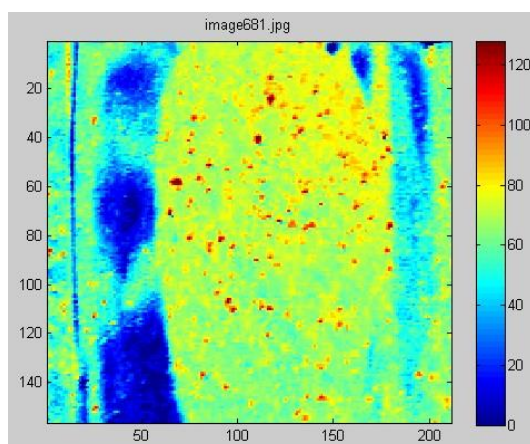


Figure 46. Image intensity map obtained via method 1. Darker red areas in the screenshot are areas of denser fouling on the glass wall. Lighter areas can be attributed to crystals moving freely in the bulk solution and these intensities will vary slightly and not remain constant due to the nature of the fluid flow in the system.

It can be seen from Figure 46 that the clear fouling areas on the glass wall have a higher threshold value than the other areas of the image. Areas coloured in red have the highest threshold value of 100 and are regions of severe fouling.

6.3.1.1 Issues with the Imaging Technique for Monitoring Fouling

The main problem with using imaging to monitor fouling was that it was imperative that the lighting conditions remained constant for all experiments to ensure the most accurate fouling induction times were obtained. The experiments in this study suffered mainly due to problems surrounding this issue. For example, it was evident from most experiments that the lower camera fouled more slowly than the upper camera due to the temperature drift in the equipment. This was expected since the lower camera focused on a region that was normally about 2°C warmer than the upper camera. However, in some cases where it was clear from the raw images that the lighting conditions were not equal in each camera environment (the lower camera had more light than the upper camera), the opposite results were obtained. Creating

the optimal lighting environment whilst keeping the experiments practical was challenging. It was also concerning that if there was not enough light for the camera then the true fouling induction would be missed.

The area of the image that was being analysed in Matlab may have missed the fouling induction if it occurred first in an area that was discarded or not even imaged. The particular two cells that were chosen for imaging may not have been the region which fouled first. This was why the region was kept the same for all experiments to give a fair comparison.

Choosing a suitable background subtraction was also important. It was the first image in the set that was used as the background and this was subtracted from all other images. Other methods were used previously where the contrast was enhanced, but this was thought to give an unrealistic view of what was actually occurring in the equipment.

There could also be issues with bubbles nucleating on the jacket side of the glass wall. This was problematic as they could be mistaken for crystal growth and it would obscure any other data that was collected. If bubble nucleation was found to happen during an experiment then that image set was useless and was repeated once the bubbles were removed.

6.3.1.2 Obtaining Correct Timescale

When running the YAWCAM software with the two webcams it was a possibility to choose a time interval for the image capture. Each image taken was saved with a timestamp. It was assumed that if a time step of one second was chosen when running the image capture then after 60 images one minute would have passed. However it was discovered that the images were being taken at inconsistent time intervals over the course of the experiment.

Code developed by Dr Jerzy Dziewierz at the University of Strathclyde in the Centre of Ultrasonic Engineering allowed this problem to be overcome. A summary of the Matlab code is given here to explain its function [102].

The script was able to read all of the .jpg image files, convert them to grayscale and then cut each image to the size of the timestamp area as shown in Figure 47.



Figure 47. Raw webcam image showing area where the time stamp region (highlighted in red) was cut for analysis by the Matlab code for obtaining real time of image capture.

The data contained within that timestamp is then recognised and translated into a number which corresponds to the number of seconds that has passed since year 0 until the date and time that has been read on the image. This number is given in the new file name of the image when it is replicated by the code.

The times were easily converted into minutes to obtain the real time data for each image so that the time axis was then correct.

6.3.2 Method 2: Fouling Graphical User Interface

6.3.2.1 Theory and Algorithm Development

The webcam images were converted to greyscale so that all pixel values were between 0 (black) and 255 (white) shown in the first stage in Figure 48. The images were then cropped to 100 x 100 pixel size to eliminate reflections.

The outline given in Figure 48 was the proposed method to distinguish crystal growth in the bulk solution from crystal growth on the glass wall of the reactor. The mean grey intensity was determined for every image and the number of pixels above a certain high intensity (the fouling threshold) were counted to create the image sequence which could be analysed further. The images were then put through an

Intensity Outlier Detector which picked out the pixels with the higher intensity (fouling threshold). These high intensity pixels were then processed by the Fouled Pixel Classifier which decided whether or not the pixel was fouled. In order for them to be fouled they had to be consistent for over 5 frames in the image sequence. The bulk pixels were processed further to create the mean grey intensity plot over time and this signal trace was used to obtain the bulk nucleation induction time. The fouled pixels were counted to give a fouling index indicator which was used to estimate the fouling induction time.

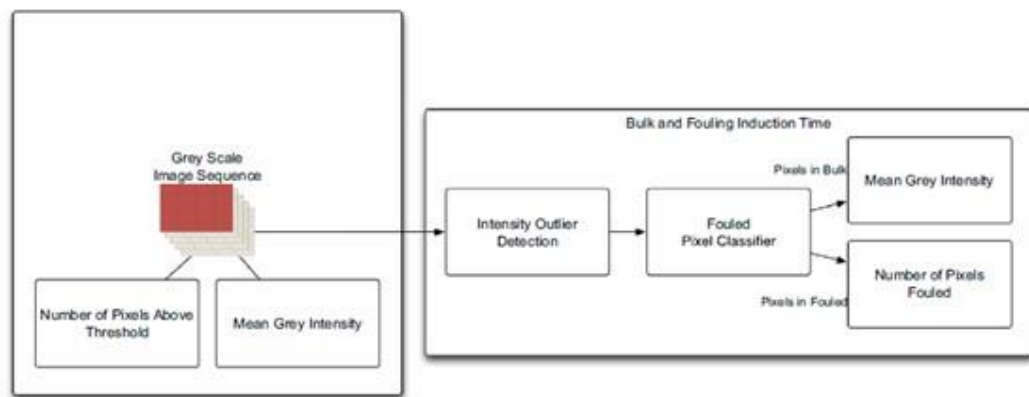


Figure 48. Signals that are available in order to obtain times for the combined induction time as well as the technique suggested for separating bulk and surface nucleation [101].

In this work a Bayesian Online Changepoint Detection technique was used to automatically detect the induction time based on the signal trace generated from the pixel intensities in the images sets.

A paper by Adams and MacKay [103] describes in detail the theory behind this technique. They look at the situation where the parameters in the model (which are aiming to detect the severe changes in the data (change point detection)) are not influenced by the factors which created the change point in the first place. It is therefore stated that the parameters before and after this change point are independent and an online algorithm is produced to detect the most recent

change point in the system. This approach is versatile and can be applied to a variety of data types.

The change point detection method described above was used to estimate the combined induction time through using signal traces taken from the mean grey intensity of the captured images. As more crystals were formed, either through bulk or wall nucleation and growth, the intensity increased and levelled off when the crystallisation was complete.

The next step was to separate the bulk and fouling induction time through analysing the webcam images in a statistical manner. Crystals which foul on the glass wall will have significantly higher pixel intensities than those moving in the bulk fluid. The crystals in the bulk fluid will also have appreciable intensity but these intensities will not be consistently high for consecutive frames due to their constant movement.

There were two main steps which were carried out to achieve the separation:

- 1) Pixels with the highest intensity were identified.
- 2) Pixels which have the highest intensity for a consecutive number of frames were identified. This was crucial to prevent false positives where larger and hence brighter crystals pass through the imaged region.

Pixels fitting this criteria were deemed to correspond to fouled and these pixels were counted as the percentage of pixels fouled over time and plotted to create a signal trace from which change point detection could estimate the fouling induction time.

Pixels not fitting this criteria were deemed to be bulk crystallisation and hence these pixels were treated with the mean grey intensity approach to detecting the change point and hence the bulk induction time for crystallisation.

6.3.2.2 Cropping Methodology for Application to Experimental Work

This section outlines how the FoulingGUI algorithm was used on real data.

Whilst running FoulingGUI on a regular laptop there were issues with the amount of data the machine could handle at once. The processor was unable to deal with running the algorithm when longer experiments were carried out as longer experiments meant a larger image data set with over 5000 images per camera.

To fix this the large webcam images had to be pre-cropped before any analysis with the FoulingGUI was carried out each time so that the computer could handle the amount of data. Matlab was used to pre-crop all the images before analysis and the procedure is outlined here and was the same for every image data set.

The same pixel coordinates were used for the upper and lower camera images for all experimental runs (see Figure 49 and Figure 50). These areas were chosen as they have minimal reflections.

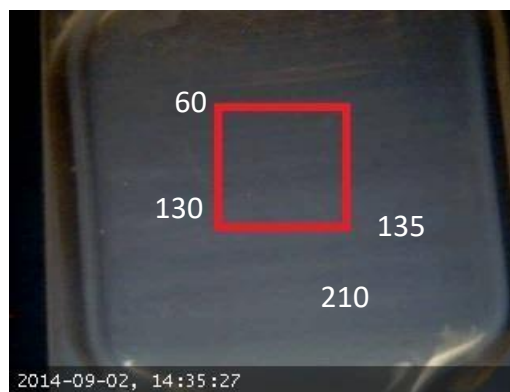


Figure 49. Lower camera raw image showing cropped region.

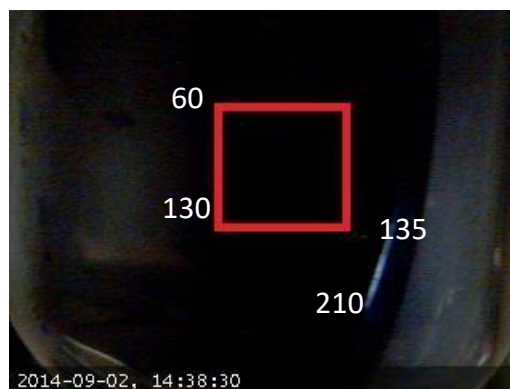


Figure 50. Upper camera raw image showing cropped region.

The pre-cropping method developed in Matlab (i.e. out with the FoulingGUI) was used in some cases where the GUI would crash due to the large file size of some image folders. Manual cropping within the GUI was then used to select the entire cropped area before processing. The pre-cropping method ensured that the same coordinates were selected as in the GUI pixel coordinate cropping method.

7 EXPERIMENTAL RESULTS FROM THE MOVING FLUID OSCILLATORY BAFFLED CRYSTALLISER

7.1 CHAPTER OUTLINE

This chapter outlines all experimental work and results carried out in the Moving Fluid Oscillatory Baffled Crystalliser which is referred to as the MFOBC for simplicity. Two compounds – L-glutamic acid and glycine both in aqueous solution were studied under different concentrations and oscillation conditions. Fouling induction times were obtained through analysing images taken of the glass wall during the crystallisation process.

Two methods of analysing the images were carried out:

- 1) Averaging method based on thresholding in Matlab (not differentiating between bulk and fouling induction time).
- 2) Algorithm method differentiating between fouled and non-fouled pixels based on intensity and persistence of pixels (allowing the estimation of the true fouling induction time).

In this chapter the comparison between the two methods is carried out to see how both approaches dealt with the real data.

7.2 SUMMARY OF EXPERIMENTAL CONDITIONS

The experiment setup construction was discussed in detail in Chapter 5. It shows all temperature and camera positions which are referred to in the main text throughout this chapter.

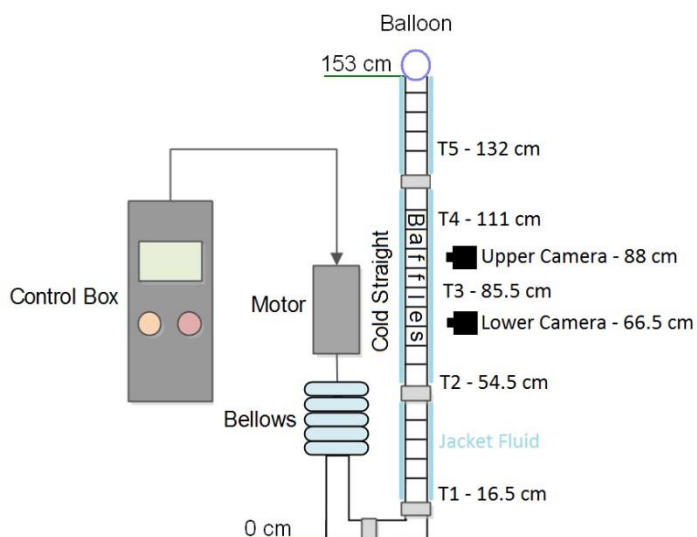


Figure 51. Moving fluid oscillatory baffled crystalliser setup showing temperature and camera positions as well as the mechanism for generating the oscillatory flow – i.e. the bellows moved by the motor which is controlled via the control box where the amplitude (mm) and frequency (Hz) of the oscillation is selected.

Table 3 gives all the experimental conditions that were used with the Moving Fluid Oscillatory Baffled Crystalliser setup with both aqueous L-glutamic acid and glycine solutions.

Table 3. Moving Fluid Oscillatory Baffled Crystalliser Experiment Summaries

Compound	Concentration (g/L)	Supersaturation	Crystallisation Temperature in Cold Straight (°C)	Frequency (Hz)	Amplitude (mm)
L-glutamic acid	21.19	3	20	2	45
				1	
	28.26	4		2	
				1	
	42.39	6		1	
				2	
		4.17	30	1	
				2	
Glycine	299.06	1.4	20	1	45
	320.42	1.5			
	384.51	1.8		1	45
				2	
				1	23
				2	

7.3 L-GLUTAMIC ACID EXPERIMENTS

Experiments carried out in the MFOBC with aqueous L-glutamic acid solutions were characterised into two separate sets - set 1 and set 2 - based on the conditions

chosen. The crystallisation temperature in the cold straight was 20°C and 30°C for set 1 and set 2 respectively. The details are discussed in detail below.

7.3.1 Temperature and Supersaturation vs. Height for Moving Fluid Oscillatory

Baffled Crystalliser for L-glutamic Acid Experiments

As described previously in Chapter 5, the MFOBC had to be calibrated so that the required temperatures were achieved within the equipment at the desired height of the system. Through calibration with water alone and adjusting the jacket temperatures of each glass straight, ultimately:

- 1) The crystallisation temperature in the cold straight was maintained at 20°C.
- 2) The temperature at position T1 was high enough to achieve undersaturation, preventing nucleation in the bellows section.
- 3) Temperature position T5 (see Figure 51) was kept warmer than the crystallisation straight. T5 did not achieve undersaturation but on average had an induction period much longer than the induction period of the crystallisation straight. Nucleation was therefore guaranteed to take place in the cold straight first where the greatest supersaturation driving force was.

By using solubility data from literature [86], the supersaturations vs. the height of the MFOBC was also determined to rationalise the temperature choices, especially for T5.

The results for the L-glutamic acid Experiment set 1 temperature and supersaturation profiles with height are given in Figure 52 and Figure 53.

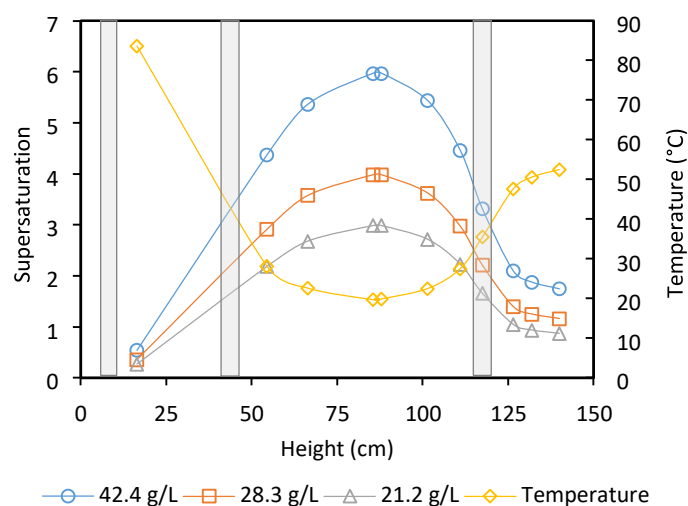


Figure 52. Measured temperature and corresponding supersaturation vs. height of the MFOBC for L-glutamic acid conditions of 1 Hz 45 mm where ○: 42.4 g/L □: 28.3 g/L Δ: 21.2 g/L where no crystals formed at this lowest concentration over the timescales used and ◇ indicates the temperature profile over the system. The bars on the chart represent the position of the collars in the MFOBC i.e. where one glass straight starts and finishes.

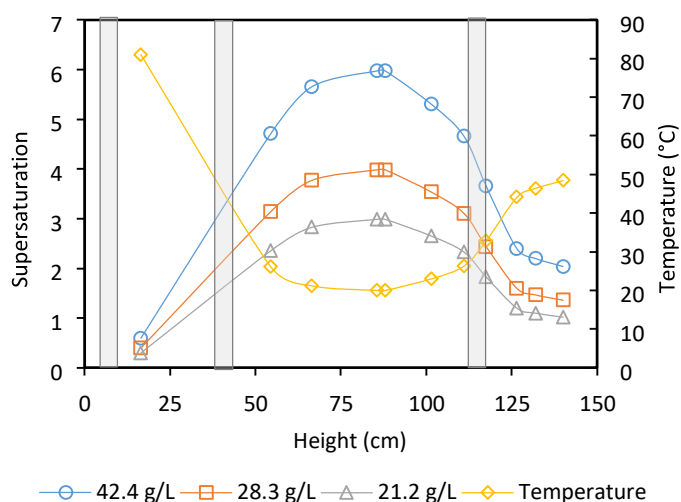


Figure 53. Measured temperature and corresponding supersaturation vs. height of the MFOBC for L-glutamic acid conditions of 2 Hz 45 mm showing data pertaining to the three concentrations which were used: ○: 42.4 g/L; □: 28.3 g/L and Δ: 21.2 g/L and the temperature profile: ◇. Collar positions on the MFOBC are indicated.

The temperature vs. height information for all conditions used with aqueous L-glutamic acid solutions are shown in Figure 54. It can be seen that despite the conditions altering from the different experiment types, the other temperature positions were always ensured to be as close to one another as was possible with the equipment available and its capabilities.

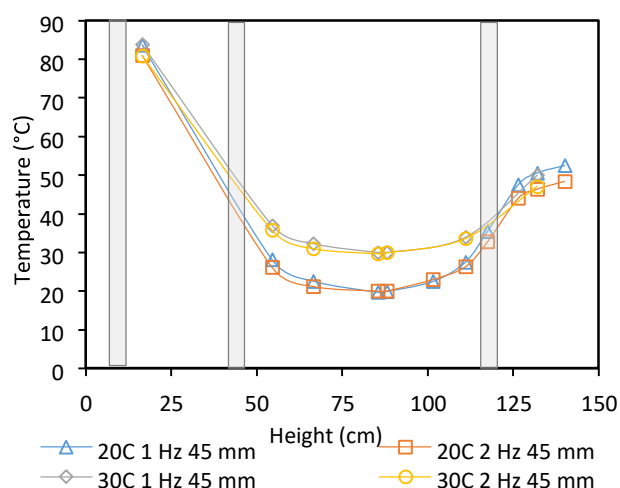


Figure 54. Measured temperature vs. height of the MFOBC for all L-glutamic acid conditions used: 1 Hz 45 mm and 2 Hz 45 mm for crystallisation temperatures of 20°C and 30°C. Δ : [20°C 1 Hz 45 mm] \square : [20°C 2 Hz 45 mm] \diamond : [30°C 1 Hz 45 mm] \circ : [30°C 2 Hz 45 mm]. Collar positions are indicated.

The supersaturation vs. height profiles are shown in Figure 55. All experiments carried out with L-glutamic acid solution of concentration 21.19 g/L did not crystallise. The shortest period of time these experiments were left for was 3.5 hours. If the supersaturation (based on solubility at 20°C) in the upper straight was kept below 3 (21.19 g/L) nucleation was not expected to occur within 3.5 hours at least. This ensured that nucleation took place in the crystallisation straight first.

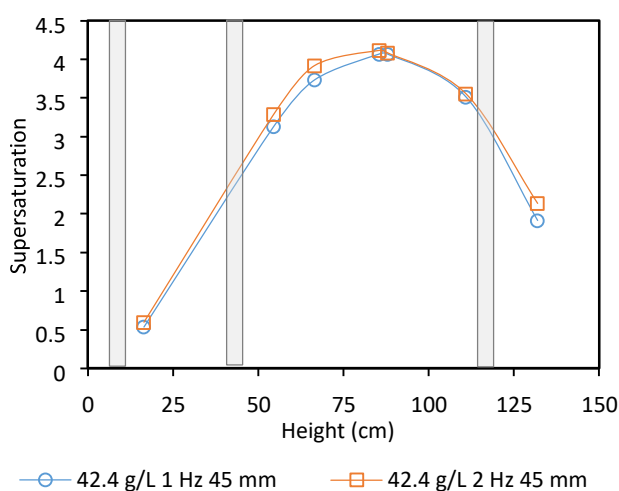


Figure 55. Supersaturation determined from measured temperature vs. height data for L-glutamic acid 42.4 g/L solution experiments under crystallisation temperature of 30°C under two oscillation conditions: 1 Hz 45 mm \circ and 2 Hz 45 mm \square . Collar positions between glass straights are indicated on the graph.

7.3.2 Summary of L-Glutamic Acid Conditions

7.3.2.1 Experiment Set 1:

Experiment set 1 refers to the L-glutamic acid investigation of three concentrations of 21.19, 28.26 and 42.39 g/L (corresponding to supersaturations 3, 4 and 6 based on the solubility at 20°C) used under two oscillation conditions: 2 Hz and 45 mm amplitude and 1 Hz 45 mm amplitude. Each condition was repeated 5 times. These experiments were carried out under the temperature conditions discussed previously. The temperature positions are indicated in Figure 51.

The 42.39 g/L solution was saturated at approximately 67°C so 80°C was chosen as a standard for T1 to ensure nucleation did not take place within the bellows. Hot supersaturated solution was prepared at 80°C (through dissolving the required mass of L-glutamic acid in water which was preheated to the high temperature to reduce the solution preparation time) and pumped in to the MFOBC using a peristaltic pump via a port at the base of the equipment. A high throughput rate was used to ensure the liquid was transferred as quickly as possible to reduce the heat loss.

The MFOBC was filled so that the upper half straight was ~75% full. At this point the oscillation was set, temperatures T1 and T2 were recorded throughout to make sure no major fluctuations were occurring and the experiment was run. The jacket temperatures of the glass straights were pre-set with water prior to the experiment being run to achieve the desired bulk temperatures. This would alter on a daily basis and so had to be carried out before every experiment. A balloon was placed over the top of the glass straight which was open to the air to reduce effects from evaporation.

The total volume of solution present in the equipment, including the fluid inside the unjacketed bellow section was approximately 420 ml in each experiment.

7.3.2.2 Experiment Set 2:

Experiment set 2 concerns the L-glutamic acid experiments which were carried out under the following conditions: concentration 42.39 g/L (supersaturation 6 based on solubility at 20°C) was used under oscillation conditions of 1 Hz 45 mm and 2 Hz 45 mm where in all cases the crystallisation temperature was set to 30°C instead of 20°C which was previously used in Experiment set 1. This was to determine the effects on fouling of increasing the crystallisation temperature to determine whether or not the data from the average pixel intensities of the image would give the expected result of slower nucleation and growth on the wall due to the increased temperature and hence lowered supersaturation.

Each condition was repeated at least four times in this case. The solution was prepared and introduced into the MFOBC in the same way as outlined for Experiment Set 1.

7.3.3 Average Pixel Intensities of Images for L-glutamic Acid Crystallisations

The average pixel intensities over time were plotted in Figure 56 for both oscillation conditions of 1 Hz 45 mm and 2 Hz 45 mm. The two conditions were clearly separated in that induction times for the higher frequency were shorter. These induction times were obtained using the thresholding method in Matlab. The maximum pixel intensities for the higher frequency were also greater than those of the 1 Hz frequency.

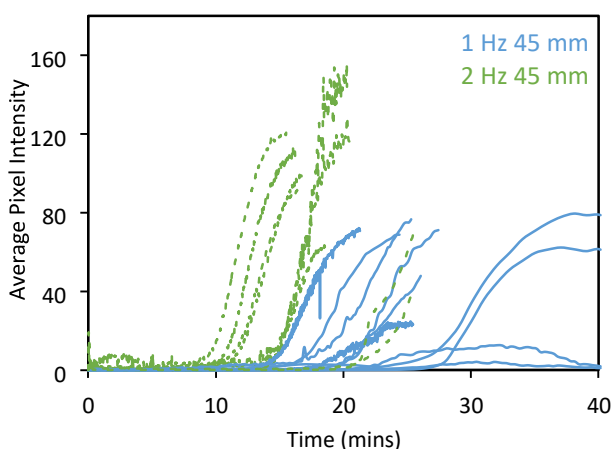


Figure 56. Plots of average pixel intensity vs. time for all L-glutamic acid 42.39 g/L experiments under the two oscillation conditions of 1 Hz 45 mm (solid blue line) and 2 Hz 45 mm (dashed green line).

28.26 g/L solution results, shown in Figure 57, were found to follow the same trends as described for the 42.39 g/L data set. Unfortunately, 5 data sets in total have been omitted due to the data being non-ideal due to reflections and inexplicable spiking in the intensities. Despite them being omitted, induction times were able to be obtained from the image intensity maps. On average the fouling induction time for the 28.21 g/L solution was 75.43 mins for the higher frequency and 127.1 mins for the lower frequency.

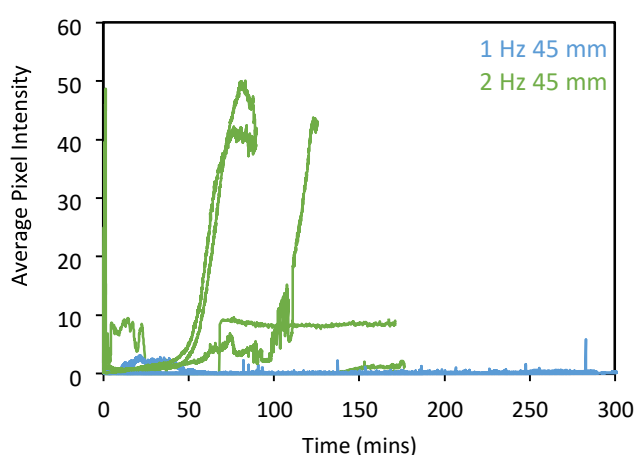


Figure 57. Plots of average pixel intensity vs. time for all L-glutamic acid 28.26 g/L experiments under the two oscillation conditions of 1 Hz 45 mm (blue) and 2 Hz 45 mm (dashed green line).

The next point of investigation was to ascertain the effects that the crystallisation temperature had on the fouling behaviour. All previous experiments were taking place at 20°C in the crystallisation straight of the MFOBC. Further experiments were carried out at 30°C with the aim of calibrating the main temperature points as close to the conditions that were present in the previous runs for Experiment set 1 (T1, Upper camera position and T5). Figure 58 depicts the data of average pixel intensity vs. time for the high oscillation experiments that were carried out (2 Hz 45 mm), as well as the previous 20°C experiments for comparison purposes.

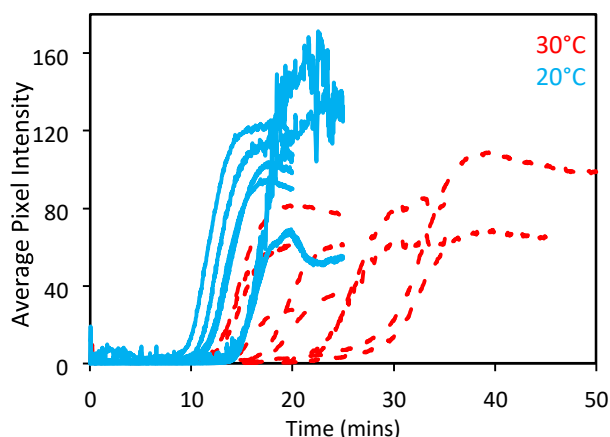


Figure 58. Plots of average pixel intensity over time for L-glutamic acid 42.39 g/L at 2 Hz 45 mm oscillation at crystallisation temperatures of 20°C: (solid blue line) and 30°C: (dashed red line).

The induction times were longer and the maximum pixel intensities were lower for the crystallisation taking place at 30°C in the cold straight. Similar information was also deduced from the same plot but for the lower oscillation experiments and is shown in Figure 59 with the 20°C crystallisation temperature experiments to compare.

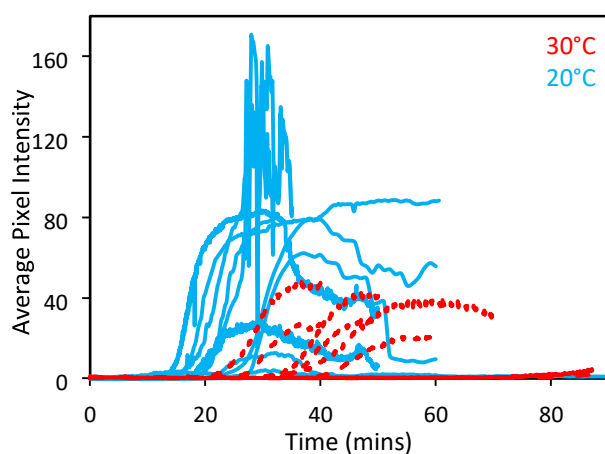


Figure 59. Plots of average pixel intensity over time for L-glutamic acid 42.39 g/L at 1 Hz 45 mm oscillation at crystallisation temperatures of 20°C: (solid blue line) and 30°C: (dashed red line).

With the lower frequency experiments the same trend was apparent in that longer induction times and lower maximum pixel intensities were found with the 30°C crystallisation. These results were expected as the temperature is increased the supersaturation created will be less with 30°C than the 20°C used previously. The supersaturation at the 30°C condition was $S=4.07$. The solubility data used from literature [87] is given below in Figure 60 indicating the difference in solubility when the temperature is increased from 20 to 30°C in green and orange respectively.

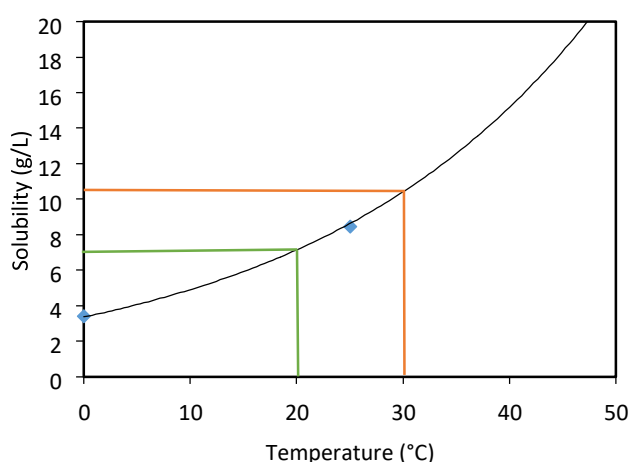


Figure 60. Solubility of L-glutamic acid in water: solubility at 20°C in green and at 30°C in orange [87].

7.3.4 Fouling Induction Times for L-Glutamic Acid

For each oscillation and concentration at least five repetitions were carried out. Figure 61 presents the fouling induction times obtained for experiments in set 1 with logarithmic timescale. Note that the experiments concerning 21.19 g/L solutions are not present here as crystallisation did not occur within the time the experiments were run for (between 3 and 5.5 hours). The induction time was obtained via the image intensity maps from Matlab that were mentioned previously. When several pixels were visible on the map for a prolonged period of time at a higher intensity than the background noise, this was the fouling induction period taken.

Increasing the supersaturation reduced the fouling induction time. The effect of oscillation frequency is shown here in that longer fouling induction times occur with lower frequency.

Figure 61 combines the data from all oscillations and from both the upper and lower cameras (two data points per experiment).

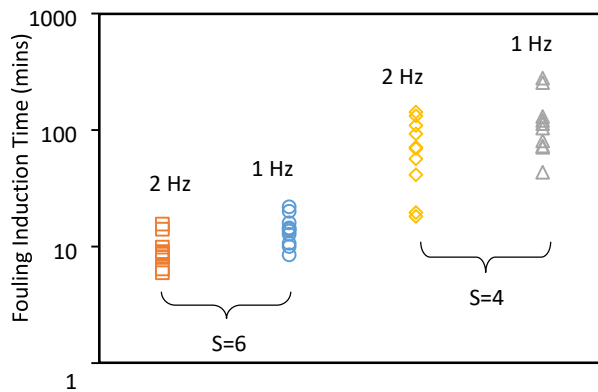


Figure 61. Chart showing all fouling induction times for L-glutamic acid experiments at concentration 42.39 g/L under the following oscillation conditions: ○: 1 Hz 45 mm □: 2 Hz 45 mm and 28.26 g/L at: ◇: 2 Hz 45 mm Δ: 1 Hz 45 mm all at 20°C crystallisation temperature.

Figure 62 shows the fouling induction time comparison for L-glutamic acid 42.39 g/L experiments at the two different crystallisation temperatures and oscillation conditions.

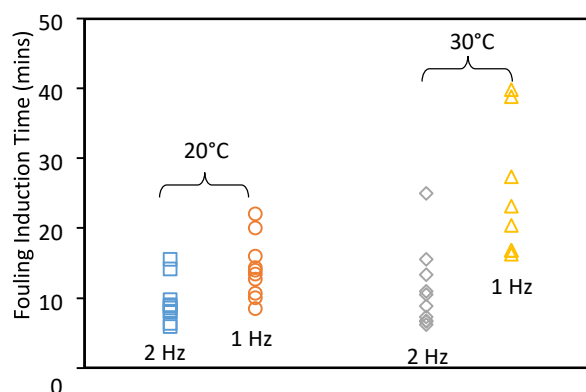


Figure 62. Summary of fouling induction times for L-glutamic acid 42.39 g/L under two different crystallisation temperatures of 20°C and 30°C. □: 20°C 2 Hz 45 mm ○: 20°C 1 Hz 45 mm ◊: 30°C 2 Hz 45 mm Δ: 30°C 1 Hz 45 mm.

On average, the fouling induction times are longer for the higher temperature experiments. It also shows the effect of oscillation on the fouling induction where increasing the frequency decreases the induction period. This was apparent previously for the 20°C runs and is now reinforced by the 30°C data.

7.4 GLYCINE EXPERIMENTS

This section discusses the experimental data obtained for Experiment Set 3 which involved using one concentration of aqueous glycine solutions under 4 different oscillation conditions within the MFOBC.

7.4.1 Temperature and Supersaturation vs. Height for Moving Fluid Oscillatory

Baffled Crystalliser for Glycine Experiments

For Experiment set 3, which includes all glycine experiments carried out at 384.51 g/L which corresponds to supersaturation 1.8 (based on solubility at 20°C) under 4 different oscillations the following temperature profiles over the height of the MFOBC were used and are shown in Figure 63. Note that despite the oscillation conditions

differing, the temperature profiles remain as constant as was possible with the equipment available.

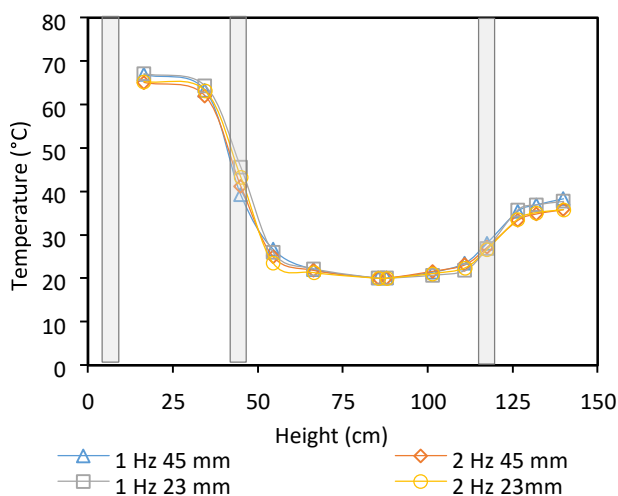


Figure 63. Temperature vs. height data for all glycine oscillation conditions used with concentration 384.51 g/L:
□: 1 Hz 23 mm; Δ: 1 Hz 45 mm; ○: 2 Hz 23 mm and ◇: 2 Hz 45 mm with collar positions indicated.

The supersaturation vs. height data is shown in Figure 64 and was constructed using solubility data from literature [104]. An experiment carried out with glycine at 299.06 g/L (supersaturation 1.4 based on 20°C solubility) under oscillation conditions of 1 Hz 45 mm was found to not crystallise over a period of approximately 4 hours. Therefore, as before with the L-glutamic acid solutions, it was deemed sufficient to keep the solution in the upper half straight of the MFOBC under supersaturation 1.4 in order to ensure nucleation did not occur in this area first.

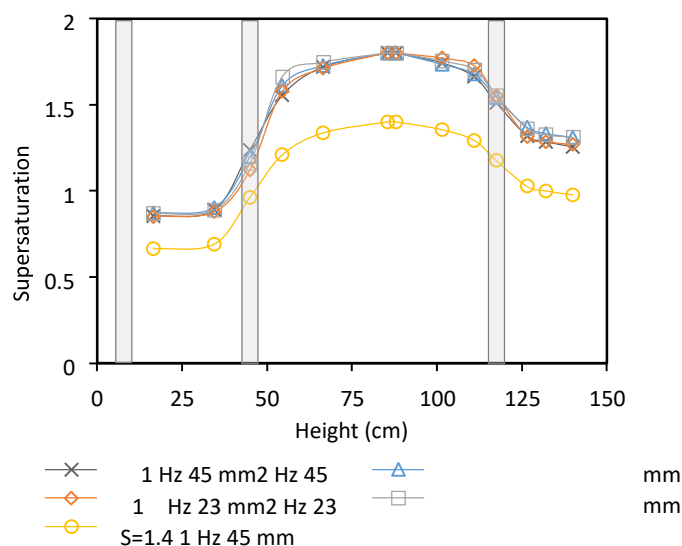


Figure 64. Supersaturation vs. height for all glycine conditions used at concentration 384.51 g/L: ○: 1 Hz 23 mm; X: 1 Hz 45 mm; □: 2 Hz 23 mm and Δ: 2 Hz 45 mm. The supersaturation profile corresponding to a concentration of 299.06 g/L under crystallisation temperature 20°C and oscillation conditions of 1 Hz 45 mm [○] where after 4 hours no crystals were formed in the MFOBC. Collar positions are also indicated.

7.4.2 Summary of Glycine Conditions

Experiment set 3 consists of the aqueous glycine experiments using supersaturation 1.8 under these oscillation conditions: 1 Hz 45 mm, 2 Hz 45 mm, 1 Hz 23 mm and 2 Hz 23 mm. Each condition was repeated ten times.

384.51 g/L of aqueous glycine solution is saturated at 53.8°C therefore 65°C was chosen as the temperature to be achieved in the bottom section of the MFOBC to prevent nucleation in the bellows by keeping the solution undersaturated.

Hot solution was again prepared out with the MFOBC and the same procedure as outlined in Experiment Set 1 for L-glutamic acid was used.

7.4.3 Average Pixel Intensities of Images for Glycine Crystallisations

The following plots of average pixel intensity vs. time in Figure 65 and Figure 66 depict the differences in crystallisation behaviour for glycine when the frequency and when the amplitude was altered.

Figure 65 shows the effect when amplitude was changed from 23 mm to 45 mm at a constant frequency of 2 Hz. It can be seen from the plot that the average induction times are much lower when the amplitude was increased. Not only this, the gradients of the curves are steeper.

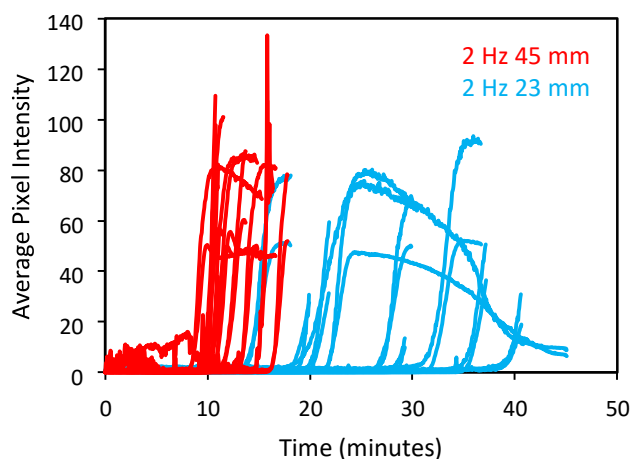


Figure 65. Plots of average pixel intensity vs. time for all glycine 384.51 g/L experiments under the two oscillation conditions of 2 Hz 45 mm (red line) and 2 Hz 23 mm (blue line).

Figure 66 depicts the effect when the amplitude was kept constant at 45 mm but the frequency was changed from 1 to 2 Hz. The induction periods were shorter for the higher frequency.

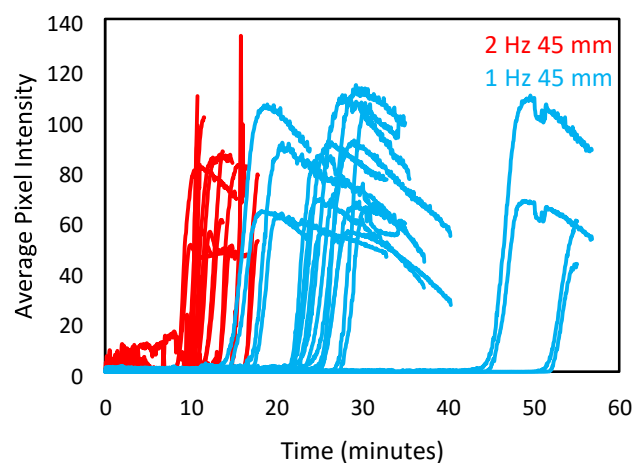


Figure 66. Plots of average pixel intensity vs. time for all glycine 384.51 g/L experiments under the two oscillation conditions of 2 Hz 45 mm (red line) and 1 Hz 45 mm (blue line).

2.1.1 Fouling Induction Times for Glycine

Figure 67 summarises all the results for the fouling induction times recorded for all glycine experiments with logarithmic timescale. These were all carried out at 20°C crystallisation temperature and under the conditions outlined in Experiment set 3 section.

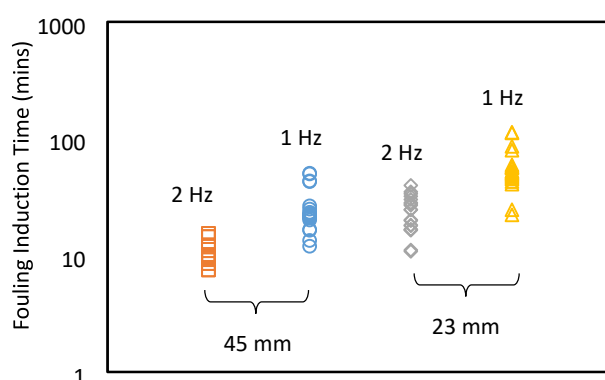


Figure 67. Chart showing summary of all fouling induction times for glycine experiments at 384.51 g/L - □: 2 Hz 45 mm ○: 1 Hz 45 mm ◊: 2 Hz 23 mm and Δ: 1 Hz 23 mm at 20°C crystallisation temperature.

This study of glycine incorporated the effects of amplitude changes in the oscillation as well as frequency. This was possible due to the higher solubility compared to Lglutamic acid. Lower temperatures could be used which meant the competition between the three sections was minimised when amplitude was altered.

Table 4 gives the average fouling induction times for each condition showing that increasing the amplitude or frequency or both in turn decreases the fouling induction time.

Table 4. Average Fouling Induction Times for Glycine Experiments

Frequency (Hz)/Amplitude (mm)	1/45	1/23	2 /45	2 /23
-------------------------------	------	------	-------	-------

Fouling Induction Time (mins)	25.5	56.7	10.5	22.3
--------------------------------------	------	------	------	------

7.5 NUCLEATION KINETICS FOR L-GLUTAMIC ACID AND GLYCINE

The ter Horst model for determining nucleation rates from probability distributions of induction times [51] was used here to analyse all the data collected for L-glutamic acid and glycine, despite there being fewer repetitions than ideally desired. It is known that more data points would give more robust results, however so long as the errors are taken into account then this is a sufficient method for comparing the results from different conditions within the MFOBC to verify the general trends. These calculations were based on the total volume of the MFOBC taken to be 420 ml. The units for the nucleation rate J are $\text{m}^{-3} \text{min}^{-1}$ and the units for the growth time t_g are in minutes.

Cumulative probability distributions with ter Horst model fits for the all L-glutamic acid experiments are shown in Figure 68.

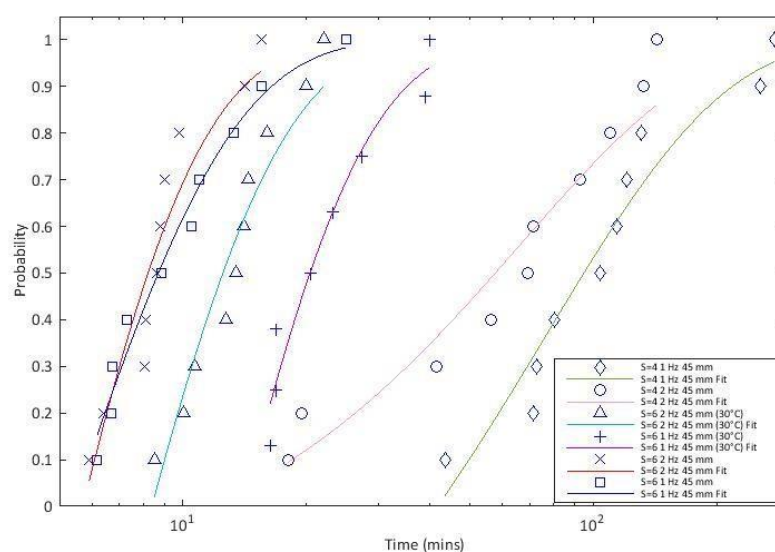


Figure 68. Cumulative probability distributions of induction times for all L-glutamic acid experiments under 1 Hz 45 mm 28.26 g/L [◇]; 2 Hz 45 mm 28.26 g/L [○]; 1 Hz 45 mm 42.39 g/L [□]; 2 Hz 45 mm 42.39 g/L [X]; 1 Hz 45 mm 42.39 g/L 30°C crystallisation temperature [+] and 2 Hz 45 mm 42.39 g/L 30°C crystallisation temperature [Δ] with ter Horst fits shown.

Figure 69 shows the data for the L-glutamic acid experiments. The errors here are large as fewer repetitions were carried out - there were only 10 data points per fit.

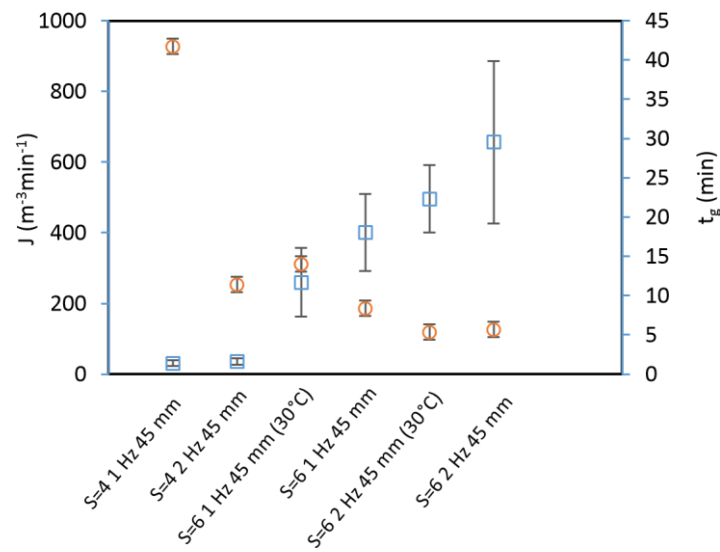


Figure 69. Chart depicting the growth times (\circ) and nucleation rates (\square) for L-glutamic acid experiments under 2 different oscillation conditions which are 1 Hz 45 mm and 2 Hz 45 mm and under two different concentrations of 28.26 and 42.39 g/L all of which are indicated.

The nucleation rate increased with increasing concentration and frequency of oscillation and with decreasing the crystallisation temperature. The same is true for the growth time decreasing.

Cumulative probability distributions with ter Horst model fits for the glycine experiments are shown in Figure 70.

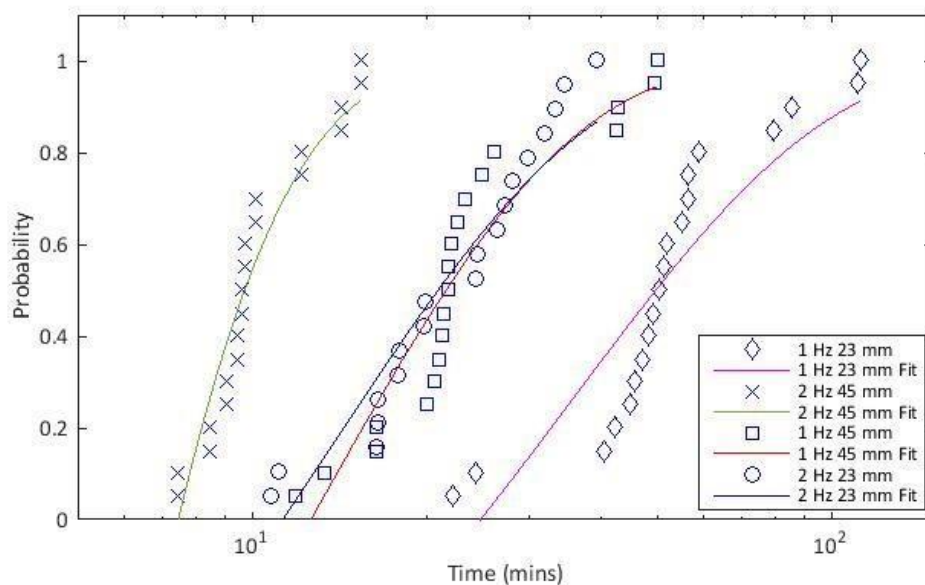


Figure 70. Cumulative probability distributions of induction times for 384.51 g/L glycine experiments under 1 Hz 23 mm[◇]; 1 Hz 45 mm [□]; 2Hz 23 mm [○] and 2 Hz 45 mm [X] oscillation with ter Horst fits shown.

The results for the glycine experiments are given in Figure 71.

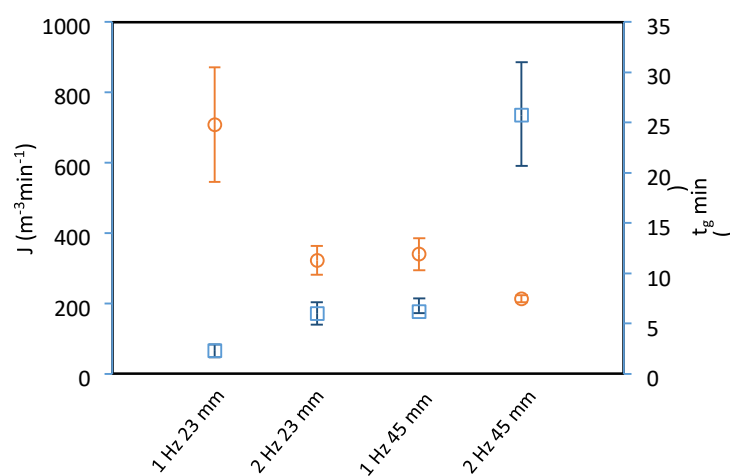


Figure 71. Chart depicting the growth times (○) and nucleation rates (□) for 384.51 g/L glycine experiments under the 4 different oscillation conditions which are 1 Hz 23 mm, 2 Hz 23 mm, 1 Hz 45 mm and 2 Hz 45 mm indicated above.

We can see that the nucleation rate J increases when a) the amplitude of the oscillation increases b) the frequency of oscillation increases and c) the

supersaturation increases as was the case with L-glutamic acid. The same points are also true where the growth time t_g decreases.

7.6 FOULINGGUI ALGORITHM DATA FOR L-GLUTAMIC ACID AND GLYCINE

The aforementioned algorithm discussed in Chapter 6 reported by Tachtatzis et al. [101] was used to distinguish between bulk and wall crystallisation (fouling) for every data set.

The algorithm is based on change point detection and it estimates:

- 1) the bulk induction time
- 2) the fouling induction time
- 3) the combined induction time

Figure 72 shows a correlation plot comparing the two methods for detecting the time where fouling occurs in the MFOBC for L-glutamic acid under the conditions of 2 Hz 45 mm and 42.39 g/L. These methods were discussed in detail in Chapter 6 and were reiterated in the introduction to this chapter.

The algorithm works with a much smaller cropped area of the image compared to the Matlab technique which is based on visual inspection and thresholding as mentioned earlier. However, the same area was cropped each time and is defined via pixel coordinates.

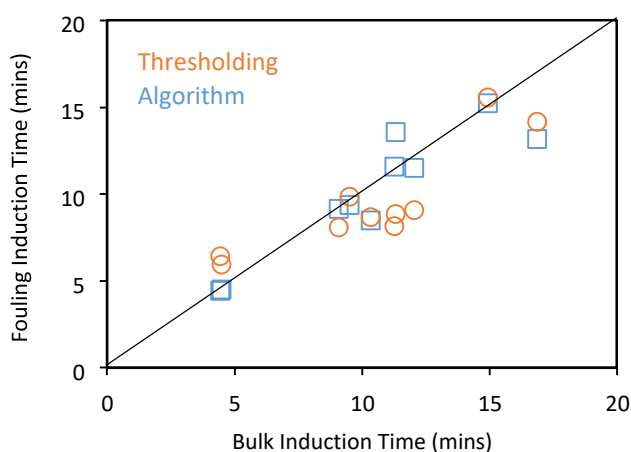


Figure 72. Correlation plot based on thresholding (○) and algorithm data (□) for comparing fouling induction times obtained for the same image sets of L-glutamic acid solution at 42.39 g/L with oscillation conditions of 2 Hz 45 mm.

Figure 72 gives an indication of the agreement between the two methods of obtaining fouling induction times and it can be seen that there are only minor differences for this experiment set, and in some cases no differences in the fouling time at all. This data set shows when the algorithm works fairly well and agrees with the thresholding method in most cases with only small variations.

7.6.1 FoulingGUI vs. Thresholding Method - Fouling vs. Bulk for Aqueous L-Glutamic Acid and Glycine Solutions

This section aims to probe the comparison between the two induction time determination techniques further, by ascertaining the causes of the differences between the fouling induction time values of the two methods.

The colour coded key below gives an indicator as to the reason behind any issues present in the experimental results given in the following tables all experiments carried out in the MFOBC. There were four reasons found for any differences.

KEY:

Fouling occurring before bulk nucleation	Red
Spike in the algorithm data (either fouling or bulk or both)	Green
Issue with the algorithm not detecting the correct change point and defaulting to the last image in the set	Yellow
Region selection issue where the algorithm window is too small to detect the true fouling induction time of the cell	Blue
These experiments are in agreement with both methods	Black

In Table 5 there is a summary of the data contained within Figure 73 for aqueous Lglutamic acid solution at supersaturation 4. The following tables and figures explain the other data sets in a similar fashion.

Table

5. Induction Times for L Glutamic Acid 28.26 g/L [2 Hz 45 mm]

	Induction Time (minutes)				
Date/Camera:	Combined	Bulk	Fouling: Algorithm	Fouling: Thresholding	
21.1.14 low	142.35	142.52	58.68	92.85	
21.1.14 up	119.95	120.3	122.67	109.78	
30.1.14 low	171.7	171.7	133.95	132.93	
30.1.14 up	68.13	67.97	138.2	142.78	
7.11.13 low	112.95	112.95	151.28	71.47	
7.11.13 up	58.42	158.18	69.08	69.1	
4.3.15 low	46.27	46.38	42.07	41.4	
4.3.15 up	31.22	31.22	21.4	56.48	
6.3.15 low	46.18	46.43	42.52	19.52	
6.3.15 up	35.38	38.58	57.18	18.03	

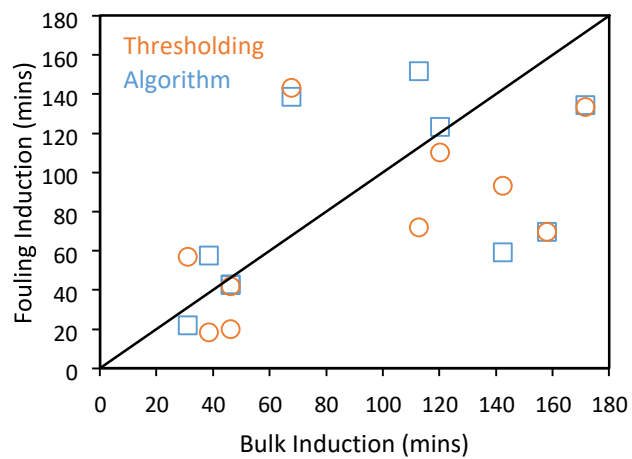












Figure 73. Correlation plot of Algorithm fouling induction time [□] vs. thresholding fouling induction time [○] for L-glutamic acid 28.26 g/L under oscillation conditions of 2 Hz 45 mm.

6. Induction Times for L Glutamic Acid 28.26 g/L [1 Hz 45 mm]

	Induction Time (minutes)				
Date/Camera:	Combined	Bulk	Fouling: Algorithm	Fouling: Thresholding	
10.4.14 low	159.02	159.02	116.35	72.63	
10.4.14 up	195.27	195.27	17.4	43.53	
11.4.14 low	187.05	187.05	92.92	130.9	
11.4.14 up	187.03	187.07	25.7	104.1	
12.2.14 low	262.25	259.33	201.73	80.45	
12.2.14 up	72.72	72.72	193.1	114.25	
13.2.14 low	222.93	222.93	149.15	71.53	
13.2.14 up	192.88	193.05	194.07	120.72	
4.4.14 low	171.95	171.95	38.6	277.9	
4.4.14 up	49.73	49.77	29.28	255.18	

Table

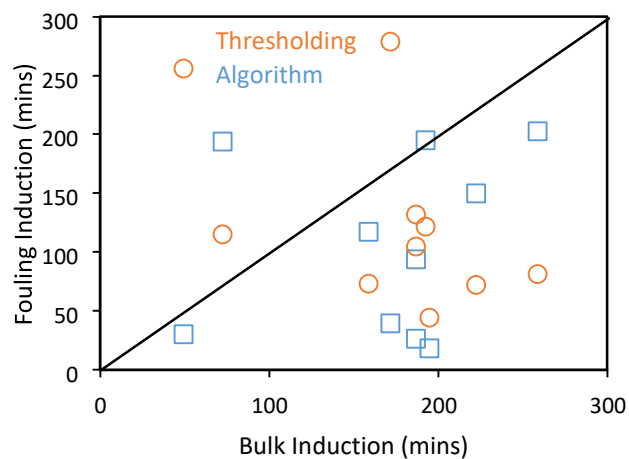


Figure 74. Correlation plot of Algorithm fouling induction time [□] vs. thresholding fouling induction time [○] for L-glutamic acid 28.26 g/L under oscillation conditions of 1 Hz 45 mm.

7. Induction Times for L Glutamic Acid 42.39 g/L [2 Hz 45 mm]

	Induction Time (minutes)				
Date/Camera:	Combined	Bulk	Fouling: Algorithm	Fouling: Thresholding	
1.11.13 low1	9.95	4.47	4.38	6.38	
1.11.13 up1	4.5	4.52	4.47	5.92	
6.11.13 low	10.33	10.35	8.47	8.62	
6.11.13 up	9.07	9.1	9.13	8.05	
12.11.13 low	11.38	11.35	13.55	8.82	
12.11.13 up	11.3	11.3	11.57	8.13	
29.11.13 low	12.08	12.08	11.48	9.05	
29.11.13 up	9.53	9.53	9.33	9.82	
27.2.15 low	14.53	14.95	15.2	15.53	
27.2.15 up	16.88	16.88	13.13	14.15	

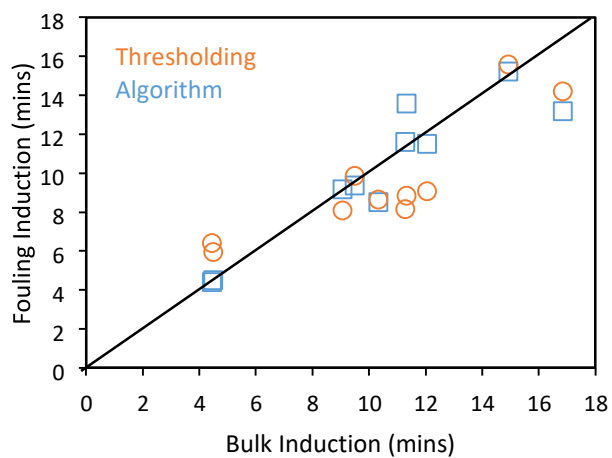


Figure 75. Correlation plot of Algorithm fouling induction time [□] vs. thresholding fouling induction time [○] for L-glutamic acid 42.39 g/L under oscillation conditions of 2 Hz 45 mm.

8. Induction Times for L Glutamic Acid 42.39 g/L [1 Hz 45 mm]

	Induction Time (minutes)				
Date/Camera:	Combined	Bulk	Fouling: Algorithm	Fouling: Thresholding	
3.9.13 low	39.05	39.05	39.05	22.03	Yellow
3.9.13 up	26.02	26.02	26.02	20.02	Black
8.10.13 low	12.97	12.97	10.22	13.47	Black
8.10.13 up	8.22	8.58	8.25	8.52	Green
25.9.13 low1	17.05	19.07	15.05	14.03	Red
25.9.13 up1	10.35	10.68	12.7	10.02	Green
25.9.13 low2	17.38	20.73	16.72	14.4	Red
25.9.13 up2	14.38	14.72	17.07	10.7	Green
29.1.14 low	21.03	21.2	27.57	12.75	Blue
29.1.14 up	19.45	19.45	20.95	16.02	Black

Table

-

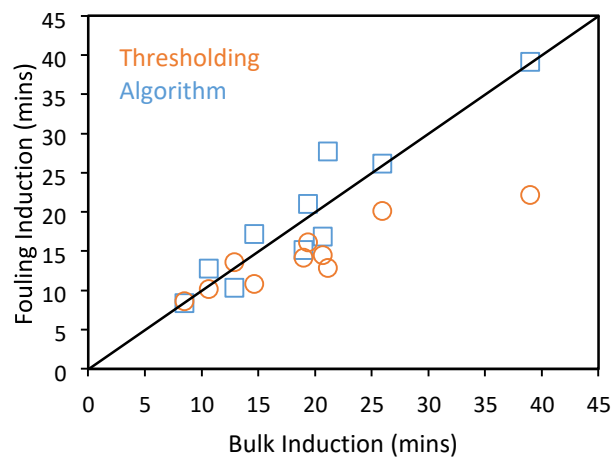


Figure 76. Correlation plot of Algorithm fouling induction time [□] vs. thresholding fouling induction time [○] for L-glutamic acid 42.39 g/L under oscillation conditions of 1 Hz 45 mm.

Table 9. Induction Times for L-Glutamic Acid 42.39 g/L [2 Hz 45 mm] with Crystallisation Temperature 30°C

	Induction Time (minutes)				
Date/Camera:	Combined	Bulk	Fouling: Algorithm	Fouling: Thresholding	
20.5.14 low	12.13	11.92	30.37	15.58	
20.5.14 up	14.95	14.85	18.25	24.98	
21.5.14 low	16.18	16.13	19.98	13.33	
21.5.14 up	18.78	18.78	18.73	6.18	
22.5.14 low	9.08	9.13	9.82	6.67	
22.5.14 up	8.3	8.2	12.68	6.72	
23.5.14 low1	16.53	16.63	19.52	10.47	
23.5.14 up1	15.27	14.8	15.93	10.97	
23.5.14 low2	12.63	12.58	12.78	8.85	
23.5.14up2	8.9	8.9	12.85	7.28	

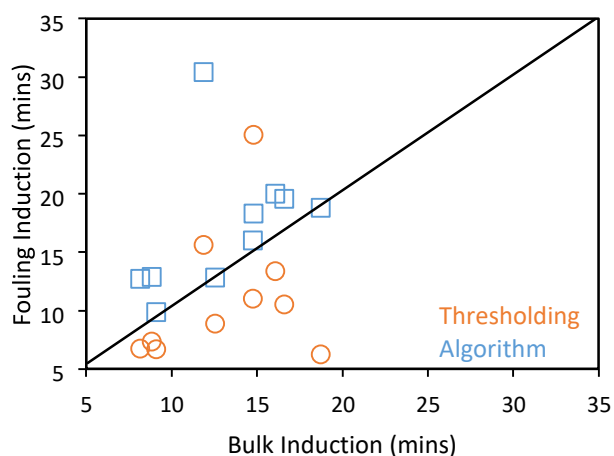


Figure 77. Correlation plot of Algorithm fouling induction time [□] vs. thresholding fouling induction time [○] for L-glutamic acid 42.39 g/L under oscillation conditions of 2 Hz 45 mm and crystallisation temperature 30°C.

Table 10. Induction Times for L-Glutamic Acid 42.39 g/L [1 Hz 45 mm] with Crystallisation Temperature 30°C

	Induction Time (minutes)				
Date/Camera:	Combined	Bulk	Fouling: Algorithm	Fouling: Thresholding	

Table . Induction Times for Glycine 384.51 g/L []

2.6.14 low	77.78	84.33	66.05	38.87	
2.6.14 up	73.52	69.25	68.87	39.87	
3.6.14 low	23.05	23.05	18.28	16.87	
3.6.14 up	19.83	19.37	21.83	20.45	
29.5.14 low	36.48	36.7	22.5	27.35	
29.5.14 up	26.08	24.25	20.82	23.18	
30.5.14 low	27	27	31.88	16.85	
30.5.14 up	26.68	25.1	30.03	16.32	

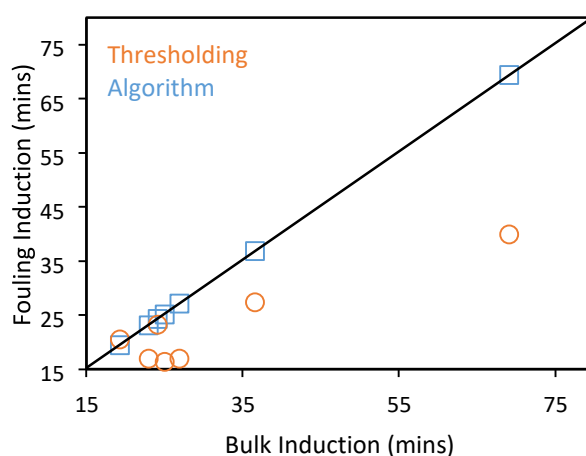


Figure 78. Correlation plot of Algorithm fouling induction time [□] vs. thresholding fouling induction time [○] for L-glutamic acid 42.39 g/L under oscillation conditions of 1 Hz 45 mm and crystallisation temperature 30°C.
11 1 Hz 23 mm

	Induction Time (minutes)				
Date/Camera:	Combined	Bulk	Fouling: Algorithm	Fouling: Thresholding	
2.2.15 low	51.97	51.97	42.97	51.98	
2.2.15 up	51.93	51.93	42.93	44.85	
4.2.15 low 2	44.27	44.27	25.13	49.27	
4.2.15 up 2	35.8	35.8	14.22	48.47	

6.2.15 low	49.65	49.65	52.63	51.4	
6.2.15 up	29.18	30.43	8.33	50.33	
10.12.14 low	43.17	43.17	77.85	85.37	
10.12.14 up	77.32	77.32	56.2	79.47	
11.12.14 low	54.67	54.83	71.4	111.23	
11.12.14 up	67.17	67.17	112.9	112.42	
20.1.15 low	55.4	55.4	55.52	56.73	
20.1.15 up	43.95	43.95	43.95	55.2	
21.1.15 low 1	39.57	39.4	38.93	42.37	
21.1.15 up 1	40.88	41.1	25.8	40.52	
21.1.15 low 2	59.95	60.43	49.35	58.9	
21.1.15 up 2	56.4	56.4	56.4	56.73	
22.1.15 low	22.08	22.08	22.33	24.35	
22.1.15 up	20.52	20.52	29.28	22.2	
3.2.15 low	47.9	48.17	15.37	47.13	
3.2.15 up	27.6	27.6	28.67	45.78	

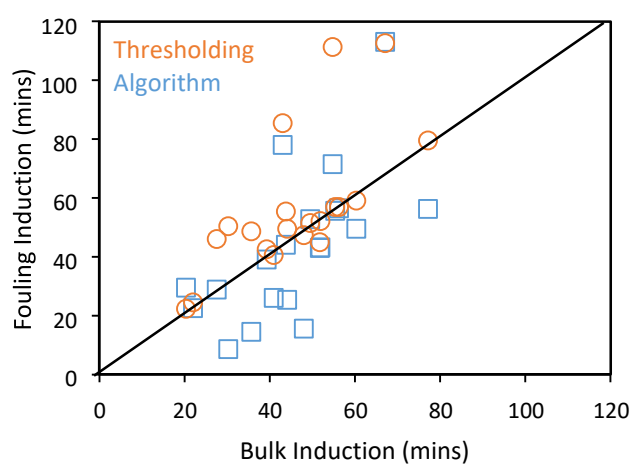


Figure 79. Correlation plot of Algorithm fouling induction time [□] vs. thresholding fouling induction time [○] for Glycine 384.51 g/L under oscillation conditions of 1 Hz 23 mm.

Table . Induction Times for Glycine 384.51 g/L []
12 2 Hz 45 mm

	Induction Time (minutes)				
Date/Camera:	Combined	Bulk	Fouling: Algorithm	Fouling: Thresholding	
9.10.14 low1	11.28	11.28	5.17	9.62	
9.10.14 up1	11	11	10.83	10.12	
9.10.14 low2	9.05	9.05	8.5	8.1	
9.10.14 up2	8.43	8.43	8.48	8.43	
10.10.14 up	13.42	13.42	12.85	12.17	
10.10.14 low	13.65	13.65	7	12.38	
13.10.14 low1	10.82	10.82	11.32	9.18	
13.10.14 up1	8.4	8.4	8.45	9.42	
13.10.14 low2	16.78	16.78	11.52	15.32	
13.10.14 up2	12.63	12.63	9.88	15.4	
14.10.14 low	15.2	15.2	16.38	13.88	
14.10.14 up	13.72	13.72	15.67	14.28	
16.10.14 low1	12.22	12.22	10.78	8.9	
16.10.14 up1	12.07	12.07	11.45	9.6	
16.10.14 low2	10.18	10.18	8.6	8.72	
16.10.14 up2	9.9	9.9	9.53	7.43	
17.10.14 low	10.35	10.35	9.12	9.85	
17.10.14 up	10.17	10.17	10.22	9.72	
20.10.14 up	10.95	10.9	10.48	9.07	
20.10.14 low	10.1	10.1	7.58	8.47	

Table . Induction Times for Glycine 384.51 g/L []

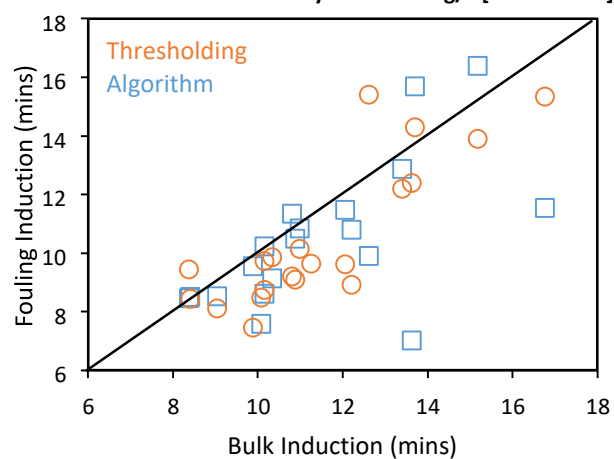


Figure 80. Correlation plot of Algorithm fouling induction time [□] vs. thresholding fouling induction time [○] for Glycine 384.51 g/L under oscillation conditions of 2 Hz 45 mm.

13

1 Hz 45 mm

	Induction Time (minutes)				
Date/Camera:	Combined	Bulk	Fouling: Algorithm	Fouling: Thresholding	
2.9.14 low	25.72	25.72	23.37	21.8	
2.9.14 up	24	24	22.12	21.8	
3.9.14 low1	15.5	15.5	12.65	13.33	
3.9.14 up1	13.8	13.75	13.55	11.88	
3.9.14 low2	25.6	25.53	6.98	23.33	
3.9.14 up2	23.3	23.33	23.08	22.57	
3.9.14 low3	23.07	23.07	21.65	21.03	
3.9.14 up3	21.93	21.87	21.3	21.3	
22.8.14 low1	22.27	22.27	3.7	20	
22.8.14 up1	19.62	19.62	17.62	20.63	
22.8.14 low2	24.1	24.1	14.1	21.37	
22.8.14 up2	11.92	11.8	21.19	22.05	
25.8.14 low	17.87	17.87	5.75	16.43	
25.8.14 up	15.77	15.72	16.33	16.38	
26.8.14 low	27.95	27.95	4.8	26.18	
26.8.14 up	26.28	26.18	26.23	24.87	
27.8.14 low	45.38	45.43	38.35	42.87	

Table . Induction Times for Glycine 384.51 g/L []

27.8.14 up	43.65	43.55	43.03	42.62	
29.8.14 low	52.02	52.02	50.57	50	
29.8.14 up	51.02	51.02	50.33	49.53	

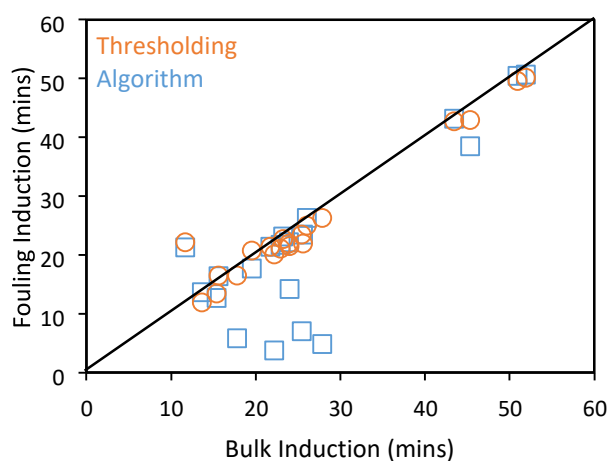


Figure 81. Correlation plot of Algorithm fouling induction time [□] vs. thresholding fouling induction time [○] for Glycine S=1.8 under oscillation conditions of 1 Hz 45 mm.

14

2 Hz 23 mm

Date/Camera:	Combined	Bulk	Fouling: Algorithm	Fouling: Thresholding	
1.12.14 low1	18.78	18.8	19.77	16.5	
1.12.14 up1	17.83	17.83	18.82	16.4	
1.12.14 low2	26.75	26.7	20.05	24.38	
1.12.14 up2	23.98	23.98	18.18	24.45	
3.12.14 low1	28.85	28.85	24.32	27.27	
3.12.14 up1	27.98	27.98	28.23	28.08	
[3.12.14 low2	dark	dark	dark	dark	
3.12.14 up2	18.93	18.93	18.58	16.48	
4.12.14 low1	39.68	39.68	37.92	26.55	
4.12.14 up1	39.32	39.2	26.43	39.37	
4.12.14 low2	35.42	35.42	32.38	31.88	
4.12.14 up2	34.7	34.48	34.12	34.58	

Table . Induction Times for Glycine 384.51 g/L []

25.11.14 low1	32.03	32.03	32.82	29.92	
25.11.14 up1	31.18	31.18	30.72	33.35	
25.11.14 low2	20.28	20.28	21	17.95	
25.11.14 up2	18.37	18.37	18.93	17.87	
27.11.14 low1	21.9	21.85	22.85	19.82	
27.11.14 up1	15.58	15.58	20.87	19.87	
27.11.14 low2	14.23	14.23	13.32	11.08	
27.11.14 up2	5.73	5.73	8.78	10.78	

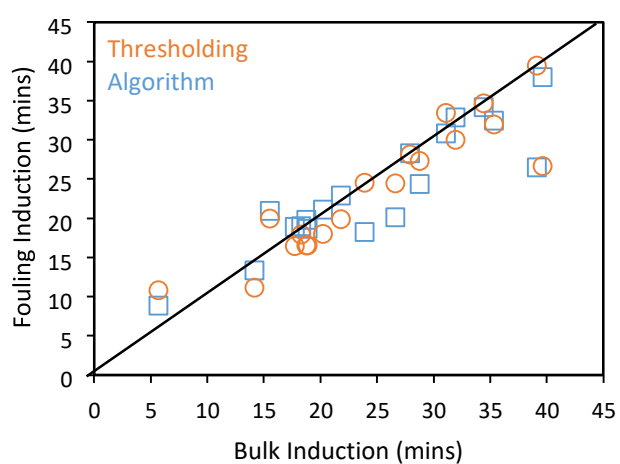


Figure 82. Correlation plot of Algorithm fouling induction time [□] vs. thresholding fouling induction time [○] for Glycine 384.51 g/L under oscillation conditions of 2 Hz 23 mm.

7.7 DISCUSSION OF THE MOVING FLUID OSCILLATORY BAFFLED CRYSTALLISER RESULTS

7.7.1 Average Pixel Intensities vs. Time

On further inspection of the average pixel intensity plots of the 42.39 g/L experiments for L-glutamic acid ($S=6$), some clear differences were seen with regards to the oscillation conditions. There was a notable difference between frequencies of oscillation. Decreasing the frequency from 2 to 1 Hz resulted in the fouling induction time increasing from 9.5 to 14.2 minutes on average (taking into account all upper and lower camera values).

Larger frequency increased the shear and eddies within the MFOBC and appears to promote nucleation when compared to lower frequency. This effect can be expected to be independent of whether nucleation occurs on the glass surface or in the bulk liquid first, as both will be enhanced by increased agitation within the fluid. Other studies by Kumaraswamy et al. [105], Koscher et al. [106], Jawor-Baczynska et al. [35] and Forsyth et al. [11] report findings of increased shear rate increasing the rate of crystallisation.

The differences between the 1 Hz data from the 2 Hz data reveal two further points:

- 1) The maximum average pixel intensities for the 2 Hz experiments are larger on average owing to the greater amount of fouling which forms (the crystals appear brighter on the glass wall as they are more in focus).
- 2) The initial slopes of the curves are steeper for the 2 Hz experiments as nucleation and growth and/or fouling all take place at a greater rate.

Data for 28.26 g/L solutions ($S=4$) were found to follow the same trends as described for the 42.39 g/L data. On average the fouling induction time was 75.43 mins for the higher frequency and 127.1 mins for the lower frequency.

The induction times shown for the experiments performed at 30°C were longer and the slopes of the graphs were shallower when compared to the runs at 20°C. The maximum pixel intensities are also lower on average at 30°C than for those at 20°C.

This shows that nucleation takes longer at the higher temperature and the resulting crystallisation and fouling is less than when 20°C is used. The rate of crystallisation and fouling is also reduced when using the higher temperature. These results were expected due to the lower supersaturation achieved with the higher temperature and they show that the imaging technique was sensitive enough to detect that.

For the glycine experiments there were similar findings where gradients of the average pixel intensity curves were steeper with increasing either the amplitude or the frequency or both. This meant faster nucleation and growth took place due to the increased agitation caused by the amplitude and/or frequency increase. The same trends were apparent for the different pairings of conditions i.e. comparing frequencies when 23 mm amplitude is kept constant and comparing amplitude when 1 Hz frequency is kept constant.

This reinforces the fact that the change in oscillation has a noticeable effect on the crystallisation behaviour both in the bulk and on the glass surface.

7.7.2 Estimation of Fouling Induction Times Using Graphical User Interface Algorithm

When the Fouling Graphical User Interface (FoulingGUI) algorithm was used with real experimental data flagged up some disadvantages and points that were highlighted in the results section.

The difficulties appeared when spikes occurred in the image set due to uncontrolled lighting issues. This could involve light changes in the laboratory as the MFOBC reflects light despite the areas where the cameras reside being boxed in. The curvature of the glass and the arrangement of the baffles aid in the internal reflection of light in the system. Bubbles occurring either in the bulk fluid or in the jacket fluid

also caused light fluctuations from time to time. Strong reflections on the glass from the LED torches could also feed false information to the algorithm since it is missing the human input to distinguish between true crystals and scratches or reflections on the glass. These issues can help explain the spikes in the data giving false results for the induction time from the algorithm as it does not have any method of background subtraction to eliminate noise or initiative to ignore scratches which become enhanced due to light fluctuations. Such issues are easier to realise when using the thresholding method mentioned previously.

The fact that a smaller region of the image was used for the algorithm meant that sometimes the true fouling induction time of that cell in the MFOBC was missed. It can be seen however that if the image set is of good quality then the two methods were comparable meaning that the algorithm can be used in real life crystallisation situations if the conditions are well controlled.

The issues shown in the key and highlighted in the tables and graphs in section 7.6 show spiking issues highlighted in green. This meant that the values obtained for the fouling and/or bulk induction times were estimated incorrectly as a spike too early on in the data set to be the correct induction time. This is taken as the sharpest change and hence calculated as the induction time from the change point detection method.

All experiments highlighted in red indicated runs where the fouling appeared to occur on the glass wall before bulk nucleation according to the bulk induction time obtained from the FoulingGUI algorithm. These could present data sets which may be of interest for further study for pure fouling with bulk nucleation being delayed.

Experiments highlighted in yellow showed data which the algorithm could not seem to analyse and chose the last image in the data set as either the fouling, bulk or both induction times. This mainly seemed to be caused by larger change points being created after the true induction period had passed.

Region selection issues within the image were shown in blue. This issue arises due to choice of the window of analysis. The thresholding method involved the entire cell of the MFOBC being scanned, whereas the algorithm scanned a much smaller area and could therefore miss the true fouling induction within that cell.

The experiments which were highlighted in black showed good agreement between both methods for determining the fouling induction time.

The rest of the tables and figures in that section showed that some conditions were more suited to the algorithm method than others, the correlation plots illustrate this and aid in the visualisation of the comparison between the two methods.

The agreement between the two methods was better for the glycine experiments compared to the L-glutamic acid ones. This could be due to the difference in concentrations being used in each case. The solubility of glycine is much higher in water than that of L-glutamic acid and so there was a much larger potential mass of crystals being produced in the MFOBC with glycine. This greater number of crystals would be brighter and hence would be picked up more clearly by the webcam and in turn producing a better image data set. The better the data set and the clearer the crystals are in the images the better the FoulingGUI works and so the agreement between the thresholding and algorithm methods is better.

7.7.3 Estimation of Nucleation Kinetics

When analysing the ter Horst model fits that were carried out, it was evident that there was a general trend of decreasing growth time with increasing nucleation rates for both glycine and L-glutamic acid. The expected trend of nucleation rates increasing with increased concentration and increased frequency of oscillation were evident for both compounds as well. Each case provided more favourable conditions for nucleation events to occur. With increased concentration, more solute molecules were present in solution and hence the chance of successful and stable nuclei formation was increased. The step up in frequency from 1 to 2 Hz created a more

vigorous mixing environment for the solute molecules. In turn the turbulent forces in the liquid enhanced the probability of molecular collisions. When a stable nucleus formed, this increase in mixing reduced the diffusivity layer which meant that further molecular attachment to the nucleus was simpler as the resistance to attachment was lowered. This was true for both glycine and L-glutamic acid.

The trends in the nucleation rate and growth time reflect the hypothesis related to the effect oscillation has on the fouling induction times. When focusing on the glycine experiments, it was found that changing the amplitude by 22 mm had approximately the same effect on the J and t_g values as changing the frequency by 1 Hz. This suggests that perhaps amplitude and frequency hold the same effect over the fouling process under these conditions when they are altered by certain amounts. However, more work would be required to confirm this.

7.8 CONCLUSIONS FROM MOVING FLUID OSCILLATORY BAFFLED CRYSTALLISER EXPERIMENTS

The average pixel intensity graphs along with the plots of fouling induction time vs. experimental conditions show the key results. When the frequency or amplitude or concentration was increased, the fouling induction time decreased. This was also accompanied by an increase in the maximum pixel intensity and a steeper gradient in the average pixel intensity curve. This shows that the fouling and bulk crystallisation was faster and that more substance was found on the glass wall. When the temperature of the cold straight was increased the fouling induction was increased and the opposite was true of the average pixel intensity curves.

The Fouling Graphical User Interface (FoulingGUI) had advantages and disadvantages associated with it, most of which surrounded the image quality. The algorithm behind the FoulingGUI could not deal well with lighting issues, reflections, bubbles in the jacket fluid, and scratches on the glass surface and had no method of background subtraction to help minimise these issues. In order to deal with these issues, a smaller region of the image had to be used and hence only a limited subset of data was used.

However, it was a successful way to separate the bulk from surface induction time and the agreement between experimental and FoulingGUI was good when a good quality image set was obtained. The GUI seemed to work better with glycine, probably due to its higher solubility and there being more solid particles present within the crystalliser for the webcam to pick up and so the results were clearer.

The ter Horst model backed up the raw experimental data in that decreased growth time accompanied an increase in nucleation rate with increasing supersaturation for both compounds. The nucleation rate increased with increasing concentration, frequency and amplitude of oscillation despite fewer repetitions being carried out that would be desired. The methods developed in this work present new tools for monitoring fouling on crystalliser vessel walls. They allow to separately observe induction times for bulk and surface nucleation, and thus study fouling mechanisms in more depth using *in-situ* monitoring during real crystallisation processes.

8 LIGHT SCATTERING MEASUREMENTS

8.1 CHAPTER OUTLINE

Chapter 8 describes in detail the systems that were chosen for this study and the conditions used for light scattering measurements carried out with glycine and urea solutions. All results are presented in this chapter. Dynamic light scattering (backscattering angle of 173°) with the Malvern Zetasizer and Brownian microscopy with the NanoSight software were used to obtain particle sizes of the nanospecies (mesoscale clusters) present in supersaturated and undersaturated solutions of glycine and urea where the effect of changing temperature was investigated. All experimental conditions are summarised in Table 15:

Table 15. Summary of all Light Scattering Experimental Conditions

Compound	Concentration (g/L)	Filtration	DLS Temperature Range (°C)	NanoSight Temperature Range (°C)
Glycine	154.90	Unfiltered	10-80-10	15-50-15
		PTFE		
	234.98	Unfiltered		
		PTFE		
	299.06	Unfiltered	30-80-30	30-50-30
		PTFE		
Urea	522.61	Unfiltered	10-80-10	15-50-15
		PTFE		
	785.15	Unfiltered		
		PTFE		
	1149.74	Unfiltered	50-80-30	
		PTFE		

8.2 SYSTEMS USED IN PRENUCLEATION STUDY

The two systems used in the prenucleation study were aqueous solutions of glycine and urea. These systems have been investigated previously and are known to exhibit

clustering behaviour. Solubility data was also easily accessible. L-glutamic acid was not chosen for this study as the solubility of this substance in water was low, so that the signal detected in the NanoSight experiments was too low.

Concentrations of aqueous glycine that were used in this work were 154.9, 234.98 and 299.06 g/L. The solubility of glycine was taken from literature [104] and is shown in Figure 83.

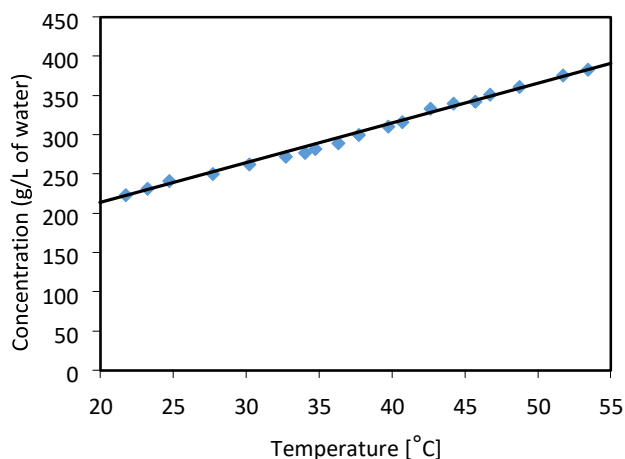


Figure 83. Solubility of glycine in water [104].

The molecular structure of urea is shown in Figure 84.

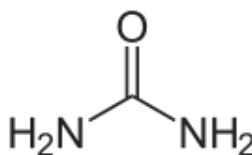


Figure 84. Molecular structure of urea.

The concentrations of urea that were used were 522.61, 785.15 and 1149.74 g/L and the solubility taken from literature [107] is given in Figure 85.

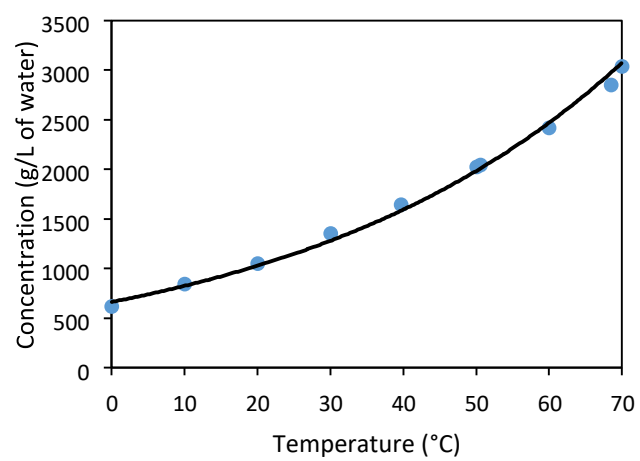


Figure 85. Solubility of urea in water [107].

8.3 TEMPERATURE CYCLE EXPERIMENTAL PROCEDURES

8.3.1 Experimental Conditions

Undersaturated and supersaturated solutions of glycine and urea were tested in light scattering temperature cycle experiments to analyse the effect of temperature change on the mesoscale clusters in solution with and without filtering.

The temperature cycles had different ranges depending on the equipment being used. NanoSight had temperature limitations due to the method of temperature control and so the temperature cycle could only range from 15 to 50°C. The Zetasizer had a much larger temperature range and so a maximum temperature cycle from 10 to 80°C was used.

Hydrophobic polytetrafluoroethylene (PTFE) syringe filters with 0.1 µm pore diameter were used.

Solutions were prepared within an incubator set to 60°C which in reality provides an environment of approximately 50°C due to heat losses through the door panel. Table 16 summarises the concentrations used for the aqueous glycine and urea solutions. These concentrations were chosen specifically due to the supersaturation considerations. The low concentration of glycine was chosen to have a supersaturation value of 0.95 based on solubility at 10°C so that at the lowest point in the temperature cycle (10°C) the solution would be undersaturated and hence crystallisation was always impossible. The medium concentration of glycine was chosen to have supersaturation 1.1 based on 20°C – in other words close to saturated and therefore crystallisation would be prolonged so that measurements of the solution properties could be made. The high concentration of glycine was chosen based on how high it could be pushed while still eliminating crystallisation in the equipment – in this case the concentrations had supersaturation values of 1.4 based on their solubility at 20°C. For urea solutions, the crystallisation was much quicker and some difficulties were observed when using supersaturation 1.1 based on 20°C. Sometimes this would spontaneously nucleate before measurements could be made.

This was deemed the highest concentration. The medium concentration had supersaturation 0.95 at 10°C and the lowest concentration has supersaturation 0.5 based on solubility at 20°C.

Table 16. Summary of Concentrations Used for Aqueous Glycine and Urea

System	Low Concentration (g/L water)	Medium Concentration (g/L water)	High Concentration (g/L water)
Glycine	154.90	234.98	299.06
Urea	522.61	785.15	1149.74

The required amount of glycine or urea was weighed into a 50 ml glass bottle with 25 ml of Millipore distilled water and left to stir in the incubator for at least 3 hours. The incubator takes approximately 45 minutes (see Figure 86) to reach a steady state temperature, however the supersaturations being used were so low that the solution visibly dissolves well before the 3 hour minimum stirring period. Figure 86 shows that the temperature of 60°C was never reached and this was with the incubator door closed.

The thermocouple was placed in the centre of the incubator to record the most accurate temperature possible as this was where the stirrer plate would be placed.

The system is not 100% sealed to the outside environment and therefore some heat losses are inevitable. When experiments were running, a cable to operate the stirrer plate was passed through the incubator door creating a small gap. This accounts for the further heat losses in the incubator resulting in the average temperature inside only reaching ~ 55°C despite the set point being 60°C.

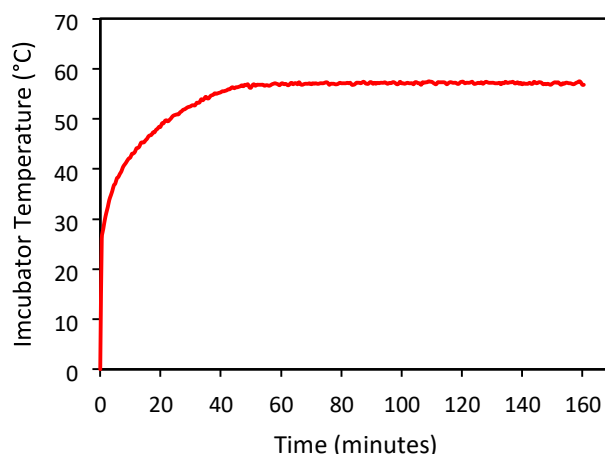


Figure 86. Incubator temperature profile determining the point where a steady state temperature is achieved within the incubator after ~45 minutes with no partial opening of the incubator door.

All filters, syringes and cuvettes were preheated and then the solution was either transferred directly to the NanoSight or placed in a quartz cuvette for dynamic light scattering (DLS) analysis in the Zetasizer. Filtering was carried out inside the incubator prior to transferring the solution to the NanoSight instrument or the cuvette for DLS measurements in the Zetasizer.

8.3.2 Dynamic Light Scattering Experiments with Zetasizer

A larger range of temperatures were available with the Zetasizer than with the NanoSight and as aqueous solutions were being used it was desirable to stay well below the boiling point so as to limit evaporation. The temperature cycle chosen is depicted in Figure 87.

The solution was transferred to the quartz cuvette, covered in a plastic cap to reduce evaporation effects (if any – none were observed), placed in the Zetasizer and the same standard operating procedure (SOP) was used each time just with the temperature being altered after each measurement.

The solution was first measured at 10°C then up to 80°C in steps of 10°C and back down to 10°C again in the same manner to test the reversibility of the system.

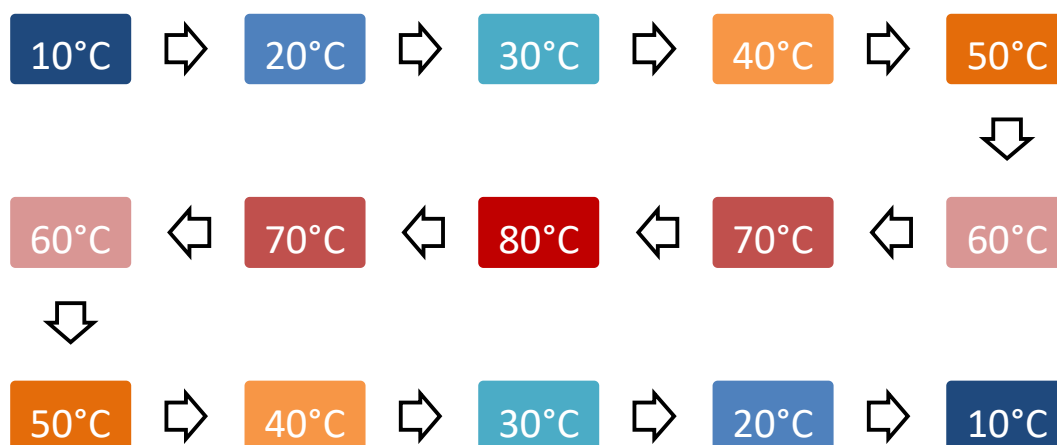


Figure 87. Temperature cycle in the Zetasizer for dynamic light scattering experiments for exploring the temperature effects on mesoscale cluster size and concentration and whether or not they are reversible.

At each temperature 10 runs with a duration of 10 seconds were carried out and this procedure was repeated 3 times to give average autocorrelation functions at each stage in the cycle. With each change in temperature the solution was allowed to equilibrate for 2 minutes before any measurement was taken. It was these average autocorrelation plots that were then analysed further to obtain the particle sizes, after determining the decay rates.

Note that even when supersaturated solutions were used (based on their solubility at 20°C) there was no crystallisation taking place when the temperature was reduced to 10°C as the time taken for an un-sheared solution of glycine or urea to crystallise is in general longer than the measurement period.

Crystallisation was never taking place in any of the experiments analysed in this work, and if in the rare occasion this did occur the experiment would be repeated with new solution. This was verified through the light scattering measurements. If any crystals were forming in the sample, the intensities of the light being scattered would increase

significantly and this was never the case. Visual observation of the sample at the lowest temperature also confirmed that no visible crystals of were present.

8.3.3 Brownian Microscopy Experiments with NanoSight

In these experiments, the temperature capabilities were more limited and hence the same temperature cycle as was used in the Zetasizer could not be replicated. The same procedure was carried out but with temperatures ranging from 15-50°C as is shown below in Figure 88.

15°C was chosen as the starting point as this was the lowest temperature that could be reached without the temperature becoming unstable – i.e. it could not reach its set point.

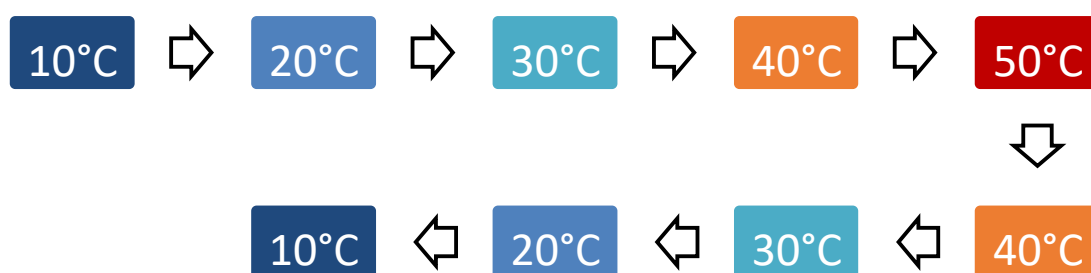


Figure 88. Temperature cycle in the NanoSight for Brownian motion experiments for exploring the temperature effects on mesoscale cluster size and concentration and whether or not they are reversible.

After the solution was transferred into the cell, the temperature of the stage was set to the desired value and allowed to equilibrate for 2 minutes. After this period, the camera settings were adjusted to the automatic option to optimise the screen gain and camera level and the measurements were run.

For each measurement at each temperature, 3 videos of duration 20 seconds were recorded and analysed so that an average particle size distribution based on number concentration could be obtained. After a few experiments this was increased to 5 videos with duration 60 seconds to obtain more robust data.

8.4 LIGHT SCATTERING MEASUREMENTS FOR WATER

In order to have a reference for all future light scattering measurements for aqueous glycine and urea solutions, unfiltered water taken from the in-house Millipore water

purification system was exposed to the same temperature conditions. This was the same water used to prepare all aqueous glycine and urea solutions. The results are presented here. Only the heating stage was carried out in each case: 10-60°C for dynamic light scattering and 15-50°C for NanoSight measurements. The autocorrelation functions obtained are given in Figure 89.

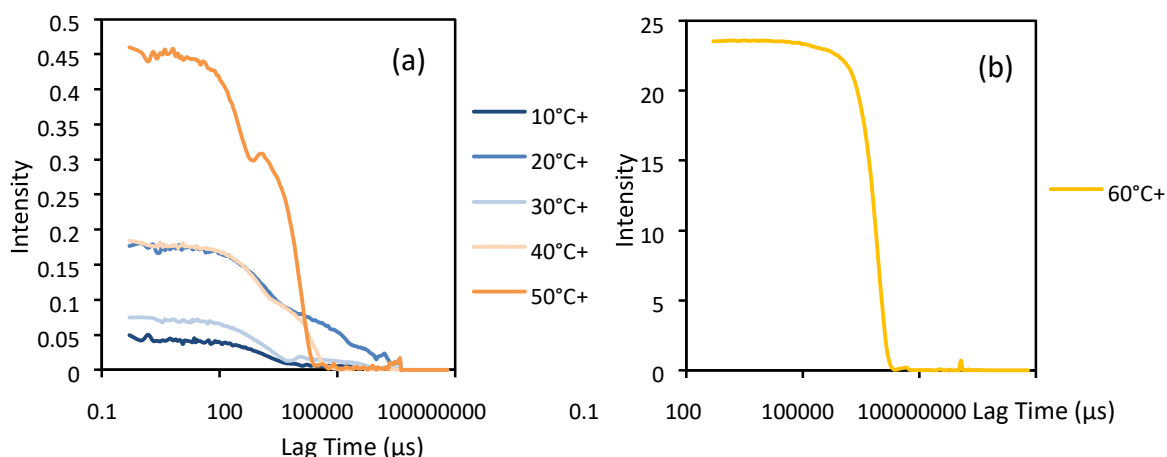


Figure 89. Autocorrelation functions for unfiltered water during heating from 10 to 50°C (a) and 60°C (b).

The heating stage was stopped at 60°C because dissolved oxygen emerged from the solution and bubbles remained on the quartz cuvette wall. This did not happen with any glycine or urea solutions. Part (b) of Figure 89 shows the sharp increase in intensity caused by the presence of bubbles. However the data from the 10-50°C heating stage shows low intensities for the unfiltered water compared to the intensities for the unfiltered solutions.

Below in Figure 90 is the average mean count rate plotted against temperature for this unfiltered water experiment. The values obtained here are significantly lower than any values obtained for the glycine or urea solutions.

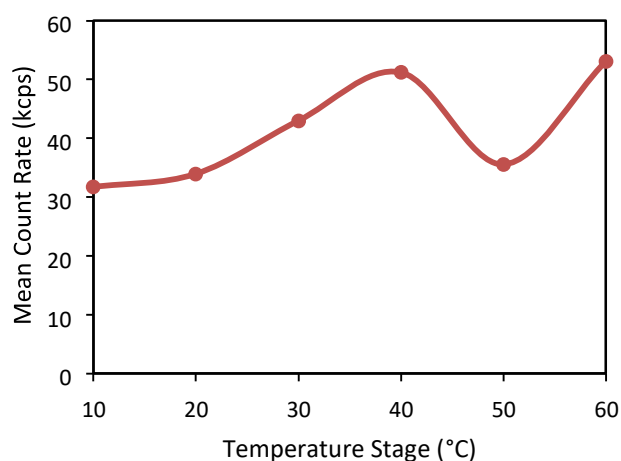


Figure 90. Mean count rate for unfiltered water during the heating stage from 10 to 60°C.

Filtered water could not be run in the Zetasizer because no autocorrelation function was obtained and hence the data could not be processed. This meant that the water was clear of any significant species.

The particle size distribution from the NanoSight experiment are shown in Figure 91 for the unfiltered water. The particle concentrations are again lower than those observed for glycine or urea solutions and the shift to larger sizes with increasing temperature is not observed.

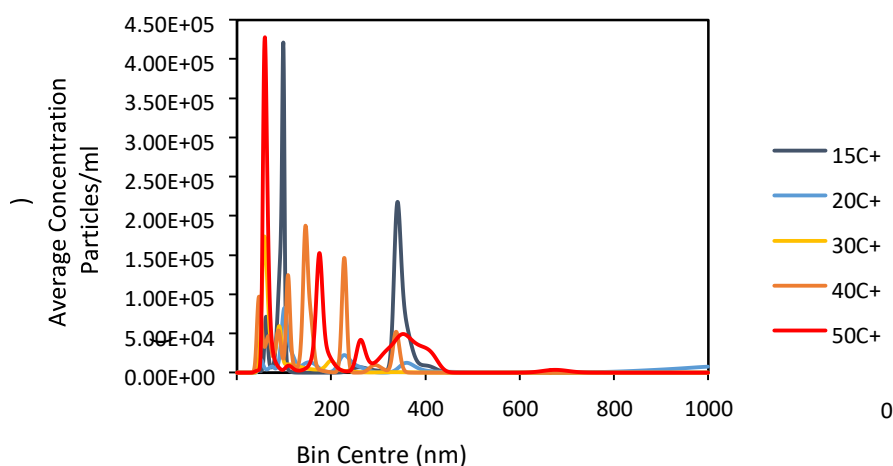


Figure 91. Particle size distributions from NanoSight measurements of unfiltered water during the heating stage from 15 to 50°C

8.5 GLYCINE SOLUTIONS DYNAMIC LIGHT SCATTERING RESULTS

This section gives all experimental data from dynamic light scattering for the 3 concentrations of aqueous glycine solution with and without filtration with the 0.1 μm PTFE syringe filter. The first and second runs of the solutions are presented throughout this chapter.

8.5.1 Glycine Solutions Autocorrelation Functions

The autocorrelation functions are the raw data obtained from the measurements. It is a measure of fluctuations of the scattered light intensity over time as species move in and out of the laser beam over time as described in Chapter 3. Raw data is only presented for the first repetition as the trends are similar for the second run. The autocorrelation functions for the repetition are given in section 10.1 (Appendix).

8.5.1.1 Unfiltered Glycine Solutions 154.9 g/L

Unfiltered glycine solutions with concentration 154.9 g/L yielded the autocorrelation functions given in Figure 92.

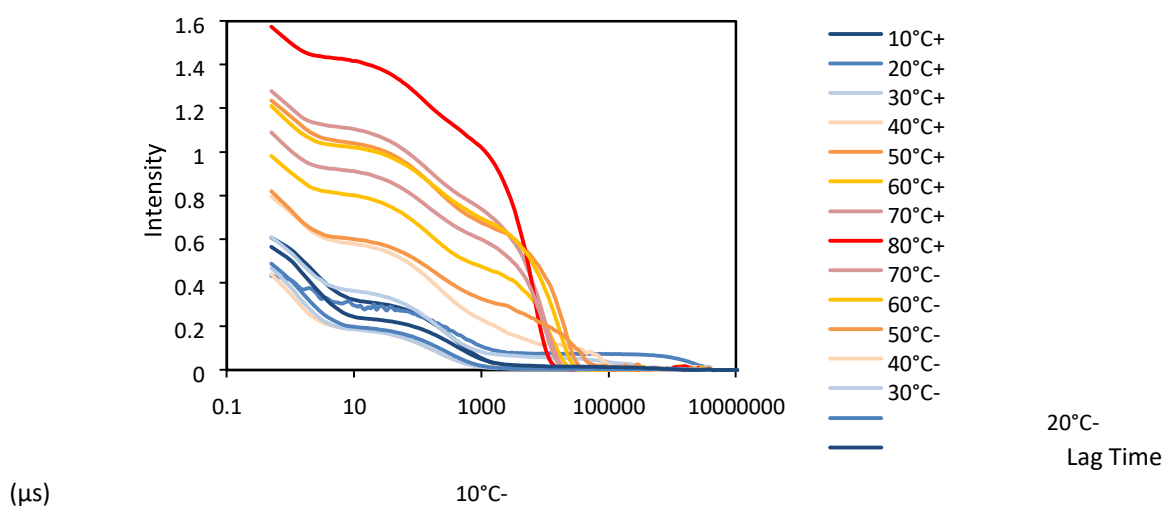


Figure 92. Autocorrelation functions from dynamic light scattering measurements (angle 173°) of temperature cycle from 10-80-10°C with the first run of unfiltered aqueous glycine solution of concentration 154.9 g/L which is undersaturated at 10°C (at this temperature the solution has supersaturation value of $S=0.95$).

It can be seen that as the temperature was increased from 10 to 80°C, the autocorrelation functions not only increased in intensity but after approximately 30°C in the heating stage, a 3rd decay becomes apparent in the functions. This extra decay at longer lag times persists until 30°C is reached again in the cooling stage where the functions return to exhibiting 2 decays. The reversibility of the temperature cycle is evident here as the heating and cooling as the 10°C functions for heating and cooling match each other fairly well. This experiment experienced a sudden drop in mean count rate at 20°C during the heating stage as can be seen from Figure 93 below:

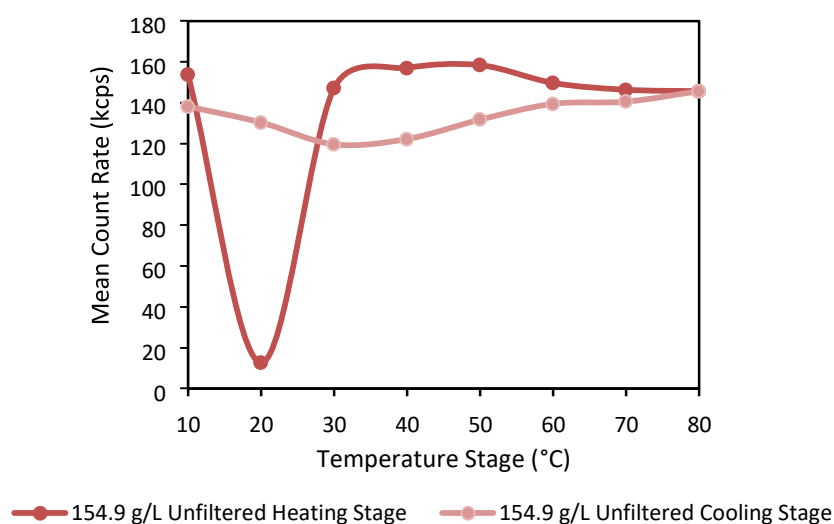


Figure 93. Mean count rate recorded in kilo counts per second for the temperature stages during the dynamic light scattering measurements for glycine concentration 154.9 g/L for unfiltered solution where dark red is the heating stage and light red is the cooling stage.

The experiment was repeated and the autocorrelation functions obtained from the repetition are shown in Figure 94. It can be seen here that the drop at 20°C is no longer present and hence must have been an artefact before.

8.5.1.2 Repeat of Unfiltered Glycine Solutions 154.9 g/L

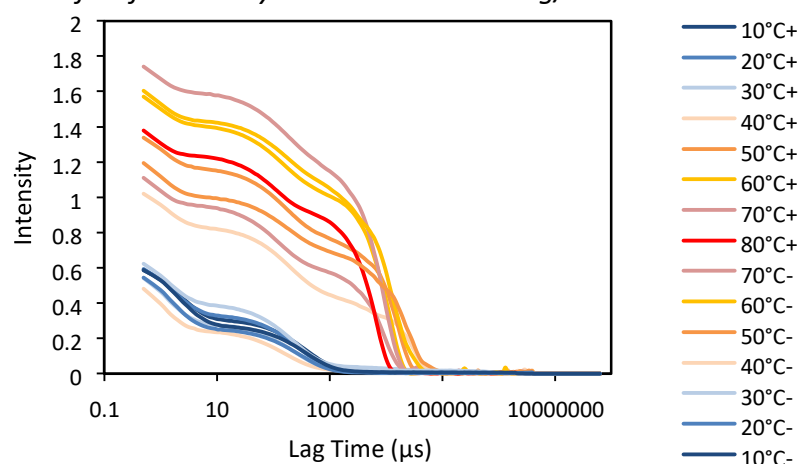


Figure 94. Autocorrelation functions from dynamic light scattering measurements (angle 173°) of temperature cycle from 10-80-10°C with unfiltered aqueous glycine solution of concentration 154.9 g/L which is undersaturated still at 10°C (at this temperature the solution has supersaturation value of $S=0.95$).

As before, the same pattern can be seen with regards to intensity and the presence of the 3rd decay after temperatures of 30°C during the heating and cooling stage.

8.5.1.3 0.1 μm PTFE Filtered Glycine Solutions 154.9 g/L

The same concentration of glycine was then filtered with the 0.1 μm PTFE syringe filter and ran through the same procedure of temperature cycling with the Zetasizer. The autocorrelation functions are given in Figure 95 where an enlarged image of the y-axis is shown.

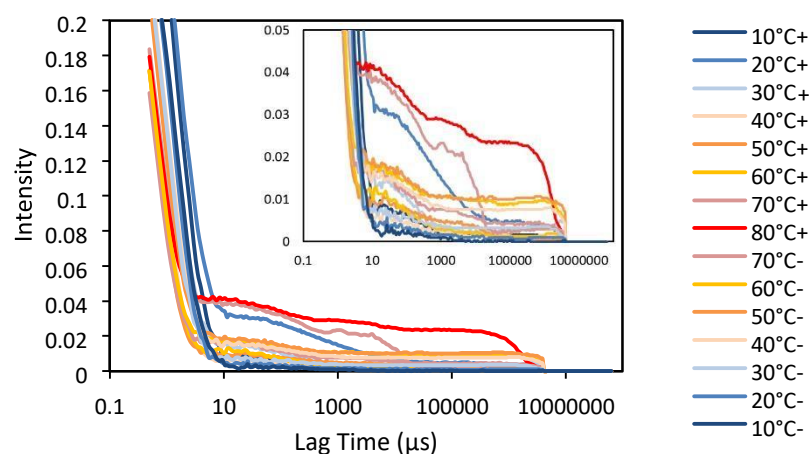


Figure 95. Autocorrelation functions from dynamic light scattering measurements (angle 173°) of temperature cycle from 10-80-10°C with aqueous glycine solution of concentration 154.9 g/L which is undersaturated still at 10°C (at this temperature the solution has supersaturation value of $S=0.95$). This solution was filtered through a PTFE syringe filter with pore diameter 0.1 μm . The graph section in the top right corner shows a zoomed image of the y-axis on the scale from 0 to 0.05 to show the separation of the autocorrelation functions more clearly.

After filtration, the intensities drop significantly for this concentration however the same pattern can be seen from the enhanced image whereby larger intensities are present. The existence of the 3rd decay at higher temperatures is less obvious here.

The mean count rates vs. temperature for both repetitions with the 154.9 g/L are shown in Figure 96.

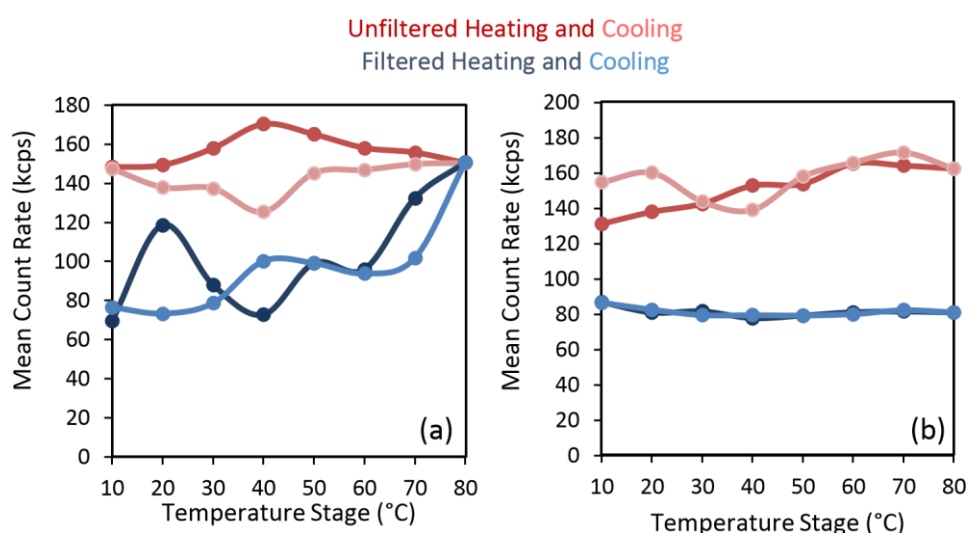


Figure 96. Mean count rate recorded in kilo counts per second for each temperature stage during the dynamic light scattering measurements for glycine concentration 154.9 g/L both for unfiltered (red) and 0.1 μm PTFE

filtered (blue) solution and for the first (a) and second (b) repetition. The heating stages are presented in the darker colour.

8.5.1.4 Unfiltered and 0.1 μm PTFE Filtered Glycine Solutions 234.98 g/L

Figure 97 depicts the autocorrelation functions for both the filtered and unfiltered temperature cycles of aqueous glycine of concentration 234.98 g/L which has supersaturation 1.1 at a temperature of 20°C.

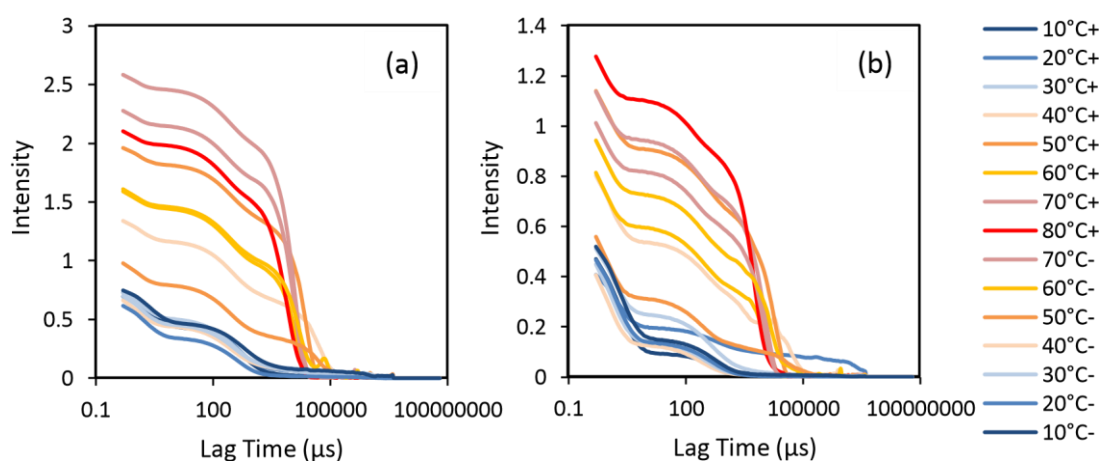


Figure 97. Autocorrelation functions from dynamic light scattering measurements (angle 173°) of temperature cycle from 10-80-10°C with unfiltered (a) and 0.1 μm PTFE syringe filtered (b) aqueous glycine solution of concentration 234.98 g/L.

It is clear again that the same pattern of increased intensity and 3rd decay occurs at temperatures above 30°C on the heating and cooling regions of the cycle.

The filtered 234.98 g/L sample was repeated due to concerns over the filter being faulty. The autocorrelation functions for this repetition are represented in Figure 98.

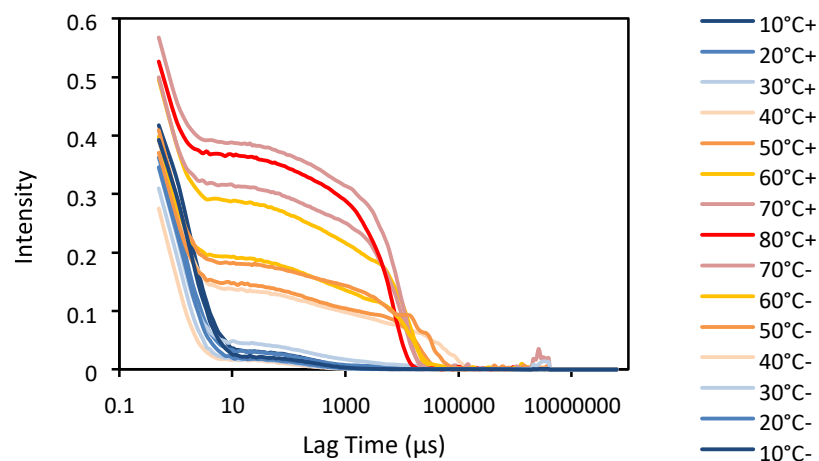
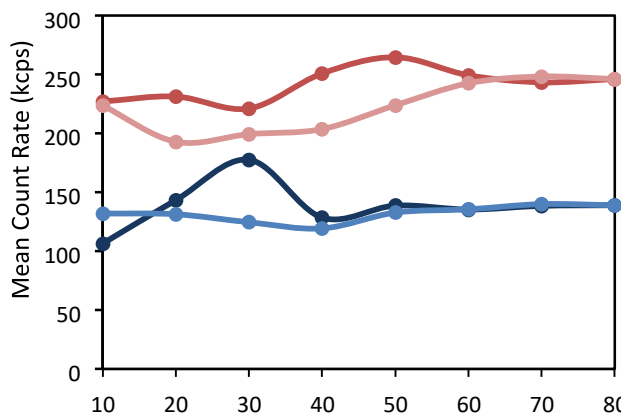


Figure 98. Autocorrelation functions from dynamic light scattering measurements (angle 173°) of temperature cycle from 10-80-10°C with aqueous glycine solution of concentration 234.98 g/L. This solution was filtered through a PTFE syringe filter with pore diameter 0.1 μm.

Slightly lower intensities were observed in this repetition, however the same patterns observed with the 154.9 g/L solutions are evident.

The mean
the
for the
for the
unfiltered
given in
100 gives the
except this is
of the filtered sample.



count rates over
temperature range
234.98 g/L solution
filtered and
conditions are
Figure 99. Figure
same information
with the repetition

Unfiltered Heating and Cooling
Filtered Heating and Cooling

Temperature Stages (°C)

Figure 99. Mean count rate recorded in kilo counts per second for each temperature stage during the dynamic light scattering measurements for glycine concentration 234.98 g/L both for unfiltered (red) and 0.1 μm PTFE filtered (blue) solution. The heating stages are presented in the darker colour.

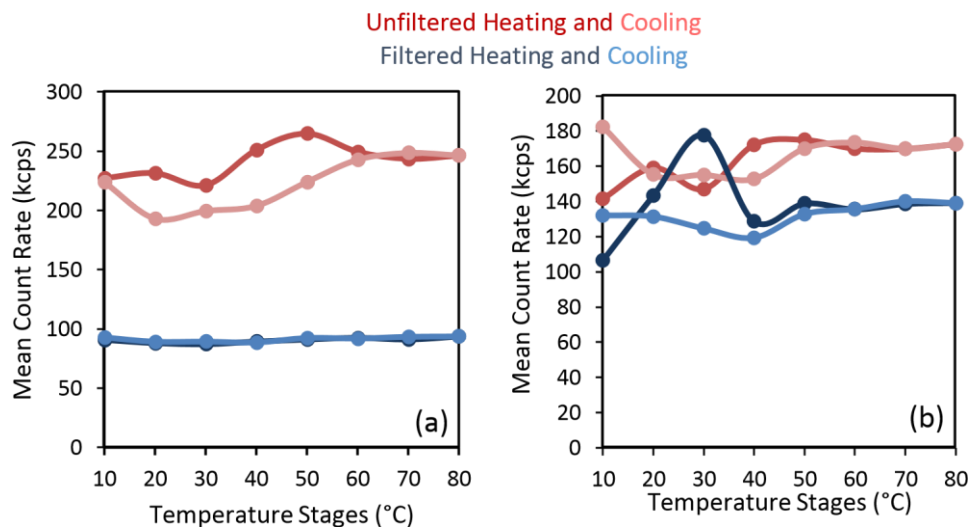


Figure 100. Mean count rate recorded in kilo counts per second for each temperature stage during the dynamic light scattering measurements for glycine concentration 234.98 g/L both for unfiltered (red) and 0.1 μm PTFE filtered (blue) solution when the solution was filtered again due to unusual high autocorrelation function diameters previously (a) and (b) shows the second run of the data. The heating stages are presented in the darker colour.

Overall, the mean count rates for the filtered samples are lower than the unfiltered in both cases.

8.5.1.5 Unfiltered and 0.1 μm PTFE Filtered Glycine Solutions 299.06 g/L

Next are the results from the highest concentration used (299.06 g/L), the filtered and unfiltered results with a zoomed view of the filtered results to give clarity are shown in Figure 101. The temperatures below 30 °C are not present, this was due to unwanted crystallisation taking place due to the higher supersaturation ($S=1.4$ based on 20 °C).

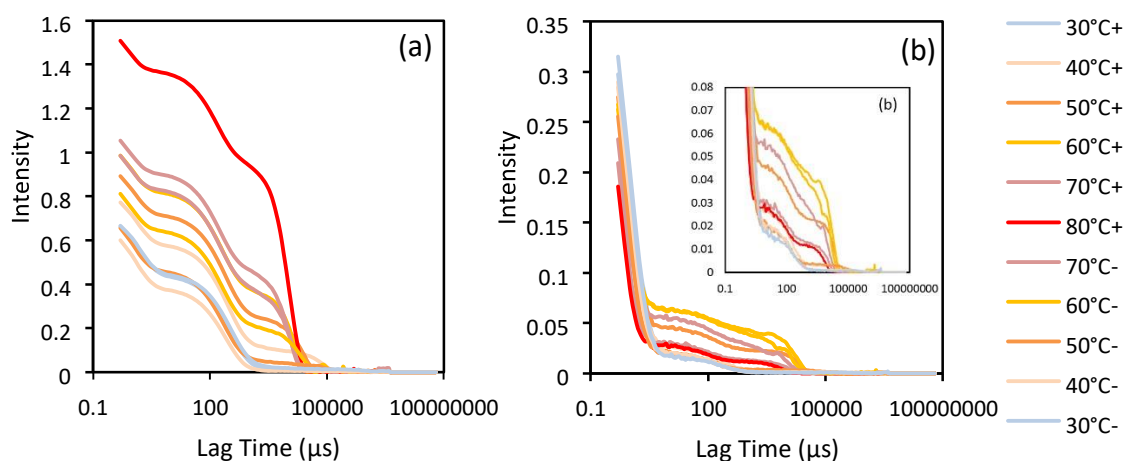


Figure 101. Autocorrelation functions from dynamic light scattering measurements (angle 173°) of temperature cycle from 30-80-30°C with aqueous glycine solution of concentration 299.06 g/L both unfiltered (a) and 0.1 μm PTFE filtered (b). An enhanced view of the y-axis zoomed to scale 0 to 0.08 is given in (b) for a more detailed view.

The same trends are present for this concentration as well. The filtered sample however, has much lower intensities akin to the 154.9 g/L solution. The zoomed image shows that the higher temperatures have higher intensity, but unlike the 154.9 g/L solution it is visible that a 3rd decay evolves when the temperature is increased and disappears when the sample is cooled.

The mean count rates for the filtered and unfiltered 299.06 g/L solution are plotted in Figure 102.

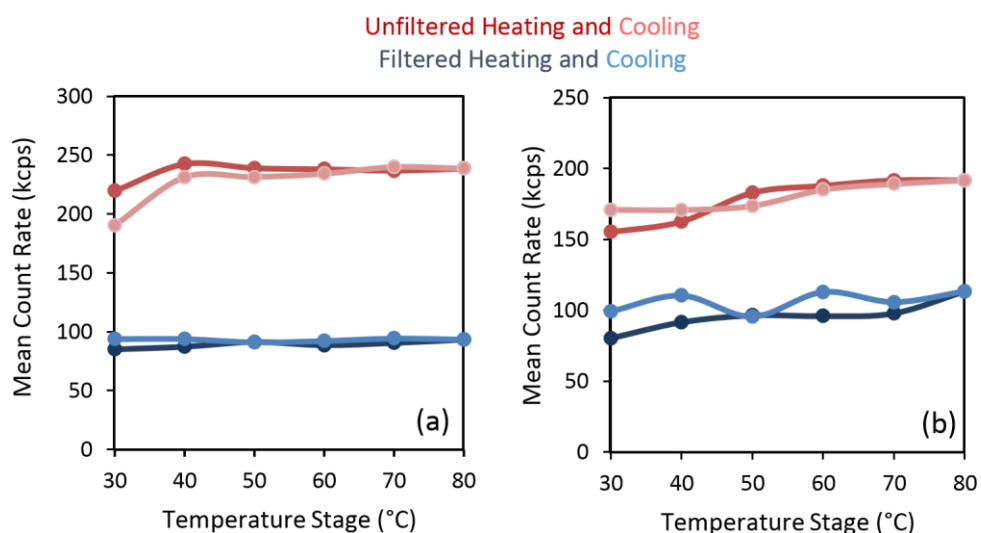


Figure 102. Mean count rate recorded in kilo counts per second for each temperature stage during the dynamic light scattering measurements for glycine concentration 299.06 g/L both for unfiltered (red) and 0.1 µm PTFE filtered (blue) solution. The heating stages are presented in the darker colour. (a) is for the first run and (b) is for the second run of the solution.

As before, filtered mean count rates are significantly lower than those of the unfiltered sample.

8.5.2 Deconvolution of Autocorrelation Functions: Analysis of Three Decays vs.

Temperature

When the three decay exponential expression (shown again in Equation 40) was fitted to the autocorrelation functions, the A, B and C values indicate how much that decay contributes to the entire curve. The calculated values from the interactive curve fitter were added up and each coefficient was determined as a fraction of the

total i.e. $\frac{A}{(A+B+C)}$ or $\frac{B}{(A+B+C)}$ or $\frac{C}{(A+B+C)}$ to allow for comparison. These calculated fractions were plotted against the temperature cycle and are given in Figure 103 and Figure 104. For temperatures below 40 °C, two decays were fitted and 3 decays were fitted for all other temperatures. The 3rd decay values are therefore zero for the 10, 20 and 30 °C stages in the cycle.

Equation 40

$$G_2(\tau) = Ae^{-\frac{1}{\alpha}\tau} + Be^{-\frac{1}{\beta}\tau} + Ce^{-\frac{1}{\gamma}\tau}$$

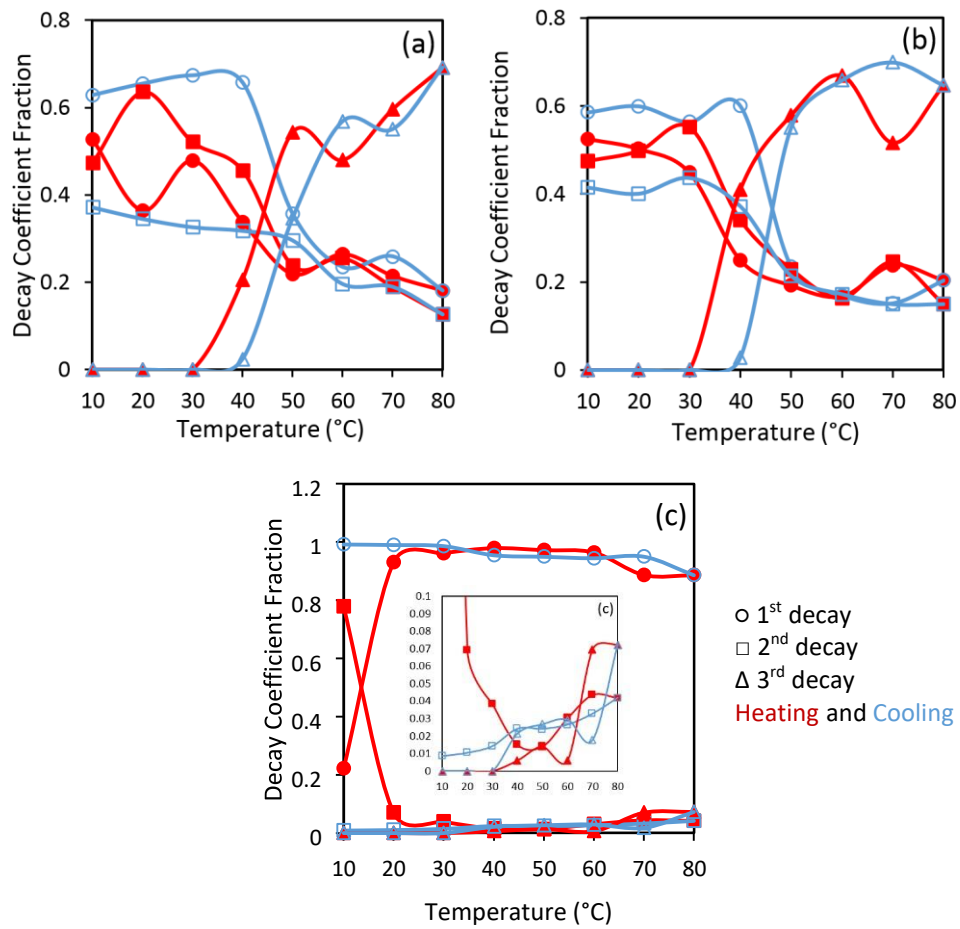


Figure 103. Coefficient values from the decay fitting with 3 decays present in the autocorrelation curves for all 154.9 g/L aqueous glycine solutions of the first run of experiments for the 1st decay [○], 2nd decay [□] and 3rd decay [Δ]. The heating stages are in red and the cooling stages are in blue. (a) 154.9 g/L unfiltered (b) 154.9 g/L repeat of the unfiltered sample and (c) 154.9 g/L filtered with 0.1 µm PTFE syringe filter.

Figure 103 shows that for all samples there is a decrease in the contributions of the 1st and 2nd decays coupled with an increase in the 3rd decay contribution when the temperature is increased. This is true also for the 154.9 g/L filtered solution, despite the increase being over a smaller scale as can be seen from the enlarged graph. The trends are reversible with respect to the temperature cycle. Although there appears to be some hysteresis. Figure 104 shows similar data but for the two higher concentrations of glycine.

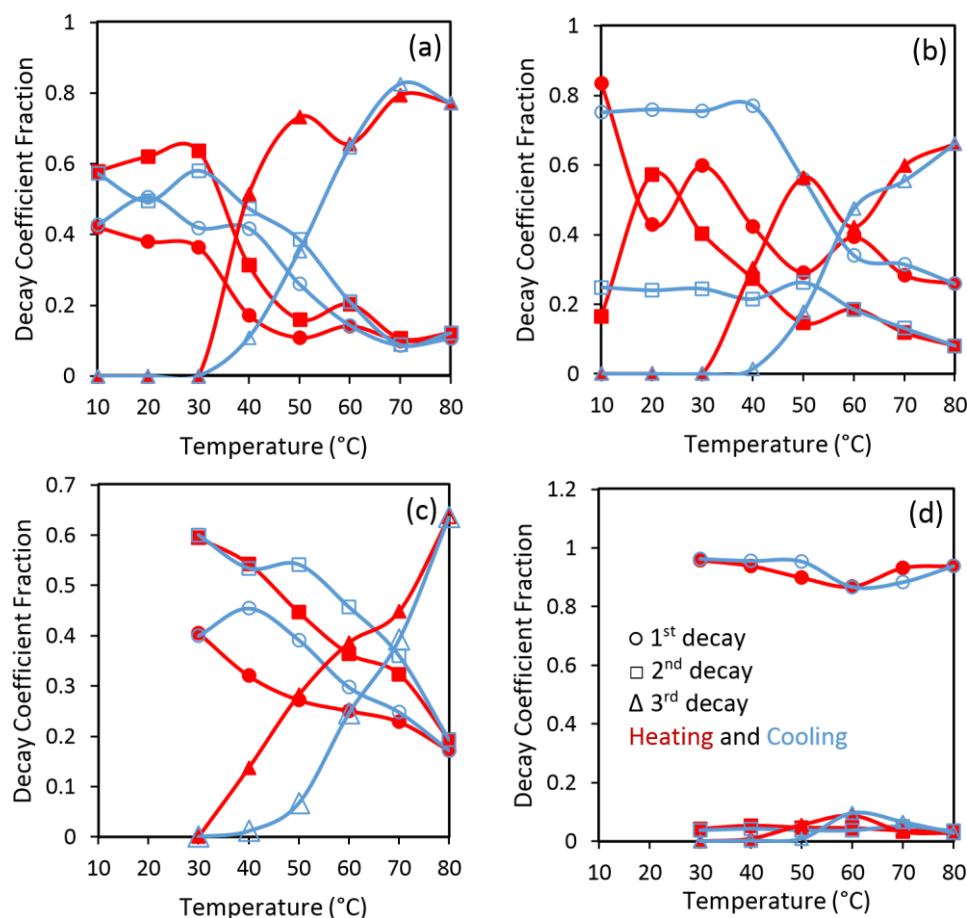


Figure 104. Coefficient values from the decay fitting with 3 decays present in the autocorrelation curves for the first run of the 234.98 and 299.06 g/L aqueous glycine solutions for the 1st decay [○], 2nd decay [□] and 3rd decay [△]. The heating stages are in red and the cooling stages are in blue. (a) 234.98 g/L unfiltered (b) 234.98 g/L filtered with 0.1 µm PTFE syringe filter (c) 299.06 g/L unfiltered and (d) 299.06 g/L filtered with 0.1 µm PTFE syringe filter.

For these samples the same trend as mentioned previously for the 154.9 g/L experiments is apparent, except for (d) 299.06 g/L with filtration where only the 2nd

decay shows this behaviour. The other two decays follow the same pattern as before until 60°C and then behave differently. The 1st decay decreases slightly after 60°C and the contribution from the 2nd and 3rd decay increases slightly after 60°C. The coefficients calculated for the second run of glycine experiments are given in Figure 105.

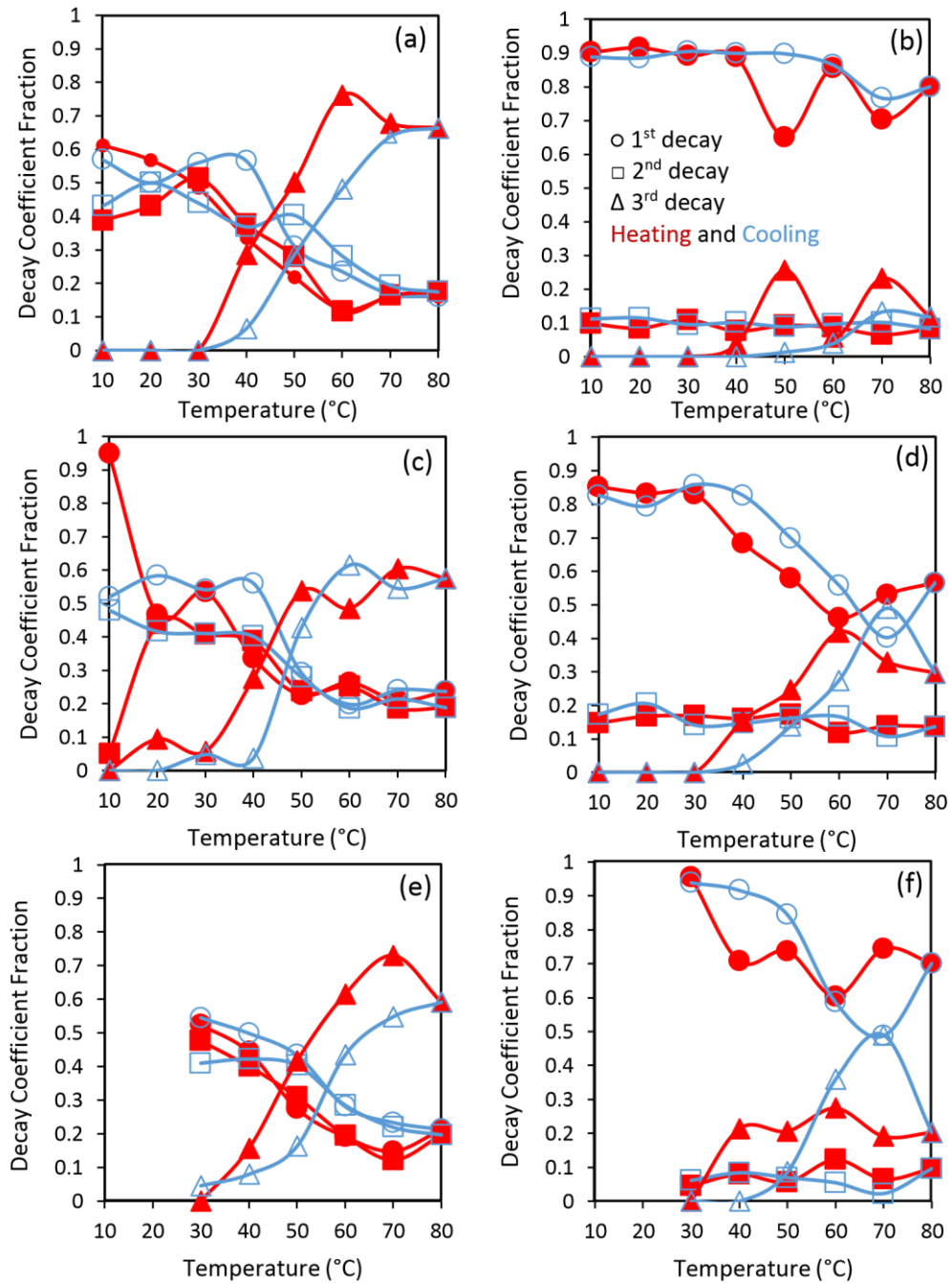


Figure 105. Coefficient values from the decay fitting with 3 decays present in the autocorrelation curves for the second runs of the 234.98 and 299.06 g/L aqueous glycine solutions for the 1st decay [○], 2nd decay [□] and 3rd decay [Δ]. The heating stages are in red and the cooling stages are in red and the cooling stages are in blue. (a) 154.9 g/L unfiltered, (b) 154.9 g/L filtered with 0.1 μm PTFE syringe filter, (c) 234.98 g/L unfiltered, (d) 234.98 g/L filtered with 0.1 μm PTFE syringe filter, (e) 299.06 g/L unfiltered and (f) 299.06 g/L filtered with 0.1 μm PTFE syringe filter.

8.5.3 Mean Cluster Diameters vs. Temperature

The average hydrodynamic diameters for each experiment (and for each of the 3 decays in the function) were plotted against the temperature cycle. These are given in Figure 106, Figure 107 and Figure 108 for the 1st, 2nd and 3rd decay diameters respectively. The y-axis is presented in logarithmic scale for the 1st, 2nd and 3rd decays.

For the 1st decay the data for PTFE filtered 234.98 g/L was omitted, for the 2nd decay the PTFE filtered 154.9 g/L was omitted and the 154.9 g/L PTFE filtered data was omitted in the plot for the 3rd decay. This was due to these curves having particularly poor fitting.

All the raw data obtained from the curve fitting tool in Matlab which was ultimately used to calculate these average hydrodynamic diameters is given in the Appendix in section 10.3. This section contains both the parameters for the first and second run of the glycine solutions.

Decay

8.5.3.1 1st

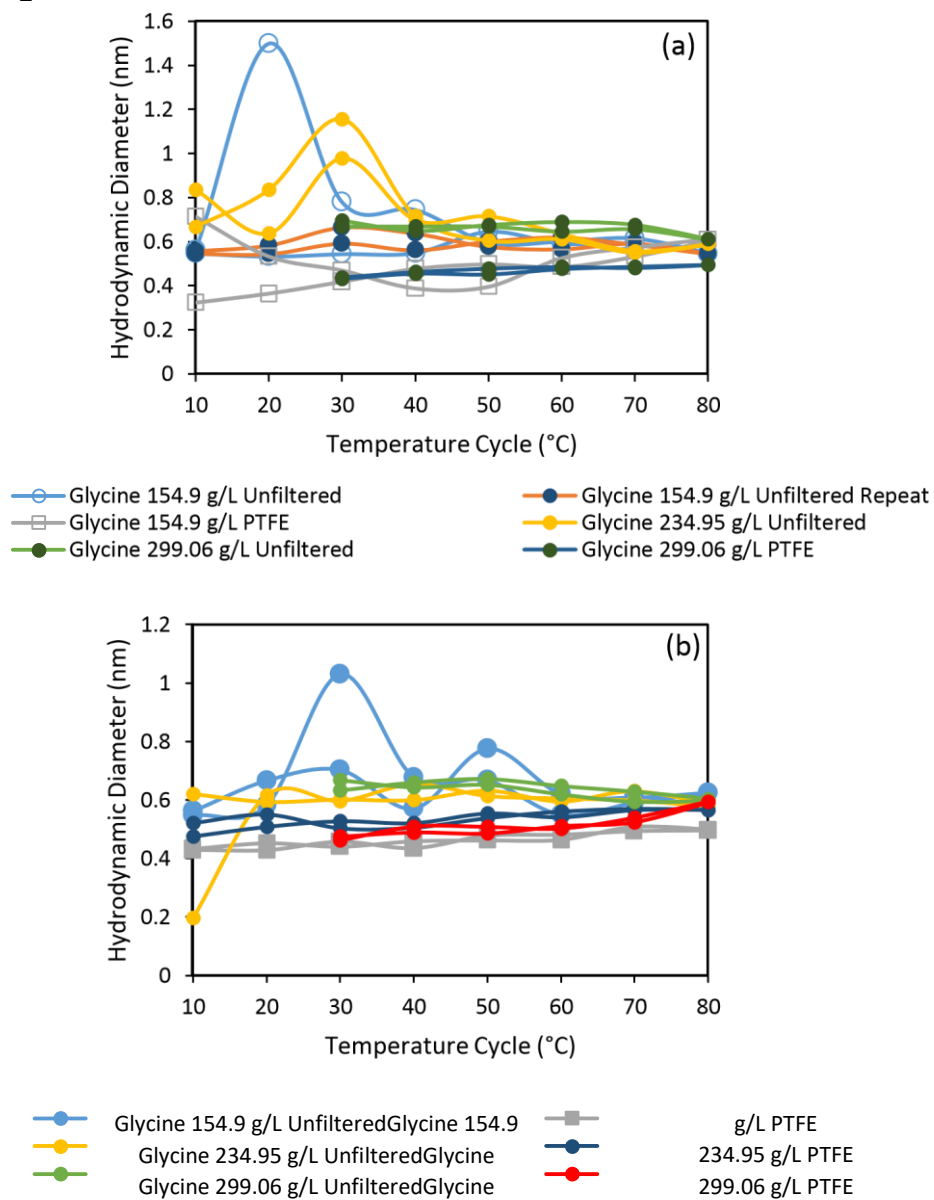


Figure 106. Average hydrodynamic diameters plotted against temperature for all glycine experiments both filtered and unfiltered corresponding to the first decay in the autocorrelation function for the first (a) and second run (b) of experiments.

Decay
8.5.3.2 2nd

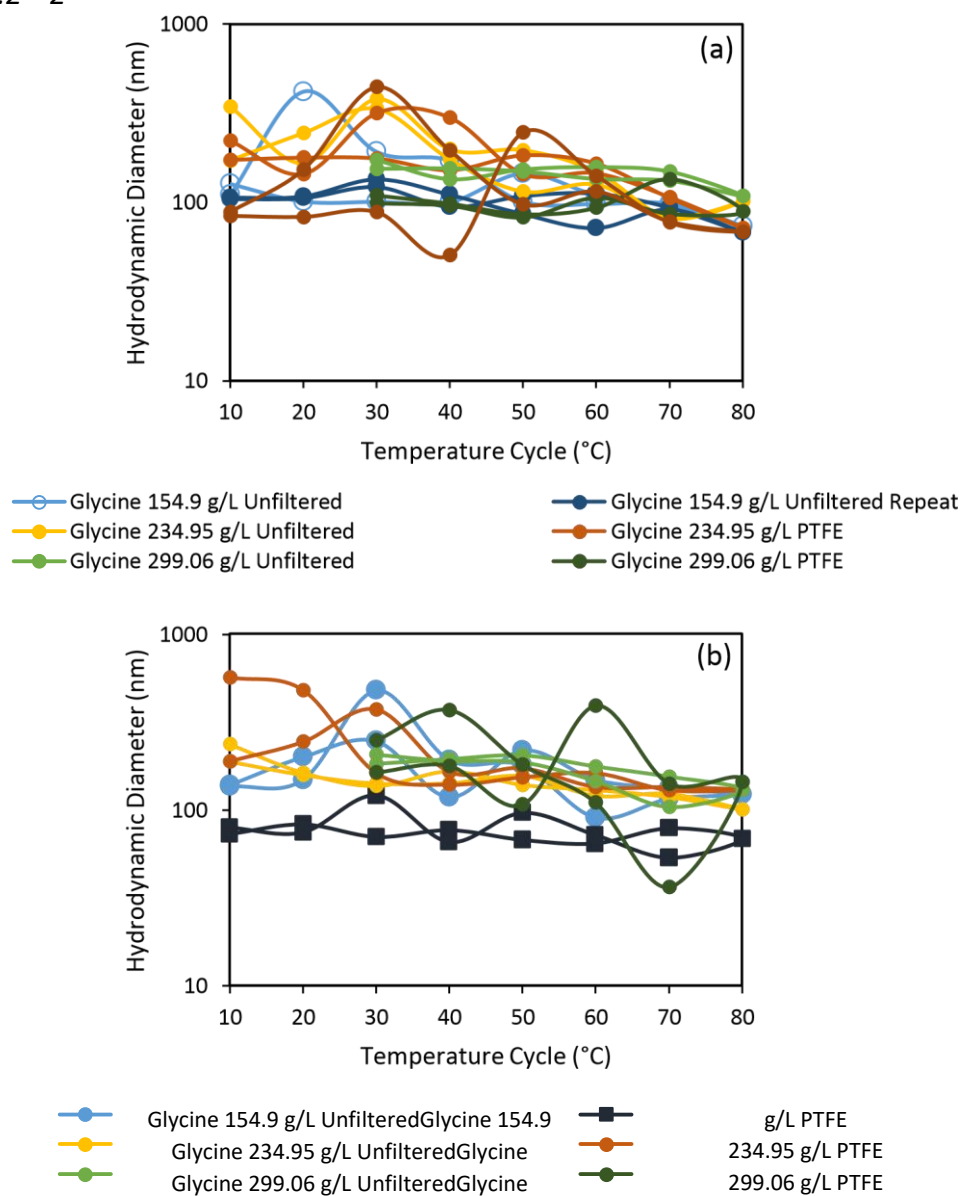
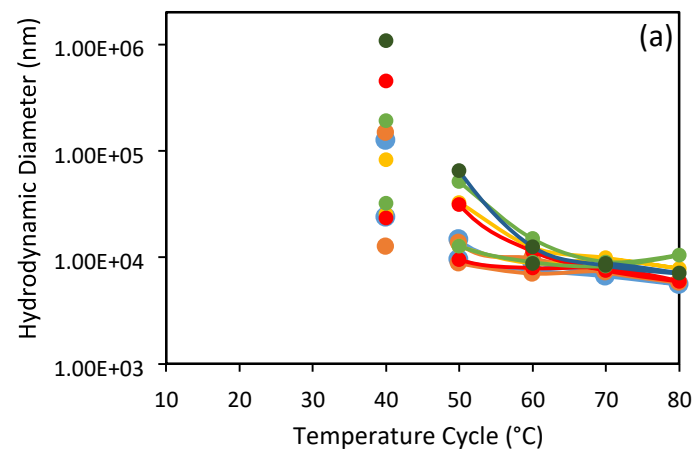
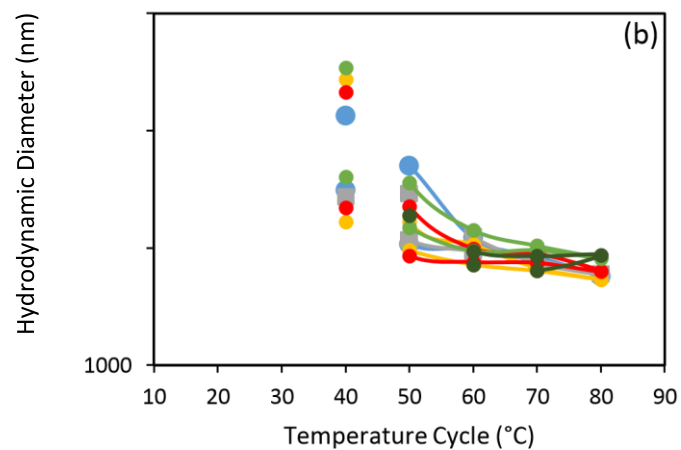


Figure 107. Average hydrodynamic diameters plotted against temperature for all glycine experiments both filtered and unfiltered corresponding to the second decay in the autocorrelation function for the first (a) and second run (b) of experiments.

8.5.3.3 ^{3rd} Decay



Glycine 154.9 g/L Unfiltered
 Glycine 234.95 g/L Unfiltered
 Glycine 299.06 g/L Unfiltered
 Glycine 154.9 g/L Unfiltered Repeat
 Glycine 234.95 g/L PTFE
 Glycine 299.06 g/L PTFE



Glycine 154.9 g/L Unfiltered
 Glycine 234.95 g/L Unfiltered
 Glycine 299.06 g/L Unfiltered
 Glycine 154.9 g/L PTFE
 Glycine 234.95 g/L PTFE
 Glycine 299.06 g/L PTFE

Decay

Glycine 299.06 g/L Unfiltered Glycine 299.06 g/L PTFE

Figure 108. Average hydrodynamic diameters plotted against temperature for all glycine experiments both filtered and unfiltered corresponding to the third decay in the autocorrelation function for the first (a) and second run (b) of experiments.

Note that the diameters obtained for the third decay fits are of the order 10 μm and the light scattering technique is unable to detect particles of this large size. After the transition point, the solution can no longer be characterised by the Stokes-Einstein equation.

8.5.3.4 Example of the Analysis of Curve Fitting before and after the Transition Peak in Hydrodynamic Diameter Changes with Temperature

An example of how the curve fitting changes with temperature is given here. The curve fitting from the unfiltered 234.98 g/L experiment is presented for 10, 30 and 50°C. This gives a view of the changes that happen before and after the generation of the third decay in the data that occurs after 30°C. The following figures (Figure 109, Figure 110 and Figure 111) are screenshots of the fits that were carried out on those three temperatures.

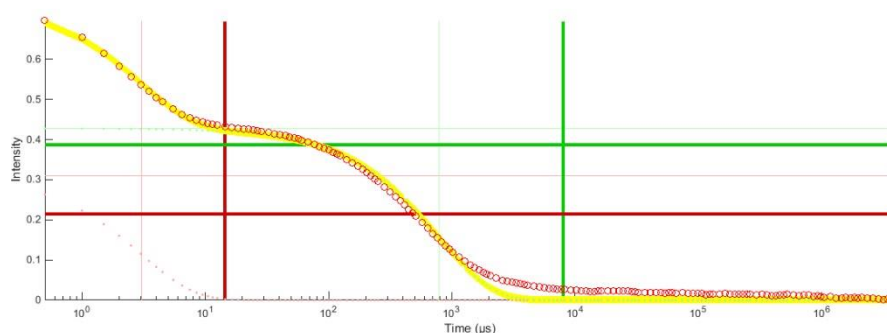


Figure 109. Screenshot of curve fitting of 10°C heating stage for 234.98 g/L glycine solution from the first run of experiments. Experimental data is given in red and the curve fitting is shown in yellow.

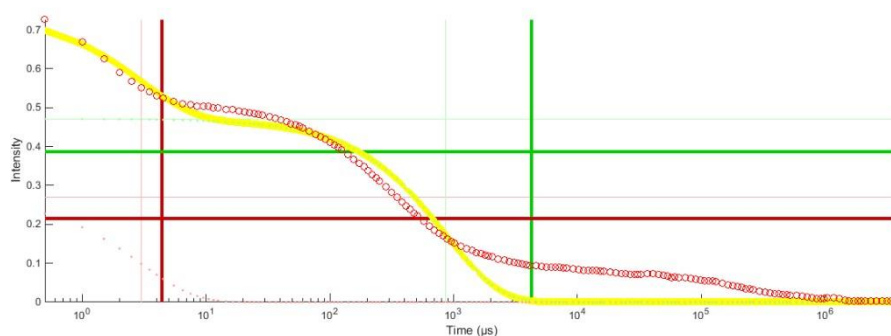


Figure 110. Screenshot of curve fitting of 30°C heating stage for 234.98 g/L glycine solution from the first run of experiments. Experimental data is given in red and the curve fitting is shown in yellow.

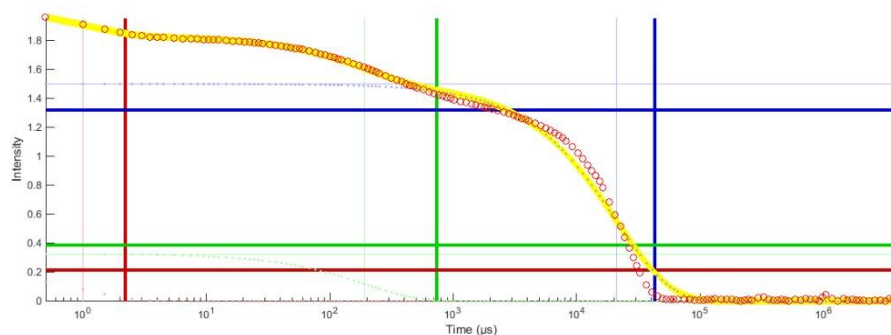


Figure 111. Screenshot of curve fitting of 50°C heating stage for 234.98 g/L glycine solution from the first run of experiments. Experimental data is given in red and the curve fitting is shown in yellow.

Table 17 presents all the numerical fitting data from the curve fitter in Matlab. When referring back to the equation that was used to fit the data (given again here in Equation 41).

Equation 41

$$G_2(\tau) = Ae^{-\frac{1}{\alpha}\tau} + Be^{-\frac{1}{\beta}\tau} + Ce^{-\frac{1}{\gamma}\tau}$$

Table 17. Parameters from the 2nd Decay Curve Fitting of 10, 30 and 50°C of Unfiltered 234.98 g/L Glycine

	Decay 1		Decay 2		Decay 3		
Temperature (°C)	A	α	B	β	C	γ	RMS
10	0.31	3.03	0.43	780.97	-	-	0.21
30	0.27	3.00	0.47	866.30	-	-	0.61
50	0.22	1.004	0.33	191.20	1.50	21195.73	0.54

It can be seen that at 30°C the curve fitting error (RMS in Table 17) is largest. The lag time for the entire function becomes significantly longer when 50°C is reached (shown in Figure 111 where the curve ends at approximately $10^5 \mu\text{s}$ rather than $10^4 \mu\text{s}$ for the other two autocorrelation functions). The 3rd decay in the data does not

appear until after 30°C in the temperature cycle. The influence of the 1st and 2nd decays is seen to drop after the transition point at 30°C.

8.6 GLYCINE SOLUTIONS NANOSIGHT RESULTS

This section presents the NanoSight data obtained for all glycine solutions. The same temperature cycle used in the dynamic light scattering experiments could not be replicated due to the equipment limitations.

8.6.1 Particle Size Distributions

The particle size distributions plotted as average concentration in particles per ml.

8.6.1.1 Unfiltered and 0.1 μm PTFE Filtered Glycine Solution 154.9 g/L

The cluster size distributions for the lowest glycine concentration are given in Figure 112 and Figure 113 for unfiltered and filtered samples respectively.

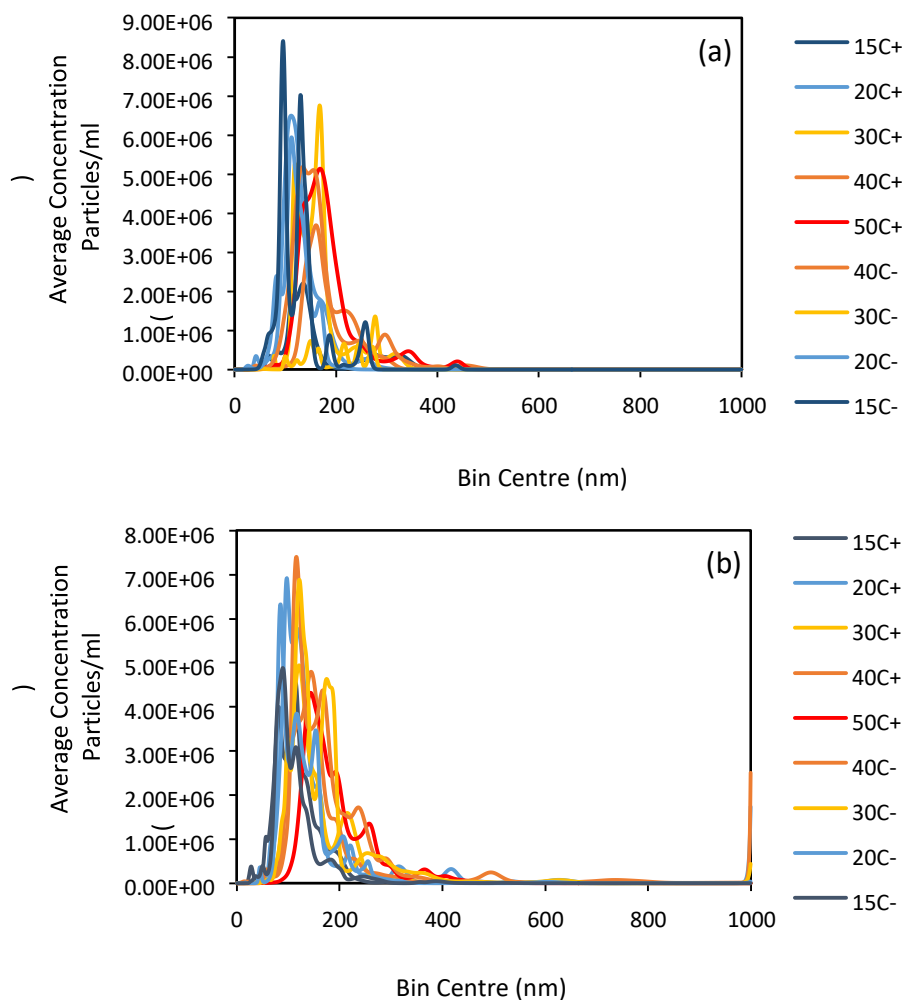


Figure 112. Cluster size distributions from NanoSight measurements of temperature cycle from 15-50-15°C with unfiltered aqueous glycine solution of concentration 154.9 g/L for the first (a) and second (b) repetition.

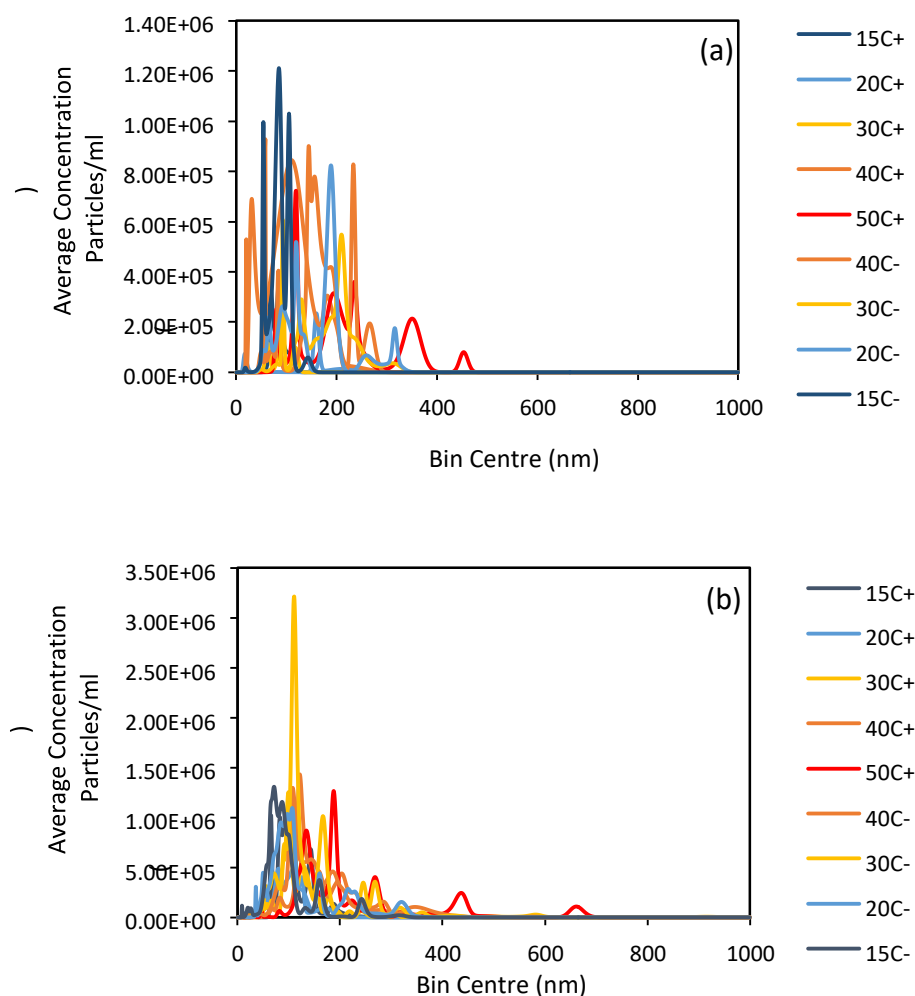


Figure 113. Cluster size distributions from NanoSight measurements of temperature cycle from 15-50-15°C with 0.1 μm PTFE filtered aqueous glycine solution of concentration 154.9 g/L for the first (a) and second (b) repetition.

The results show that the cluster number concentration is lower for the filtered samples at all temperatures in the cycle and that a shift towards larger diameters is observed when the temperature is increased. Reversibility of this effect is also witnessed.

8.6.1.2 Unfiltered and 0.1 μm PTFE Filtered Glycine Solution 234.98 g/L

The results from NanoSight measurements for the unfiltered and filtered 234.98 g/L solution experiments are presented in Figure 114 and Figure 115 respectively

accompanied by the distribution for the repetition of the filtered experiment shown in Figure 116.

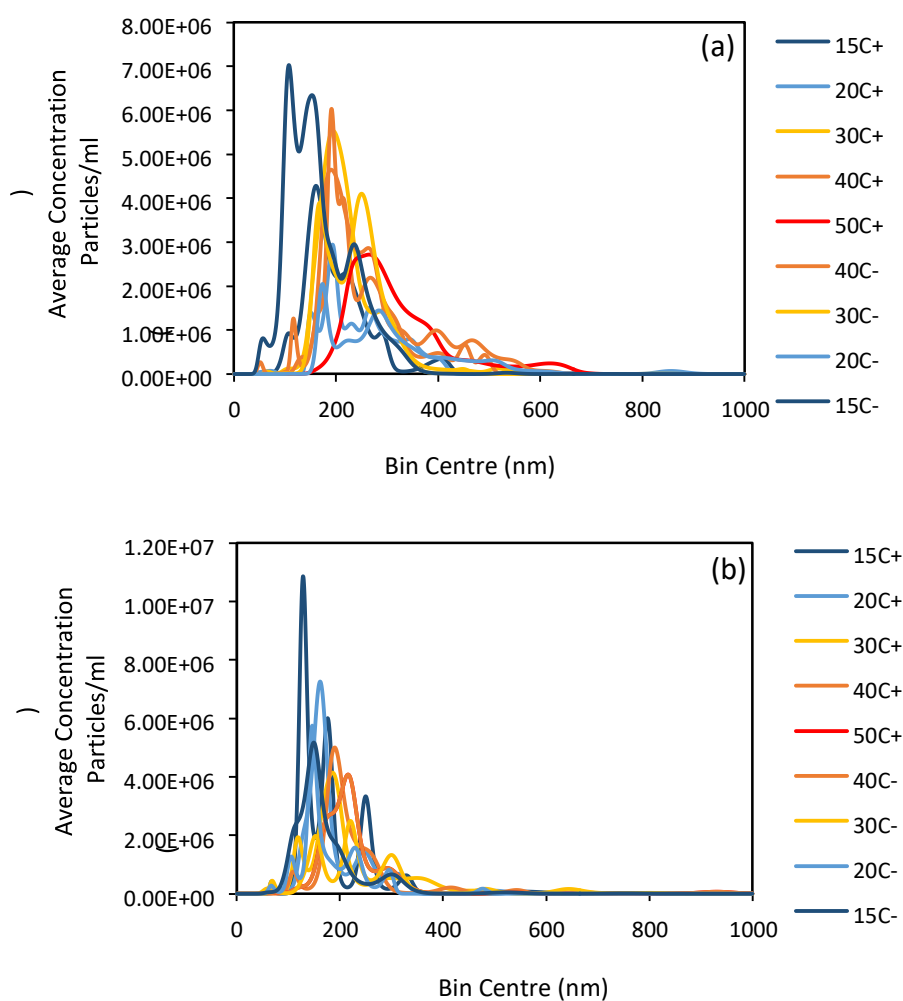


Figure 114. Cluster size distributions from NanoSight measurements of temperature cycle from 15-50-15°C with unfiltered aqueous glycine solution of concentration 234.98 g/L for the first (a) and second (b) repetition.

For these experiments, the cluster number concentration for both filtered and unfiltered are comparable and as before with the 154.9 g/L experiments there is a shift in the distribution to larger sizes as the temperature increases towards 50°C and returns to smaller sizes when reduced back to 15°C.

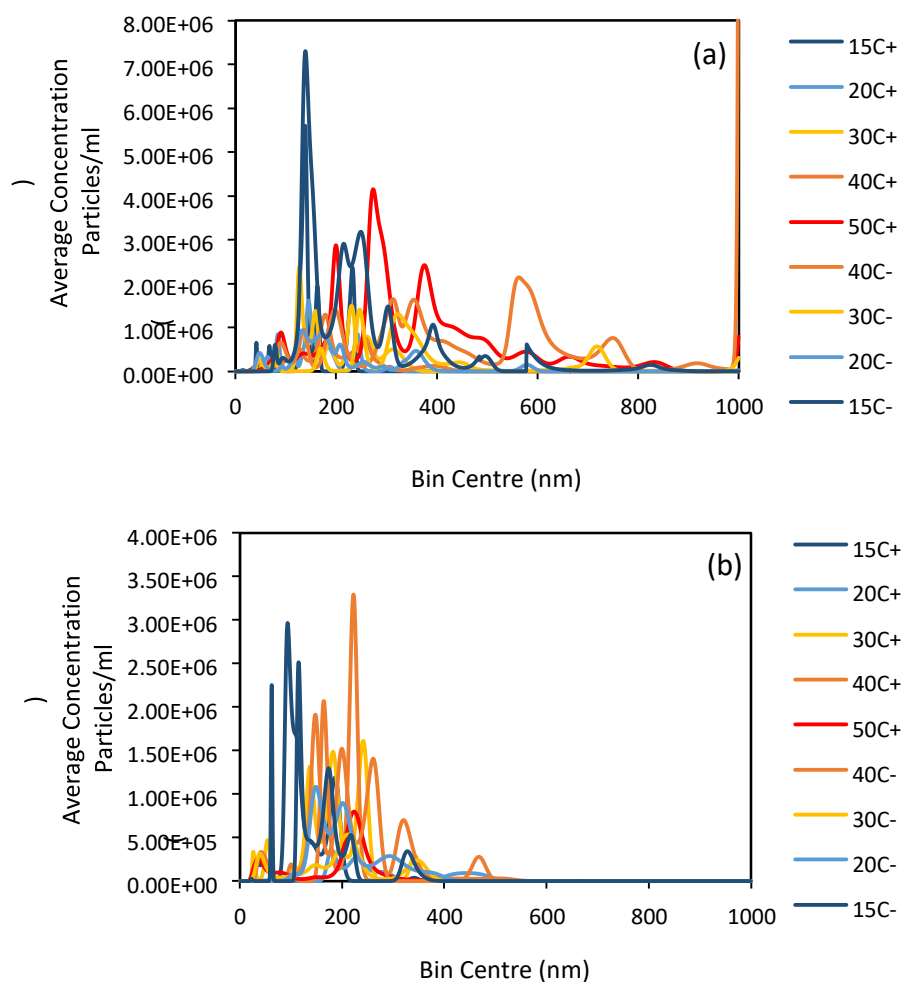


Figure 115. Cluster size distributions from NanoSight measurements of temperature cycle from 15-50-15°C with 0.1 μ m PTFE filtered aqueous glycine solution of concentration 234.98 g/L for the first (a) and second (b) repetition.

The repeat of the first run of the filtered solution in Figure 116 showed that there was not an issue with the filter as similar cluster number concentrations were obtained.

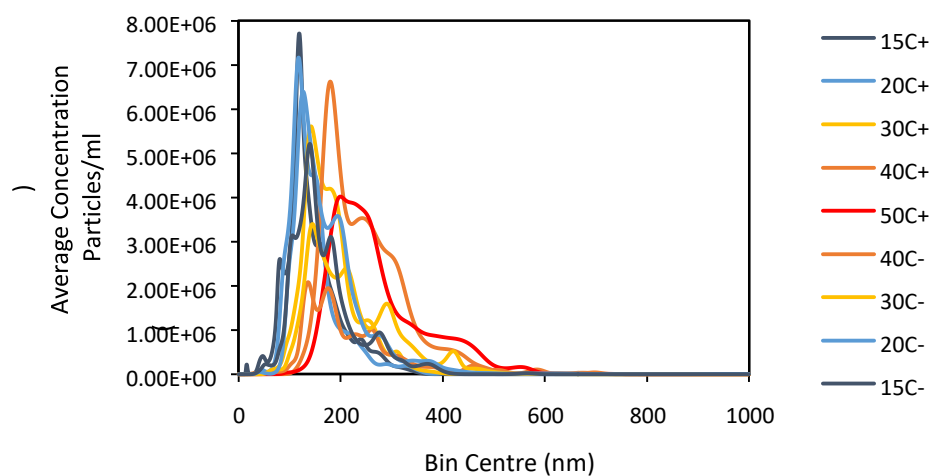


Figure 116. Cluster size distributions from NanoSight measurements of temperature cycle from 15-50-15°C with the repetition of the first run 0.1 μ m PTFE filtered aqueous glycine solution of concentration 234.98 g/L.

8.6.1.3 Unfiltered and 0.1 μm PTFE Filtered Glycine Solution 299.06 g/L

Results pertaining to the highest glycine concentration for unfiltered and filtered solution are shown in Figure 117 and Figure 118 respectively. A temperature cycle of only 30-50-30°C was carried out here due to unwanted nucleation taking place at the lower temperatures.

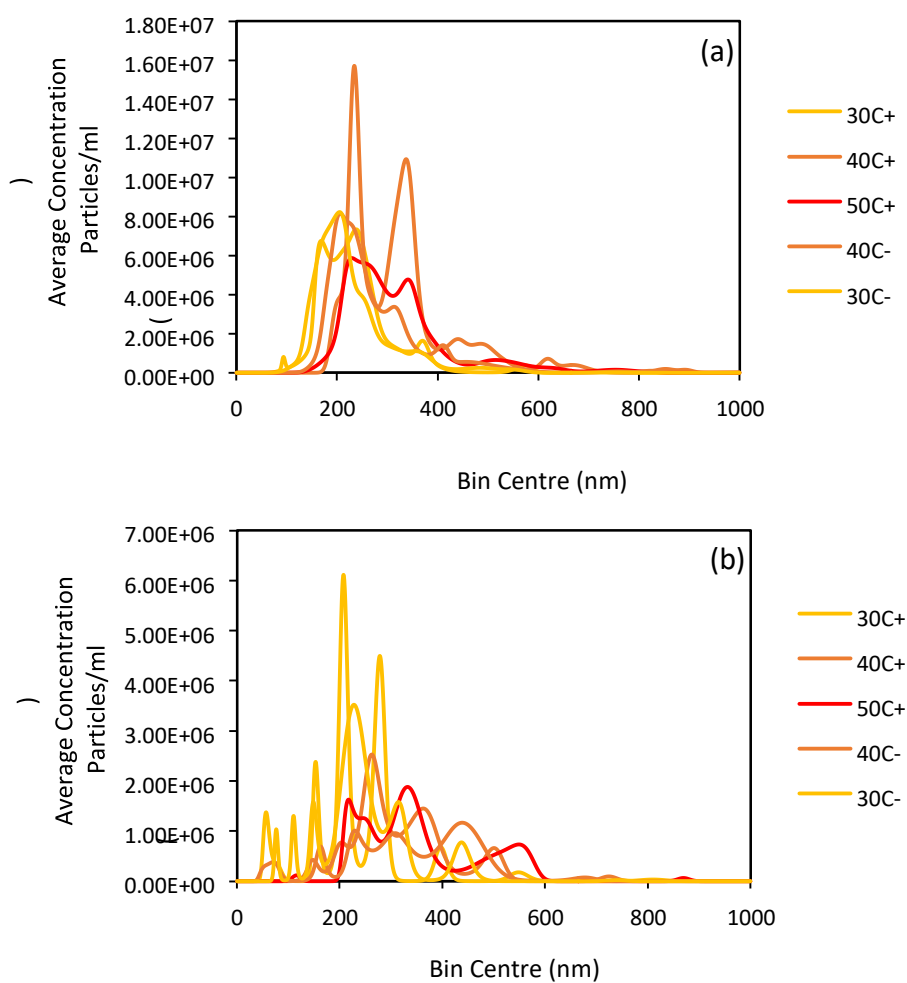


Figure 117. Cluster size distributions from NanoSight measurements of temperature cycle from 30-50-30°C with unfiltered aqueous glycine solution of concentration 299.06 g/L for the first (a) and second (b) repetition.

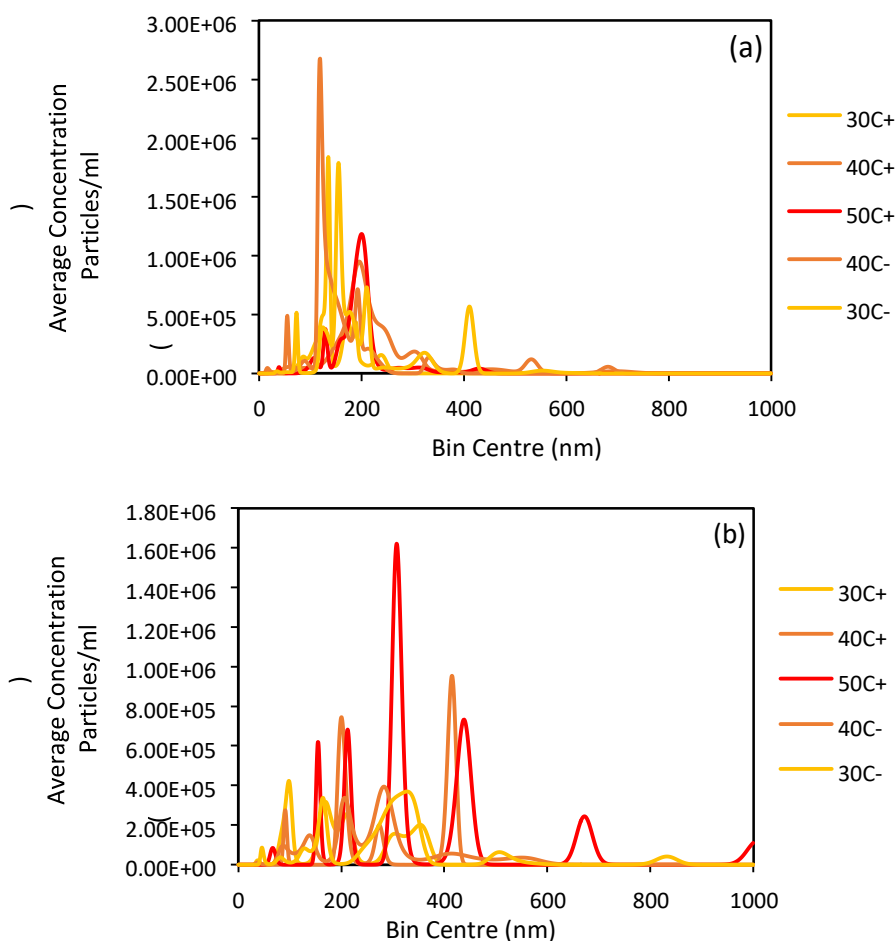


Figure 118. Cluster size distributions from NanoSight measurements of temperature cycle from 30-50-30°C with 0.1 μm PTFE filtered aqueous glycine solution of concentration 299.06 g/L for the first (a) and second (b) repetition.

From the results there was a clear order of magnitude difference between the cluster number concentrations of filtered and unfiltered samples. The distribution shift from 30 to 50°C was also evident despite not being as clear as the lower temperatures were not measured.

8.6.2 Cluster Size Distributions with 20 nm Bin Size

The cluster size distributions shown previously were re-binned to present the data in a different form, only showing the heating stage of the temperature cycle. The data presented is only for the first run, the data obtained for the second run is given in the appendix in section 10.1.

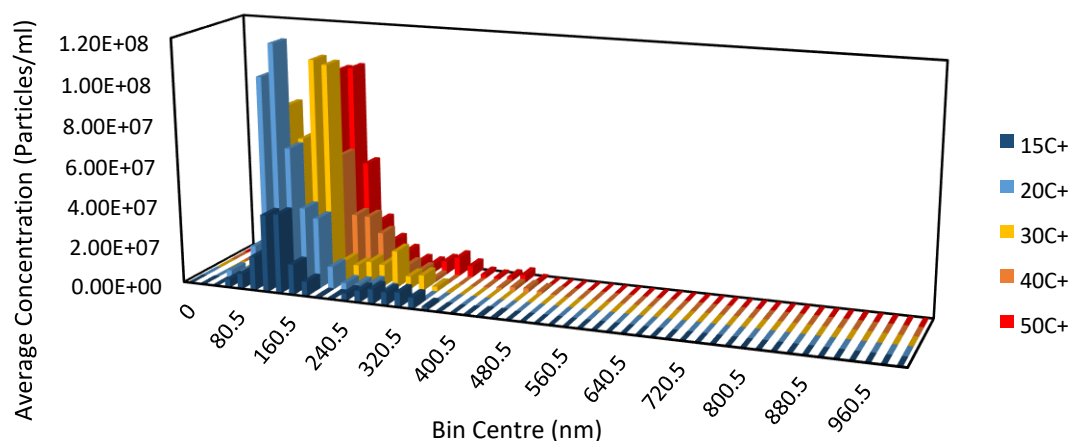


Figure 119. Cluster size distributions from NanoSight measurements of temperature cycle from 15-50-15°C with the first run of unfiltered aqueous glycine solution of concentration 154.9 g/L with 20 nm bin sizes for the axis.

Figure 120 to Figure 124 show all of the previous data again but in this new format. The same trends as were mentioned previously were still visible however for clarity only the heating stage of the temperature cycle was plotted. Concentrations were lower for filtered samples except for the 234.98 g/L concentration which equated to supersaturation 1.1 based on solubility at 20°C.

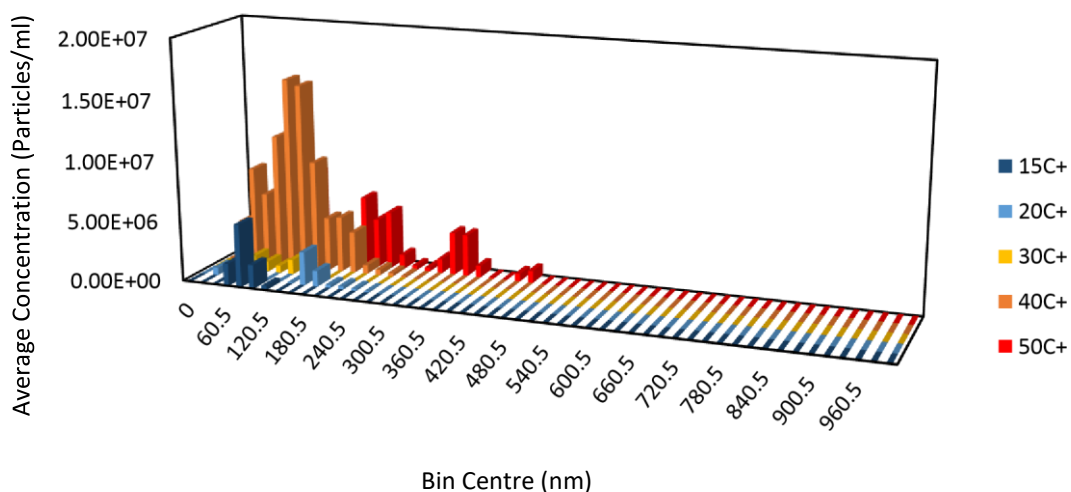


Figure 120. Cluster size distributions from NanoSight measurements of temperature cycle from 15-50-15°C with the first run of 0.1 µm PTFE filtered aqueous glycine solution of concentration 154.9 g/L with 20 nm bin sizes for the x-axis.

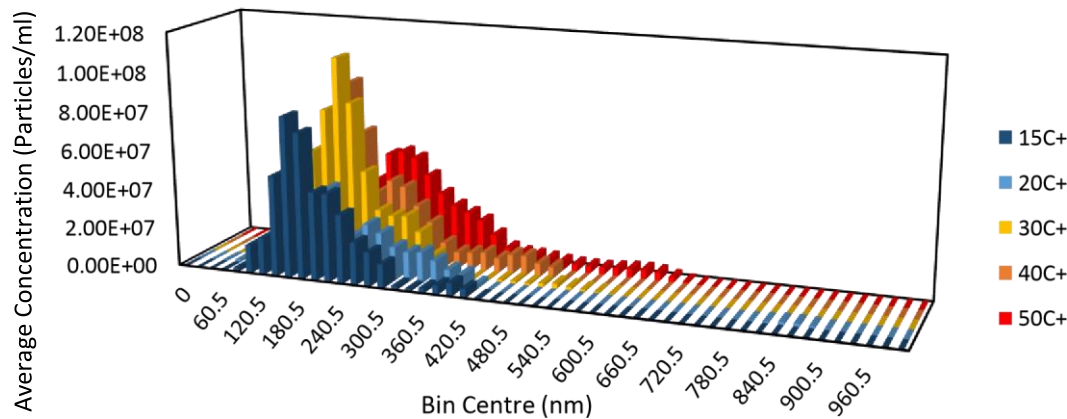


Figure 121. Cluster size distributions from NanoSight measurements of temperature cycle from 15-50-15°C with the first run of unfiltered aqueous glycine solution of concentration 234.98 g/L with 20 nm bin sizes for the xaxis.

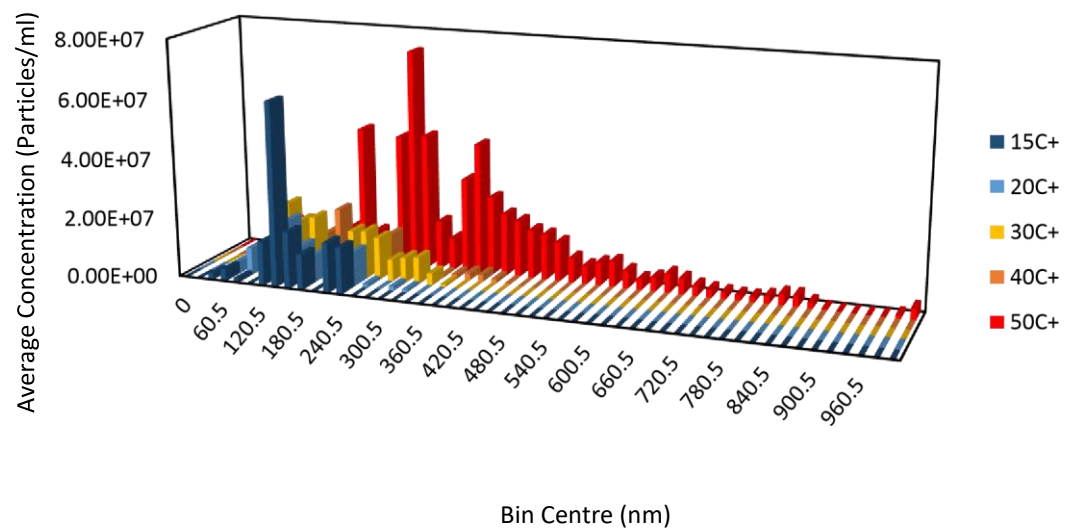


Figure 122. Cluster size distributions from NanoSight measurements of temperature cycle from 15-50-15°C with the first run of 0.1 µm PTFE filtered aqueous glycine solution of concentration 234.98 g/L with 20 nm bin sizes for the x-axis.

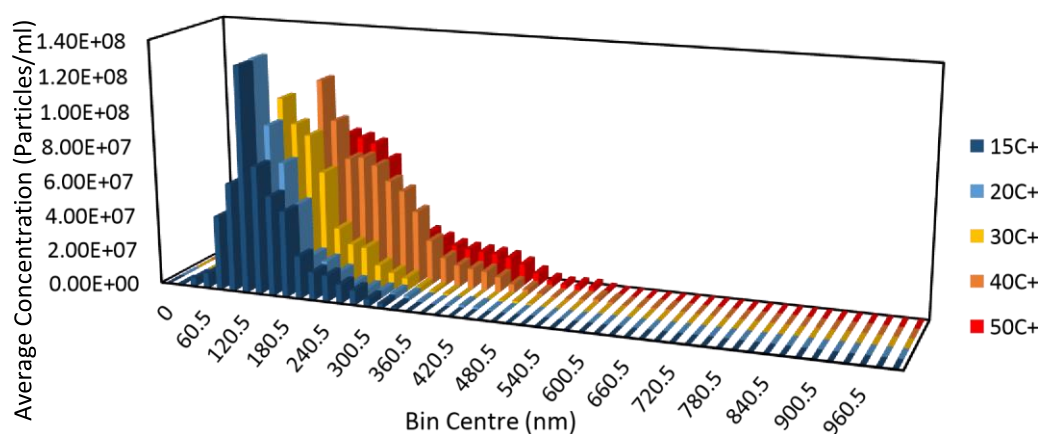


Figure 123. Cluster size distributions from NanoSight measurements of temperature cycle from 15-50-15°C with the repeat of the first run of 0.1 μm PTFE filtered aqueous glycine solution of concentration 234.98 g/L with 20 nm bin sizes for the x-axis.

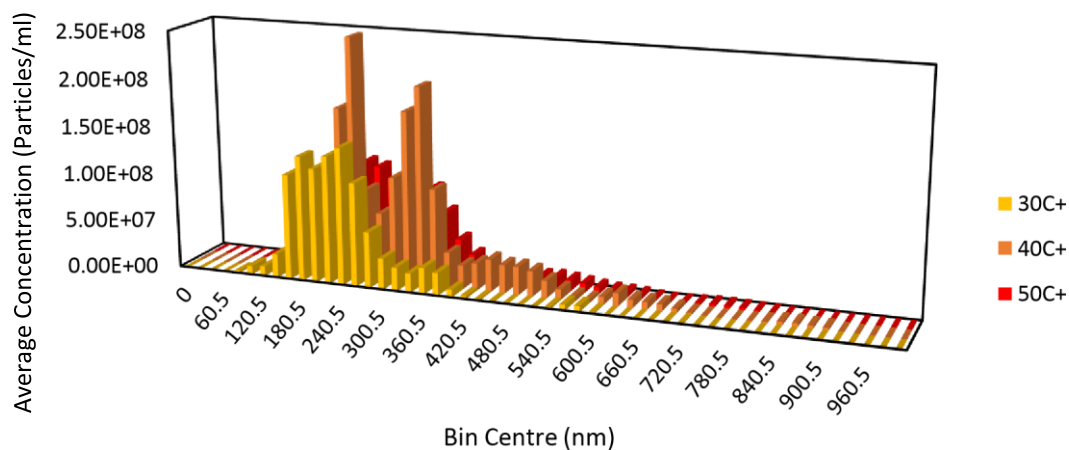


Figure 124. Cluster size distributions from NanoSight measurements of temperature cycle from 30-50-30°C with the first run of unfiltered aqueous glycine solution of concentration 299.06 g/L with 20 nm bin sizes for the xaxis.

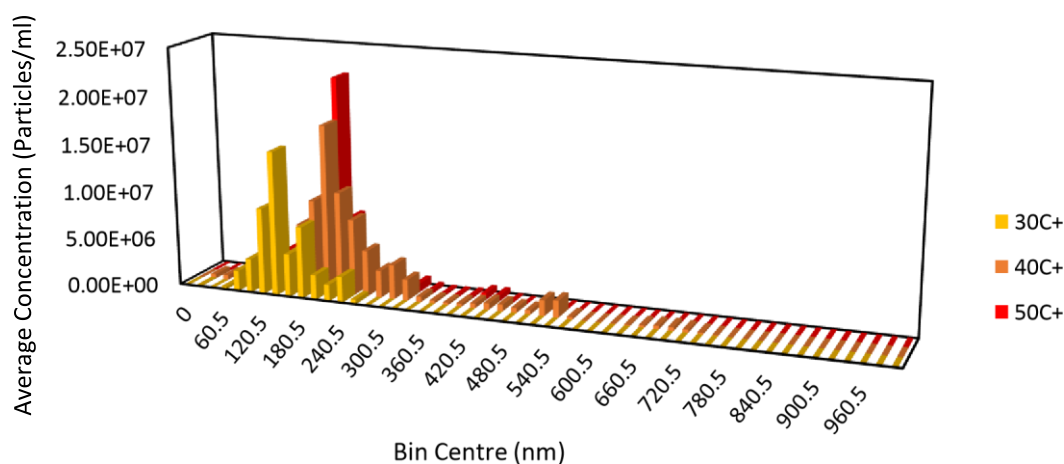


Figure 125. Cluster size distributions from NanoSight measurements of temperature cycle from 30-50-30°C with the first run of 0.1 μm PTFE filtered aqueous glycine solution of concentration 299.06 g/L with 20 nm bin sizes for the x-axis.

8.6.3 Changes in Average Cluster Diameter with Temperature for Glycine Solutions

The following plots depict the changes in the average cluster diameter with changes in the temperature cycle for the first and second experimental runs. Figure 126, Figure 127 and Figure 128 give results for 154.9, 234.98 and 299.06 g/L respectively.

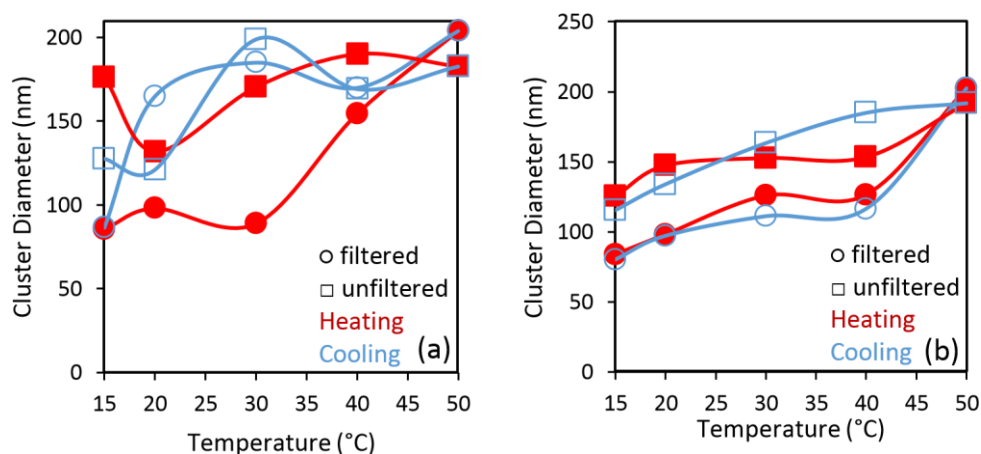


Figure 126. NanoSight measurements of the average cluster diameters with temperature for 154.9 g/L aqueous glycine solution for filtered [○] and unfiltered [□] samples with the heating stages given in red and the cooling stages presented in blue. The first (a) and second run (b) are shown.

From Figure 126 and Figure 127 it was determined that all the measurements for the PTFE filtered 154.9 and 234.98 g/L solutions had larger diameters on the cooling stages than on the heating stages. This was not as significant for the unfiltered experiments. Figure 128 had less points due to difficulties with the measurements and therefore the same trend cannot be said to be true here.

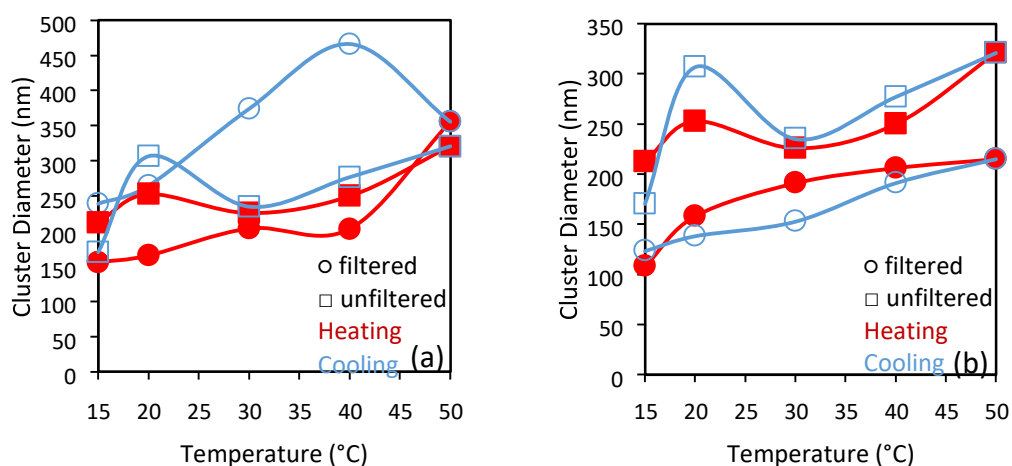


Figure 127. NanoSight measurements of the average cluster diameters with temperature for 234.98 g/L aqueous glycine solution for filtered [o] and unfiltered [□] samples with the heating stages given in red and the cooling stages presented in blue. The first (a) and second run (b) are shown.

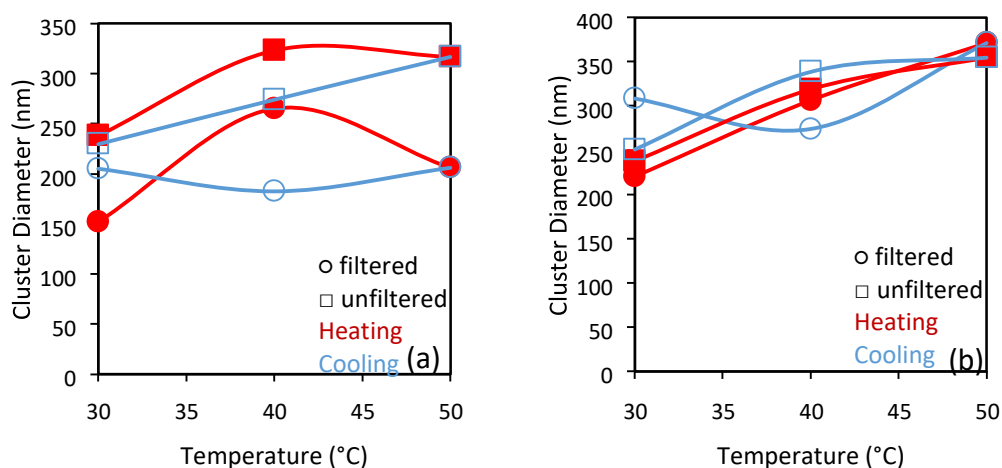


Figure 128. NanoSight measurements of the average cluster diameters with temperature for 299.06 g/L aqueous glycine solution for filtered [o] and unfiltered [□] samples with the heating stages given in red and the cooling stages presented in blue. The first (a) and second run (b) are shown.

The data given here shows that in general the average cluster size increased with increasing temperature and decreased as the sample was cooled.

8.7 DISCUSSION OF LIGHT SCATTERING RESULTS FOR GLYCINE SOLUTIONS

The data presented in this chapter was for aqueous glycine solutions of three concentrations and two filtration conditions (filtered or unfiltered). The dynamic light scattering data and the NanoSight data complemented each other in that similar trends and results were observed.

Dealing first with the dynamic light scattering results; the common theme of increased intensity and the appearance of a 3rd decay in the functions was evident when the temperature was increased. This was both true for the filtered and unfiltered experiments. The third decay almost always started to appear at 40°C. The intensities for the PTFE filtered samples were much lower than those for the unfiltered samples (except in the case of the 234.98 g/L solution) and this meant that the presence of a 3rd decay was difficult to observe.

Through analysis of the autocorrelation functions, via fitting a three term exponential decay, the significance of this 3rd decay could be detected more easily by noting the change in the coefficient values. The coefficient values corresponding to the 3rd decay were found to increase dramatically after 30°C in the temperature cycle and then return to lower values when the sample was being cooled. This was more significant for the unfiltered experiments but was not observed for the filtered 299.06 g/L solution. In this case the trend was observed up to a temperature of 60°C and not for the 70°C and 80°C temperature stages. Reasoning for this could be that under these conditions the nanodroplet species increase in size up to 60°C and this is the most stable temperature for the newly formed larger clusters. It was clear from the autocorrelation functions for this filtered solution that the 60°C function had the highest intensity and then the intensities dropped for the 70 and 80°C functions.

Temperatures above this may start to break down the aggregated clusters again. NanoSight data would have been useful to back this up however higher temperatures were unattainable. Further work is necessary in this area.

Accompanied with this increase in 3rd decay significance was a decrease in that of the 1st and 2nd decay (except for the aforementioned filtered 299.06 g/L solution). It seems that a transition with the nanospecies in solution takes place at this temperature. The smaller clusters measured by the 1st and 2nd decay decrease and larger species evolve which is indicated by the generation of the 3rd decay.

When the average hydrodynamic diameters were plotted against temperature it was found that a large fluctuation in particle diameter was observed at 40°C for the 3rd decay. The sizes for the 1st and 2nd decays remain fairly consistent throughout the temperature cycle. After 30°C the third decay in the data seems to be more noticeable. The before and after curve fitting for the transition point in the second decay showed that the fit was not as good for the 30°C curve. Then the curve fitting improved at 50°C showing that the solution seemed to pass through a transition point where after this temperature a 3rd decay evolved representing the presence of larger species in the sample. After establishing this third decay the fitting improved. The NanoSight data supports this as it shows the particle diameters increased from 1550°C in the temperature cycle. All of the effects that were found in this data were reversible with respect to the temperature cycle. The diameters obtained for the 3rd decay were larger than the light scattering techniques can possibly detect ~ 10 µm. The solution had undergone a transition such that it could no longer be described by the Stokes-Einstein equation and the hard-sphere model. The clustering species had to have reordered themselves in such a way that could not be successfully measured by these techniques anymore. The actual transformation cannot be stated at this stage and would require further work.

For the NanoSight results the number concentrations were higher for the unfiltered samples than for the filtered ones, except for the 234.98 g/L solutions where the number concentrations of filtered and unfiltered were on similar scales. This could be

due to the nature of the mesoscale clusters at this concentration, where they can pass more easily through the filter. This relates back to the DLS data where the intensities in the autocorrelation functions were comparable and the other filtered intensities were considerably lower than that of the unfiltered experiment. When the temperature was raised, the cluster size distributions were found to shift to larger diameters. DLS data did not give a particle distribution, only an average diameter for each decay, and so NanoSight gives more detailed information on particle size. The polydispersity of the sample makes diameter analysis more difficult with DLS than NanoSight because the results work with averages and not distributions.

Average cluster diameters were plotted against temperature and it was found that the general trend for all experiments was the diameter increased with temperature and then decreased with the cooling stage. Commonly the largest diameters were found at 40°C, this was the temperature at which the 3rd decay became present in the autocorrelation functions for DLS data. Reasons for this shift to larger cluster diameters when the temperature was increased could be explained through the solution trying to achieve a more thermodynamically favourable state through creating larger clusters. This could possibly occur via smaller clusters self-assembling to larger aggregates in mutual equilibrium with each other.

The results in the NanoSight data also showed reversibility with respect to the temperature cycle. The glycine solution experiments were all repeated once more under the same conditions and the same trends were evident as before. The reproducibility for the glycine solutions was reasonable.

Evidence for the presence of liquid-like mesoscale clusters in solution can be found in the analysis of the filtered experiments. When solution passes through filters with 100 nm pore diameter, species larger than this should be removed from solution. However on both pieces of equipment and for most of the experiments, species of diameters exceeding this value were detected. Further evidence was found when unfiltered water was exposed to the same experimental procedure. The results for the water showed no changes with increasing temperature and the intensities and

concentrations obtained from DLS and NanoSight were significantly lower than the unfiltered solution of glycine. Similar work has been carried out before with similar trends and results [11] [10].

The explanation that these prenucleation species have liquid-like properties would mean they would easily pass through the filter and remain in the solution. The effects and number concentrations were clearer and stronger for the unfiltered solutions as it is proposed that during filtration the cluster structure can be disturbed and it may take some time for these species to reform in solution. As mentioned previously, evidence exists that agitation and shearing of the solution can achieve this [11].

8.8 CONCLUSIONS FOR GLYCINE SOLUTIONS

Evidence for prenucleation clusters was obtained by observing the behaviour of aqueous glycine solutions in the temperature cycling environment and by comparing the filtered and unfiltered solutions. Pure water yielded results of low intensities with scattering independent on temperature, showing that only minor impurities were present. In the solutions of glycine, species were detected with diameters larger than the 100 nm pore diameter used during the filtration. This implies that 1) the clusters likely have liquid-like properties if they can pass through diameters smaller than their diameter and 2) solid impurities have been removed by the filter and so species larger than 100 nm can only be accounted for by the clusters of molecular species in the solution. The light scattering measurements carried out for the three concentrations of glycine revealed some key points with respect to the filtration method and temperature cycling.

A 3rd decay evolved in the autocorrelation functions above 30°C in the temperature cycle for all experiments. The sizing information obtained showed that average cluster diameters were increasing with the temperature. A transition in the solution could be taking place at this temperature where the clustering species in solution undergo changes in order to stabilise the overall solution due to this temperature

change. As this stabilisation change was reversible, as shown by temperature cycling, it is likely to be thermodynamically rather than kinetically driven. In order to achieve thermodynamic equilibrium it is possible that the smaller clusters are self-assembling to create larger, more stable clusters in solution.

Overall, this set of data and results provide information to fill the gap in the literature of studying the effects temperature cycling has on the clustering behaviour of supersaturated and undersaturated solutions of aqueous glycine. The generation of a 3rd decay in autocorrelation functions has not been detected previously, and the fact that larger species are detected at higher temperatures was unexpected. The greater the supersaturation, the closer to nucleation and therefore it was expected that the diameters would increase as they became close to creating a nucleus. This was not the case from these light scattering results.

8.9 UREA SOLUTIONS DYNAMIC LIGHT SCATTERING RESULTS

As with glycine, the experiments with urea solutions were carried out with three concentrations and both unfiltered and filtered with 0.1 μm PTFE syringe filters. This system presented more issues with reproducibility than the glycine solutions and this is discussed here as well as the general trends that were found.

8.9.1 Urea Solutions Autocorrelation Functions

8.9.1.1 Unfiltered and 0.1 μm Filtered Urea Solutions 522.61 g/L

Increase in intensity with temperature and the generation of a 3rd decay, similar to those observed with glycine solutions, was evident in some of the data here but not in all.

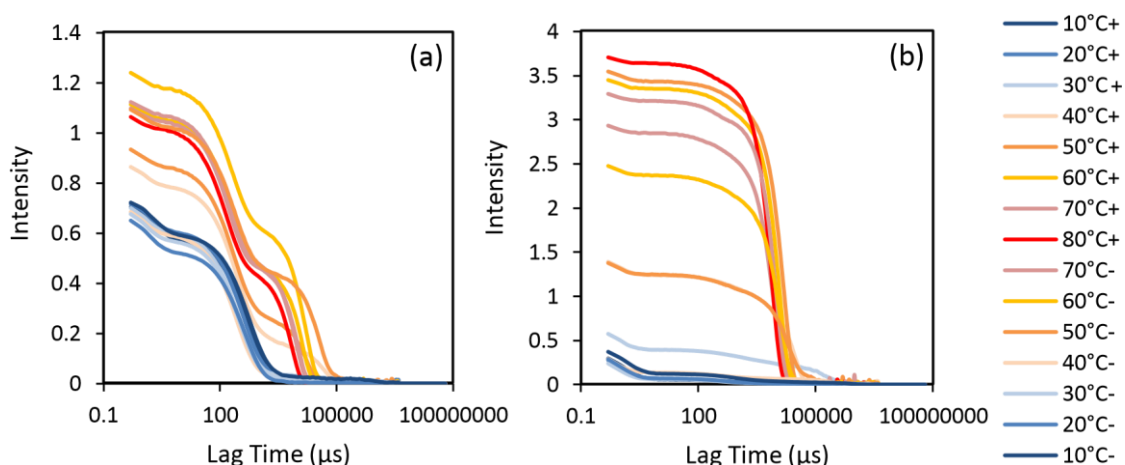


Figure 129. Autocorrelation functions from dynamic light scattering measurements (angle 173°) of temperature cycle from 10-80-10°C with unfiltered aqueous urea solution of concentration 522.61 g/L from the first experimental run (a) and second experimental run (b).

For the second run of the PTFE filtered 522.61 g/L solution shown in Figure 130, the Malvern® Zetasizer software was unable to analyse the autocorrelation functions that were obtained due to the poor data at some temperatures. This meant that some stages in the temperature cycle had to be omitted.

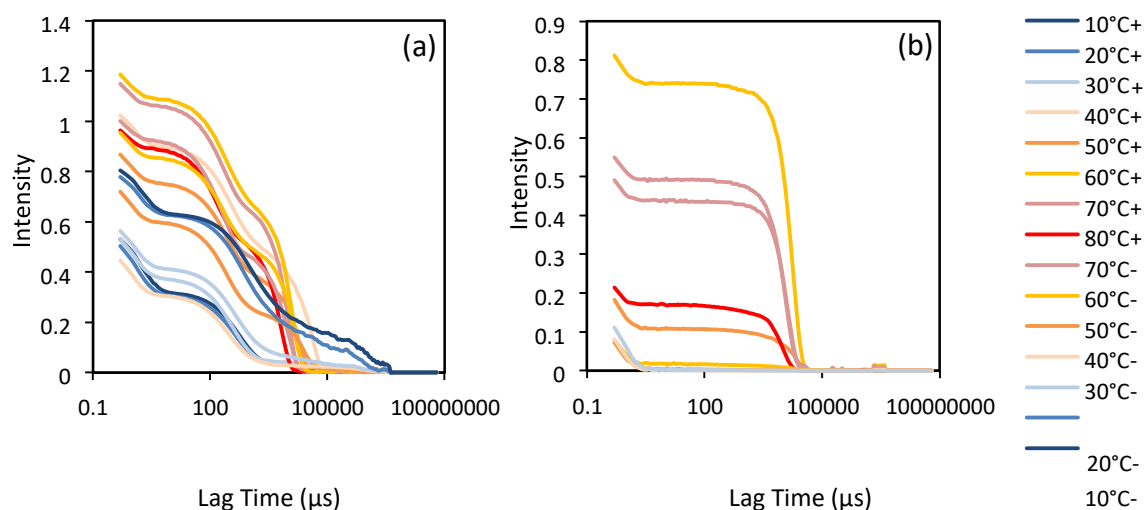


Figure 130. Autocorrelation functions from dynamic light scattering measurements (angle 173°) of temperature cycle from 10-80-10°C with 0.1 μm PTFE filtered aqueous urea solution of concentration 522.61 g/L from the first experimental run (a) and second experimental run (b).

8.9.1.2 Unfiltered and 0.1 μm Filtered Urea Solutions 785.15 g/L

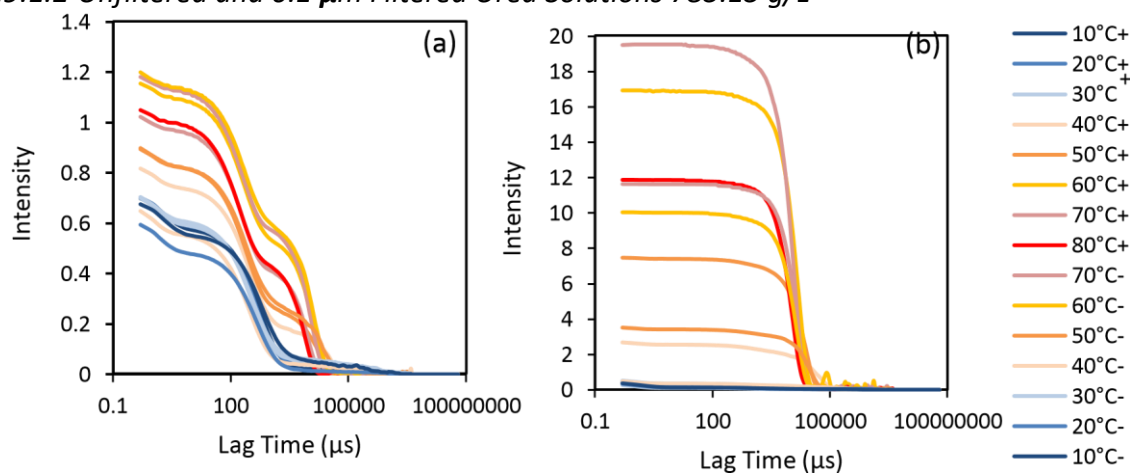


Figure 131. Autocorrelation functions from dynamic light scattering measurements (angle 173°) of temperature cycle from 10-80-10°C with unfiltered aqueous urea solution of concentration 785.15 g/L from the first experimental run (a) and second experimental run (b).

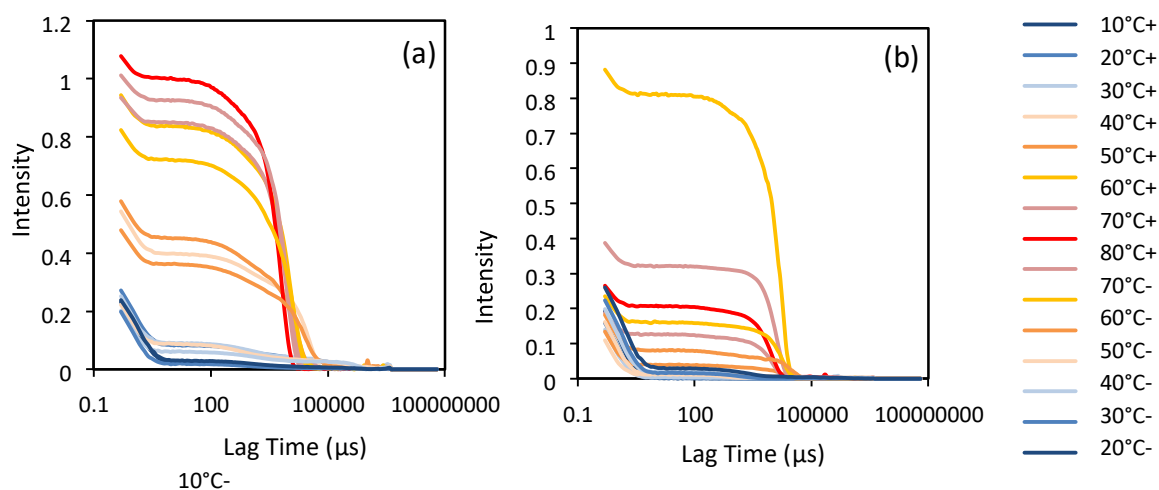


Figure 132. Autocorrelation functions from dynamic light scattering measurements (angle 173°) of temperature cycle from 10-80-10°C with 0.1 μm PTFE filtered aqueous urea solution of concentration 785.15 g/L from the first experimental run (a) and second experimental run (b).

8.9.1.3 Unfiltered and 0.1 μm Filtered Urea Solutions 1149.74 g/L

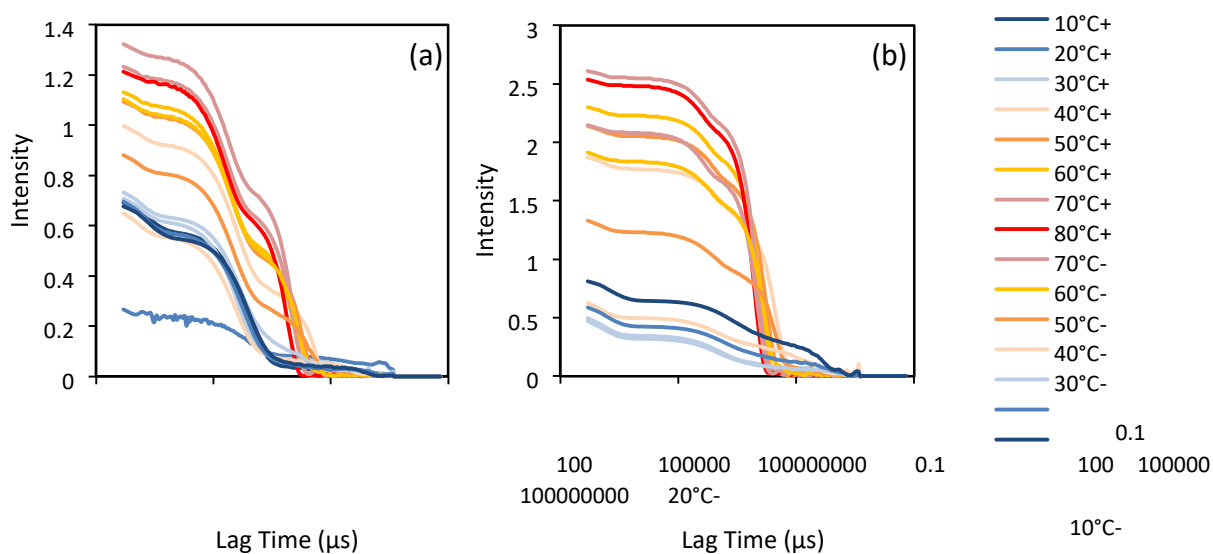


Figure 133. Autocorrelation functions from dynamic light scattering measurements (angle 173°) of temperature cycle from 10-80-10°C with unfiltered filtered aqueous urea solution of concentration 1149.74 g/L from the first experimental run (a) and second experimental run (b).

There were also issues with nucleation taking place with the highest concentration of urea and the autocorrelation functions are given in Figure 134. The lower temperatures in the cycle were therefore omitted to prevent this.

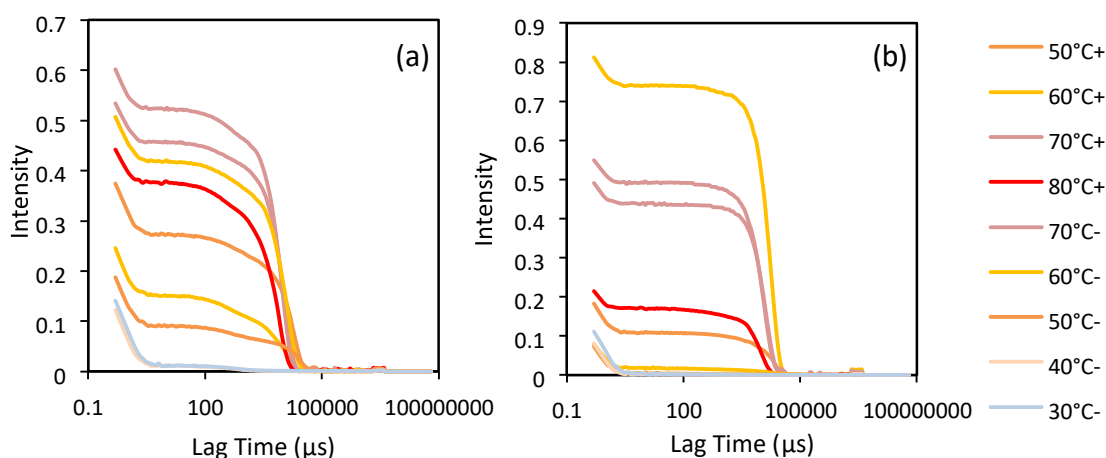


Figure 134. Autocorrelation functions from dynamic light scattering measurements (angle 173°) of temperature cycle from 50-80-30°C with 0.1 μm PTFE filtered aqueous urea solution of concentration 1149.74 g/L from the first experimental run (a) and second experimental run (b).

8.9.2 Urea Solutions Mean Count Rates vs. Temperature

The mean count rates vs. temperature are given in Figure 135, Figure 136, and Figure 137 for the 522.61, 785.15 and 1149.74 g/L solutions respectively.

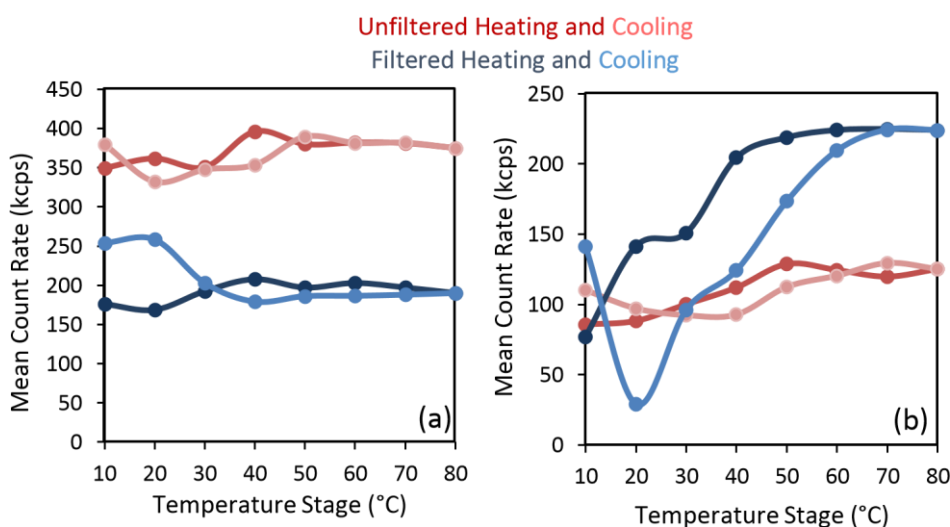


Figure 135. Mean count rate recorded in kilo counts per second for each temperature stage during the dynamic light scattering measurements for urea concentration 522.61 g/L both for unfiltered (red) and 0.1 μm PTFE

filtered (blue) solution. The heating stages are presented in the darker colour. Both the first experimental run (a) and second experimental run (b) are shown.

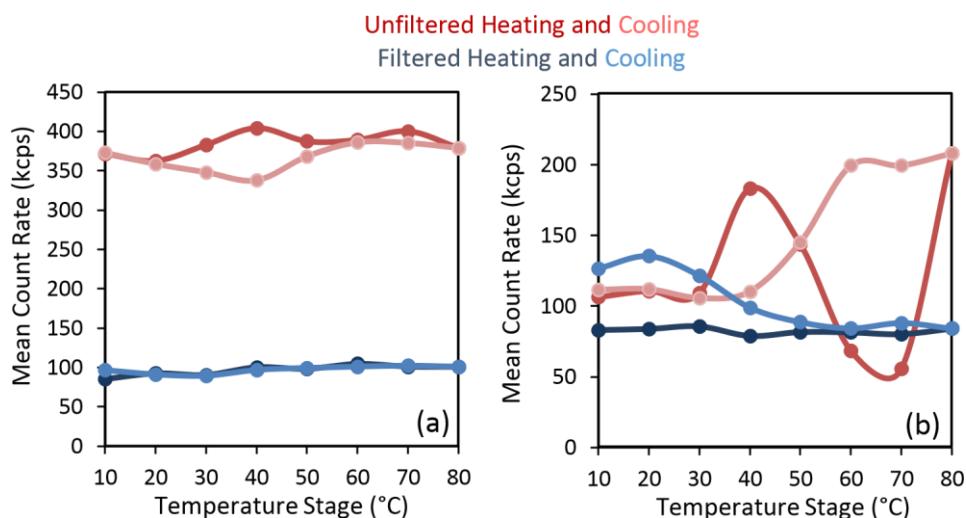


Figure 136. Mean count rate recorded in kilo counts per second for each temperature stage during the dynamic light scattering measurements for urea concentration 785.15 g/L both for unfiltered (red) and 0.1 μm PTFE filtered (blue) solution. The heating stages are presented in the darker colour. Both the first experimental run (a) and second experimental run (b) are shown.

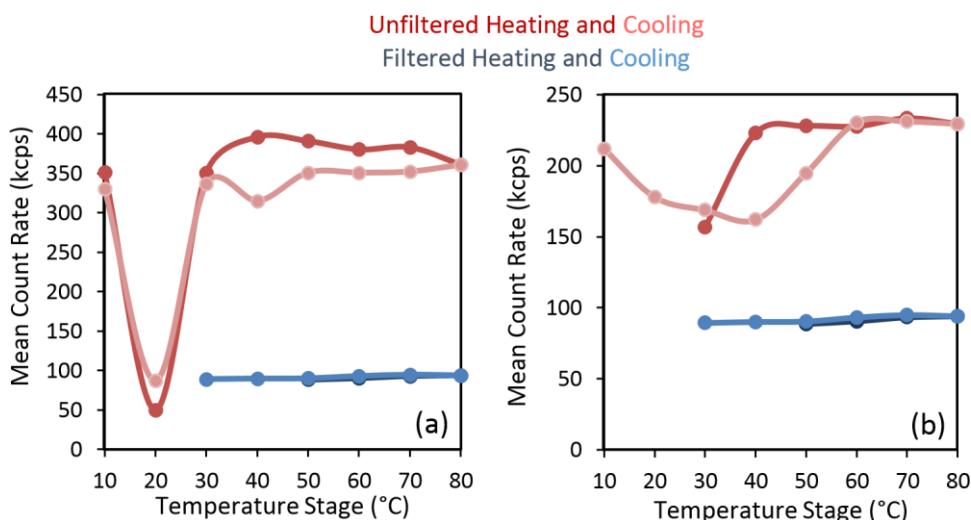


Figure 137. Mean count rate recorded in kilo counts per second for each temperature stage during the dynamic light scattering measurements for urea concentration 1149.74 g/L both for unfiltered (red) and 0.1 μm PTFE filtered (blue) solution. The heating stages are presented in the darker colour. Both the first experimental run (a) and second experimental run (b) are shown.

8.9.3 Deconvolution of Autocorrelation Functions: Analysis of Three Decays vs.

Temperature

Similarly done above for glycine solutions, the coefficients from the decay fitting equation were represented as a fraction of the total of all the coefficients from the

three decay terms and plotted in the following graphs. This gives a measure of the influence of each decay in the whole function and how that changes with temperature. The data from the first and second run is plotted.

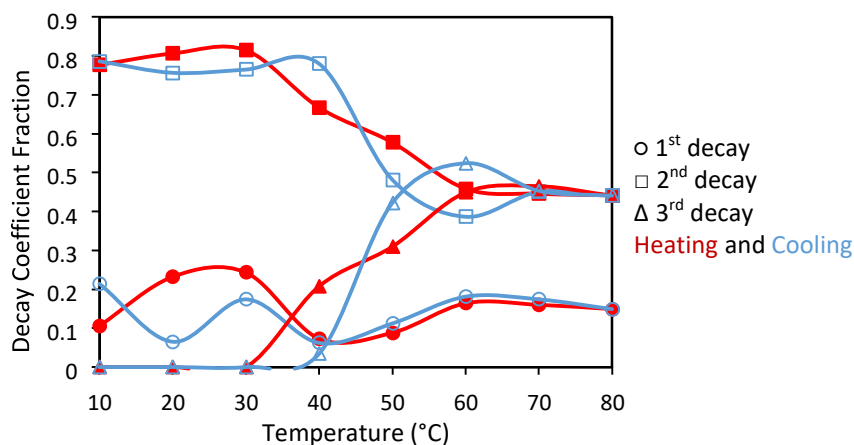


Figure 138. Coefficient values from the decay fitting with 3 decays present in the autocorrelation curve for the first run of unfiltered 522.61 g/L aqueous urea solutions for the 1st decay [○], 2nd decay [□] and 3rd decay [Δ]. The heating stages are in red and the cooling stages are in blue.

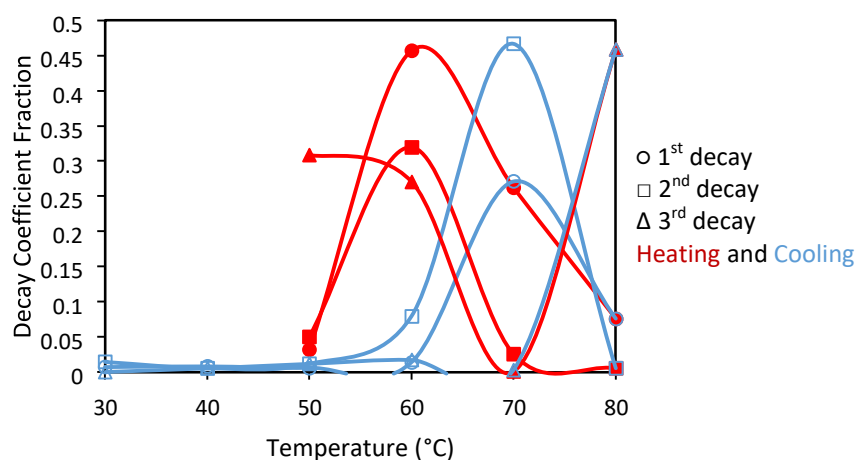


Figure 139. Coefficient values from the decay fitting with 3 decays present in the autocorrelation curve for the second run of unfiltered 522.61 g/L aqueous urea solutions for the 1st decay [○], 2nd decay [□] and 3rd decay [Δ]. The heating stages are in red and the cooling stages are in blue.

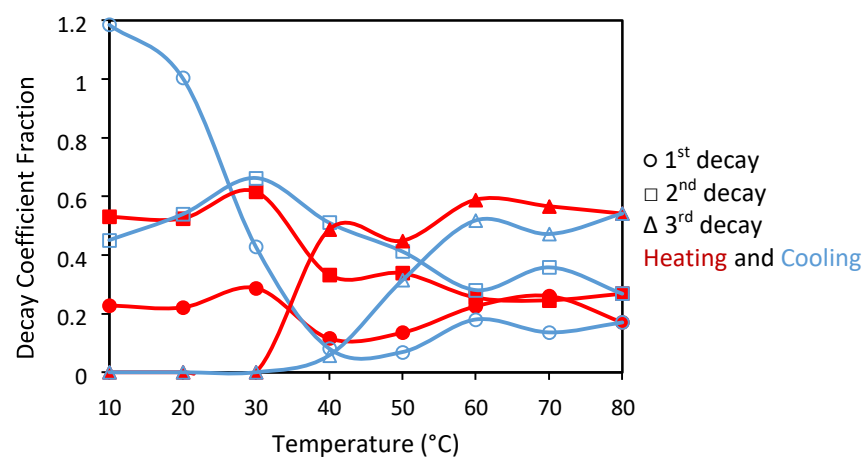


Figure 140. Coefficient values from the decay fitting with 3 decays present in the autocorrelation curve for the first run of 0.1 μm PTFE filtered 522.61 g/L aqueous urea solutions for the 1st decay [\circ], 2nd decay [\square] and 3rd decay [Δ]. The heating stages are in red and the cooling stages are in blue.

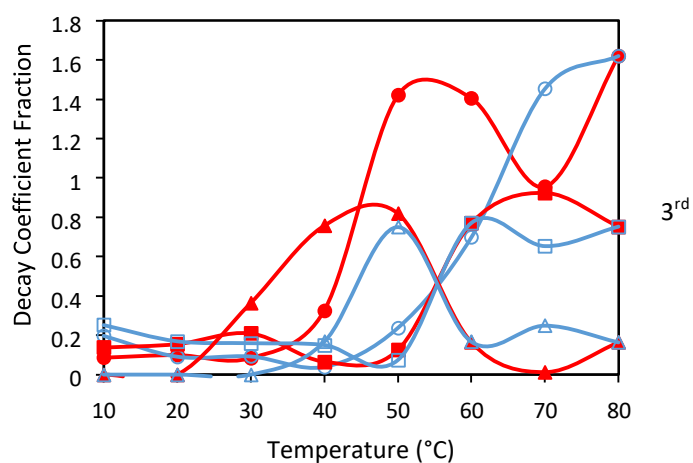


Figure 141. Coefficient values from the decay fitting with 3 decays present in the autocorrelation curve for the second run of 0.1 μm PTFE filtered 522.61 g/L aqueous urea solutions for the 1st decay [○], 2nd decay [□] and 3rd decay [Δ]. The heating stages are in red and the cooling stages are in blue.

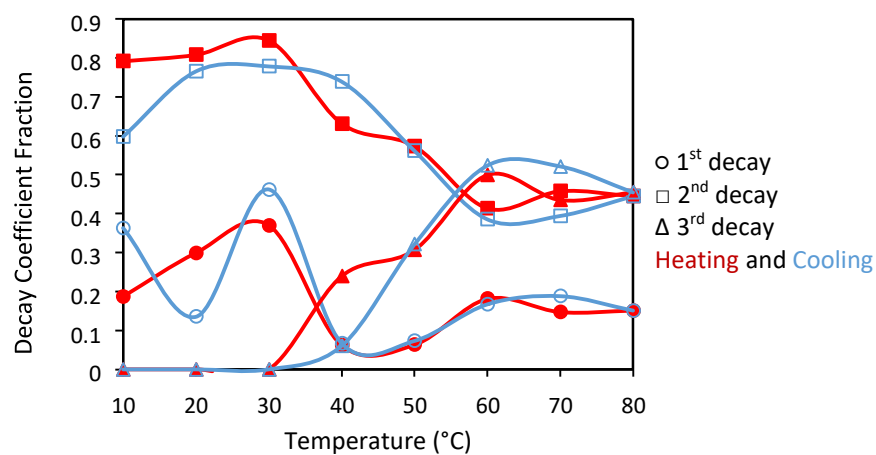


Figure 142. Coefficient values from the decay fitting with 3 decays present in the autocorrelation curve for the first run of unfiltered 785.15 g/L aqueous urea solutions for the 1st decay [○], 2nd decay [□] and 3rd decay [Δ]. The heating stages are in red and the cooling stages are in blue.

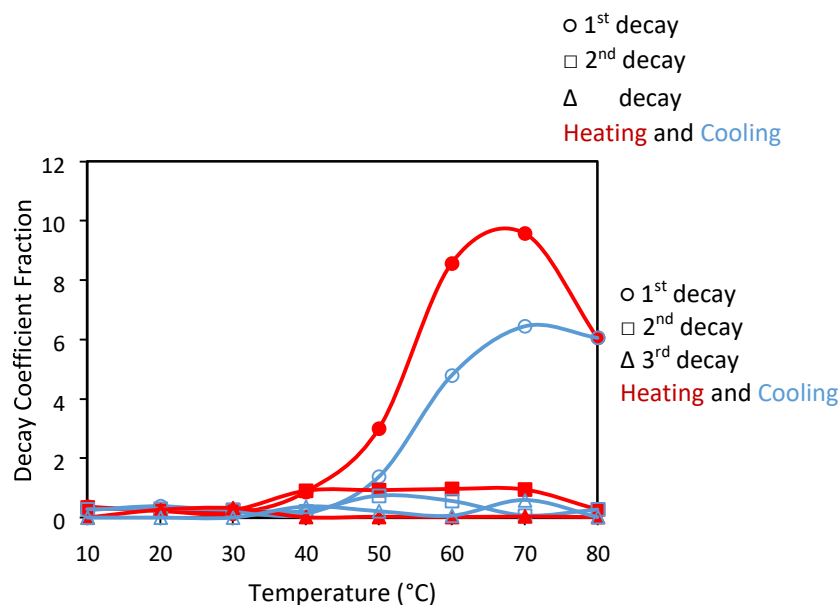


Figure 143. Coefficient values from the decay fitting with 3 decays present in the autocorrelation curve for the second run of unfiltered 785.15 g/L aqueous urea solutions for the 1st decay [○], 2nd decay [□] and 3rd decay [Δ]. The heating stages are in red and the cooling stages are in blue.

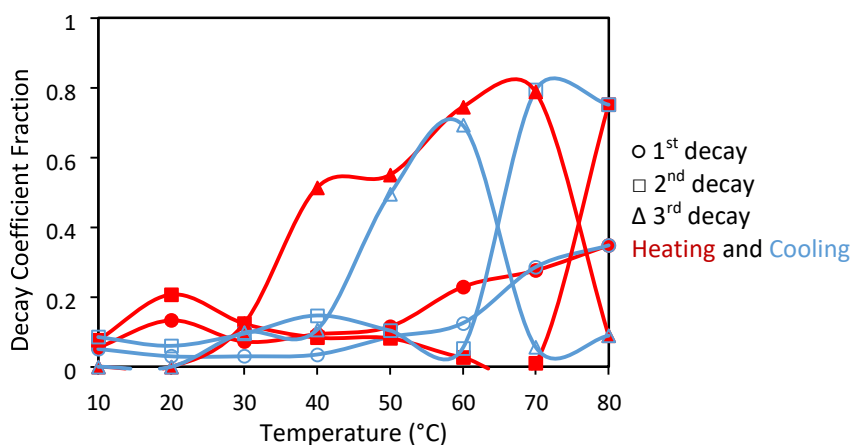


Figure 144. Coefficient values from the decay fitting with 3 decays present in the autocorrelation curve for the first run of 0.1 μ m PTFE filtered 785.15 g/L aqueous urea solutions for the 1st decay [○], 2nd decay [□] and 3rd decay [Δ]. The heating stages are in red and the cooling stages are in blue.

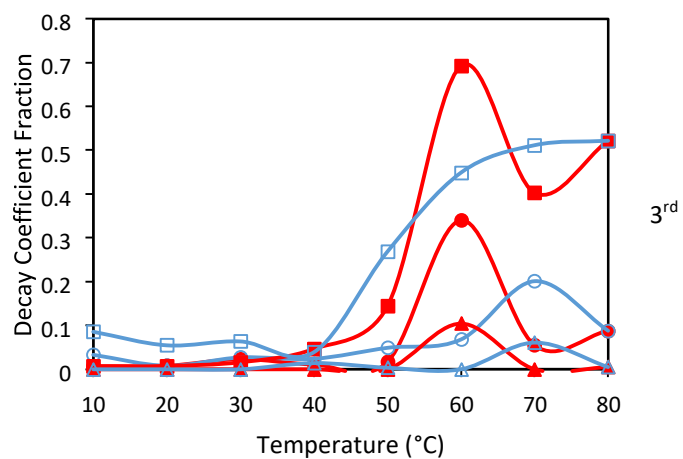


Figure 145. Coefficient values from the decay fitting with 3 decays present in the autocorrelation curve for the second run of 0.1 µm PTFE filtered 785.15 g/L aqueous urea solutions for the 1st decay [○], 2nd decay [□] and 3rd decay [Δ]. The heating stages are in red and the cooling stages are in blue.

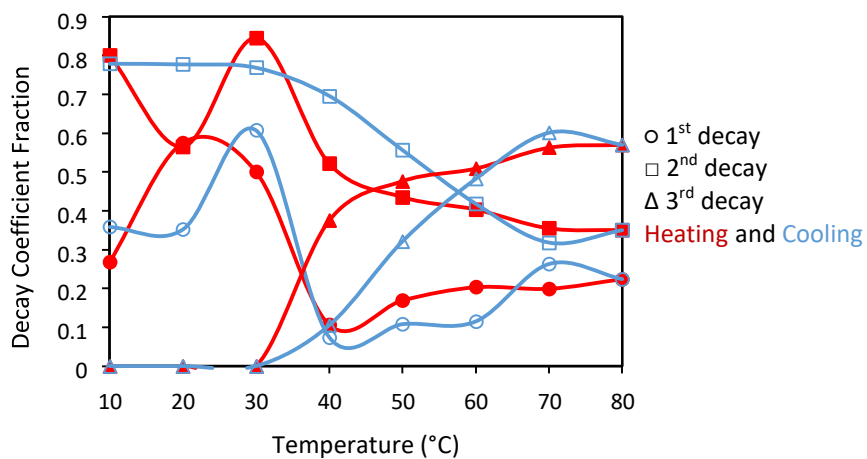


Figure 146. Coefficient values from the decay fitting with 3 decays present in the autocorrelation curve for the first run of unfiltered 1149.75 g/L aqueous urea solutions for the 1st decay [○], 2nd decay [□] and 3rd decay [Δ]. The heating stages are in red and the cooling stages are in blue.

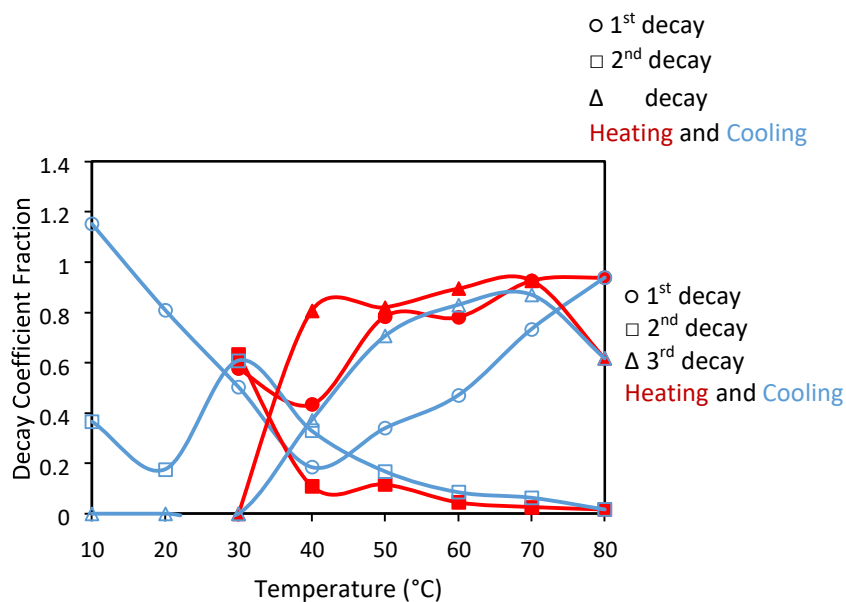


Figure 147. Coefficient values from the decay fitting with 3 decays present in the autocorrelation curve for the second run of unfiltered 1149.75 g/L aqueous urea solutions for the 1st decay [○], 2nd decay [□] and 3rd decay [Δ]. The heating stages are in red and the cooling stages are in blue.

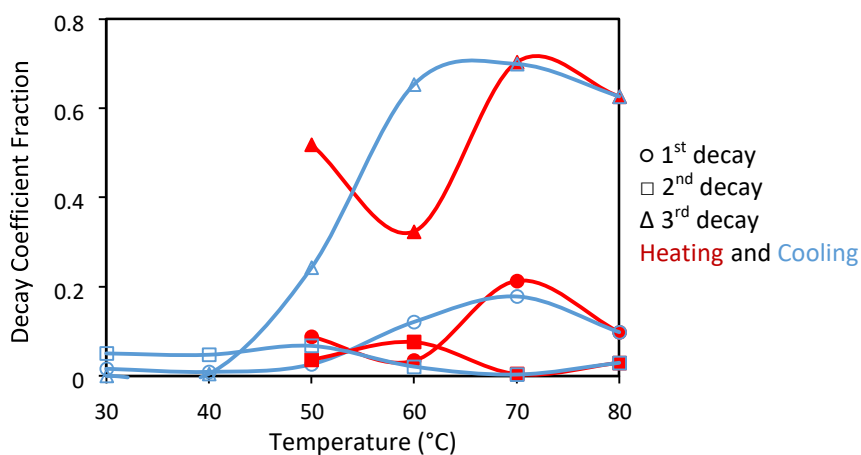


Figure 148. Coefficient values from the decay fitting with 3 decays present in the autocorrelation curve for the first run of 0.1 μ m PTFE filtered 1149.74 g/L aqueous urea solutions for the 1st decay [○], 2nd decay [□] and 3rd decay [Δ]. The heating stages are in red and the cooling stages are in blue.

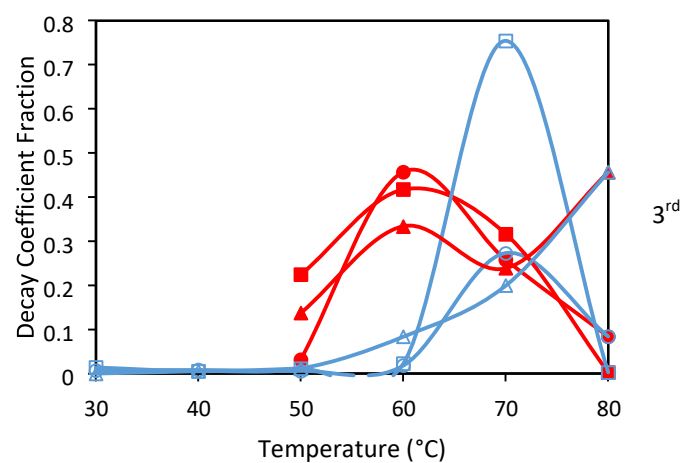


Figure 149. Coefficient values from the decay fitting with 3 decays present in the autocorrelation curve for the second run of 0.1 μm PTFE filtered 1149.74 g/L aqueous urea solutions for the 1st decay [○], 2nd decay [□] and 3rd decay [Δ]. The heating stages are in red and the cooling stages are in blue.

○ 1st decay
 □ 2nd decay
 Δ decay
 Heating and Cooling

8.9.4 Mean Cluster Diameters vs. Temperature

The changes in average hydrodynamic diameter with temperature were plotted for the first, second and third decay in the autocorrelation function and are given in Figure 150, Figure 151 and Figure 152 for both the first and second runs.

8.9.4.1 1st Decay

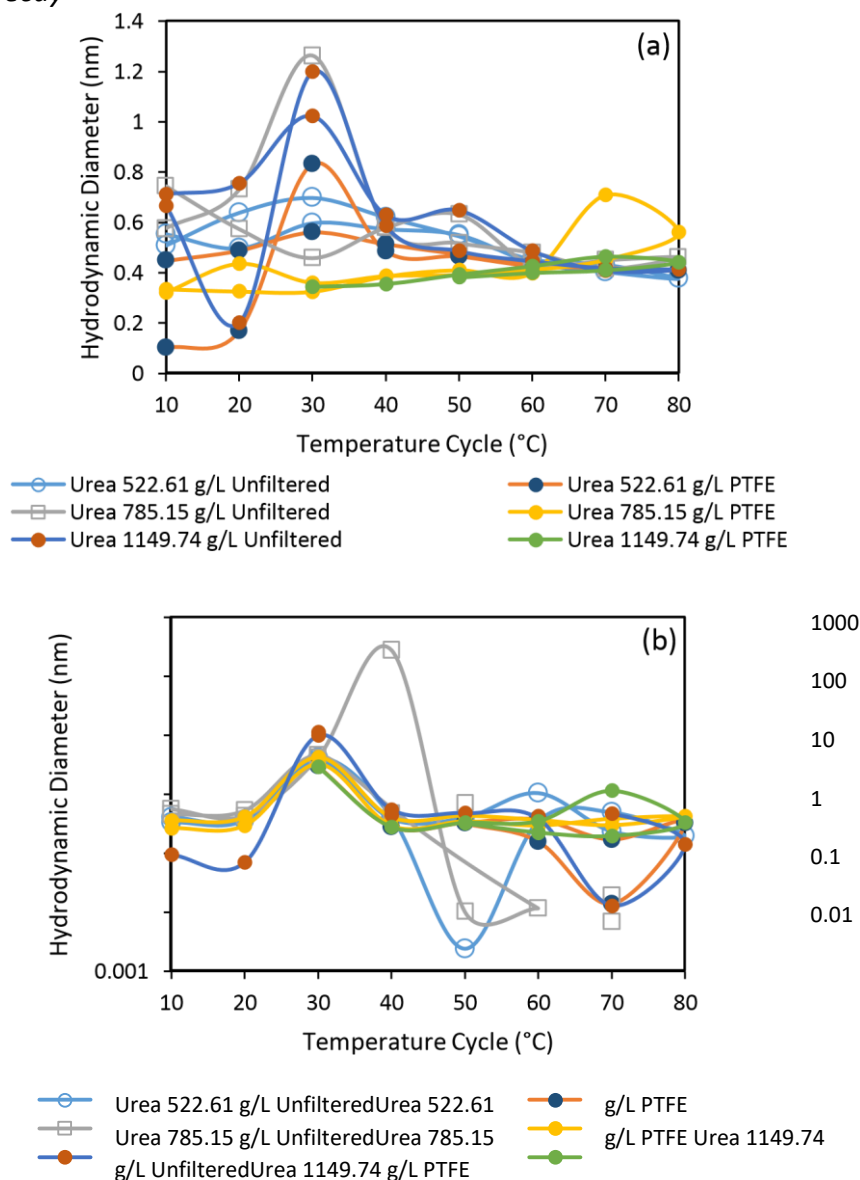


Figure 150. Average hydrodynamic diameters plotted against temperature for all urea experiments both filtered and unfiltered corresponding to the first decay in the autocorrelation function for the first (a) and second run (b) of experiments.

8.9.4.2 2nd Decay

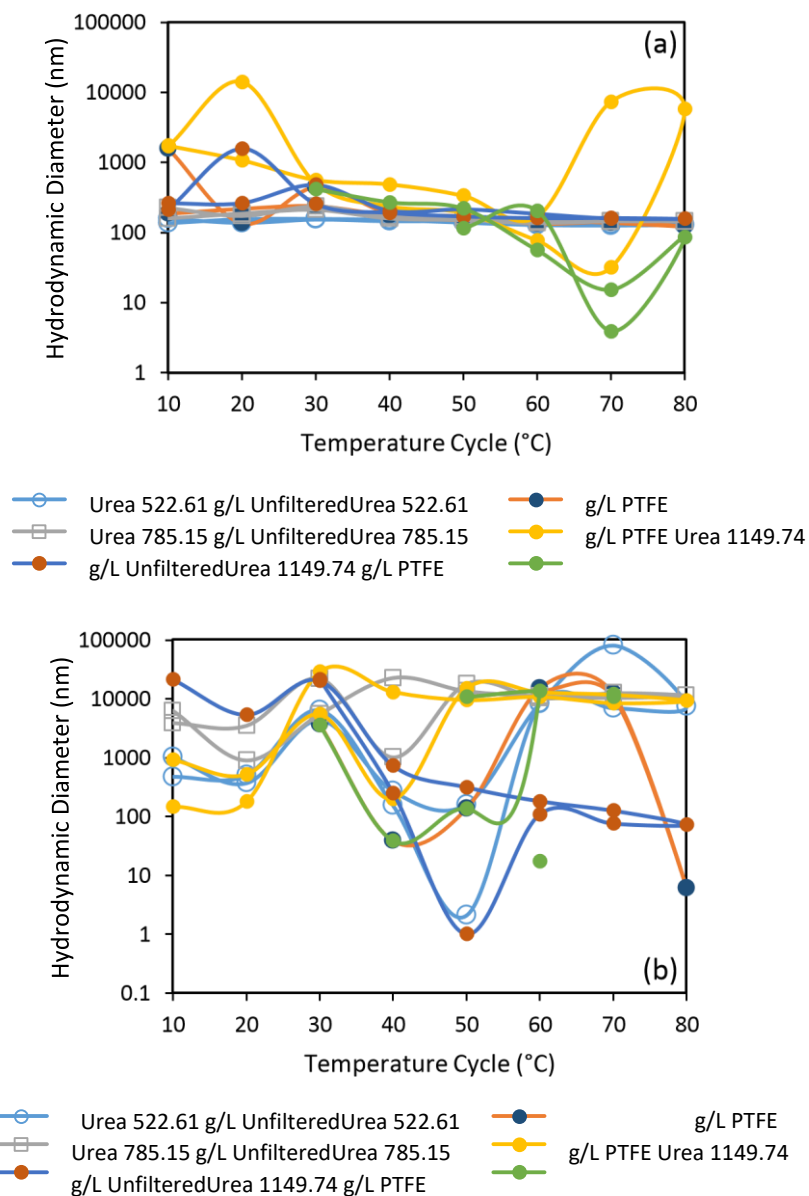


Figure 151. Average hydrodynamic diameters plotted against temperature for all urea experiments both filtered and unfiltered corresponding to the second decay in the autocorrelation function for the first (a) and second run (b) of experiments.

8.9.4.3 3rd Decay

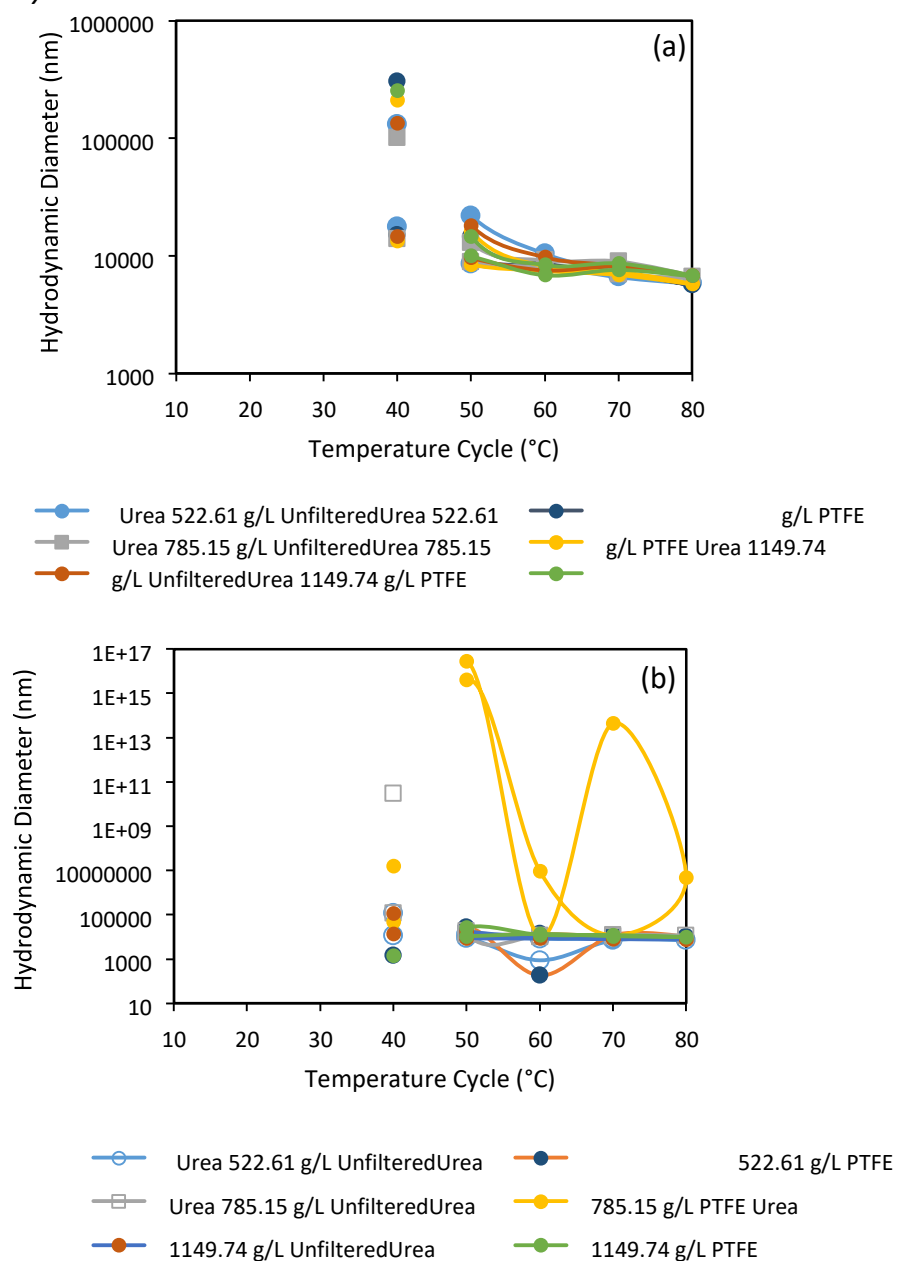


Figure 152. Average hydrodynamic diameters plotted against temperature for all urea experiments both filtered and unfiltered corresponding to the third decay in the autocorrelation function for the first (a) and second run (b) of experiments.

8.10 UREA SOLUTIONS NANOSIGHT DATA

8.10.1 Cluster Size Distributions

The cluster size distributions from the NanoSight measurements are given in the following section for both the first and second experimental runs of urea.

8.10.1.1 Unfiltered Urea Solution 522.61 g/L

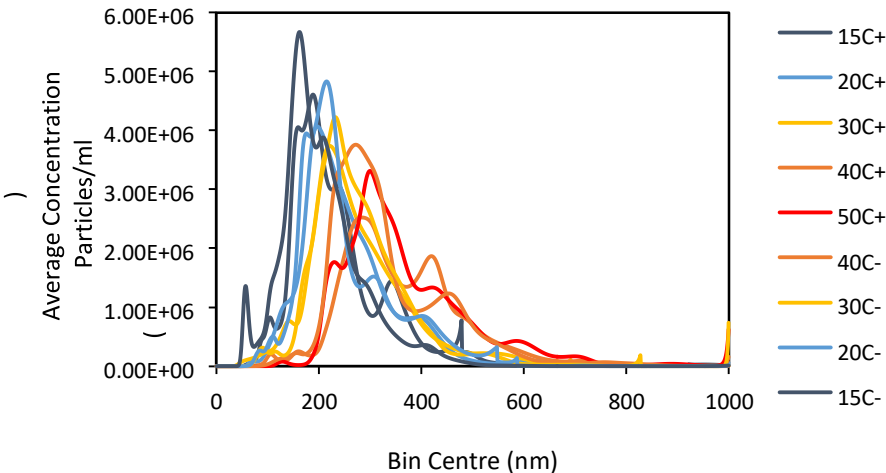


Figure 153. Cluster size distributions from NanoSight measurements of temperature cycle from 15-50-15°C with the first run of unfiltered aqueous urea solution of concentration 522.61 g/L.

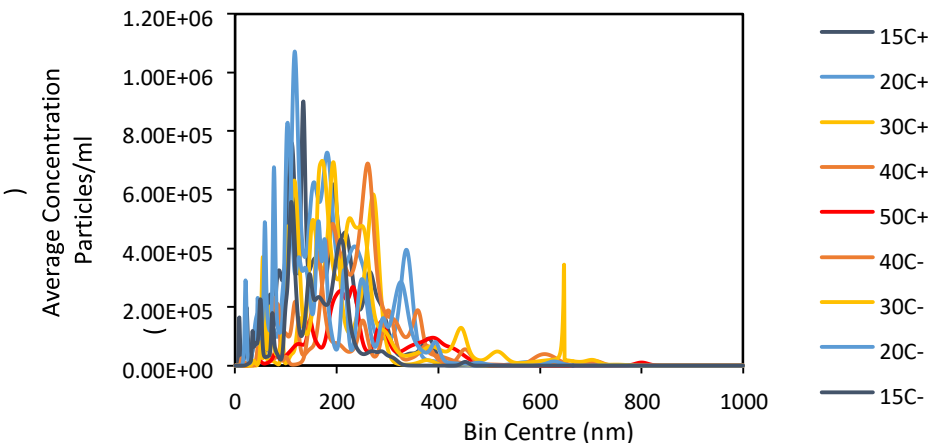


Figure 154. Cluster size distributions from NanoSight measurements of temperature cycle from 15-50-15°C with the second run of unfiltered aqueous urea solution of concentration 522.61 g/L.

0.1 μ

8.10.1.2 *m* Filtered Urea Solution 522.61 g/L

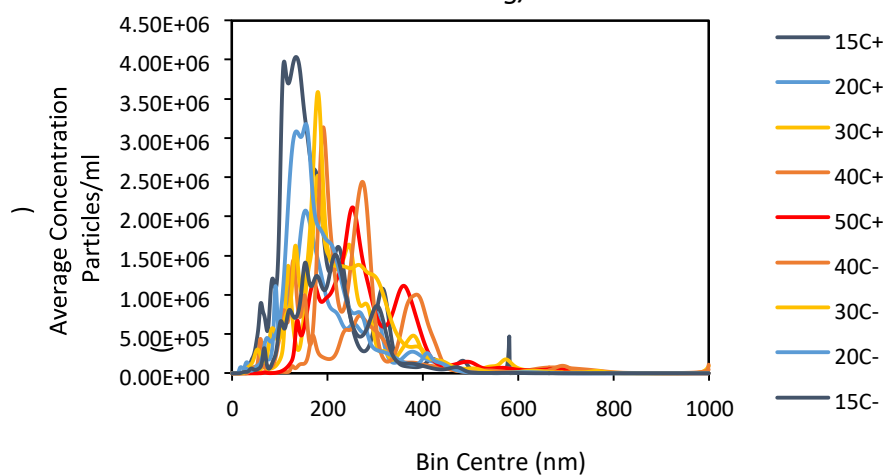


Figure 155. Cluster size distributions from NanoSight measurements of temperature cycle from 15-50-15°C with the first run of 0.1 μ m PTFE filtered aqueous urea solution of concentration 522.61 g/L.

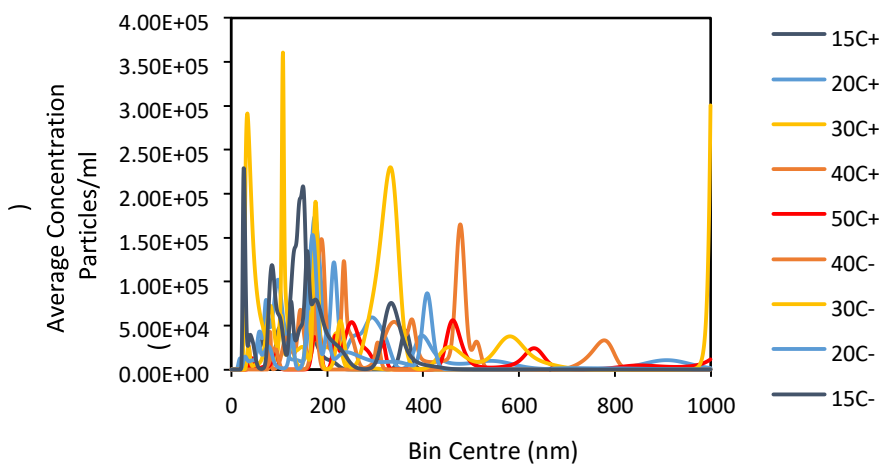


Figure 156. Cluster size distributions from NanoSight measurements of temperature cycle from 15-50-15°C with the second run of 0.1 μ m PTFE filtered aqueous urea solution of concentration 522.61 g/L.

8.10.1.3 Unfiltered Urea Solution 785.15 g/L

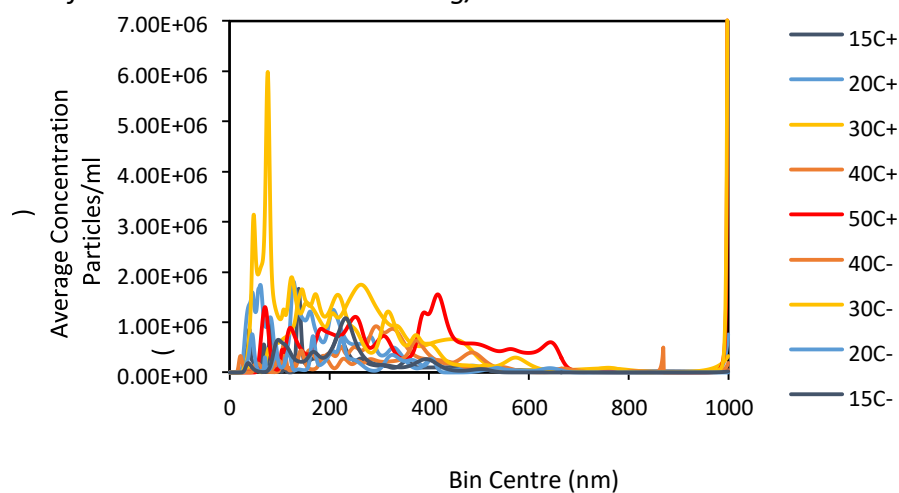


Figure 157. Cluster size distributions from NanoSight measurements of temperature cycle from 15-50-15°C with the first run of unfiltered aqueous urea solution of concentration 785.15 g/L.

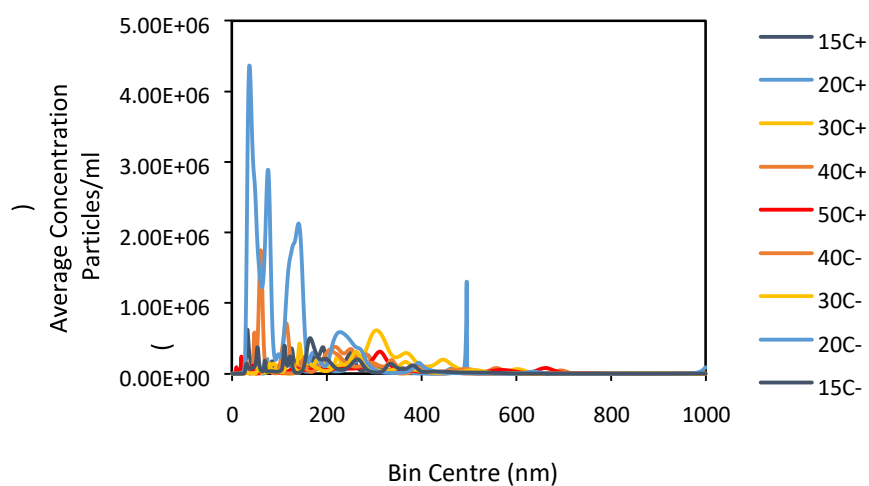


Figure 158. Cluster size distributions from NanoSight measurements of temperature cycle from 15-50-15°C with the second run of unfiltered aqueous urea solution of concentration 785.15 g/L.

0.1 μ

8.10.1.4 m Filtered Urea Solution 785.15 g/L

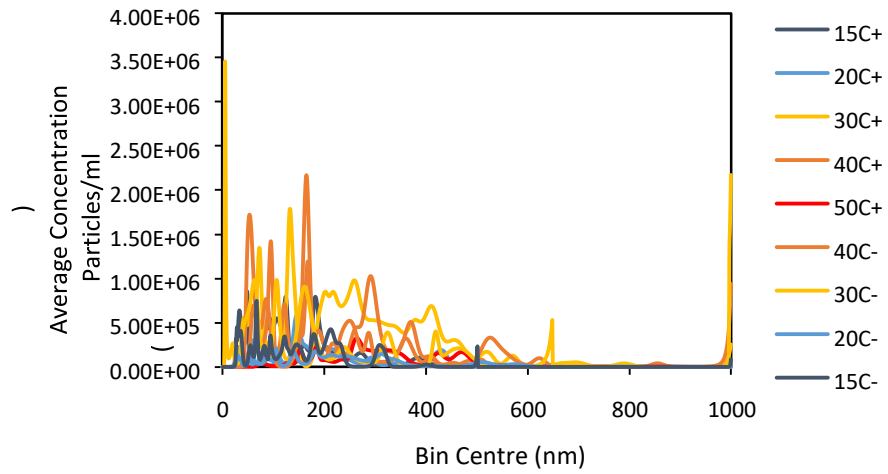


Figure 159. Cluster size distributions from NanoSight measurements of temperature cycle from 15-50-15°C with the first run of 0.1 μ m PTFE filtered aqueous urea solution of concentration 785.15 g/L.

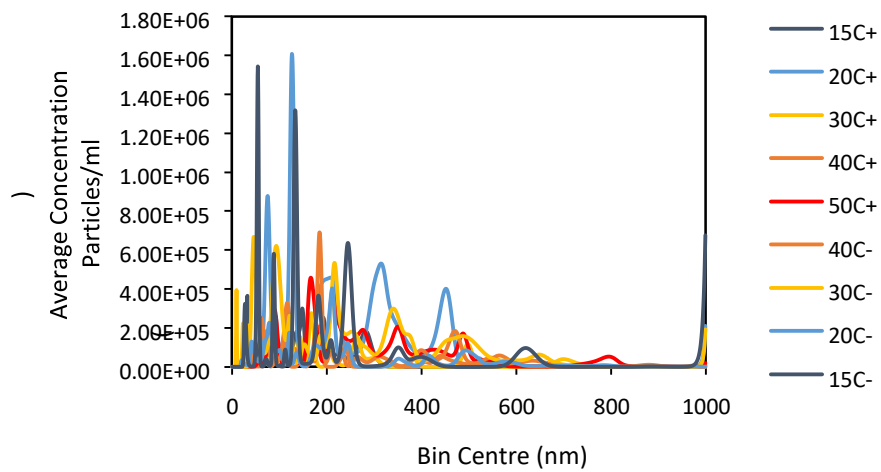


Figure 160. Cluster size distributions from NanoSight measurements of temperature cycle from 15-50-15°C with the second run of 0.1 μ m PTFE filtered aqueous urea solution of concentration 785.15 g/L.

8.10.1.5 Unfiltered Urea Solution 1149.74 g/L

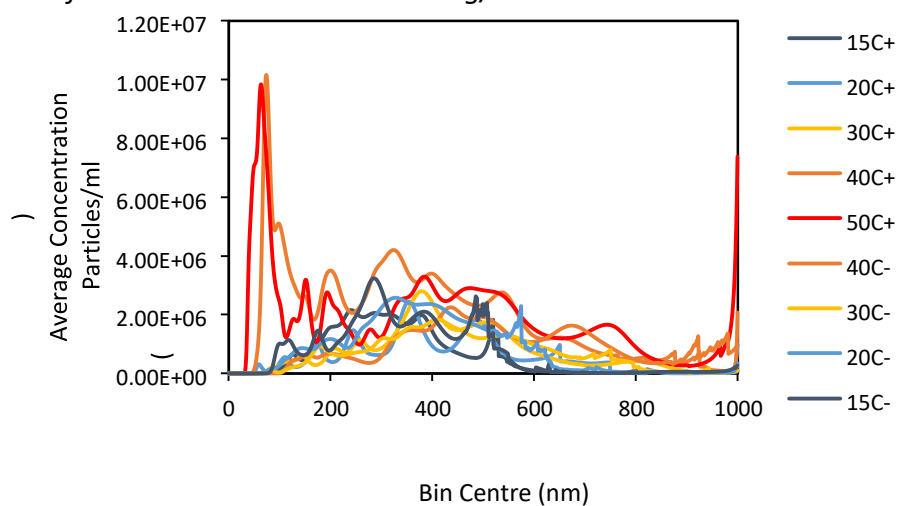


Figure 161. Cluster size distributions from NanoSight measurements of temperature cycle from 15-50-15°C with the first run of unfiltered aqueous urea solution of concentration 1149.74 g/L.

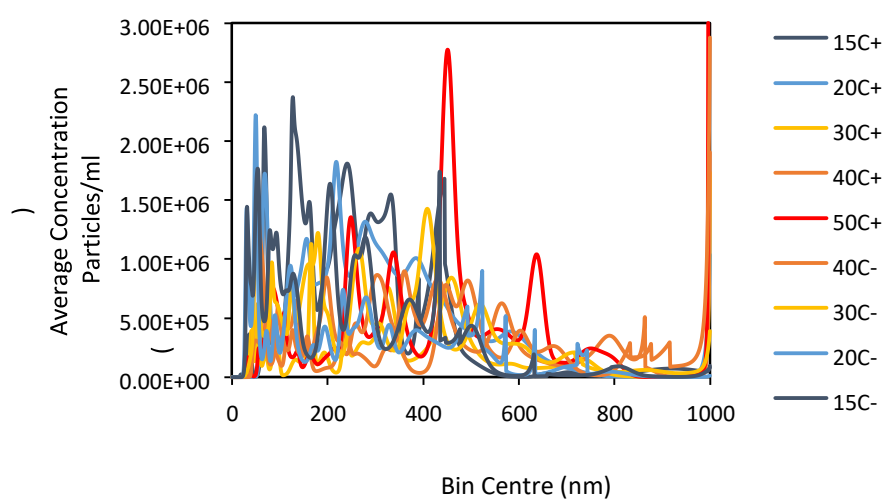


Figure 162. Cluster size distributions from NanoSight measurements of temperature cycle from 15-50-15°C with the second run of unfiltered aqueous urea solution of concentration 1149.74 g/L.

0.1 μ

8.10.1.6 m PTFE Filtered Urea Solution 1149.74 g/L

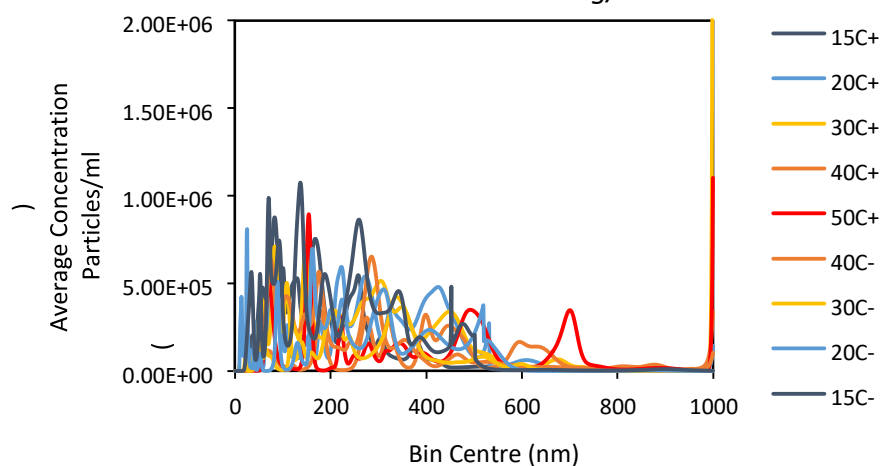


Figure 163. Cluster size distributions from NanoSight measurements of temperature cycle from 15-50-15°C with the first run of 0.1 μ m PTFE filtered aqueous urea solution of concentration 1149.74 g/L.

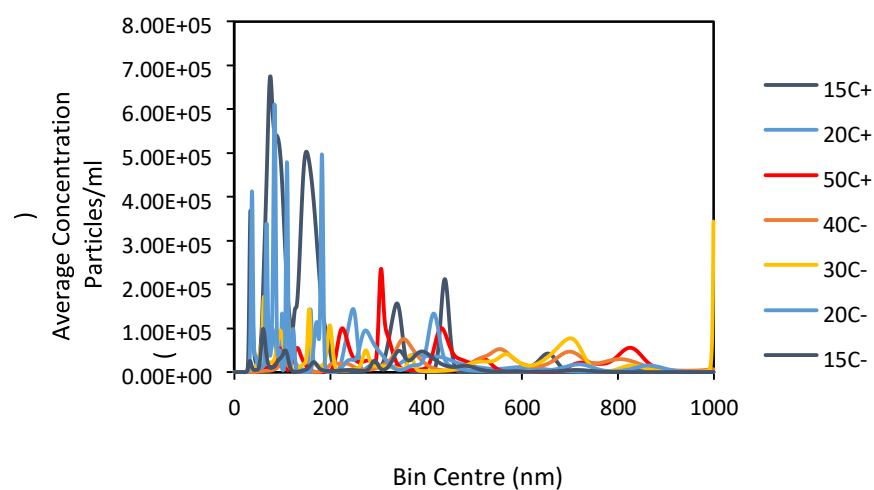


Figure 164. Cluster size distributions from NanoSight measurements of temperature cycle from 15-50-15°C with the second run of 0.1 μ m PTFE filtered aqueous urea solution of concentration 1149.74 g/L.

8.10.2 Cluster Size Distributions with 20 nm Bin Size for First Run of Urea

The data was re-plotted and re-binned in order to see more clearly the shift in size distribution with the temperature change. The first run of urea is presented here and the second run can be found in the appendix in section 10.2.

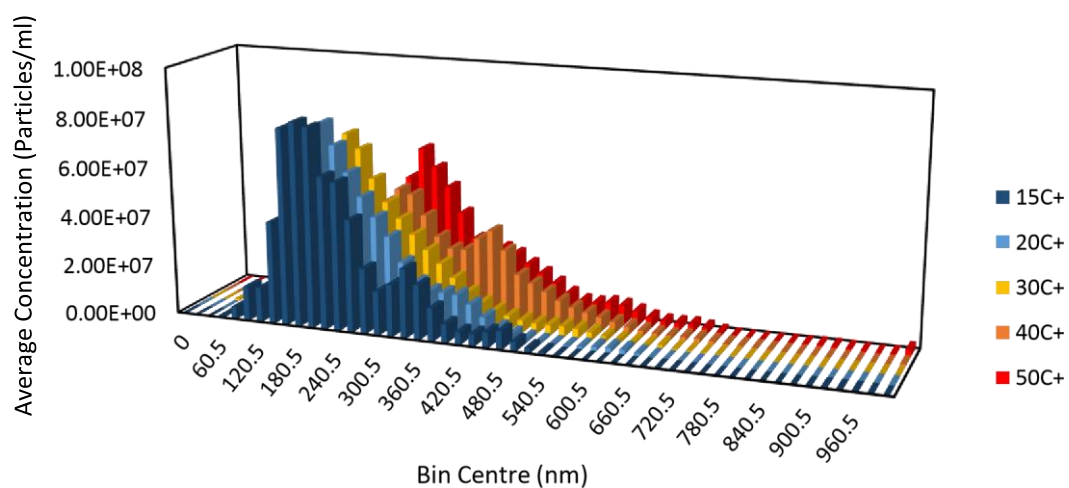


Figure 165. Cluster size distributions from NanoSight measurements of temperature cycle from 15-50-15°C with the first run of unfiltered filtered aqueous urea solution of concentration 522.61 g/L with 20 nm bin sizes for the x-axis.

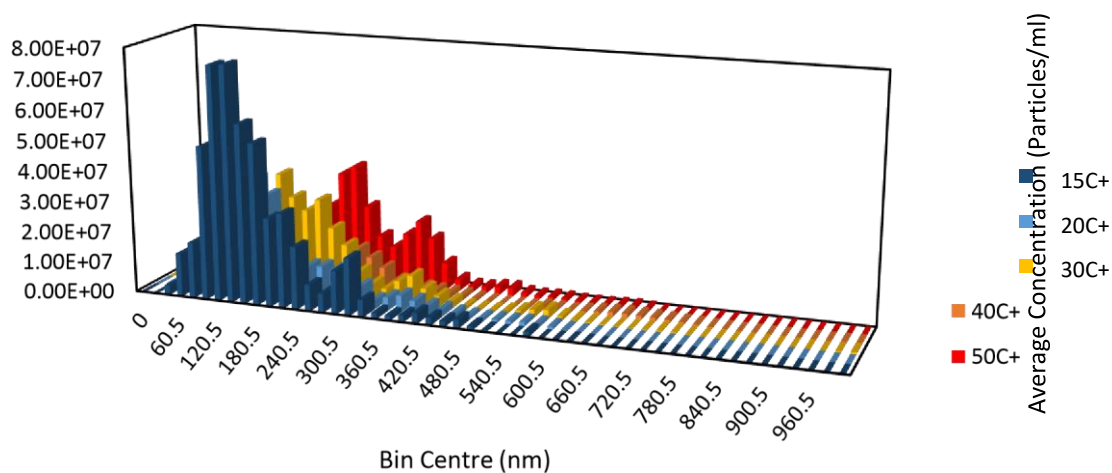


Figure 166. Cluster size distributions from NanoSight measurements of temperature cycle from 15-50-15°C with the first run of 0.1 µm PTFE filtered aqueous urea solution of concentration 522.61 g/L with 20 nm bin sizes for the x-axis.

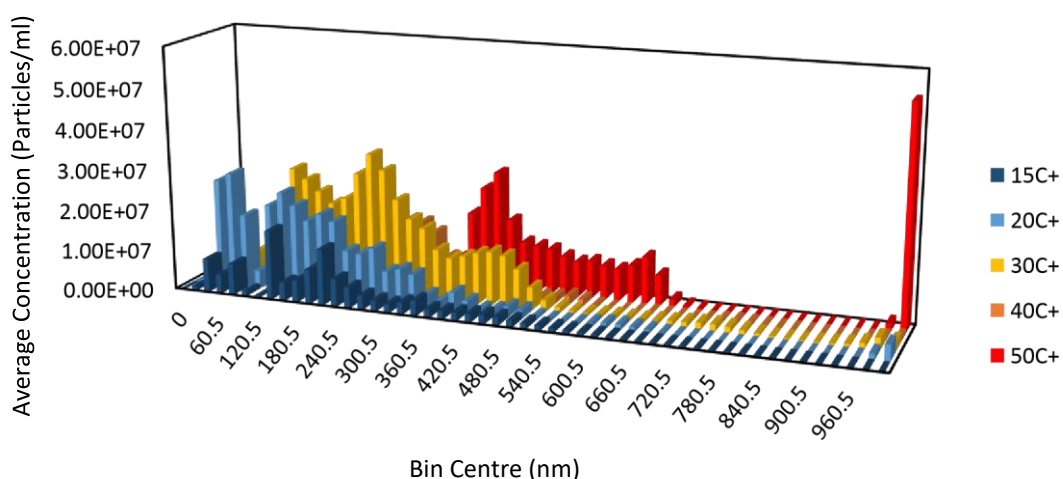


Figure 167. Cluster size distributions from NanoSight measurements of temperature cycle from 15-50-15°C with the first run of unfiltered filtered aqueous urea solution of concentration 785.15 g/L with 20 nm bin sizes for the x-axis.

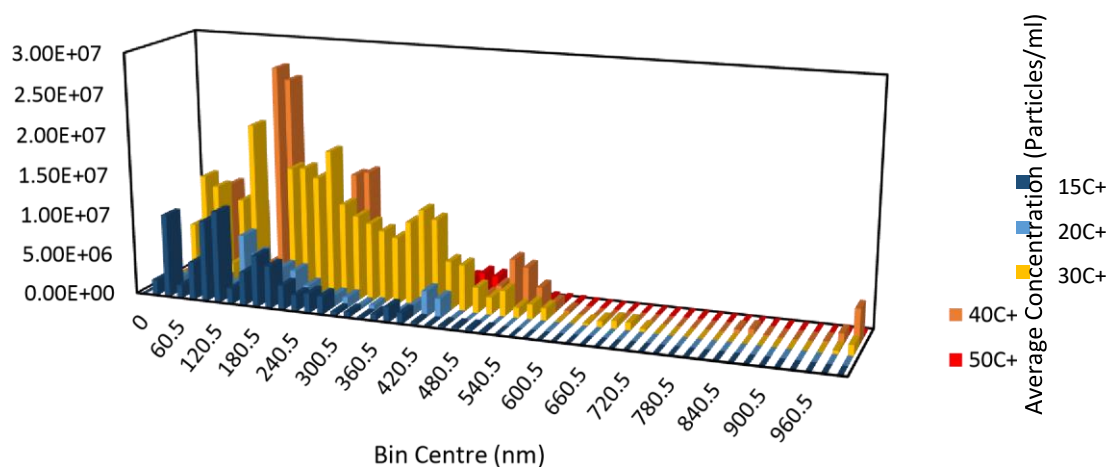


Figure 168. Cluster size distributions from NanoSight measurements of temperature cycle from 15-50-15°C with the first run of 0.1 µm PTFE filtered aqueous urea solution of concentration 785.15 g/L with 20 nm bin sizes for the x-axis.

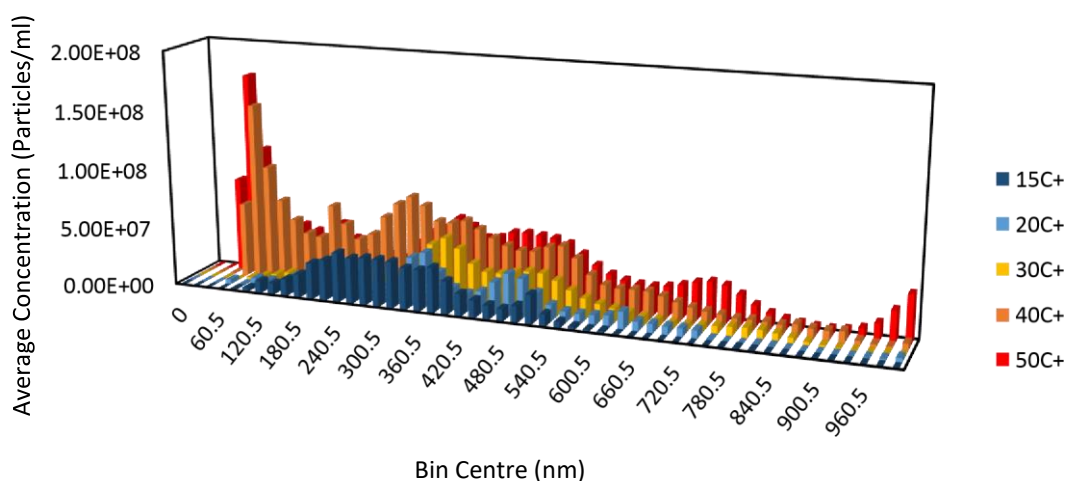


Figure 169. Cluster size distributions from NanoSight measurements of temperature cycle from 15-50-15°C with the first run of unfiltered aqueous urea solution of concentration 1149.74 g/L with 20 nm bin sizes for the x-axis.

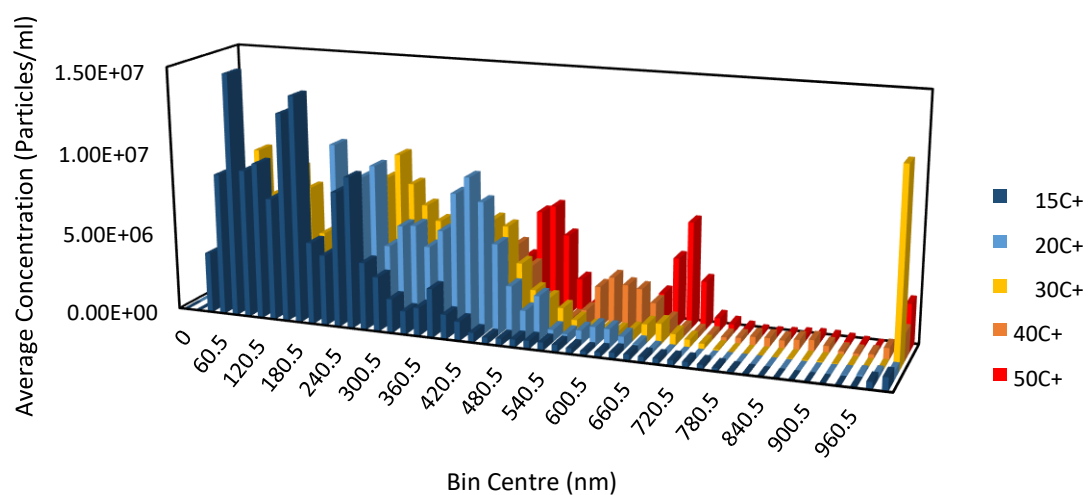


Figure 170. Cluster size distributions from NanoSight measurements of temperature cycle from 15-50-15°C with the first run of 0.1µm PTFE filtered aqueous urea solution of concentration 1149.74 g/L with 20 nm bin sizes for the x-axis.

8.10.3 Changes in Average Cluster Diameter with Temperature for Urea Solutions The changes in average cluster diameter with temperature are plotted for the first and second runs of urea solutions and are given as part (a) and (b) of the following figures respectively.

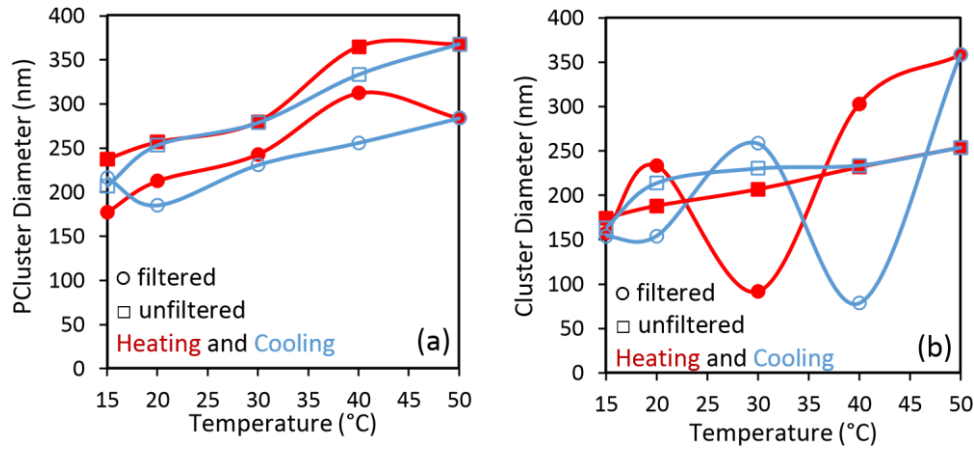


Figure 171. NanoSight measurements of the average cluster diameters with temperature for 522.61 g/L aqueous urea solution for filtered [○] and unfiltered [□] samples with the heating stages given in red and the cooling stages presented in blue. (a) Refers to the first and (b) to the second experimental run.

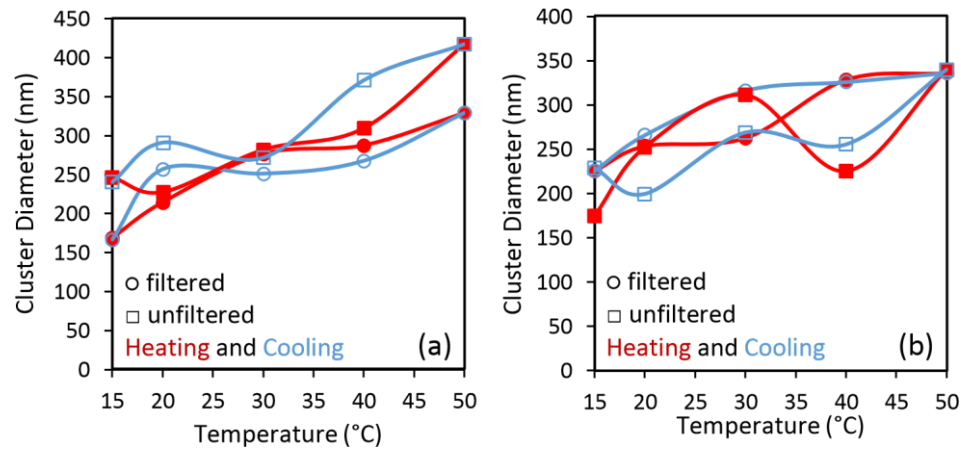


Figure 172. NanoSight measurements of the average cluster diameters with temperature for 785.15 g/L aqueous urea solution for filtered [○] and unfiltered [□] samples with the heating stages given in red and the cooling stages presented in blue. (a) Refers to the first and (b) to the second experimental run.

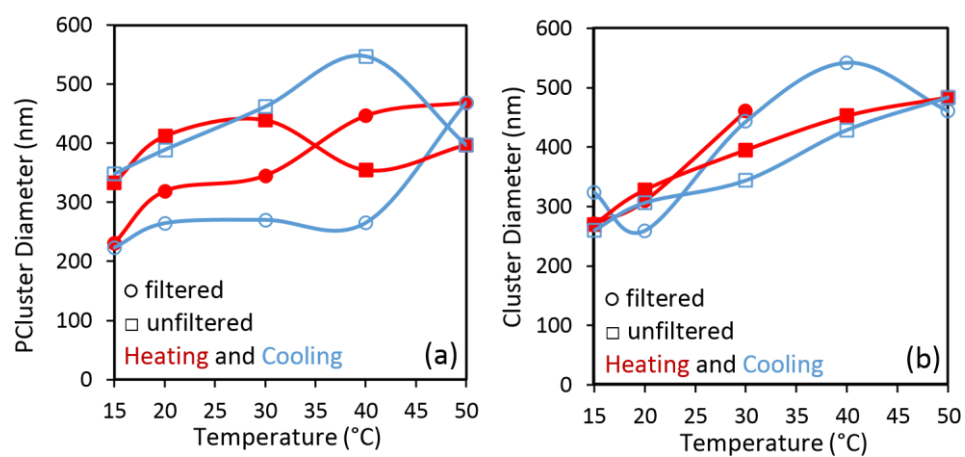


Figure 173. NanoSight measurements of the average cluster diameters with temperature for 1149.74 g/L aqueous urea solution for filtered [○] and unfiltered [□] samples with the heating stages given in red and the cooling stages presented in blue. (a) Refers to the first and (b) to the second experimental run.

8.11 DISCUSSION OF LIGHT SCATTERING RESULTS FOR UREA SOLUTIONS

Urea system was more difficult with regards to the reproducibility in both the dynamic light scattering and NanoSight measurements. There were some trends that carried throughout the repetitions and some of the data is very different as could be seen from the results section previously.

There were similarities when studying the autocorrelation functions where the intensity was found to increase in general with increasing temperature. This was also a feature of the glycine solution experiments. The mean count rate data for the first run had higher values for the unfiltered sample and lower values for the filtered sample, this is expected since 1) impurities are being removed after filtration and 2) it is possible some of the clustering species are being disrupted during filtration and take some time to recover in the filtrate. Again, this was true for glycine solutions. However, when the second run of urea solutions were analysed, the mean count rate values dropped significantly compared to the first run and the results for the filtered solutions were not always lower than the filtered count rates. This may indicate that urea solutions may not have been fully equilibrated and that some kinetic effects were present.

The evolution of a 3rd decay in the autocorrelation functions was found to appear during the first run but was not evident in the second. Analysis of the coefficient values from the curve fitting procedure to obtain decay rates reinforces this. For the first set, the contribution from the 3rd decay was found to increase, but unlike the glycine solutions this did not always come with a noticeable decrease in the contributions from the 1st and 2nd decays. There were no clear trends for the second run of urea experiments and sometimes the autocorrelation functions were poor. Despite the varying trends in the decay contributions the effects were reversible during the heating and cooling. After plotting the average hydrodynamic diameters vs. temperature, the 1st and 2nd decay diameters for the 1st and 2nd runs were unclear and inconsistent. For the first run there was a transition peak at 40°C for the 3rd decay. Diameters determined from the second run were much larger for the 1st decay

despite some fits being poor, the diameters calculated for the 2nd decay were comparable to the first with respect to size range and the 3rd decay was larger by several orders of magnitude. The data here was particularly problematic due to poor autocorrelation functions.

The NanoSight data fared slightly better than the dynamic light scattering. This could be due to the difference in how the sample is introduced i.e. a cuvette vs. a sample cell where the surface to volume ratios are different. This in turn could influence the behaviour of the solution in the cell and hence the result. For the urea NanoSight data in both runs, the average particle diameters were found to increase with temperature for both the first and second runs, except the repeat of unfiltered 522.61 g/L solutions. The cluster size distributions showed a shift to larger diameters with increasing temperature, however this trend was clearer and more consistent with the data from the first run. Data for the unfiltered 1149.75 g/L solution repetition did not follow this trend. This increase in size accounts for the increase in intensity in the autocorrelation functions as larger species scatter more light.

Reasoning behind these issues with urea are unknown and difficult to explain without further research into this compound and its behaviour under these conditions. It could be that the solutions were unable to reach equilibrium in the timeframe set for the measurements, and that the new solution was somehow requiring more time to equilibrate. There could have been an effect from the solution preparation time, for example the temperature history of the solution may have an effect on its behaviour. If the first solution was left in the incubator for less time before the measurements were made this could influence the clustering behaviour of the molecules. Thermal history may have some impact here however further study would be required for this. It was also noted that when urea solutions were prepared the density was found to increase significantly, in the case of the highest concentration the volume of the sample almost doubled compared to the original volume of water that was added. Perhaps these changes in density could cause fluctuations in the sample and the

thermal history again would come into play as molecular motion within a more dense liquid becomes less predictable.

Also, urea has been known to form networks with water in solutions. This is not the case for glycine and hence this specific interaction with water could be an area of further interest.

8.12 CONCLUSIONS FOR UREA SOLUTIONS

The aqueous urea solutions presented many more issues compared to the aqueous glycine solutions. The first and second runs were not directly comparable, especially with the dynamic light scattering data. The NanoSight information was of better quality in terms of the two experimental runs agreeing with one another. This could be due to the nature of the sample cell or fundamental molecular properties of urea solutions. It may be an issue that the solution did not reach equilibrium in the allotted time for the experiment and hence the DLS measurements were not stable resulting in poor fits to the autocorrelation functions. The time that the solution spent at higher temperature in the incubator before measurements were taken could perhaps alter the solution in such a way that the clustering species form differently over time. This delves into the effects of thermal history and more work would need to be carried out to investigate if this had an effect on the outcome of these light scattering experiments.

Overall, this set of data and results were problematic, and while they provided some data useful for seeing trends during the temperature cycle process, it was not as clear as it was with glycine and therefore more work would be required to properly understand aqueous urea.

9 OVERALL CONCLUSIONS

This section covers all the main conclusions from the thesis and refers back to the original project outline given in section 1.1. The topic of unwanted nucleation was explored in the form of fouling on the glass wall of a crystalliser using the MFOBC

setup which was specifically constructed for this purpose. The setup was designed to mimic continuous crystallisation system so that the findings could aid in developing fully continuous COBC rigs.

The quantitative analysis of fouling was based on image analysis, using a 'Fouling Graphical User Interface' along with a 'Visual Thresholding Method' to analyse the raw images. In turn, kinetic information was deduced via fouling induction times and then analysis of these induction time probability distributions via the ter Horst model to obtain nucleation rate and growth time data with respect to the surface nucleation. Never before has fouling been the main focus of study during a crystallisation process with a focus on its induction time only, not to mention this has not been carried out in an oscillatory flow reactor like the one used here. Fouling induction times were obtained via two methods, bulk nucleation time was separated from the surface nucleation and image intensity maps were used to compare kinetics of combined nucleation on the glass surface and in the bulk solution. Being able to separate bulk and surface nucleation during one crystallisation experiment has also never been achieved before. Insight into the effects of oscillatory flow parameters on fouling induction time revealed that increasing the shear in the system by larger frequency or amplitude or both decreased the fouling induction times, increased the rate of both surface and bulk nucleation and increased the amount of fouling on the glass wall. Increasing the solution supersaturation had the same effect.

Investigation of clustering in solutions prior to nucleation was done using light scattering techniques. It was thought that agitation could influence the behaviour of prenucleation clusters in solution and their interaction with the vessel surface, leading to increased fouling on vessel surfaces. It was found that nanoscale species were detected in undersaturated and supersaturated solutions, both unfiltered and filtered. Cluster diameters increased with increasing temperature and decreased in diameter when the temperature was reduced, again showing the effect was reversible. This process has never been carried out before with solutions with the prime focus being prenucleation cluster behaviour. The change in size with

temperature was thought to be because the solution was maintaining thermodynamic equilibrium via self-assembly of smaller clusters with increasing temperature. The glycine solutions undergo a transformation above 30°C (the exact temperature was not pinpointed in each case because the temperature was increased in steps of 10°C) where this shift to larger mesoscale clusters occurs. The larger species indicated by the 3rd decay presence, yielded diameters of too large a size because the solution must have undergone a transformation that the model and equations used to obtain the diameters could no longer described the solution at this stage in the cycle. The lower temperatures producing the smallest prenucleation clusters was unexpected as this is the stage in the cycle with highest supersaturation and closest to nucleation.

To conclude, this work has probed areas of crystallisation which have been difficult to quantify previously and provides groundwork for further study in this area. New tools and techniques have been created to obtain kinetic data for surface nucleation and fouling induction times. Imaging has been used specifically to monitor fouling induction times in a way which has not been done before. Temperature cycling was employed to explore mesoscale cluster behaviour in undersaturated and supersaturated conditions that mimicked cooling crystallisation. Mesoscale cluster species have been studied before, but not using a temperature cycling method to test their thermodynamic reversibility. Discovering their shift to much larger sizes above certain transition temperatures shows that the theory of nucleation is quite far from being fully understood as the structure and behaviour of the solutions prior to nucleation has yet to be fully comprehended.

10 APPENDIX

10.1 SECOND RUN OF GLYCINE SOLUTION LIGHT SCATTERING EXPERIMENTS

The experiments carried out with aqueous glycine solutions that were described and analysed in detail in Chapter 8 were repeated once more to test the reproducibility of the data obtained and is presented briefly here.

10.1.1 Dynamic Light Scattering Results

10.1.1.1 Autocorrelation Functions and Mean Count Rates for the Three Concentrations and both Filtered and Unfiltered

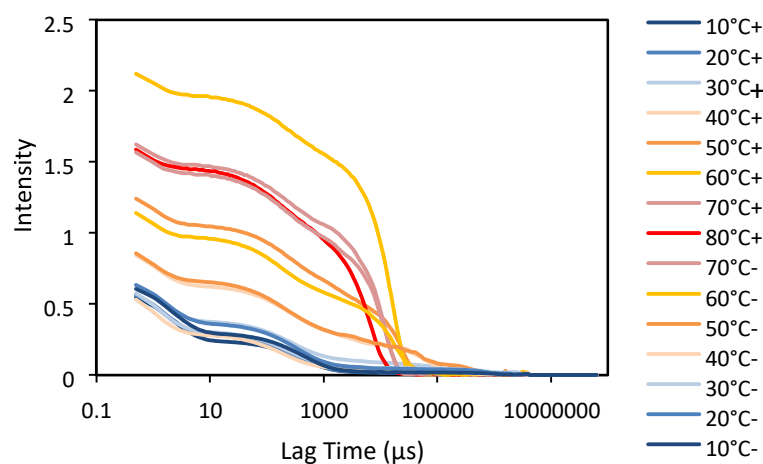


Figure 174. Second run of autocorrelation functions from dynamic light scattering measurements (angle 173°) of temperature cycle from 10-80-10°C with unfiltered aqueous glycine solution of concentration 154.9 g/L which is undersaturated still at 10°C (at this temperature the solution has supersaturation value of $S=0.95$).

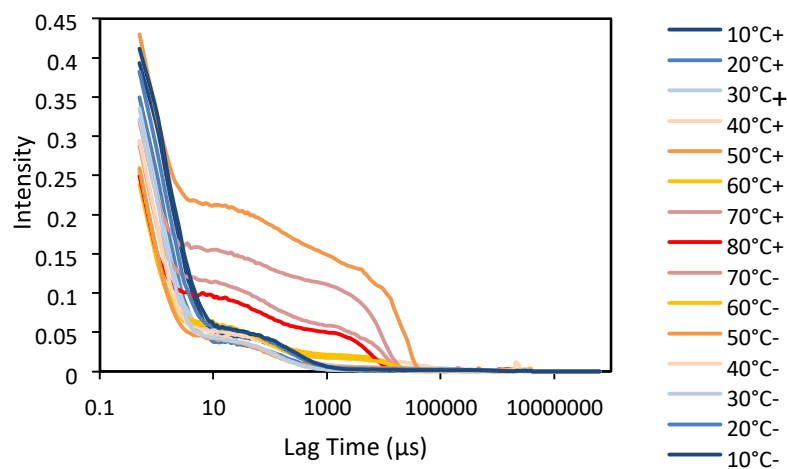


Figure 175. Second run of autocorrelation functions from dynamic light scattering measurements (angle 173°) of temperature cycle from 10-80-10°C with aqueous glycine solution of concentration 154.9 g/L which is undersaturated still at 10°C (at this temperature the solution has supersaturation value of $S=0.95$). This solution was filtered through a PTFE syringe filter with pore diameter 0.1 μm .

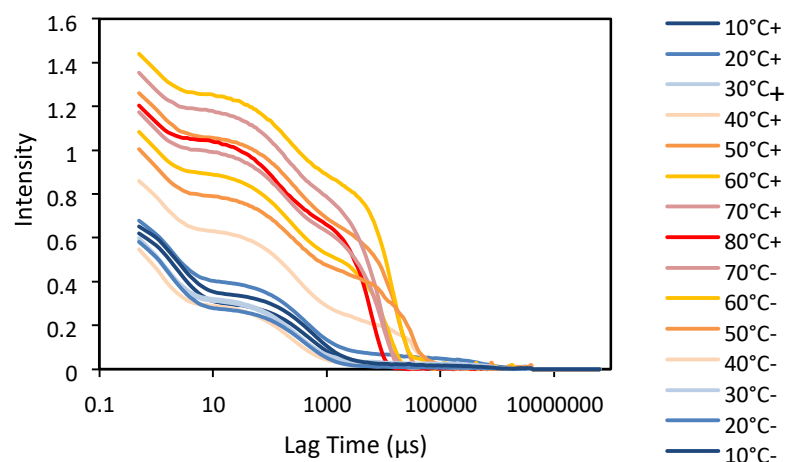


Figure 176. Second run of autocorrelation functions from dynamic light scattering measurements (angle 173°) of temperature cycle from 10-80-10°C with unfiltered aqueous glycine solution of concentration 234.98 g/L.

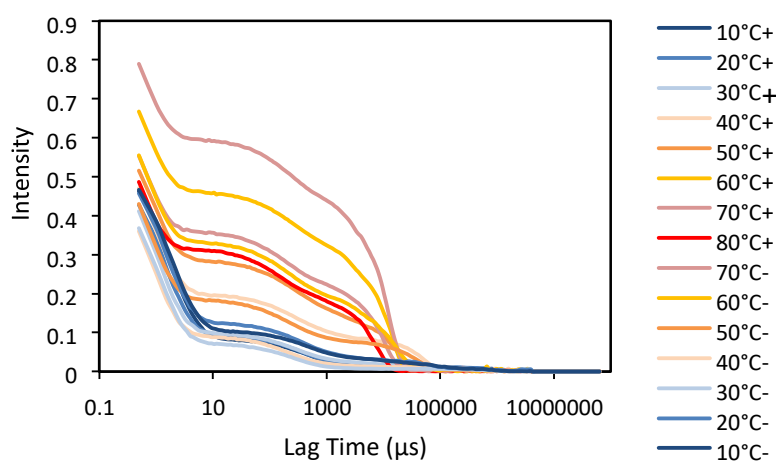


Figure 177. Second run of autocorrelation functions from dynamic light scattering measurements (angle 173°) of temperature cycle from 10-80-10°C with aqueous glycine solution of concentration 234.98 g/L. This solution was filtered through a PTFE syringe filter with pore diameter 0.1 μm .

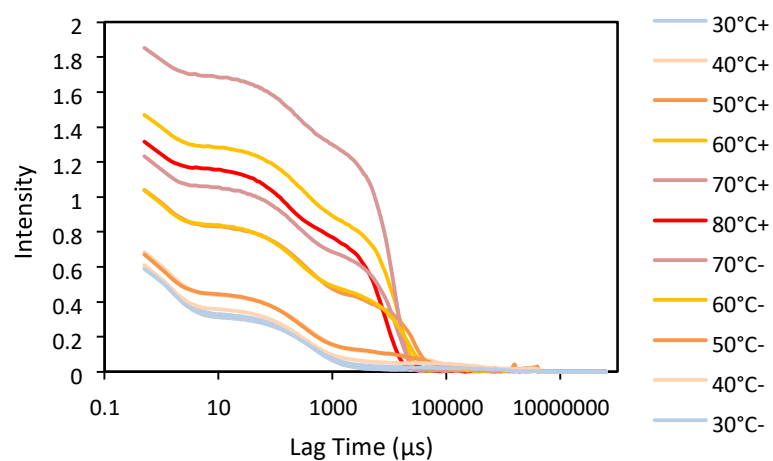


Figure 178. Second run of autocorrelation functions from dynamic light scattering measurements (angle 173°) of temperature cycle from 10-80-10°C with unfiltered aqueous glycine solution of concentration 299.06 g/L.

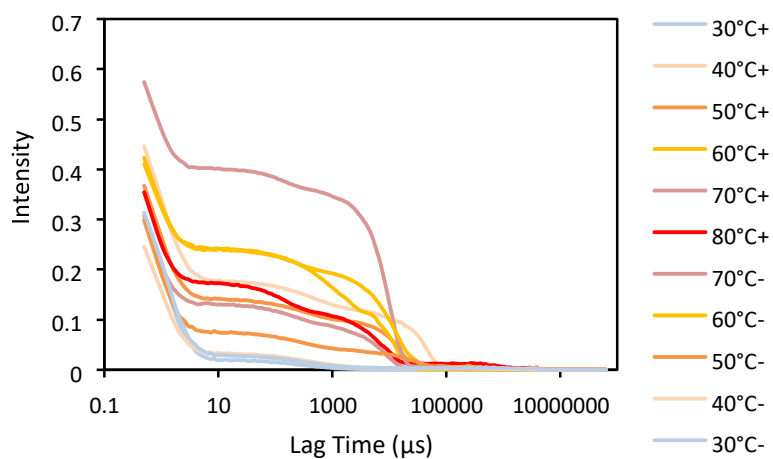


Figure 179. Second run of autocorrelation functions from dynamic light scattering measurements (angle 173°) of temperature cycle from 10-80-10°C with aqueous glycine solution of concentration 299.06 g/L. This solution was filtered through a PTFE syringe filter with pore diameter 0.1 μm .

10.1.2 NanoSight Results

10.1.2.1 Cluster Size Distributions with 20 nm Bin Size

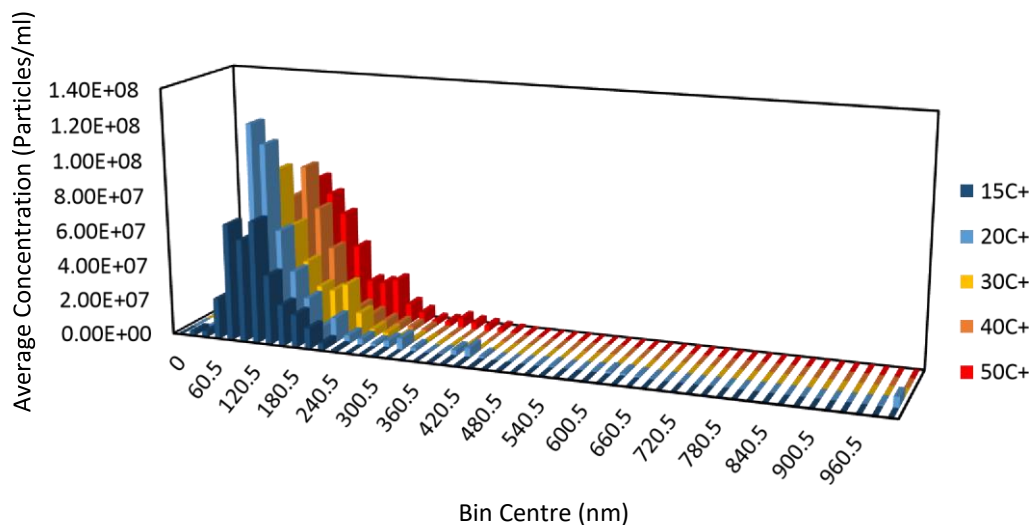


Figure 180. Second run of cluster size distributions from NanoSight measurements of temperature cycle from 15-50-15°C with unfiltered aqueous glycine solution of concentration 154.9 g/L with 20 nm bin sizes for the x-axis.

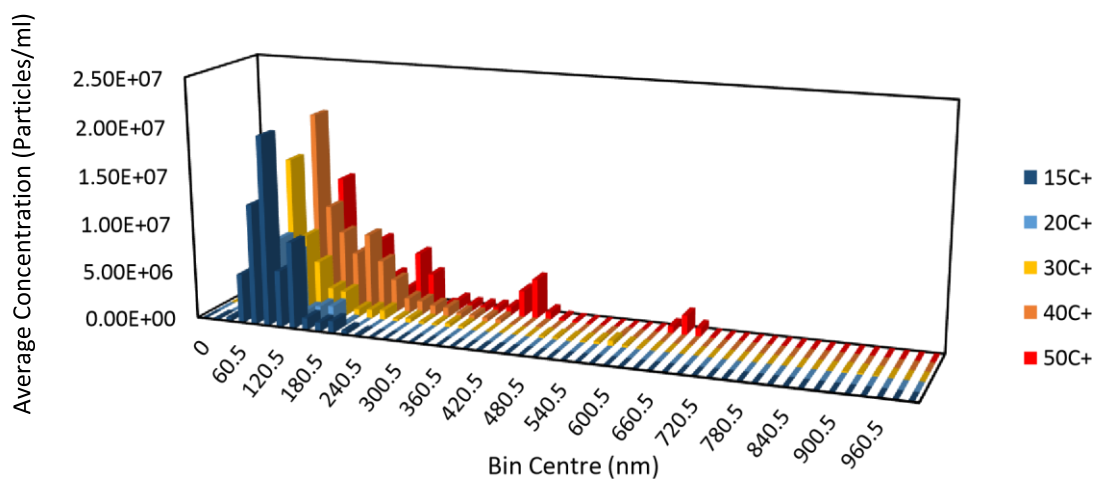


Figure 181. Second run of cluster size distributions from NanoSight measurements of temperature cycle from 15-50-15°C with 0.1 μm PTFE filtered aqueous glycine solution of concentration 154.9 g/L with 20 nm bin sizes for the x-axis.

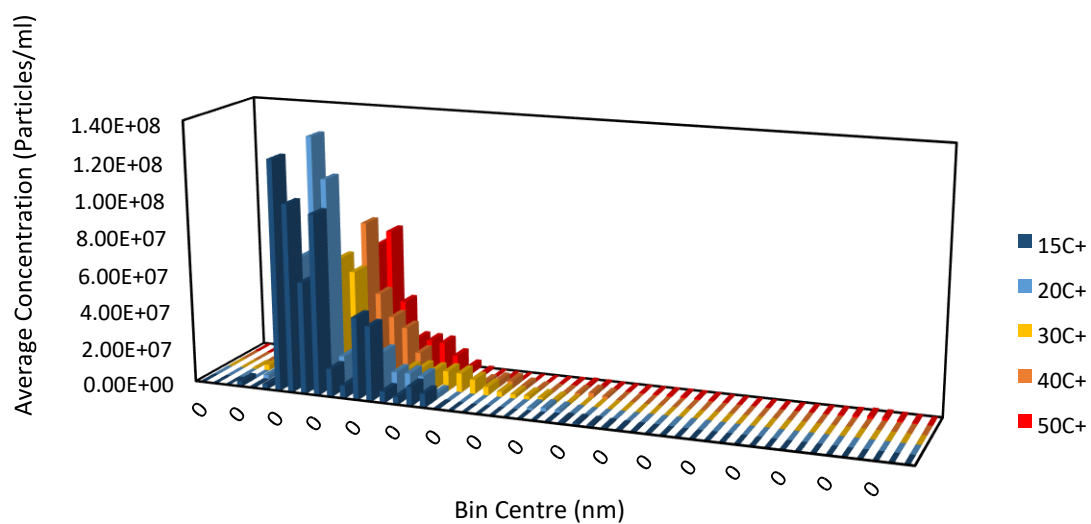


Figure 182. Second run of cluster size distributions from NanoSight measurements of temperature cycle from 15-50-15°C with unfiltered aqueous glycine solution of concentration 234.98 g/L with 20 nm bin sizes for the xaxis.

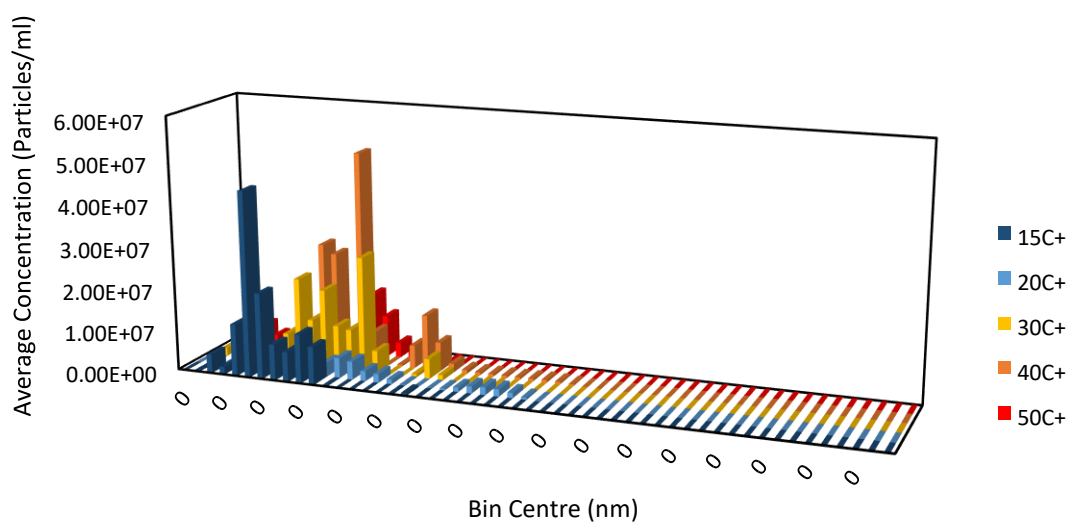


Figure 183. Second run of cluster size distributions from NanoSight measurements of temperature cycle from 15-50-15°C with 0.1 μ m PTFE filtered aqueous glycine solution of concentration 234.98 g/L with 20 nm bin sizes for the x-axis.

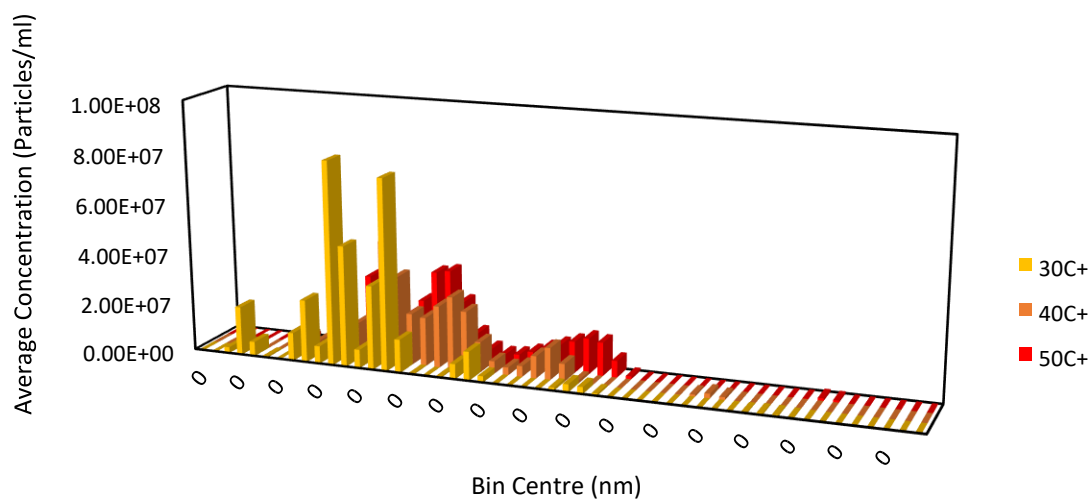


Figure 184. Second run of cluster size distributions from NanoSight measurements of temperature cycle from 30-50-30°C with unfiltered aqueous glycine solution of concentration 299.06 g/L with 20 nm bin sizes for the x-axis.

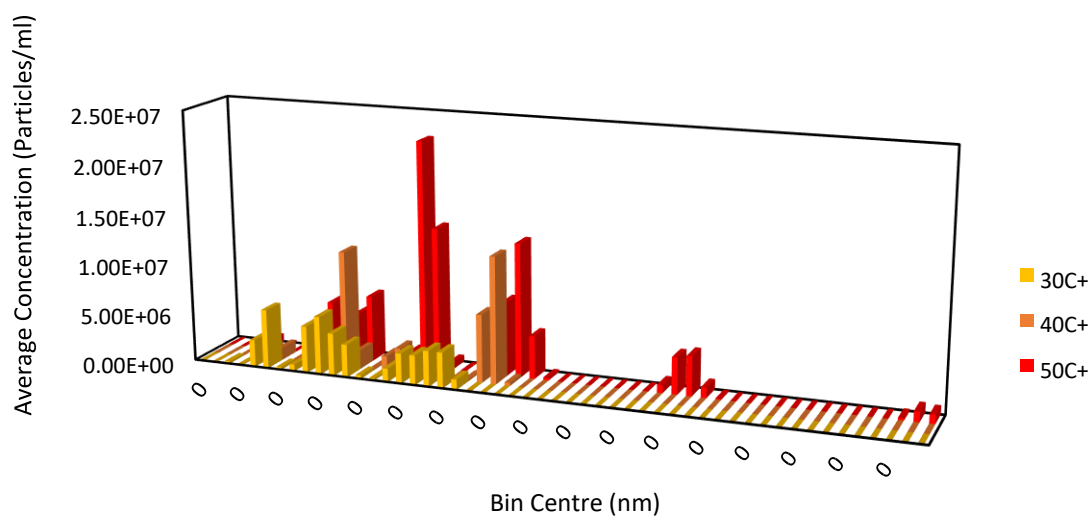


Figure 185. Second run of cluster size distributions from NanoSight measurements of temperature cycle from 30-50-30°C with 0.1 µm PTFE filtered aqueous glycine solution of concentration 299.06 g/L with 20 nm bin sizes for the x-axis.

10.2 UREA SOLUTION SECOND RUN 20 NM BIN CLUSTER SIZE DISTRIBUTIONS

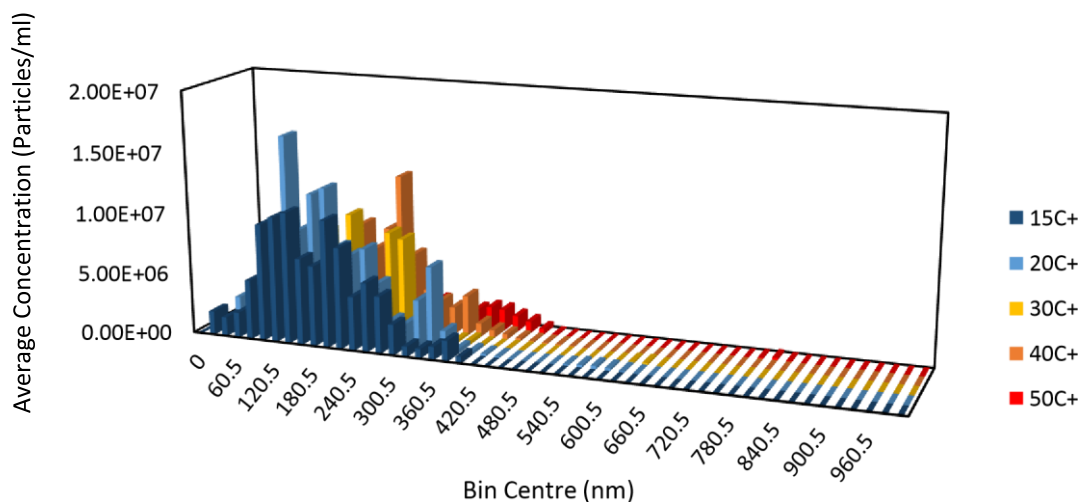


Figure 186. Cluster size distributions from NanoSight measurements of temperature cycle from 15-50-15°C with the second run of unfiltered aqueous urea solution of concentration 522.61 g/L with 20 nm bin sizes for the xaxis.

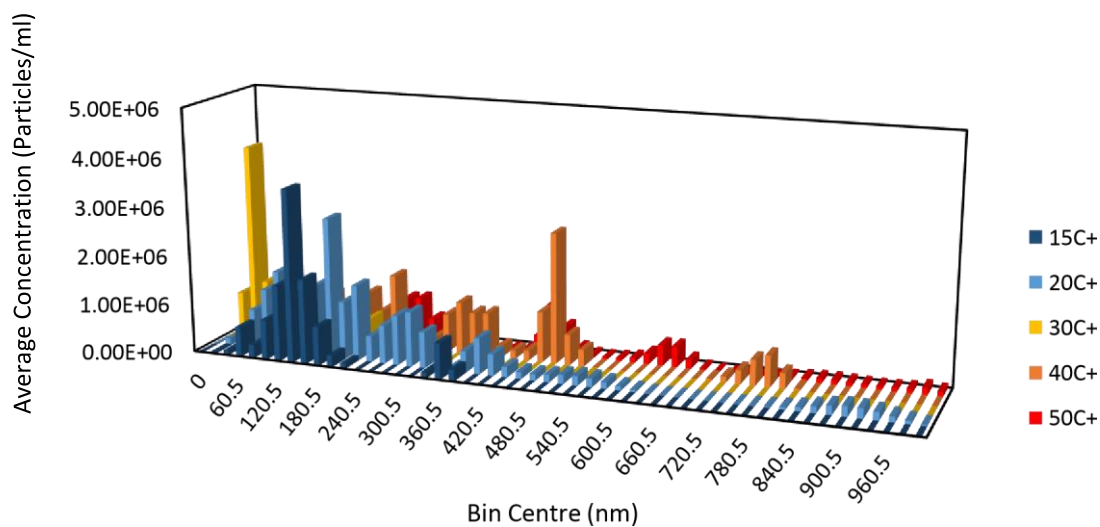


Figure 187. Cluster size distributions from NanoSight measurements of temperature cycle from 15-50-15°C with the second run of 0.1 µm PTFE filtered aqueous urea solution of concentration 522.61 g/L with 20 nm bin sizes for the x-axis.

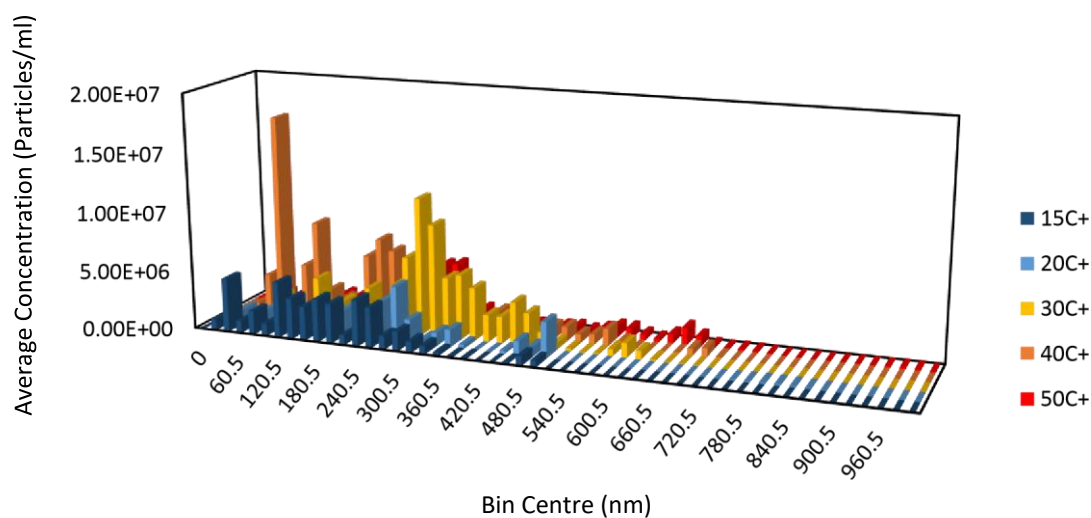


Figure 188. Cluster size distributions from NanoSight measurements of temperature cycle from 15-50-15°C with the second run of unfiltered aqueous urea solution of concentration 785.15 g/L with 20 nm bin sizes for the xaxis.

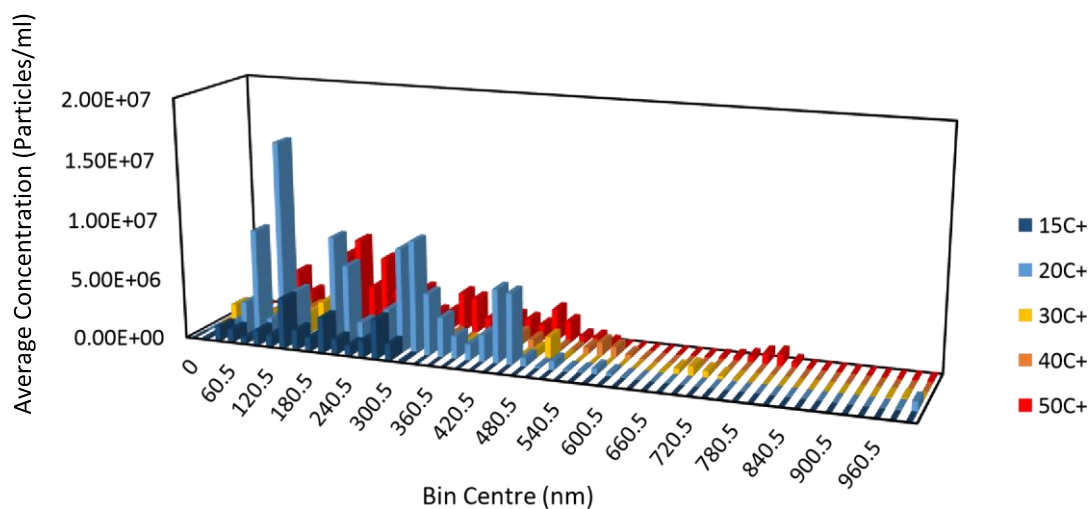


Figure 189. Cluster size distributions from NanoSight measurements of temperature cycle from 15-50-15°C with the second run of 0.1 µm PTFE filtered aqueous urea solution of concentration 785.15 g/L with 20 nm bin sizes for the x-axis.

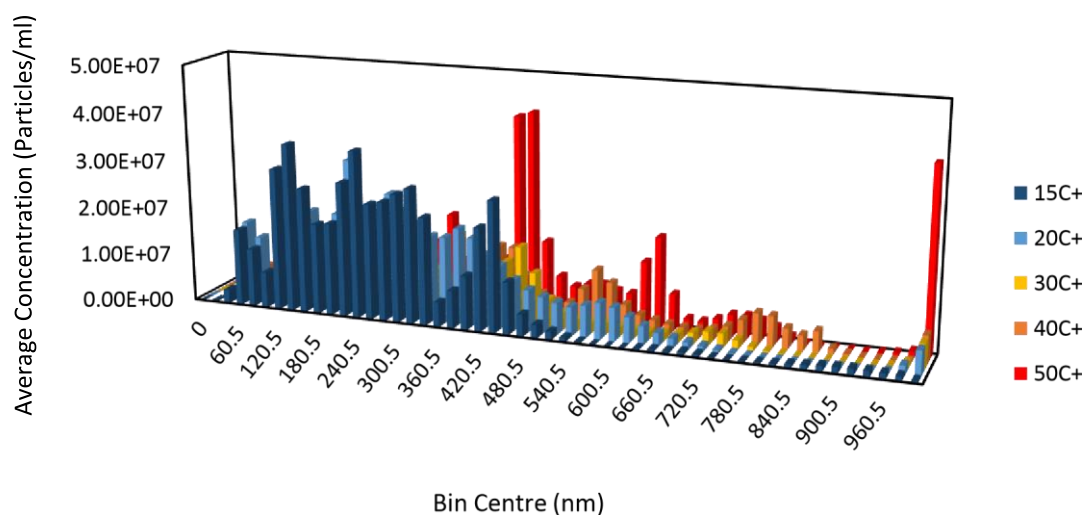


Figure 190. Cluster size distributions from NanoSight measurements of temperature cycle from 15-50-15°C with the second run of unfiltered aqueous urea solution of concentration 1149.74 g/L with 20 nm bin sizes for the xaxis.

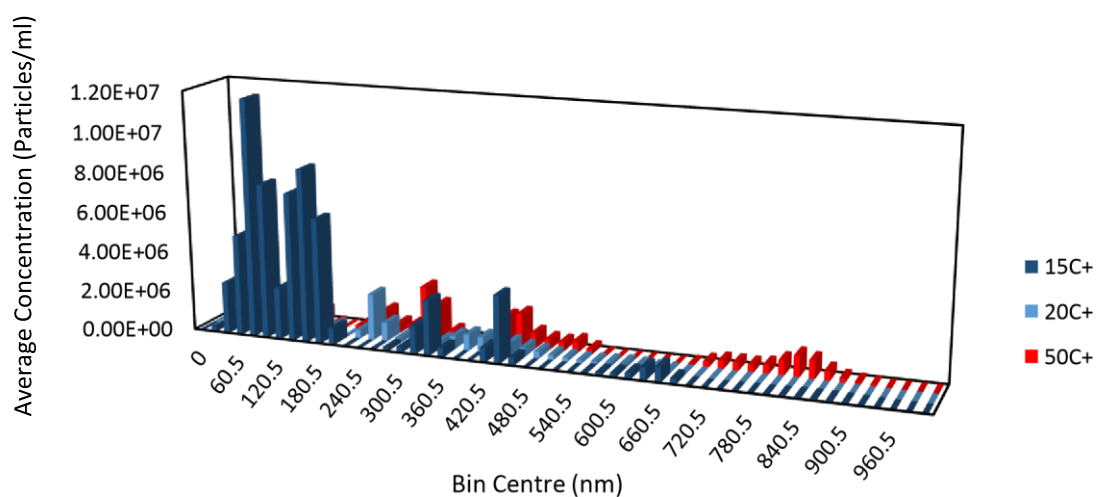


Figure 191. Cluster size distributions from NanoSight measurements of temperature cycle from 15-50-15°C with the second run of 0.1 µm PTFE filtered aqueous urea solution of concentration 1149.74 g/L with 20 nm bin sizes for the x-axis.

10.3 CALCULATED PARAMETERS FROM INTERACTIVE CURVE FITTING TOOL TO OBTAIN HYDRODYNAMIC DIAMETERS

FROM DYNAMIC LIGHT SCATTERING

10.3.1 First Run of Glycine Experiments

Table 18. 1st Run of Unfiltered Glycine 154.9 g/L

	Decay 1		Decay 2		Decay 3		RMS	Diffusion Coefficient 1 (m ² /s)	Diffusion Coefficient 2 (m ² /s)	Diffusion Coefficient 3 (m ² /s)	Hydrodynamic Diameter (nm)		
T (°C)	A	α	B	β	C	γ					Decay 1	Decay 2	Decay 3
10	0.351	2.542	0.315	499.664			0.112	5.66052E-10	2.87974E-12	0	0.560393316	110.1527795	0
20	0.153	5.035	0.267	1405.019			0.627	2.8578E-10	1.02412E-12	0	1.498987715	418.2931917	0
30	0.319	2.015	0.347	497.145			0.443	7.14096E-10	2.89433E-12	0	0.7789438511	192.1826506	0
40	0.294	1.525	0.396	351.699	0.179	48444.093	0.202	9.43543E-10	4.09129E-12	2.97023E-14	0.744192862	171.6274658	23640.49063
50	0.296	0.991	0.322	167.739	0.736	15864.629	0.222	1.45197E-09	8.57823E-12	9.06988E-14	0.595753922	100.8387156	9537.2502
60	0.295	0.827	0.285	134.94	0.535	10481.038	0.157	1.73991E-09	1.06633E-11	1.37286E-13	0.600350488	97.95803495	7608.580753
70	0.308	0.711	0.272	113.811	0.856	7696.99	0.2	2.02377E-09	1.26429E-11	1.86944E-13	0.614537884	98.37014218	6652.731288
80	0.321	0.538	0.224	72.541	1.226	5500.917	0.34	2.67454E-09	1.98357E-11	2.61575E-13	0.544614945	73.43292329	5568.553178
70-	0.327	0.683	0.239	110.583	0.694	8077.872	0.216	2.10674E-09	1.3012E-11	1.78129E-13	0.590336673	95.58008833	6981.938628
60-	0.319	0.814	0.266	151.275	0.772	12364.844	0.194	1.76769E-09	9.51184E-12	1.1637E-13	0.590913298	109.8162275	8976.106571
50-	0.337	1.072	0.279	241.938	0.327	24240.912	0.098	1.34226E-09	5.9474E-12	5.93585E-14	0.644448239	145.444513	14572.77336
40-	0.377	1.123	0.182	205.395	0.014	257534.05	0.03	1.2813E-09	7.00554E-12	5.58723E-15	0.548018744	100.2317986	125675.4095
30-	0.393	1.405	0.19	260.642			0.06	1.02413E-09	5.52061E-12	0	0.5431345463	100.7570636	0

Table 1st

20-	0.378	1.786	0.199	339.655			0.06	8.05657E-10	4.23637E-12	0	0.531716397	101.1198952	0
10-	0.398	2.479	0.235	575.334			0.144	5.80437E-10	2.50099E-12	0	0.546504732	126.8345113	0

Table 19. Repeat of 1st Run of Unfiltered Glycine 154.9 g/L

	Decay 1		Decay 2		Decay 3		RMS	Diffusion Coefficient 1 (m ² /s)	Diffusion Coefficient 2 (m ² /s)	Diffusion Coefficient 3 (m ² /s)	Hydrodynamic Diameter (nm)		
T (°C)	A	α	B	β	C	γ					Decay 1	Decay 2	Decay 3
10	0.338	2.522	0.306	482.013			0.098	5.7054E-10	2.9852E-12	0	0.555984241	106.2615512	0
20	0.334	1.955	0.331	362.871			0.109	7.36012E-10	3.96533E-12	0	0.582029987	108.0316129	0
30	0.312	1.716	0.384	348.32			0.243	8.38522E-10	4.13098E-12	0	0.6633586345	134.6509788	0
40	0.276	1.303	0.377	226.254	0.454	25719.659	0.149	1.1043E-09	6.35968E-12	5.59457E-14	0.635857901	110.410893	12551.07321
50	0.279	0.958	0.333	143.059	0.842	14610.384	0.293	1.50199E-09	1.00581E-11	9.8485E-14	0.575915497	86.00197813	8783.242755
60	0.286	0.778	0.279	98.822	1.143	9720.878	0.356	1.84949E-09	1.45606E-11	1.48022E-13	0.56477954	71.73861665	7056.751941
70	0.302	0.683	0.312	105.767	0.655	8536.489	0.176	2.10674E-09	1.36045E-11	1.68559E-13	0.590336673	91.4174801	7378.334578
80	0.321	0.537	0.236	66.748	1.019	5713.939	0.341	2.67952E-09	2.15572E-11	2.51823E-13	0.54360265	67.56869583	5784.194377
70-	0.287	0.677	0.283	108.137	1.323	8316.07	0.358	2.12541E-09	1.33063E-11	1.73027E-13	0.585150699	93.46593972	7187.820055
60-	0.294	0.852	0.299	154.176	1.142	13465.025	0.192	1.68885E-09	9.33286E-12	1.06862E-13	0.618498931	111.9221728	9774.76945
50-	0.309	0.997	0.281	180.445	0.725	22631.776	0.13	1.44323E-09	7.97419E-12	6.35789E-14	0.599360908	108.4771105	13605.41808
40-	0.366	1.148	0.227	193.211	0.017	302552.99	0.033	1.2534E-09	7.44731E-12	4.75587E-15	0.560218627	94.28606365	147644.4405
30-	0.36	1.528	0.279	315.35			0.171	9.4169E-10	4.56288E-12	0	0.5906829799	121.9056791	0
20-	0.38	1.822	0.254	354.836			0.059	7.89738E-10	4.05512E-12	0	0.542434085	105.6394846	0

10-	0.384	2.471	0.272	473.326			0.087	5.82316E-10	3.03998E-12	0	0.544741103	104.3464699	0
-----	-------	-------	-------	---------	--	--	-------	-------------	-------------	---	-------------	-------------	---

20. Run of PTFE Filtered Glycine 154.9 g/L

	Decay 1		Decay 2		Decay 3		RMS	Diffusion Coefficient 1 (m ² /s)	Diffusion Coefficient 2 (m ² /s)	Diffusion Coefficient 3 (m ² /s)	Hydrodynamic Diameter (nm)		
T (°C)	A	α	B	β	C	γ					Decay 1	Decay 2	Decay 3
10	0.153	3.232	0.539	1187.179			0.358	4.45205E-10	1.21204E-12	0	0.712506371	261.7180078	0
20	0.376	1.788	0.028	2261.785			0.049	8.04756E-10	6.3618E-13	0	0.532311824	673.3640375	0
30	0.374	1.214	0.015	436.207			0.031	1.18526E-09	3.29867E-12	0	0.4692991738	168.6256876	0
40	0.326	0.794	0.005	178.323	0.002	6430104.5	0.012	1.81222E-09	8.06908E-12	2.23776E-16	0.387468284	87.02078933	3137860.892
50	0.346	0.657	0.005	149.908	0.005	26051.396	0.009	2.19011E-09	9.59857E-12	5.52332E-14	0.394965012	90.11935312	15661.17189
60	0.319	0.723	0.01	197.79	0.002	10249902	0.012	1.99018E-09	7.2749E-12	1.40382E-16	0.524852966	143.5832202	7440790.42
70	0.305	0.663	0.015	130.183	0.024	14286.114	0.027	2.17029E-09	1.10529E-11	1.0072E-13	0.573050094	112.5209358	12347.90192
80	0.318	0.599	0.015	191.94	0.026	1756600.8	0.021	2.40218E-09	7.49663E-12	8.19141E-16	0.606364967	194.2999862	1778199.001
70-	0.319	0.615	0.011	186.481	0.006	3159042.8	0.013	2.33968E-09	7.71608E-12	4.55487E-16	0.531562305	161.180927	2730452.188
60-	0.321	0.667	0.009	149.152	0.01	9023958.5	0.023	2.15728E-09	9.64723E-12	1.59454E-16	0.484200454	108.2750617	6550831.789
50-	0.355	0.826	0.009	141.609	0.01	15977413	0.02	1.74201E-09	1.01611E-11	9.00586E-17	0.496561796	85.13028975	9605052.204
40-	0.356	0.976	0.009	188.387	0.008	12648327	0.021	1.47429E-09	7.63802E-12	1.13762E-16	0.476283432	91.93197423	6172324.449

Table 1st

30-	0.347	1.081	0.005	3027956			0.021	1.33109E-09	4.75206E-16	0	0.4178850139	1170524.82	0
20-	0.381	1.223	0.004	912.919			0.012	1.17654E-09	1.57616E-12	0	0.364103669	271.7883547	0
10-	0.349	1.466	0.003	369.486			0.01	9.81516E-10	3.89434E-12	0	0.32318513	81.45455727	0

Table 1st

21. Run of Unfiltered Glycine 234.98 g/L

	Decay 1		Decay 2		Decay 3		RMS	Diffusion Coefficient 1 (m ² /s)	Diffusion Coefficient 2 (m ² /s)	Diffusion Coefficient 3 (m ² /s)	Hydrodynamic Diameter (nm)		
T (°C)	A	α	B	β	C	γ					Decay 1	Decay 2	Decay 3
10	0.311	3.027	0.428	780.965			0.209	4.75356E-10	1.84247E-12	0	0.667313362	172.1666269	0
20	0.29	2.808	0.473	822.751			0.464	5.1243E-10	1.74889E-12	0	0.835979643	244.9441195	0
30	0.269	2.991	0.471	866.294			0.607	4.81078E-10	1.66099E-12	0	1.156238739	334.8855506	0
40	0.243	1.468	0.441	357.03	0.725	52371.995	0.137	9.80179E-10	4.0302E-12	2.74747E-14	0.716377129	174.2289689	25557.28843
50	0.221	1.004	0.328	191.194	1.502	21195.726	0.543	1.43317E-09	7.52588E-12	6.78865E-14	0.603569059	114.9390266	12742.11594
60	0.24	0.842	0.345	173.529	1.115	12117.604	0.36	1.70891E-09	8.292E-12	1.18745E-13	0.611239554	125.9712453	8796.625731
70	0.241	0.635	0.256	95.474	1.915	11074.938	0.713	2.26599E-09	1.50712E-11	1.29924E-13	0.548848884	82.52094222	9572.389538
80	0.237	0.582	0.272	100.607	1.733	7768.703	0.382	2.47234E-09	1.43022E-11	1.85218E-13	0.589155944	101.844007	7864.222598
70-	0.233	0.644	0.239	94.252	2.241	11452.214	0.76	2.23432E-09	1.52666E-11	1.25644E-13	0.556627844	81.46473224	9898.480107
60-	0.246	0.875	0.361	205.001	1.111	17118.729	0.421	1.64446E-09	7.01901E-12	8.40543E-14	0.635195499	148.817957	12427.13097
50-	0.279	1.189	0.414	326.968	0.38	54361.325	0.117	1.21018E-09	4.40075E-12	2.64692E-14	0.714784474	196.5615221	32680.09342
40-	0.3136	1.431	0.356	406.498	0.082	169334.18	0.15	1.00552E-09	3.53975E-12	8.49742E-15	0.698321302	198.3691213	82634.28822
30-	0.307	2.531	0.425	982.554			0.497	5.68512E-10	1.46445E-12	0	0.9784153286	379.8284847	0
20-	0.347	2.141	0.339	556.602			0.154	6.72071E-10	2.58516E-12	0	0.637404707	165.7079563	0
10-	0.329	3.784	0.441	1566.728			0.564	3.8026E-10	9.18413E-13	0	0.834196816	345.3909907	0

Table 1st

22. Run of PTFE Filtered Glycine 234.98 g/L

	Decay 1		Decay 2		Decay 3		RMS	Diffusion Coefficient 1 (m ² /s)	Diffusion Coefficient 2 (m ² /s)	Diffusion Coefficient 3 (m ² /s)	Hydrodynamic Diameter (nm)		
T (°C)	A	α	B	β	C	γ					Decay 1	Decay 2	Decay 3
10	0.463	2.285	0.092	1006.616			0.085	6.29717E-10	1.42945E-12	0	0.503736714	221.9122257	0
20	0.095	2345496	0.127	484.719			0.389	6.13475E-16	2.96853E-12	0	698285.9739	144.3074133	0
30	0.358	1.65	0.241	819.947			0.156	8.72062E-10	1.75487E-12	0	0.6378448409	316.9690689	0
40	0.39	1.323	0.252	612.478	0.279	47652.631	0.16	1.08761E-09	2.34931E-12	3.01957E-14	0.645617808	298.8863972	23254.26088
50	0.375	0.981	0.188	239.913	0.727	15880.367	0.168	1.46677E-09	5.9976E-12	9.06089E-14	0.589742278	144.2271551	9546.711325
60	0.391	0.807	0.185	200.777	0.419	10940.138	0.133	1.78303E-09	7.16667E-12	1.31525E-13	0.585831734	145.7515961	7941.858756
70	0.379	0.681	0.158	123.897	0.798	9211.548	0.211	2.11293E-09	1.16137E-11	1.56206E-13	0.588608015	107.087764	7961.807615
80	0.39	0.56	0.122	71.124	0.997	5905.043	0.242	2.56947E-09	2.02309E-11	2.43674E-13	0.566885445	71.99850066	5977.648084
70-	0.381	0.677	0.159	122.534	0.672	8707.524	0.193	2.12541E-09	1.17429E-11	1.65248E-13	0.585150699	105.9096836	7526.16508
60-	0.379	0.836	0.206	227.554	0.528	15695.12	0.121	1.72118E-09	6.32335E-12	9.16784E-14	0.606883928	165.1900303	11393.67951
50-	0.401	0.996	0.188	305.555	0.127	52278.058	0.051	1.44468E-09	4.70915E-12	2.7524E-14	0.598759744	183.6887887	31427.70746
40-	0.43	1.129	0.12	310.514	0.008	924867.53	0.028	1.27449E-09	4.63394E-12	1.55579E-15	0.550946716	151.5293786	451331.0242
30-	0.432	1.447	0.14	456.193			0.077	9.94404E-10	3.15415E-12	0	0.5593705968	176.3517282	0
20-	0.43	1.826	0.136	598.992			0.046	7.88008E-10	2.40221E-12	0	0.543624939	178.3280336	0

10-	0.45	2.409	0.149	785.239			0.082	5.97303E-10	1.83244E-12	0	0.531072973	173.1088461	0
-----	------	-------	-------	---------	--	--	-------	-------------	-------------	---	-------------	-------------	---

Table 23. Repeat of 1st Run of PTFE Filtered Glycine 234.98 g/L, PTFE

	Decay 1		Decay 2		Decay 3		RMS	Diffusion Coefficient 1 (m ² /s)	Diffusion Coefficient 2 (m ² /s)	Diffusion Coefficient 3 (m ² /s)	Hydrodynamic Diameter (nm)		
T (°C)	A	α	B	β	C	γ					Decay 1	Decay 2	Decay 3
10	0.494	1.969	0.033	401.448			0.015	7.30779E-10	3.58428E-12	0	0.434073343	88.50069856	0
20	0.458	1.476	0.031	512.971			0.039	9.74867E-10	2.80504E-12	0	0.439425197	152.7184165	0
30	0.451	1.201	0.042	1147.633			0.06	1.19809E-09	1.2538E-12	0	0.4642737296	443.643508	0
40	0.426	0.953	0.045	400.468	0.092	55210.66	0.029	1.50987E-09	3.59305E-12	2.60621E-14	0.465059539	195.4265096	26942.54366
50	0.414	0.794	0.037	162.385	0.113	18993.244	0.062	1.81222E-09	8.86106E-12	7.57587E-14	0.477324535	97.62008136	11418.06216
60	0.419	0.692	0.051	158.54	0.241	11889.957	0.073	2.07934E-09	9.07596E-12	1.21018E-13	0.502348897	115.090165	8631.368189
70	0.452	0.543	0.035	90.364	0.284	8758.242	0.087	2.64991E-09	1.59234E-11	1.64291E-13	0.46933062	78.10422128	7570.002116
80	0.419	0.503	0.029	67.7	0.343	6044.981	0.08	2.86064E-09	2.12541E-11	2.38033E-13	0.509184605	68.53240108	6119.306683
70-	0.416	0.576	0.033	89.238	0.359	8922.616	0.103	2.4981E-09	1.61243E-11	1.61265E-13	0.497853475	77.13098688	7712.075323
60-	0.432	0.662	0.047	194.124	0.147	14618.488	0.039	2.17357E-09	7.41229E-12	9.84304E-14	0.480570766	140.9219325	10612.11174
50-	0.425	0.796	0.042	410.383	0.139	27660.599	0.05	1.80767E-09	3.50624E-12	5.202E-14	0.478526864	246.7076506	16628.56745
40-	0.448	0.885	0.014	103.741	0.005	890.107	0.01	1.62588E-09	1.38701E-11	1.61655E-12	0.431875858	50.62512243	434.3680497
30-	0.453	1.107	0.02	228.589			0.035	1.29982E-09	6.29472E-12	0	0.4279359023	88.36625111	0
20-	0.46	1.39	0.021	278.556			0.016	1.03518E-09	5.16558E-12	0	0.413821832	82.92989512	0

Table 1st

10-	0.474	1.899	0.024	381.38			0.017	7.57716E-10	3.77289E-12	0	0.418641584	84.07663362	0
-----	-------	-------	-------	--------	--	--	-------	-------------	-------------	---	-------------	-------------	---

Table 24. 1st Run of Unfiltered Glycine 299.06 g/L

	Decay 1		Decay 2		Decay 3		RMS	Diffusion Coefficient 1 (m ² /s)	Diffusion Coefficient 2 (m ² /s)	Diffusion Coefficient 3 (m ² /s)	Hydrodynamic Diameter (nm)		
T (°C)	A	α	B	β	C	γ					Decay 1	Decay 2	Decay 3
30	0.298	1.73	0.437	399.134			0.114	8.31736E-10	3.60506E-12	0	0.6687706513	154.2942804	0
40	0.274	1.37	0.465	318.137	0.117	65996.727	0.053	1.05029E-09	4.5229E-12	2.18026E-14	0.668553588	155.2493669	32206.09387
50	0.269	1.111	0.442	248.146	0.279	21317.669	0.074	1.29514E-09	5.79861E-12	6.74981E-14	0.66789365	149.1765416	12815.42373
60	0.277	0.889	0.403	186.508	0.427	12440.869	0.16	1.61856E-09	7.71497E-12	1.15659E-13	0.645358627	135.3931909	9031.295986
70	0.271	0.759	0.384	153.176	0.531	9568.604	0.159	1.89579E-09	9.39379E-12	1.50378E-13	0.656025673	132.3944513	8270.421453
80	0.287	0.602	0.323	107.421	1.063	10402.639	0.337	2.3902E-09	1.3395E-11	1.38321E-13	0.609401853	108.7417881	10530.54399
70-	0.277	0.782	0.403	172.535	0.438	10474.472	0.132	1.84003E-09	8.33977E-12	1.37372E-13	0.675905239	149.1269955	9053.38939
60-	0.275	0.949	0.423	217.292	0.227	20572.34	0.077	1.51623E-09	6.62198E-12	6.99436E-14	0.688914889	157.7404575	14934.23744
50-	0.299	1.123	0.414	254.813	0.051	85391.201	0.05	1.2813E-09	5.6469E-12	1.68507E-14	0.675107623	153.1845047	51334.15025
40-	0.318	1.329	0.374	276.586	0.008	395073.77	0.031	1.0827E-09	5.20237E-12	3.64211E-15	0.648545779	134.9726734	192794.1481
30-	0.294	1.798	0.442	447.034			0.166	8.0028E-10	3.21878E-12	0	0.6950575902	172.8111094	0

Table 25. 1st Run of PTFE Filtered Glycine 299.06 g/L

	Decay 1		Decay 2		Decay 3		RMS	Diffusion Coefficient 1 (m ² /s)	Diffusion Coefficient 2 (m ² /s)	Diffusion Coefficient 3 (m ² /s)	Hydrodynamic Diameter (nm)		
T (°C)	A	α	B	β	C	γ					Decay 1	Decay 2	Decay 3
30	0.453	1.131	0.02	255.723			0.014	1.27224E-09	5.6268E-12	0	0.4372136455	98.85551287	0
40	0.441	0.946	0.025	196.32	0.004	83592.394	0.017	1.52104E-09	7.32938E-12	1.72133E-14	0.461643572	95.8032411	0
50	0.424	0.794	0.022	136.91	0.026	21958.203	0.014	1.81222E-09	1.05098E-11	6.55292E-14	0.477324535	82.30541823	0
60	0.426	0.668	0.022	146.165	0.043	12127.634	0.02	2.15405E-09	9.84437E-12	1.18647E-13	0.484926392	106.1066858	8803.906887
70	0.434	0.556	0.017	99.8	0.015	10144.762	0.009	2.58796E-09	1.44179E-11	1.41837E-13	0.480566896	86.26002926	8768.411492
80	0.437	0.488	0.016	87.996	0.013	6999.613	0.028	2.94857E-09	1.63519E-11	2.05569E-13	0.494000173	89.07794927	7085.676301
70-	0.43	0.562	0.025	156.337	0.032	9661.73	0.032	2.56033E-09	9.20385E-12	1.48928E-13	0.48575287	135.1265951	8350.91295
60-	0.423	0.655	0.018	128.443	0.047	17317.761	0.022	2.1968E-09	1.12027E-11	8.30883E-14	0.475489202	93.24161763	12571.61581
50-	0.455	0.75	0.018	142.657	0.004	107979.79	0.007	1.91854E-09	1.00865E-11	1.33257E-14	0.450873301	85.76031004	64913.60464
40-	0.449	0.932	0.02	201.628	0.001	2205111.9	0.009	1.54389E-09	7.13642E-12	6.52531E-16	0.454811638	98.39352025	1076084.31
30-	0.437	1.116	0.017	282.719			0.013	1.28934E-09	5.08952E-12	0	0.431415056	109.2914276	0

10.3.2 Second Run of Glycine Experiments

Table 26. 2nd Run of Unfiltered Glycine 154.9 g/L

	Decay 1		Decay 2		Decay 3		RMS	Diffusion Coefficient 1 (m ² /s)	Diffusion Coefficient 2 (m ² /s)	Diffusion Coefficient 3 (m ² /s)	Hydrodynamic Diameter (nm)		
T (°C)	A	α	B	β	C	γ					Decay 1	Decay 2	Decay 3
10	0.373	2.482	0.236	618.227			0.128	5.79735E-10	2.32747E-12	0	0.547166093	136.2904321	0
20	0.365	1.955	0.277	499.941			0.161	7.36012E-10	2.87815E-12	0	0.582029987	148.839209	0
30	0.318	2.665	0.336	1241.29			0.591	5.39926E-10	1.1592E-12	0	1.030216061	479.8487409	0
40	0.314	1.389	0.351	395.173	0.268	63152.278	0.141	1.03593E-09	3.6412E-12	2.27847E-14	0.677825499	192.8425743	30818.01607
50	0.295	1.11	0.376	299.35	0.676	17882.738	0.206	1.29631E-09	4.80676E-12	8.04632E-14	0.667292486	179.9585636	10750.46549
60	0.275	0.757	0.261	124.916	1.719	13806.727	0.578	1.9008E-09	1.1519E-11	1.04218E-13	0.549534849	90.68123532	10022.82382
70	0.281	0.683	0.29	134.03	1.2	9635.625	0.343	2.10674E-09	1.07357E-11	1.49332E-13	0.590336673	115.8460092	8328.349643
80	0.281	0.616	0.304	121.21	1.158	5648.932	0.209	2.33588E-09	1.18712E-11	2.54721E-13	0.623573989	122.7003299	5718.388087
70-	0.289	0.704	0.333	153.974	1.094	9756.636	0.305	2.0439E-09	9.3451E-12	1.47479E-13	0.608487581	133.0841858	8432.942954
60-	0.3	0.855	0.359	204.943	0.615	16708.357	0.107	1.68293E-09	7.02099E-12	8.61188E-14	0.620676744	148.7758527	12129.22646
50-	0.294	1.29	0.381	363.819	0.269	83008.788	0.24	1.11543E-09	3.955E-12	1.73343E-14	0.775502078	218.7150314	49901.92837
40-	0.373	1.169	0.243	242.571	0.043	274240.73	0.064	1.23088E-09	5.93188E-12	5.24686E-15	0.570466528	118.3735126	133828.1907
30-	0.364	1.817	0.286	638.426			0.425	7.91911E-10	2.25383E-12	0	0.7024024702	246.7980184	0
20-	0.347	2.237	0.347	672.809			0.383	6.43229E-10	2.13865E-12	0	0.665985207	200.3043546	0
10-	0.381	2.548	0.288	630.093			0.171	5.64719E-10	2.28364E-12	0	0.561716038	138.9063357	0

Table . 2nd
27

Glycine 154.9 g/L

	Decay 1		Decay 2		Decay 3		RMS	Diffusion Coefficient 1 (m ² /s)	Diffusion Coefficient 2 (m ² /s)	Diffusion Coefficient 3 (m ² /s)	Hydrodynamic Diameter (nm)		
T (°C)	A	α	B	β	C	γ					Decay 1	Decay 2	Decay 3
10	0.442	1.949	0.048	361.081			0.02	7.38278E-10	3.98499E-12	0	0.429664269	79.60164389	0
20	0.434	1.439	0.04	251.382			0.021	9.99933E-10	5.72397E-12	0	0.428409796	74.83982716	0
30	0.428	1.183	0.052	314.213			0.048	1.21632E-09	4.57939E-12	0	0.4573154223	121.466146	0
40	0.418	0.892	0.036	135.016	0.017	55106.618	0.01	1.61312E-09	1.06573E-11	2.61113E-14	0.435291825	65.88717604	26891.77165
50	0.401	0.795	0.057	160.564	0.158	19274.396	0.052	1.80994E-09	8.96155E-12	7.46536E-14	0.477925699	96.52536098	11587.08074
60	0.374	0.663	0.038	99.316	0.025	12955.481	0.046	2.17029E-09	1.44881E-11	1.11065E-13	0.481296704	72.09722988	9404.872244
70	0.379	0.571	0.035	61.998	0.125	9057.63	0.038	2.51997E-09	2.32089E-11	1.58861E-13	0.493531831	53.58666627	7828.771832
80	0.408	0.491	0.042	67.937	0.06	5903.74	0.032	2.93056E-09	2.118E-11	2.43727E-13	0.49703706	68.7723151	5976.329063
70-	0.394	0.588	0.052	91.25	0.068	8606.791	0.017	2.44711E-09	1.57688E-11	1.67182E-13	0.508225423	78.87001673	7439.098632
60-	0.421	0.639	0.047	89.1	0.019	16938.548	0.013	2.2518E-09	1.61493E-11	8.49484E-14	0.463874198	64.6810502	12296.33079
50-	0.405	0.768	0.04	112.689	0.006	47613.436	0.01	1.87357E-09	1.27688E-11	3.02205E-14	0.46169426	67.74461526	28623.50276
40-	0.419	0.94	0.047	157.672			0.027	1.53075E-09	9.12593E-12	0	0.4587156	76.94319799	0
30-	0.428	1.139	0.045	182.149			0.016	1.2633E-09	7.89959E-12	0	0.4403062265	70.41381813	0
20-	0.446	1.518	0.058	278.808			0.031	9.47894E-10	5.16091E-12	0	0.451929166	83.00491893	0
10-	0.453	1.962	0.057	331.835			0.026	7.33386E-10	4.3362E-12	0	0.432530167	73.15425486	0

Table . 2nd Run of PTFE Filtered

28 Run of Unfiltered Glycine 234.98 g/L													
	Decay 1		Decay 2		Decay 3		RMS	Diffusion Coefficient 1 (m²/s)	Diffusion Coefficient 2 (m²/s)	Diffusion Coefficient 3 (m²/s)	Hydrodynamic Diameter (nm)		
T (°C)	A	α	B	β	C	γ					Decay 1	Decay 2	Decay 3
10	0.226	0.891	0.012	1073.739			0.016	1.61493E-09	1.34009E-12	0	0.19642425	236.7097397	0
20	0.35	2.069	0.33	547.978	0.071	437245.33	0.087	6.95458E-10	2.62584E-12	0	0.615969331	163.1404747	0
30	0.374	1.543	0.285	354.889	0.04	113893.89	0.067	9.32536E-10	4.05452E-12	0	0.5964815694	137.1903744	0
40	0.323	1.341	0.371	340.462	0.265	34042.687	0.086	1.07301E-09	4.22633E-12	4.22676E-14	0.654401723	166.1438624	16612.67191
50	0.312	1.021	0.327	231.591	0.743	15934.757	0.218	1.40931E-09	6.21312E-12	9.02997E-14	0.613788854	139.2242649	9579.408657
60	0.324	0.834	0.309	179.365	0.598	9929.872	0.153	1.7253E-09	8.02221E-12	1.44907E-13	0.605432052	130.2078178	7208.468567
70	0.318	0.692	0.282	137.335	0.918	7379.055	0.234	2.07934E-09	1.04773E-11	1.94998E-13	0.598115634	118.7026164	6377.930863
80	0.331	0.574	0.263	99.567	0.804	5328.214	0.24	2.5068E-09	1.44516E-11	2.70054E-13	0.581057581	100.7912198	5393.726719
70-	0.321	0.729	0.286	143.237	0.727	7800.549	0.155	1.9738E-09	1.00456E-11	1.84462E-13	0.630095805	123.8038859	6742.24033
60-	0.314	0.819	0.296	166.448	0.975	14728.853	0.28	1.7569E-09	8.64476E-12	9.76928E-14	0.594542987	120.8308804	10692.22986
50-	0.33	1.051	0.316	260.529	0.483	27823.338	0.094	1.36908E-09	5.52301E-12	5.17157E-14	0.631823786	156.6207604	16726.40034
40-	0.377	1.228	0.27	291.382	0.025	559304.2	0.046	1.17175E-09	4.9382E-12	2.57267E-15	0.599258252	142.1930521	272937.8317
30-	0.372	1.556	0.282	366.755	0.033	695242.09	0.049	9.24745E-10	3.92334E-12	0	0.6015070136	141.7774452	0
20-	0.388	1.993	0.277	532.031			0.105	7.21978E-10	2.70455E-12	0	0.593343101	158.3928367	0
10-	0.368	2.814	0.34	856.269			0.196	5.11337E-10	1.68043E-12	0	0.620356723	188.7676727	0

Table . 2nd

29 Glycine 234.98 g/L													
	Decay 1		Decay 2		Decay 3		RMS	Diffusion Coefficient 1 (m²/s)	Diffusion Coefficient 2 (m²/s)	Diffusion Coefficient 3 (m²/s)	Hydrodynamic Diameter (nm)		
T (°C)	A	α	B	β	C	γ					Decay 1	Decay 2	Decay 3
10	0.474	2.155	0.082	862.109			0.082	6.67704E-10	1.66905E-12	0	0.475077732	190.0551223	0
20	0.447	1.706	0.09	821.923			0.115	8.43437E-10	1.75065E-12	0	0.507899313	244.6976126	0
30	0.452	1.364	0.092	969.224			0.136	1.05491E-09	1.48459E-12	0	0.5272850684	374.6754715	0
40	0.431	1.067	0.101	338.47	0.097	45301.072	0.037	1.34855E-09	4.2512E-12	3.17631E-14	0.520691006	165.1717757	22106.7111
50	0.395	0.921	0.117	288.651	0.168	14300.825	0.039	1.56233E-09	4.98492E-12	1.00617E-13	0.553672414	173.5267057	8597.146904
60	0.397	0.745	0.102	186.82	0.361	10451.182	0.091	1.93141E-09	7.70208E-12	1.37679E-13	0.540823596	135.6196835	7586.907156
70	0.411	0.654	0.107	156.697	0.255	8647.346	0.058	2.20016E-09	9.18271E-12	1.66398E-13	0.565271134	135.4377535	7474.151492
80	0.414	0.559	0.1	129.218	0.217	6251.526	0.051	2.57407E-09	1.11355E-11	2.30168E-13	0.565873149	130.8067918	6328.391244
70-	0.404	0.659	0.108	150.269	0.492	10374.575	0.13	2.18346E-09	9.57552E-12	1.38695E-13	0.569592778	129.8818471	8967.045521
60-	0.422	0.772	0.126	223.806	0.208	13627.347	0.034	1.86386E-09	6.42924E-12	1.05589E-13	0.560423914	162.4692157	9892.605112
50-	0.426	0.895	0.099	255.925	0.085	37578.167	0.053	1.60771E-09	5.62236E-12	3.82909E-14	0.538042139	153.8529995	22590.65628
40-	0.434	1.035	0.077	286.027	0.014	437570.12	0.029	1.39024E-09	5.03065E-12	3.28839E-15	0.505075156	139.5798372	213532.1685

Table . 2nd Run of PTFE Filtered

30-	0.432	1.301	0.071	420.708			0.064	1.106E-09	3.42019E-12	0	0.5029309927	162.6341984	0
20-	0.44	1.848	0.114	1621.779			0.183	7.78627E-10	8.87237E-13	0	0.550174637	482.8255804	0
10-	0.448	2.364	0.094	2584.845			0.162	6.08673E-10	5.56669E-13	0	0.521152556	569.8386545	0

30

Run of Unfiltered Glycine 299.06 g/L

	Decay 1		Decay 2		Decay 3		RMS	Diffusion Coefficient 1 (m ² /s)	Diffusion Coefficient 2 (m ² /s)	Diffusion Coefficient 3 (m ² /s)	Hydrodynamic Diameter (nm)		
T (°C)	A	α	B	β	C	γ					Decay 1	Decay 2	Decay 3
30	0.36	1.727	0.327	535.517			0.122	8.33181E-10	2.68694E-12	0	0.6676109334	207.0162155	0
40	0.352	1.318	0.318	390.407	0.124	82561.375	0.058	1.09173E-09	3.68565E-12	1.74283E-14	0.643177831	190.5167886	40289.56456
50	0.317	1.084	0.358	311.448	0.483	24787.261	0.16	1.3274E-09	4.62004E-12	5.80501E-14	0.651662211	187.2314506	14901.21893
60	0.307	0.853	0.312	201.633	0.99	12967.073	0.288	1.68687E-09	7.13625E-12	1.10966E-13	0.619224869	146.3729988	9413.287314
70	0.297	0.687	0.245	120.53	1.468	11072.943	0.552	2.09447E-09	1.19381E-11	1.29948E-13	0.593793989	104.1775684	9570.665202
80	0.319	0.594	0.295	129.328	0.887	8045.789	0.228	2.4224E-09	1.1126E-11	1.78839E-13	0.60130349	130.9181443	8144.715492
70-	0.326	0.727	0.306	179.672	0.766	12042.61	0.225	1.97923E-09	8.0085E-12	1.19484E-13	0.628367147	155.2957112	10408.77646
60-	0.332	0.892	0.337	244.361	0.513	19540.415	0.11	1.61312E-09	5.88843E-12	7.36373E-14	0.64753644	177.3908654	14185.12417
50-	0.344	1.117	0.32	341.313	0.129	59881.985	0.079	1.28819E-09	4.21579E-12	2.4029E-14	0.671500637	205.1852254	35998.91768

Table . 2nd

40-	0.358	1.352	0.303	400.154	0.057	698924.05	0.091	1.06428E-09	3.59587E-12	2.05874E-15	0.659769672	195.273279	341071.663
30-	0.372	1.636	0.28	475.124	0.031	567414.46	0.065	8.79525E-10	3.02848E-12	0	0.632432824	183.6699346	0

31

Glycine 299.06 g/L

	Decay 1		Decay 2		Decay 3		RMS	Diffusion Coefficient 1 (m ² /s)	Diffusion Coefficient 2 (m ² /s)	Diffusion Coefficient 3 (m ² /s)	Hydrodynamic Diameter (nm)		
T (°C)	A	α	B	β	C	γ					Decay 1	Decay 2	Decay 3
30	0.418	1.194	0.02	424.124			0.015	1.20511E-09	3.39265E-12	0	0.4615677212	163.9547305	0
40	0.43	1.043	0.048	366.041	0.13	40114.539	0.045	1.37958E-09	3.93099E-12	3.58699E-14	0.508979118	178.6262947	0
50	0.403	0.845	0.031	178.784	0.113	14451.966	0.044	1.70284E-09	8.04828E-12	9.95645E-14	0.507983919	107.4785764	0
60	0.37	0.692	0.075	541.711	0.168	9914.208	0.05	2.07934E-09	2.65622E-12	1.45135E-13	0.502348897	393.2484443	7197.097479
70	0.389	0.624	0.034	163.623	0.1	7436.574	0.026	2.30593E-09	8.79401E-12	1.9349E-13	0.539341265	141.4240959	6427.6462
80	0.415	0.586	0.057	142.742	0.12	8602.683	0.074	2.45547E-09	1.00804E-11	1.67262E-13	0.593205126	144.4970753	8708.456747
70-	0.385	0.606	0.018	42.094	0.387	9845.49	0.16	2.37443E-09	3.41831E-11	1.46148E-13	0.523783344	36.38306284	8509.742038
60-	0.343	0.703	0.032	151.863	0.21	12900.313	0.039	2.0468E-09	9.47501E-12	1.1154E-13	0.510334212	110.2430789	9364.823713

Table . 2nd Run of PTFE Filtered

50-	0.412	0.807	0.034	301.836	0.042	31455.422	0.026	1.78303E-09	4.76717E-12	4.57442E-14	0.485139672	181.4530583	18909.87994
40-	0.349	1.002	0.032	761.478			0.029	1.43603E-09	1.88962E-12	0	0.48897131	371.5976998	0
30-	0.427	1.227	0.028	645.683			0.036	1.1727E-09	2.2285E-12	0	0.474324618	249.603376	0

10.3.3 First Run of Urea Experiments

Table 32. 1st Run of Unfiltered Urea 522.61 g/L

	Decay 1		Decay 2		Decay 3		RMS	Diffusion Coefficient 1 (m ² /s)	Diffusion Coefficient 2 (m ² /s)	Diffusion Coefficient 3 (m ² /s)	Hydrodynamic Diameter (nm)		
T (°C)	A	α	B	β	C	γ					Decay 1	Decay 2	Decay 3
10	0.164	2.307	0.571	615.21			0.106	6.23712E-10	2.33888E-12	0	0.508586695	135.6253232	0
20	0.144	2.145	0.599	519.686			0.232	6.70817E-10	2.76879E-12	0	0.638595561	154.717563	0
30	0.135	1.805	0.593	405.278			0.243	7.97176E-10	3.55041E-12	0	0.6977635986	156.6693827	0
40	0.113	1.272	0.601	309.441	0.187	36237.77	0.073	1.13121E-09	4.65001E-12	3.97073E-14	0.620730046	151.0057596	17683.86214
50	0.111	0.907	0.567	230.087	0.304	14191.925	0.088	1.58644E-09	6.25373E-12	1.01389E-13	0.545256112	138.3201137	8531.680101
60	0.109	0.624	0.539	175.916	0.528	11234.359	0.164	2.30593E-09	8.17949E-12	1.28081E-13	0.452985133	127.7040587	8155.444876
70	0.107	0.5	0.532	145.595	0.555	7612.245	0.16	2.87781E-09	9.88292E-12	1.89025E-13	0.432164475	125.8419735	6579.483731
80	0.138	0.372	0.516	127.274	0.515	5765.662	0.149	3.86802E-09	1.13056E-11	2.49564E-13	0.376573903	128.8388894	5836.553334
70-	0.113	0.467	0.529	149.654	0.532	8421.124	0.174	3.08116E-09	9.61487E-12	1.70868E-13	0.40364162	129.3502848	7278.621269
60-	0.117	0.608	0.505	184.444	0.685	14335.147	0.181	2.36662E-09	7.8013E-12	1.00376E-13	0.441370129	133.8948555	10406.42382
50-	0.11	0.916	0.549	241.94	0.481	36318.342	0.112	1.57085E-09	5.94735E-12	3.96192E-14	0.550666592	145.4457153	21833.29434
40-	0.136	1.175	0.57	296.692	0.025	268450.58	0.062	1.2246E-09	4.84982E-12	5.36003E-15	0.5733945	144.7843073	131002.6241
30-	0.174	1.544	0.566	396.047			0.174	9.31932E-10	3.63316E-12	0	0.596868142	153.1009307	0
20-	0.169	1.669	0.525	460.687			0.065	8.62135E-10	3.12339E-12	0	0.496883912	137.1527614	0
10-	0.16	2.51	0.588	717.753			0.214	5.73268E-10	2.00473E-12	0	0.553338797	158.2313074	0

Table . 1st Run of PTFE Filtered

33 Urea 522.61 g/L													
	Decay 1		Decay 2		Decay 3		RMS	Diffusion Coefficient 1 (m²/s)	Diffusion Coefficient 2 (m²/s)	Diffusion Coefficient 3 (m²/s)	Hydrodynamic Diameter (nm)		
T (°C)	A	α	B	β	C	γ					Decay 1	Decay 2	Decay 3
10	0.276	2.03	0.311	839.213			0.228	7.08819E-10	1.71459E-12	0	0.447521019	185.0076143	0
20	0.271	1.639	0.299	730.229			0.221	8.77915E-10	1.97048E-12	0	0.487952505	217.3990666	0
30	0.227	1.45	0.364	614.751			0.287	9.92347E-10	2.34063E-12	0	0.5605303147	237.6459114	0
40	0.199	1.052	0.365	358.618	0.535	30755.346	0.115	1.36778E-09	4.01236E-12	4.67855E-14	0.513371076	175.0039054	15008.46489
50	0.206	0.788	0.326	248.641	0.433	15275.824	0.135	1.82602E-09	5.78707E-12	9.41948E-14	0.473717548	149.474118	9183.281594
60	0.204	0.599	0.332	204.245	0.767	11070.537	0.225	2.40218E-09	7.04499E-12	1.29976E-13	0.43483669	148.2691481	8036.520308
70	0.249	0.482	0.325	158.849	0.749	8336.589	0.26	2.98528E-09	9.05831E-12	1.72601E-13	0.416606554	137.2977895	7205.555221
80	0.213	0.403	0.299	119.843	0.604	5525.515	0.17	3.57048E-09	1.20066E-11	2.60411E-13	0.407955061	121.3165221	5593.453621
70-	0.192	0.487	0.403	164.688	0.531	8390.143	0.136	2.95463E-09	8.73715E-12	1.71499E-13	0.420928199	142.3446062	7251.843493
60-	0.218	0.588	0.303	182.969	0.56	12007.045	0.18	2.44711E-09	7.86419E-12	1.19838E-13	0.426851375	132.8240974	8716.366784
50-	0.227	0.774	0.341	283.61	0.26	24027.748	0.069	1.85905E-09	5.07353E-12	5.98851E-14	0.465301247	170.4962359	14444.62675
40-	0.232	0.995	0.274	387.656	0.031	618861.23	0.081	1.44613E-09	3.7118E-12	2.32508E-15	0.485555343	189.1743135	302001.3821
30-	0.198	2.152	0.389	1145.685			0.428	6.68635E-10	1.25593E-12	0	0.8319043015	442.8904645	0

20-	0.497	0.567	0.581	453.353			1.004	2.53775E-09	3.17391E-12	0	0.168803582	134.9693302	0
10-	0.721	0.459	0.592	7145.422			1.185	3.13487E-09	2.01374E-13	0	0.10118825	1575.234746	0

Table 34. 1st Run of Unfiltered Urea 785.15 g/L

	Decay 1		Decay 2		Decay 3		RMS	Diffusion Coefficient 1 (m ² /s)	Diffusion Coefficient 2 (m ² /s)	Diffusion Coefficient 3 (m ² /s)	Hydrodynamic Diameter (nm)		
T (°C)	A	α	B	β	C	γ					Decay 1	Decay 2	Decay 3
10	0.151	2.62	0.572	722.125			0.187	5.492E-10	1.9926E-12	0	0.577588704	159.195131	0
20	0.139	2.455	0.583	625.338			0.299	5.86111E-10	2.301E-12	0	0.730886761	186.1715948	0
30	0.109	3.269	0.593	544.639			0.37	4.40166E-10	2.64194E-12	0	1.26370593	210.5425311	0
40	0.111	1.191	0.541	324.944	0.205	28364.428	0.062	1.20815E-09	4.42816E-12	5.07291E-14	0.581202425	158.5711511	13841.7081
50	0.114	0.862	0.542	250.498	0.29	14701.978	0.063	1.66926E-09	5.74417E-12	9.78714E-14	0.518203714	150.5904803	8838.305807
60	0.106	0.661	0.502	187.044	0.606	11016.844	0.181	2.17686E-09	7.69286E-12	1.30609E-13	0.479844828	135.7822935	7997.542535
70	0.119	0.482	0.504	168.088	0.479	8051.33	0.147	2.98528E-09	8.56042E-12	1.78716E-13	0.416606554	145.2833246	6958.997609
80	0.114	0.456	0.502	143.765	0.513	6499.07	0.151	3.15549E-09	1.00087E-11	2.21401E-13	0.461606719	145.5326535	6578.978906
70-	0.106	0.521	0.492	166.789	0.651	10382.793	0.188	2.76181E-09	8.62709E-12	1.38585E-13	0.450315383	144.1605613	8974.148576
60-	0.116	0.594	0.488	196.471	0.663	12587.461	0.167	2.4224E-09	7.32374E-12	1.14312E-13	0.431207001	142.6257084	9137.712647
50-	0.111	1.051	0.528	276.717	0.302	21474.663	0.073	1.36908E-09	5.19991E-12	6.70047E-14	0.631823786	166.3524097	12909.80293
40-	0.14	1.186	0.515	341.534	0.042	205520.03	0.067	1.21324E-09	4.21306E-12	7.00128E-15	0.578762449	166.6669934	100292.8122

Table . 1st Run of PTFE Filtered

30-	0.167	1.186	0.585	609.348			0.462	1.21324E-09	2.36138E-12	0	0.4584751402	235.5572594	0
20-	0.147	1.927	0.479	579.049			0.135	7.46706E-10	2.48494E-12	0	0.573694007	172.3907323	0
10-	0.363	3.377	0.539	1014.625			0.363	4.26089E-10	1.41816E-12	0	0.744472158	223.6778394	0

35

Urea 785.15 g/L

	Decay 1		Decay 2		Decay 3		RMS	Diffusion Coefficient 1 (m ² /s)	Diffusion Coefficient 2 (m ² /s)	Diffusion Coefficient 3 (m ² /s)	Hydrodynamic Diameter (nm)		
T (°C)	A	α	B	β	C	γ					Decay 1	Decay 2	Decay 3
10	0.291	1.461	0.024	7659.916			0.055	9.84875E-10	1.87848E-13	0	0.322082862	1688.656854	0
20	0.272	1.464	0.071	47506.99			0.133	9.82857E-10	3.02882E-14	0	0.435852634	14143.47575	0
30	0.274	0.932	0.045	1291.166	0.045	173838.66	0.072	1.54389E-09	1.11442E-12	8.27723E-15	0.3602856919	499.1294375	0
40	0.27	0.793	0.056	483.579	0.344	27390.862	0.093	1.81451E-09	2.97553E-12	5.25322E-14	0.386980288	235.9842885	13366.61245
50	0.266	0.651	0.059	316.568	0.397	14017.318	0.115	2.2103E-09	4.54532E-12	1.02652E-13	0.391358025	190.3094123	8426.712588
60	0.249	0.566	0.029	105.859	0.812	10239.507	0.229	2.54223E-09	1.35926E-11	1.40525E-13	0.410880745	76.84704033	7433.244291
70	0.216	0.522	0.011	36.512	0.842	7960.567	0.276	2.75652E-09	3.9409E-11	1.80754E-13	0.451179712	31.55837864	6880.54852
80	0.19	0.553	0.894	5687.596	0.106	5687.596	0.348	2.60199E-09	2.5299E-13	2.5299E-13	0.559799377	5757.527478	5757.527478
70-	0.163	0.82	0.859	8509.106	0.061	8509.106	0.286	1.75476E-09	1.69102E-13	1.69102E-13	0.708749739	7354.666658	7354.666658
60-	0.247	0.549	0.052	230.874	0.673	11167.599	0.125	2.62095E-09	6.23242E-12	1.28846E-13	0.398539804	167.6001435	8106.981275
50-	0.243	0.683	0.063	556.001	0.3	26868.966	0.085	2.10674E-09	2.58795E-12	5.35526E-14	0.410595286	334.2480085	16152.66587

40-	0.254	0.789	0.05	995.276	0.036	432321	0.035	1.8237E-09	1.44573E-12	3.32832E-15	0.385028307	485.6900295	210970.6235
30-	0.255	0.84	0.03	1445.953	0.031	619260.77	0.03	1.71298E-09	9.95124E-13	2.32358E-15	0.3247210099	558.9658553	0
20-	0.282	1.093	0.018	3605.78			0.03	1.31647E-09	3.99055E-13	0	0.325400908	1073.489558	0
10-	0.29	1.517	0.027	7847.191			0.051	9.48519E-10	1.83365E-13	0	0.334428269	1729.942322	0

Table 36. Run of Unfiltered Urea 1149.75 g/L

	Decay 1		Decay 2		Decay 3		RMS	Diffusion Coefficient 1 (m ² /s)	Diffusion Coefficient 2 (m ² /s)	Diffusion Coefficient 3 (m ² /s)	Hydrodynamic Diameter (nm)		
T (°C)	A	α	B	β	C	γ					Decay 1	Decay 2	Decay 3
10	0.142	3.023	0.568	961.562			0.268	4.75985E-10	1.49642E-12	0	0.666431547	211.9799045	0
20	0.157	0.676	0.204	5276.21			0.575	2.12855E-09	2.72715E-13	0	0.201254359	1570.7992	0
30	0.11	3.099	0.6	660.311			0.5	4.64312E-10	2.17913E-12	0	1.197988583	255.2581604	0
40	0.107	1.202	0.539	390.918	0.388	29986.285	0.106	1.19709E-09	3.68083E-12	4.79854E-14	0.586570374	190.7661543	14633.16673
50	0.101	0.809	0.497	282.139	0.544	15929.024	0.169	1.77862E-09	5.09998E-12	9.03322E-14	0.486342001	169.6119231	9575.962181
60	0.105	0.614	0.481	220.593	0.607	10358.852	0.203	2.34349E-09	6.52289E-12	1.38906E-13	0.445725756	160.1367779	7519.881327
70	0.108	0.484	0.463	186.483	0.734	9409.491	0.199	2.97294E-09	7.716E-12	1.5292E-13	0.418335212	161.1826557	8132.89548
80	0.103	0.408	0.451	154.27	0.734	6672.049	0.224	3.52672E-09	9.32717E-12	2.15661E-13	0.413016538	156.1668171	6754.084758
70-	0.113	0.471	0.445	182.991	0.841	9548.596	0.263	3.055E-09	7.86324E-12	1.50693E-13	0.407098936	158.164419	8253.127959
60-	0.116	0.671	0.488	254.479	0.563	13394.143	0.115	2.14442E-09	5.65431E-12	1.07428E-13	0.487104205	184.7359032	9723.313533
50-	0.113	1.079	0.514	356.82	0.297	29947.287	0.108	1.33355E-09	4.03257E-12	4.80479E-14	0.648656389	214.5074818	18003.24287
40-	0.138	1.29	0.483	419.473	0.073	275335.42	0.074	1.11543E-09	3.43026E-12	5.226E-15	0.629513962	204.7008606	134362.3972
30-	0.18	2.647	0.598	1232.669			0.607	5.43598E-10	1.16731E-12	0	1.023257754	476.5160983	0
20-	0.16	2.538	0.558	882.355			0.352	5.66944E-10	1.63075E-12	0	0.755596985	262.6890378	0
10-	0.153	3.232	0.539	1187.179			0.358	4.45205E-10	1.21204E-12	0	0.712506371	261.7180078	0

37

Urea 1149.75 g/L

	Decay 1		Decay 2		Decay 3		RMS	Diffusion Coefficient 1 (m ² /s)	Diffusion Coefficient 2 (m ² /s)	Diffusion Coefficient 3 (m ² /s)	Hydrodynamic Diameter (nm)		
T (°C)	A	α	B	β	C	γ					Decay 1	Decay 2	Decay 3
50	0.22	0.634	0.018	191.729	0.256	16547.328	0.088	2.26956E-09	7.50488E-12	8.69568E-14	0.381138231	115.2606496	9947.664536
60	0.23	0.55	0.029	281.757	0.124	9418.41	0.034	2.61619E-09	5.10689E-12	1.52776E-13	0.399265742	204.5380321	6837.179013
70	0.218	0.474	0.003	4.521	0.523	8801.153	0.213	3.03566E-09	3.18271E-10	1.6349E-13	0.409691923	3.907631185	7607.091335
80	0.199	0.437	0.017	84.07	0.362	6659.716	0.098	3.29268E-09	1.71155E-11	2.16061E-13	0.442373106	85.10367739	6741.600118
70-	0.194	0.537	0.002	17.598	0.455	9976.335	0.178	2.67952E-09	8.17651E-11	1.44232E-13	0.464144646	15.21046087	8622.83516
60-	0.203	0.587	0.013	77.126	0.407	11500.225	0.121	2.45128E-09	1.86565E-11	1.2512E-13	0.426125437	55.98867203	8348.447032
50-	0.205	0.654	0.02	365.151	0.072	24285.478	0.026	2.20016E-09	3.94057E-12	5.92495E-14	0.393161519	219.5157824	14599.56485
40-	0.22	0.728	0.011	552.031	0.001	521989.02	0.009	1.97652E-09	2.60656E-12	2.75658E-15	0.355260592	269.3885441	254728.1985
30-	0.226	0.891	0.012	1073.74			0.016	1.61493E-09	1.34009E-12	0	0.3444362141	415.0784966	0

10.3.4 Second Run of Urea Experiments

Table 38. 2nd Run of Unfiltered Urea 522.06 g/L

	Decay 1		Decay 2		Decay 3		RMS	Diffusion Coefficient 1 (m ² /s)	Diffusion Coefficient 2 (m ² /s)	Diffusion Coefficient 3 (m ² /s)	Hydrodynamic Diameter (nm)		
T (°C)	A	α	B	β	C	γ					Decay 1	Decay 2	Decay 3
10	0.333	1.525	0.053	2142.392			0.086	9.43543E-10	6.71634E-13	0	0.336191899	472.2982518	0

Table . 1st Run of PTFE Filtered

20	0.322	1.214	0.059	1687.442			0.099	1.18526E-09	8.52713E-13	0	0.361424247	502.3743451	0
30	0.29	1.083	0.142	1645.092	0.247	197524.3	0.084	1.32863E-09	8.74664E-13	0	4.186581592	6359.475424	0
40	0.267	0.856	0.099	312.95	1.143	23977.4	0.326	1.68096E-09	4.59787E-12	6.00108E-14	0.417723993	152.7181352	11700.85897
50	0.233	0.004	0.528	3.455	3.455	14222.786	1.42	3.59726E-07	4.1647E-10	1.01169E-13	0.002404658	2.077023008	8550.232635
60	0.237	0.477	2.777	11211	0.592	1211.002	1.405	3.01657E-09	1.28347E-13	1.18819E-12	0.346272289	8138.489149	879.112022
70	0.194	0.571	2.814	8020.818	0.038	8020.818	0.955	2.51997E-09	1.79396E-13	1.79396E-13	0.493531831	6932.625204	6932.625204
80	0.337	0.195	3.022	7280.543	0.657	7280.526	1.62	7.37899E-09	1.97637E-13	1.97637E-13	0.19739761	7370.060458	7370.043249
70-	0.352	0.271	2.345	93000.43	0.893	9300.425	1.453	5.30961E-09	1.5472E-14	1.54714E-13	0.234233146	80382.95973	8038.626579
60-	0.156	1.446	1.935	11516.75	0.418	11516.75	0.698	9.95092E-10	1.2494E-13	1.2494E-13	1.049705933	8360.443153	8360.443153
50-	0.268	0.666	0.112	266.521	1.14	22280.192	0.237	2.16052E-09	5.39884E-12	6.45822E-14	0.400375491	160.2229375	13394.05829
40-	0.291	0.787	0.064	548.334	0.071	245366	0.039	1.82834E-09	2.62414E-12	5.86431E-15	0.384052316	267.5844254	119737.459
30-	0.3	0.976	0.057	1122.625			0.092	1.47429E-09	1.28173E-12	0	0.3772948877	433.9760997	0
20-	0.324	1.228	0.066	1236.816			0.091	1.17175E-09	1.16339E-12	0	0.365592237	368.2168798	0
10-	0.33	1.864	0.111	4579.204			0.197	7.71944E-10	3.14226E-13	0	0.410925704	1009.502483	0

39

Urea 522.06 g/L

	Decay 1		Decay 2		Decay 3		RMS	Diffusion Coefficient 1 (m ² /s)	Diffusion Coefficient 2 (m ² /s)	Diffusion Coefficient 3 (m ² /s)	Hydrodynamic Diameter (nm)		
T (°C)	A	α	B	β	C	γ					Decay 1	Decay 2	Decay 3
50	0.191	0.533	0.015	17781.82	0.092	17781.824	0.032	2.69963E-09	8.09199E-14	8.09199E-14	0.320420626	10689.79958	10689.79958
60	0.527	0.218	0.411	18675.28	0.348	18675.304	0.457	6.60047E-09	7.70486E-14	7.70484E-14	0.158254421	13557.08642	13557.10747
70	18.708	0.016	0.489	12493.99	0.016	12493.987	0.262	8.99314E-08	1.15168E-13	1.15168E-13	0.013829263	10798.91554	10798.91467
80	0.2	0.321	0.002	5.977	0.171	9712.835	0.076	4.48256E-09	2.4074E-10	1.48144E-13	0.324946835	6.050489827	9832.258551
70-	0.508	0.198	0.447	14019.49	0.003	13829.704	0.271	7.26719E-09	1.02636E-13	1.04044E-13	0.171137132	12117.45021	11953.41354
60-	0.159	0.517	0.014	20895.46	0.003	250.382	0.014	2.78318E-09	6.8862E-14	5.74683E-12	0.375309797	15168.80534	181.7617364
50-	0.169	0.549	0.002	226.823	0.002	46523.672	0.006	2.62095E-09	6.34373E-12	3.09284E-14	0.330039256	136.3579131	27968.37544
40-	0.189	0.573	0.001	78.567	0.001	2981.601	0.008	2.51117E-09	1.83143E-11	4.82594E-13	0.279621318	38.34032826	1455.007332
30-	0.207	0.777	0.003	953.842			0.007	1.85187E-09	1.50853E-12	0	0.3003669342	368.7292113	0

Table . 2nd Run of PTFE FilteredTable 40. 2nd Run of Unfiltered Urea 785.15 g/L

	Decay 1		Decay 2		Decay 3		RMS	Diffusion Coefficient 1 (m ² /s)	Diffusion Coefficient 2 (m ² /s)	Diffusion Coefficient 3 (m ² /s)	Hydrodynamic Diameter (nm)		
T (°C)	A	α	B	β	C	γ					Decay 1	Decay 2	Decay 3
10	0.288	2.535	0.148	28279.82			0.368	5.67615E-10	5.08809E-14	0	0.55885014	6234.390626	0
20	0.281	1.448	0.133	3010.066	0.147	801851.95	0.224	9.93718E-10	4.7803E-13	0	0.431089218	896.137429	0
30	0.268	1.086	0.156	1413.334	0.197	231278.1	0.137	1.32496E-09	1.01809E-12	0	4.198178771	5463.562426	0
40	0.214	573.87	2.325	46326.67	0.031	6.024E+10	0.872	2.50737E-12	3.10599E-14	2.38881E-20	280.0458739	22607.19666	29394451256
50	0.372	0.017	7.241	22347.91	0.236	22347.913	2.998	8.46414E-08	6.43865E-14	6.43865E-14	0.010219795	13434.76975	13434.76975
60	0.323	0.016	16.908	15388.1	0.318	15388.099	8.575	8.99314E-08	9.35075E-14	9.35075E-14	0.011615003	11170.80067	11170.80139
70	0.441	0.008	19.179	11975.62	0.703	11975.62	9.579	1.79863E-07	1.20153E-13	1.20153E-13	0.006914632	10350.87507	10350.87507
80	30.414	0.016	11.562	11183.54	0.566	11183.537	6.055	8.99314E-08	1.28663E-13	1.28663E-13	0	11321.04347	11321.04347
70-	6.008	0.022	1.296	14417.57	10.603	14417.543	6.444	6.54047E-08	9.98021E-14	9.98022E-14	0.019015237	12461.52142	12461.49981
60-	6.136	0.015	9.132	14089.75	1.063	14089.753	4.791	9.59269E-08	1.02124E-13	1.02124E-13	0	10228.28307	10228.28307
50-	0.164	1.186	2.649	29834.44	0.761	29834.438	1.372	1.21324E-09	4.82296E-14	4.82296E-14	0.71298098	17935.40207	17935.40207
40-	0.241	0.969	0.126	2069.948	0.219	234247.6	0.127	1.48494E-09	6.9514E-13	6.14266E-15	0.472867464	1010.124935	114311.7304
30-	0.258	1.194	0.092	5701.491			0.201	1.20511E-09	2.52373E-13	0	0.4615677212	2204.040375	0

20-	0.276	1.777	0.12	11720.86			0.382	8.09737E-10	1.22764E-13	0	0.529036975	3489.460009	0
10-	0.305	2.064	0.119	17602.69			0.25	6.97143E-10	8.17434E-14	0	0.455016445	3880.578431	0

41 Urea 785.15 g/L													
	Decay 1		Decay 2		Decay 3		RMS	Diffusion Coefficient 1 (m ² /s)	Diffusion Coefficient 2 (m ² /s)	Diffusion Coefficient 3 (m ² /s)	Hydrodynamic Diameter (nm)		
T (°C)	A	α	B	β	C	γ					Decay 1	Decay 2	Decay 3
10	0.288	1.214	0.002	661.017			0.007	1.18526E-09	2.1768E-12	0	0.267630797	145.723646	0
20	0.26	0.994	0.002	597.727			0.008	1.44759E-09	2.40729E-12	0	0.295927267	177.951426	0
30	0.244	0.846	0.004	7469.582			0.023	1.70083E-09	1.92635E-13	0	0.3270404457	2887.535965	0
40	0.225	0.6	0.011	26742.73	0	34173967	0.011	2.39817E-09	5.38054E-14	4.21052E-17	0.292797192	13050.32658	16676735.97
50	0.226	0.581	0.038	15862.58	0	4.676E+16	0.017	2.4766E-09	9.07105E-14	3.07718E-26	0.349276517	9536.018414	2.81107E+16
60	0.209	0.408	0.711	14911.75	0.107	14725.721	0.34	3.52672E-09	9.64946E-14	9.77136E-14	0.296182587	10824.99806	10689.95622
70	0.187	0.447	0.126	9769.662	0	5.058E+13	0.055	3.21902E-09	1.47283E-13	2.84481E-23	0.386355041	8444.201703	4.37177E+13
80	0.188	0.418	0.207	9094.992	0.002	4715772.8	0.088	3.44235E-09	1.58208E-13	3.05126E-16	0.423139493	9206.818901	4773755.278
70-	0.246	0.347	0.294	13543.39	0.035	13542.846	0.201	4.14669E-09	1.06244E-13	1.06248E-13	0.299922146	11705.94579	11705.47387
60-	0.199	0.507	0.162	17682.4	0	13195138	0.068	2.83807E-09	8.13749E-14	1.09048E-16	0.36805042	12836.32174	9578848.445
50-	0.206	0.725	0.076	25188.3	0.001	6.711E+15	0.049	1.98469E-09	5.71259E-14	2.14413E-25	0.435844191	15142.30629	4.03436E+15

Table . 2nd Run of PTFE Filtered

40-	0.267	0.837	0.011	403.457	0.004	100707.71	0.024	1.71912E-09	3.56643E-12	1.42879E-14	0.408452082	196.8851276	49144.88915
30-	0.28	1.104	0.019	1404.479			0.027	1.30335E-09	1.02451E-12	0	0.4267761844	542.933142	0
20-	0.294	1.392	0.017	1746.327			0.008	1.03369E-09	8.2396E-13	0	0.414417259	519.9052074	0
10-	0.31	1.634	0.029	4161.68			0.033	8.80602E-10	3.45751E-13	0	0.360221352	917.4577708	0

2nd

Table 42. Run of Unfiltered Urea 1149.74 g/L

	Decay 1		Decay 2		Decay 3		RMS	Diffusion Coefficient 1 (m ² /s)	Diffusion Coefficient 2 (m ² /s)	Diffusion Coefficient 3 (m ² /s)	Hydrodynamic Diameter (nm)		
T (°C)	A	α	B	β	C	γ					Decay 1	Decay 2	Decay 3
30	0.182	2.931	0.314	5550.605			0.577	4.90926E-10	2.59234E-13	0	1.133044381	2145.711978	0
40	0.161	0.919	0.213	515.788	1.566	28128.676	0.434	1.56573E-09	2.78972E-12	5.11543E-14	0.448467698	251.7021298	13726.66223
50	0.155	0	0.282	1.661	1.997	14760.271	0.784	0	8.66287E-10	9.74849E-14	0	0.998534071	8873.349484
60	0.144	0.589	0.107	150.891	2.134	11710.962	0.781	2.44296E-09	9.53604E-12	1.22868E-13	0.427577313	109.5374674	8501.428968
70	0.126	0.542	0.071	87.45	2.491	9686.823	0.926	2.6548E-09	1.6454E-11	1.48542E-13	0.468466291	75.58556672	8372.601557
80	1.44	0.141	0.066	71.661	2.43	7777.37	0.939	1.0205E-08	2.00793E-11	1.85012E-13	0.142733657	72.54210331	7872.996163
70-	0.149	0.015	0.142	145.415	1.958	9284.682	0.734	9.59269E-08	9.89515E-12	1.54976E-13	0.012964934	125.6863943	8025.019448
60-	0.17	0.536	0.172	249.764	1.676	14329.11	0.471	2.68452E-09	5.76105E-12	1.00418E-13	0.389102614	181.3131069	10402.04134
50-	0.178	0.8	0.238	521.212	1	30491.436	0.34	1.79863E-09	2.76069E-12	4.71904E-14	0.480931521	313.3341001	18330.36588
40-	0.209	1.132	0.231	1491.771	0.261	245523.73	0.185	1.27112E-09	9.6456E-13	5.86055E-15	0.552410702	727.9772656	119814.4291
30-	0.188	2.571	0.293	5230.106			0.504	5.59667E-10	2.75119E-13	0	9.938782338	20218.15836	0
20-	1.813	0.234	0.389	17873.5			0.81	6.14916E-09	8.05048E-14	0	0.06966497	5321.181912	0
10-	0.971	0.43	0.561	96076.43			1.152	3.34629E-09	1.49767E-14	0	0.094795093	21180.40376	0

Table . 2nd Run of PTFE Filtered

43 Urea 1149.74 g/L													
	Decay 1		Decay 2		Decay 3		RMS	Diffusion Coefficient 1 (m²/s)	Diffusion Coefficient 2 (m²/s)	Diffusion Coefficient 3 (m²/s)	Hydrodynamic Diameter (nm)		
T (°C)	A	α	B	β	C	γ					Decay 1	Decay 2	Decay 3
50	0.191	0.533	0.067	17781.83	0.041	17781.819	0.032	2.69963E-09	8.09199E-14	8.09199E-14	0.320420626	10689.80139	10689.79658
60	0.252	0.31	0.422	18679.6	0.338	18654.737	0.457	4.64162E-09	7.70307E-14	7.71334E-14	0.225040691	13560.229	13542.17711
70	0.405	0.228	0.288	12525.51	0.217	12525.511	0.258	6.31098E-09	1.14878E-13	1.14878E-13	0.197067001	10826.16178	10826.16178
80	0.203	0.325	0.001	0	0.171	9697.874	0.084	4.42739E-09	0	1.48373E-13	0.328996017	0	9817.113599
70-	0.022	1.33	0.356	13946.55	0.094	14071.529	0.273	1.08188E-09	1.03173E-13	1.02256E-13	1.149557504	12054.40779	12162.42989
60-	0.161	0.482	0.004	23.859	0.015	17238.012	0.018	2.98528E-09	6.03086E-11	8.34727E-14	0.349901978	17.32014789	12513.723
50-	0.169	0.549	0.002	226.823	0.002	46523.673	0.006	2.62095E-09	6.34373E-12	3.09284E-14	0.330039256	136.3579131	27968.37604
40-	0.189	0.573	0.001	78.567	0.001	2981.602	0.008	2.51117E-09	1.83143E-11	4.82594E-13	0.279621318	38.34032826	1455.00782
30-	0.215	0.76	0.003	924.742			0.007	1.89329E-09	1.556E-12	0	0.2937951994	357.4799478	0

11 REFERENCES

- [1] J. W. Mullin, "Crystallization and Precipitation," in *Ullmann's Encyclopedia of Industrial Chemistry*, 6th ed., Wiley, 2003.
- [2] W. L. McCabe, J. C. Smith and P. Harriot, *Unit Operations of Chemical Engineering*, 5th ed., McGraw-Hill, 1993.
- [3] J. W. Mullin, *Crystallization*, 4th Edition ed., Butterworth Heinemann, 2001.
- [4] M. Sharaf and R. Dobbins, "A comparison of measured nucleation rates with the predictions of several theories of homogeneous nucleation," *Journal of Chemical Physics*, vol. 77, no. 3, pp. 1517-1526, 1982.
- [5] R. Strey, P. Wagner and T. Schmeling, "Homogeneous nucleation rates for alcohol vapors measured in a two-piston expansion chamber," *Journal of Chemical Physics*, vol. 84, p. 2325, 1986.
- [6] A. Laaksonen, R. McGraw and H. Vehkamäki, "Liquid-drop formalism and freeenergy surfaces in binary homogeneous nucleation theory," *Journal of Chemical Physics*, vol. 111, p. 2019, 1999.
- [7] H. Vehkamäki, *Classical Nucleation Theory in Multicomponent Systems*, Springer, 2006, pp. 113-114.
- [8] J. Drenth and C. Haas, "Nucleation in Protein Crystallisation," *Acta Crystallographica Section D: Biological Crystallography*, vol. 54, pp. 867-872, September 1998.
- [9] J. Merikanto, A. Lauri, E. Zapadinsky and H. Vehkamäki, "An Insight into the Failure of Classical Nucleation Theory," Springer, 2007.

- [10] A. Jawor-Baczynska, J. Sefcik and B. D. Moore, "250 nm Glycine-Rich Nanodroplets Are Formed on Dissolution of Glycine Crystals But Are Too Small To Provide Productive Nucleation Sites," *Crystal Growth & Design*, vol. 13, pp. 470-478, 6 December 2012.
- [11] C. Forsyth, P. A. Mulheran, C. Forsyth, M. D. Haw, I. S. Burns and J. Sefcik, "Influence of Controlled Fluid Shear on Nucleation Rates in Glycine Aqueous Solutions," *Crystal Growth and Design*, vol. 15, pp. 94-102, 2015.
- [12] T. Bott, *Fouling of Heat Exchangers*, Elsevier Science & Technology Books, 1995.
- [13] S. Lawton, G. Steele and P. Shering, "Continuous Crystallization of Pharmaceutical using a Continuous Oscillatory Baffled Crystalliser," *Organic Process Research & Development*, vol. 13, no. 6, pp. 1357-1363, 2009.
- [14] M. G. Mwaba, "Analysis of Heat Exchanger Fouling in Cane Sugar Industry," Eindhoven University Oress, 2003.
- [15] J. Holbrough, J. Campbell, E. Meldrum and H. Christenson, "Topographical Control of Crystal Nucleation," *Crystal Growth and Design*, pp. 750-755, 2012.
- [16] Y. Diao, A. S. Myerson, T. A. Hatton and B. L. Trout, "Surface Design for Controlled Crystallization: The Role of Surface Chemistry and Nanoscale Pores in Heterogeneous Nucleation," *Langmuir*, pp. 5324-5334, 2011.
- [17] J. W. Mullin, "Crystallisation and Precipitation," in *Ullmann's Encyclopedia of Industrial Chemistry*, 6th Edition ed., 2003.
- [18] D. Erdemir, A. Y. Lee and A. S. Myerson, "Nucleation of crystals from solution: Classical and Two-Step Models," *Accounts of Chemical Research*, pp. 621-629, 6 October 2008.
- [19] S. Y. Wong, A. P. Tatusko, B. L. Trout and A. S. Myerson, "Development of

- Continuous Crystallization Processes Using a Single-Stage Mixed-Suspension, Mixed-Product Removal Crystallizer with Recycle," *Crystal Growth & Design*, vol. 12, pp. 5701-5707, 2012.
- [20] Q. Su, Z. K. Nagy and C. D. Rielly, "Pharmaceutical crystallisation processes from batch to continuous operation using MSMPR stages: Modelling, design, and control," *Chemical Engineering and Processing: Process Intensification*, vol. 89, pp. 41-53, 2015.
- [21] K. Plumb, "CONTINUOUS PROCESSING IN THE PHARMACEUTICAL INDUSTRY - Changing the mind set," *Trans IChemE Part A*, vol. 83, no. A6, pp. 730-738, 2005.
- [22] S. D. Schaber, D. L. Gerogiorgis, R. Ranachandran, J. M. Evans, P. I. Barton and B. L. Trout, "Economic Analysis of Integrated Continuous and Batch Pharmaceutical Manufacturing: A Case Study," *Ind. Eng. Chem. Res.*, vol. 50, pp. 10083-10092, 2011.
- [23] A. Pelleck and P. V. Arnum, "Continuous Processing: Moving with or against the Manufacturing Flow," *Pharmaceutical Technology*, vol. 9, no. 32, pp. 5258, 2008.
- [24] B. Swichtenberg, "Moving Beyond the Batch," *Pharmaceutical Manufacturing*, vol. 7, no. 1, pp. 24-26, 2008.
- [25] O. Narducci, A. G. Jones and E. Kougoulos, "Continuous crystallization of adipic acid with ultrasound," *Chemical Engineering Science*, vol. 66, pp. 1069-1076, 2011.
- [26] R. Davey and J. Garside, *From Molecules to Crystallizers An Introduction to Crystallization*, Oxford Science Publications, 2006.
- [27] D. S. Hodgen, *13.361 An Introduction to Crystallization*, 2009.

- [28] D. Erdemir, A. Y. Lee and A. S. Myerson, "Nucleation of crystals from solution: Classical and Two-Step Models," *Accounts of Chemical Research*, vol. 42, no. 5, pp. 621-629, 6 October 2008.
- [29] D. Erdemir, A. Y. Lee and A. S. Myerson, "Nucleation of crystals from solution: Classical and Two-Step Models," *Accounts of Chemical Research*, pp. 621-629, 6 October 2008.
- [30] P. R. ten Wolde and D. Frenkel, "Enhancement of Protein Crystal Nucleation by Critical Density Fluctuations," *Science*, vol. 277, pp. 1975-1978, 1997.
- [31] D. Gebauer and H. Colfen, "Prenucleation clusters and non-classical nucleation," *Nano Today*, vol. 6, pp. 564-584, 25 November 2011.
- [32] E. Pouget, P. H. Bomans, J. A. Goos, P. M. Frederik, G. de With and N. A. Sommerdijk, "The Initial Stages of Template-Controlled CaCO₃ Formation Revealed by Cryo-TEM," *SCIENCE*, vol. 323, pp. 1455-1458, 13 March 2009.
- [33] A. Baszkin and W. Norde, *Physical Chemistry of Biological Interfaces*, CRC Press, 1999, pp. 799-800.
- [34] S. Chattopadhyay, D. Erdemir, J. M. Evans, J. Ilavsky, H. Amenitsch, C. U. Segre and A. S. Myerson, "SAXS Study of the Nucleation of Glycine Crystals from a Supersaturated Solution," *Crystal Growth and Design*, pp. 523-527, 2005.
- [35] A. Jawor-Baczynska, B. D. Moore and J. Sefcik, "Effect of mixing, concentration and temperature on the formation of mesostructured solutions and their role in the nucleation of DL-valine crystals," *Faraday Discussions*, 29 January 2015.
- [36] M. Sedlak, "Large-Scale Supramolecular Structure in Solutions of Low Molar Mass Compounds and Mixtures of Liquids: I. Light Scattering Characterization," *Journal of Physical Chemistry*, pp. 4329-4388, 2006.

- [37] M. Sedlak, "Large-Scale Supramolecular Structure in Solutions of Low Molar Mass Compounds and Mixtures of Liquids: II. Kinetics of the Formation and Long-Time Stability," *Journal of Physical Chemistry*, pp. 4339-4345, 2006.
- [38] M. Sedlak, "Large-Scale Supramolecular Structure in Solutions of Low Molar Mass Compounds and Mixtures of Liquids: III. Correlation with Molecular Properties and Interactions," *Journal of Physical Chemistry*, pp. 13976-13984, 2006.
- [39] A. D. Dinsmore, P. L. Dubin and G. M. Grason, "Clustering in Complex Fluids," *Journal of Physical Chemistry B*, pp. 7173-7174, 2011.
- [40] S. E. McLain, A. K. Soper, I. Daidone, J. C. Smith and A. Watts, "Charged-based interactions between peptides observed as the dominant force for association in aqueous solution," *Angewandte Chemie*, pp. 9059-9062, 2008.
- [41] J. Groenewold and W. K. Kegel, "Anomalously Large Equilibrium Clusters of Colloids," *Journal of Physical Chemistry*, vol. 105, pp. 11702-11709, 2001.
- [42] O. Gliko, W. Pan, P. Katsonis, N. Neumaier, O. Galkin, S. Weinkauf and P. G. Vekilov, "Metastable Liquid Clusters in Super- and Undersaturated Protein Solutions," *Journal of Physical Chemistry*, vol. 111, pp. 3106-3114, 2007.
- [43] Y. Georgalis, A. M. Kierzek and W. Saegner, "Cluster Formation in Aqueous Electrolyte Solutions Observed by Dynamic Light Scattering," *Journal of Physical Chemistry*, pp. 3405-3406, 2000.
- [44] M. R. Ward, S. W. Botchway, A. D. Ward and A. J. Alexander, "Second-harmonic scattering in aqueous urea solutions: evidence for solute clusters?," *Faraday Discussions*, vol. 167, pp. 441-454, 17 June 2013.

- [45] M. C. Stumpe and H. Grubmuller, "Aqueous Urea Solutions: Structure, Energetics, and Urea Aggregation," *Journal of Physical Chemistry B*, vol. 111, no. 22, pp. 6220-6228, 19 March 2007.
- [46] M. Abu-Hamdiyyah, "The Effect of Urea on the Structure of Water and Hydrophobic Bonding," *Journal of Physical Chemistry*, vol. 69, no. 8, pp. 2720-2725, 5 March 1965.
- [47] M. Salvalaglio, C. Perego, F. Giberti, M. Mazzotti and M. Parrinello, "Molecular dynamics simulations of urea nucleation from aqueous solution," *PNAS*, pp. 614, 6 November 2014.
- [48] C. Sun and D. Xue, "IR Spectral Study of Mesoscale Process during Urea Crystallization from Aqueous Solution," *Crystal Growth & Design*, vol. 15, pp. 2867-2873, 12 May 2015.
- [49] S. Hamad, C. E. Hughes, R. A. Catlow and K. D. Harris, "Clustering of Glycine Molecules in Aqueous Solution Studied by Molecular Dynamics Simulation," *Journal of Physical Chemistry*, vol. 112, pp. 7280-7288, 5 March 2008.
- [50] A. Jawor-Baczynska, B. D. Moore, H. S. Lee, A. V. McCormick and J. Sefcik, "Population and size distribution of solute-rich mesospecies within mesostructured aqueous amino acid solutions," *Faraday Discussions*, vol. 167, pp. 425-440, 23 May 2013.
- [51] S. Jiang and J. H. ter Horst, "Crystal Nucleation Rates from Probability Distributions of Induction Times," *Crystal Growth and Design*, vol. 11, pp. 2562-61, November 2010.
- [52] R. Finsy, "Particle Sizing by Quasi-Elastic Light Scattering," in *Advances in Colloid and Interface Science*, Elsevier Science, 1994.

- [53] Filipe, Hawe and Jiskoot, "Critical Evaluation of Nanoparticle Tracking Analysis (NTA) by Nanosight for the Measurement of Nanoparticles and Protein Aggregates," *Pharmaceutical Research*, pp. 796-810, May 2010.
- [54] K. G. Neoh, M. Li and E.-T. Kang, "Characterization of Nanomaterials/Nanoparticles," in *Nanotechnology in Endodontics*, A. Kishen, Ed., Springer, 2015, p. 25.
- [55] [Online]. Available: http://www.engineeringtoolbox.com/water-dynamickinematic-viscosity-d_596.html. [Accessed November 2015].
- [56] A. S. Myerson, *Handbook of Industrial Crystallisation*, Second ed., Butterworth-Heinemann, 2001, p. 22.
- [57] M. A. Motin, T. K. Biswas and E. M. Huque, "Volumetric and Viscometric Studies on an Aqueous Urea Solution," *Physics and Chemistry of Liquids*, vol. 40, no. 5, pp. 593-605, 2002.
- [58] Malvern, "Malvern Zetasizer Nano User Manual," Malvern, September 2015. [Online]. Available: <http://www.malvern.com/en/>.
- [59] R. F. Domingos, M. A. Baalousha, Y. Ju-Nam, M. M. Reid, N. Tufenkji, J. R. Lead, G. G. Leppard and K. J. Wilkinson, "Characterizing Manufactured Nanoparticles in the Environment: Multimethod Determination of Particle Sizes," *Journal of Environmental Science and Technology*, pp. 7277-7284, 2009.
- [60] J. A. Gallego-Urrea, J. Tuoriniemi and M. Hasselov, "Applications of particletracking analysis to the determination of size distributions and concentrations of nanoparticles in environmental, biological and food samples," *Trends in Analytical Chemistry*, vol. 30, pp. 473-483, 3 November 2011.
- [61] A. Einstein, "Investigations on the theory of the Brownian movement," *Ann. d.*

Phys., p. 549, 1905.

- [62] P. Austria, "Brownian Motion Manual," 2008.
- [63] R. Newburgh, J. Peidle and W. Rueckner, "Einstein, Perrin and the reality of atoms:1905 revisited," *American Association of Physics Teachers*, pp. 478-481, 2006.
- [64] J. Sefcik, *CP511 Colloid Engineering*, 2011.
- [65] T. Paakkonen, M. Riihimäki, E. Puhakka, E. Muurinen, C. Simonson and R. Keiski, "Crystallization Fouling of CaCO₃ - Effect of Bulk Precipitation on Mass Deposition on the Heat Transfer Surface," in *Heat Exchanger Fouling and Cleaning*, Schlading, 2009.
- [66] T. Geddert, W. Augustin and S. Scholl, "Influence of surface defects and aging of coated surfaces on fouling behaviour," in *Heat Exchanger Fouling and Cleaning*, Schlading, 2009.
- [67] T. Geddert, I. Bialuch, W. Augustin and S. Scholl, "Extending the induction period of crystallization fouling through surface coating," in *Heat Exchanger Fouling and Cleaning*, Tomar, 2007.
- [68] G. Wang, L. Zhu, H. Liu and W. Li, "Zinc-graphite composite coating for antifouling application," *Materials Letters*, pp. 3095-3097, 2011.
- [69] F. Brahim, W. Augustin and M. Bohnet, "Numerical simulation of the fouling process," *International Journal of Thermal Sciences*, pp. 323-334, 2002.
- [70] M. Bohnet, W. Augustin and H. Hirsch, "Influence of fouling layer shear strength on removal behaviour," in *Understanding Heat Exchanger Fouling and its Mitigation*, New York, United Engineering Foundation and Begell House, 1997, pp. 201-208.

- [71] M. Forster, W. Augustin and M. Bohnet, "Influence of the adhesion force crystal/heat exchanger surface on fouling mitigation," *Chemical Engineering and Processing*, pp. 449-461, 1999.
- [72] M. Vendel and A. C. Rasmuson, "Mechanisms of Initiation of Incrustation," *American Institute of Chemical Engineers*, pp. 1300-1308, 1997.
- [73] G. Di Profio, E. Fontananova, E. Curcio and E. Drioli, "From Tailored Supports to Controlled Nucleation: Exploring Material Chemistry, Surface Nanostructure, and Wetting Regime Effects in Heterogeneous Nucleation of Organic Molecules," *Crystal Growth and Design*, pp. 3749-3757, 2012.
- [74] V. Lopez-Mejías, J. L. Knight, C. L. Brooks III and A. J. Matzger, "On the Mechanism of Crystalline Polymorph Selection by Polymer Heteronuclei," *Langmuir*, pp. 7575-7579, 2011.
- [75] K. Chadwick, A. Myerson and B. Trout, "Polymorphic control by heterogeneous nucleation - A new method for selecting crystalline substrates," *CrystEngComm*, pp. 6625-6627, 2011.
- [76] S. J. Bonafede and M. D. Ward, "Selective Nucleation and Growth of an Organic Polymorph by Ledge-Directed Epitaxy on a Molecular Crystal Substrate," *American Chemical Society*, pp. 7853-7861, 1995.
- [77] C. A. Mitchell, L. Yu and M. D. Ward, "Selective Nucleation and Discovery of Organic Polymorphs through Epitaxy with Single Crystal Substrates," *American Chemical Society*, pp. 10830-10839, 2001.
- [78] P. A. Levkin, F. Svec and J. M. Frechet, "Porous Polymer Coatings: a Versatile Approach to Superhydrophobic Surfaces," *Advanced Functional Materials*, pp. 1-6, 2009.

- [79] "SPIE," [Online]. Available: <http://spie.org/x19008.xml>. [Accessed 1 November 2012].
- [80] A. Y. Lee, I. S. Lee, S. S. Dette, J. Boerner and A. S. Myerson, "Crystallization on Confined Engineered Surfaces: A Method to Control Crystal Size and Generate Different Polymorphs," *American Chemical Society*, pp. 14982-14983, 2005.
- [81] K. Kim, I. S. Lee, A. Centrone, T. A. Hatton and A. S. Myerson, "Formation of Nanosized Organic Molecular Crystals on Engineered Surfaces," *American Chemical Society*, pp. 18212-18213, 2009.
- [82] K. Kim, A. Centrone, T. A. Hatton and A. S. Myerson, "Polymorphism control of nanosized glycine crystals on engineered surfaces," *CrystEngComm*, pp. 11271131, 2010.
- [83] Y. Diao, M. E. Helgeson, Z. A. Siam, P. S. Doyle, A. S. Myerson, T. A. Hatton and B. L. Trout, "Nucleation under Soft Confinement: Role of Polymer-Solute Interactions," *Crystal Growth and Design*, pp. 508-517, 2011.
- [84] P. Maiti and M. Okamoto, "Crystallization Controlled by Silicate Surfaces in Nylon 6-Clay Nanocomposites," *Macromolecular Materials and Engineering*, pp. 440-445, 2003.
- [85] K. K. Wong, B. J. Brisdon, B. R. Heywood, A. G. Hodson and S. Mann, "Polymermediated Crystallisation of Inorganic Solids: Calcite Nucleation on the Surfaces of Inorganic Polymers," *Journal of Material Chemistry*, pp. 1387-1392, 1994.
- [86] E. Manzurola and A. Apelblat, "Solubilities of L-glutamic acid, 3-nitrobenzoic acid, p-toluic acid, calcium-L-lactate, calcium gluconate, magnesium-DL-aspartate, and magnesium-L-lactate in water," *J. chem. Thermodynamics*, pp. 1127-1136, 2002.

- [87] H. D. Belitz, W. Grosch and P. Schieberle, Food Chemistry, 4th Edition ed., Springer, 2009, p. 15.
- [88] M. Jelinska-Kazimierczuk and J. Szydlowski, "Isotope effect on the solubility of amino acids in water," *Journal of Solution Chemistry*, vol. 25, pp. 1175-1184, 1996.
- [89] N. Reis, A. P. Harvey, M. R. Mackley, A. A. Vicente and J. A. Teixeira, "Fluid mechanics and design aspects of a novel oscillatory flow screening mesoreactor," *Chemical Engineering Research and Design*, vol. 83, no. A4, pp. 357-371, 2005.
- [90] M. S. Abbott, A. P. Harvey, G. Valente Perez and M. K. Theodorou, "Biological processing in oscillatory baffled reactors: operation, advantages and potential," *Interface Focus*, vol. 3, 2013.
- [91] T. McGlone, N. E. Briggs, C. A. Clark, C. J. Brown and J. Sefcik, "Oscillatory Flow Reactors (OFRs) for Continuous Manufacturing and Crystallization," *Organic Process Research & Development*, vol. 19, pp. 1186-1202, 2015.
- [92] P. Stonestreet and A. Harvey, "A Mixing-Based Design Methodology for Continuous Oscillatory Flow Reactors," *ICHEME*, pp. 31-43, 31-43.
- [93] X.-W. Ni, "Continuous Oscillatory Baffled Reactor Technology," *Innovations in Pharmaceutical Technology*, pp. 90-96, 2006.
- [94] N. Briggs, "Polymorph Control of Pharmaceuticals within a Continuous Oscillatory Baffled Crystalliser," Glasgow, 2015.
- [95] L. L. Simon, K. Z. Nagy and K. Hungerbuhler, "Endoscopy-Based in Situ Bulk Video Imaging of Batch Crystallization Processes," *Organic Process Research & Development*, pp. 1254-1261, 2009.

- [96] H. Qu, M. Louhi-Kultanen and J. Kallas, "In-line image analysis on the effects of additives in batch cooling crystallization," *Journal of Crystal Growth*, pp. 286294, 2005.
- [97] D. Sarkar, X.-T. Doan, Z. Ying and R. Srinivasan, "In situ particle size estimation for crystallization processes by multivariate image analysis," *Chemical Engineering Science*, pp. 9-19, 2009.
- [98] D. J. Hoff and P. J. Olver, "Extensions of Invariant Signatures for Object Recognition".
- [99] C. J. Brown and X.-W. Ni, "Evaluation of Growth Kinetics of Antisolvent Crystallization of Paracetamol in an Oscillatory Baffled Crystallizer Utilizing Video Imaging," *Crystal Growth and Design*, pp. 3994-4000, 2011.
- [100] W. T. Kim, C. Bai and Y. I. Cho, "A study of CaCO₃ fouling with a microscopic imaging technique," *International Journal of Heat and Mass Transfer*, pp. 597607, 2001.
- [101] C. Tachtatzis, R. Sheridan, C. Michie, R. C. Atkinson, A. Cleary, J. Dziewierz, I. Andonovic, N. Briggs, A. J. Florence and J. Sefcik, "Image-based monitoring for early detection of fouling in crystallisation processes," *Chemical Engineering Science*, 2015.
- [102] J. Dziewierz, *Timestamp Recognition*, 2014.
- [103] R. P. Adams and D. J. MacKay, "Bayesian Online Change-point Detection," 2007.
- [104] M. Jelinska-Kazimierczuk and J. Szydlowski, "Isotope Effect on the Solubility of Amino Acids in Water," *Journal of Solution Chemistry*, vol. 25, no. 12, pp. 11751184, August 1996.

- [105] G. Kumaraswamy, A. M. Issaian and J. A. Kornfield, "Shear-Enhanced Crystallization in Isotactic Polypropylene.," *Macromolecules*, vol. 32, pp. 7537-7547, 1999.
- [106] E. Koscher and R. Fulchiron, "Influence of shear on polypropylene crystallization: morphology development and kinetics," *Polymer*, vol. 43, pp. 6931-6942, 2002.
- [107] L. A. Pinck and M. A. Kelly, "The Solubility of Urea in Water," *Journal of the American Chemical Society*, vol. 47, no. 8, pp. 2170-2172, 1925.
- [108] D. A. Dahlstrom, R. C. Bennett, R. G. Emmet, P. Harriot, T. Laros, W. Leung, S. A. Miller, B. Morey, J. Y. Oldshue, G. Priday, C. E. Silverblatt, J. S. Slottee and J. C. Smith, "Crystallization from Solution," in *Perry's Chemical Engineers' Handbook*, 7th Edition ed., McGraw Hill, 1999.
- [109] N. Rodriguez-Hornedo and D. Murphy, "Significance of Controlling Crystallization Mechanisms and Kinetics in Pharmaceutical Systems," *Journal of Pharmaceutical Science*, pp. 651-666, 1999.